THE NATURE AND ORIGIN OF THE BONANZA-GRADE BRUCEJACK EPITHERMAL AU-AG DEPOSIT, NORTHWESTERN BRITISH COLUMBIA

by

Duncan Forbes McLeish

November 2022

A thesis submitted in partial fulfillment
of the requirements for the degree of

DOCTOR OF PHILOSOPHY

Department of Earth and Planetary Sciences
McGill University
Montreal, QC, Canada

© Duncan F. McLeish, 2022

Abstract

Hydrothermal veins supply much of the Earth's gold. Their propensity to contain ultra-high-grade, or 'bonanza', concentrations of gold that are millions of times greater than the concentration of gold in the Earth's crust makes them important targets for exploration and resource development. The mechanisms by which such hyper-enrichment occurs are enigmatic. The accepted wisdom is that this enrichment reflects the saturation and precipitation of gold as crystals from hydrothermal fluids. Laboratory experiments and measurements of active hydrothermal systems, however, have shown that the solubility and concentration of this noble metal in typical ore-forming fluids are, respectively, exceptionally low. For example, gold concentrations in the fluids responsible for epithermal mineralisation are typically on the order of 10-30 ppb, which are far too low to explain concentrations of 10's of thousands grams per tonne Au in veins in some deposits. The formation of such high-grade veins by direct precipitation of native gold or electrum from the ore fluids would require that individual fractures remain open for unreasonably long periods of time (e.g., >100,000 years) or that fluid fluxes be extraordinary.

A potential solution to the paradox of ultra-high-grade gold ore formation, in a geologically realistic time-frame, is offered by the physical transport of gold in the solid state as electrically charged nanoparticles (i.e., colloidal suspensions) which flocculate to produce aggregates of gold. This study investigates gold mineralisation from the Valley of the Kings (VOK) and Eastern Promises (EP) zones of Brucejack, a large and exceptionally high-grade epithermal gold-silver deposit in British Columbia's Stewart-Eskay District, to evaluate this possibility. Images obtained using transmitted electron microscopy show that: (1) gold commonly occurs as < 1-10 nm spherical nanocrystals of electrum embedded within a calcite matrix; and (2) larger (100-500 nm) particles of electrum, also embedded in calcite, are composed of hundreds of nanoparticles, each displaying distinct crystal lattice plane orientations. These images provide compelling evidence for the formation of colloidal suspensions of gold (electrum) and their flocculation.

To better understand how flocculation occurs in a hydrothermal system, this study also examines the trace element and sulphur isotope signatures of pre- and rare syn-electrum pyrite at Brucejack. Secondary ion mass spectrometry (SIMS), laser ablation-inductively coupled plasma-mass spectrometry (LA-ICP-MS), and electron microprobe wavelength-dispersive X-ray

spectroscopy (EMP-WDS), reveal that the Brucejack hydrothermal system experienced a series of abrupt changes in fluid chemistry, which preceded and ultimately coincided with the onset of ultra-high-grade gold-silver mineralisation. These changes, which include the occurrence of extraordinarily negative $\delta^{34}S$ values (e.g., -36.0‰) in zones of pre-electrum, auriferous, arsenian pyrite, followed by sharp increases of $\delta^{34}S$ in syn-electrum zones of non-arsenian pyrite, were caused by vigorous, episodic boiling and subsequent inundation of the hydrothermal system by seawater. This influx of seawater was an essential step in creating bonanza electrum mineralisation by triggering the aggregation of colloidal gold suspensions through the addition of cationic flocculants and cooling.

LA-ICP-MS, EMP-WDS and SIMS analyses of early pyrite veins at Brucejack have also revealed that the early mineralising fluids at Brucejack were of magmatic hydrothermal origin, as evidenced by pyrite crystal cores that are relatively rich in Co and Ni and the relatively high temperatures estimated by S-isotope exchange thermometry for associated barite-pyrite mineral pairs. The Co-Ni pyrite cores are mantled by oscillatory, locally colloform pyrite growth zones that are relatively rich in Au and As and record an evolution to epithermal-type fluids during telescoping of the hydrothermal system. A narrow, outer Co-Ni growth zone commonly mantles the As-Au oscillatory zones in the early pyrite crystals, indicating a possible reversal in telescoping. All of this hydrothermal activity predated the emplacement of bonanza-grade epithermal quartz-carbonate veins, which crosscut early pyrite veins throughout the deposit. Inspired by the observation that the epithermal quartz-carbonate veins commonly contain bonanza gold where these veins cross-cut earlier pyrite veins, a model is proposed, in which charged surfaces on p-type oscillatory arsenian growth zones in Stage I pyrite electrochemically destabilise, through cationic bridging, colloidal gold suspensions circulating in the epithermal quartz-carbonate veins. This destabilisation triggers flocculation of the colloidal gold particles and the deposition of gold in bonanza concentrations.

The electrochemical flocculation of colloidal gold by semiconductive p-type arsenian pyrite offers a novel explanation for how bonanza gold may form paragenetically late in hydrothermal ore deposits, i.e., after the vast majority of sulphide mineral deposition has occurred, without the need for phase separation (boiling) or the existence of steep physicochemical gradients. The process worked in tandem with seawater mixing at Brucejack to produce a large, high-grade gold resource.

Résumé

Les veines hydrothermales fournissent une grande partie de l'or de la Terre. Leur propension à contenir des concentrations d'or à très haute teneur, ou « bonanza », qui sont des millions de fois supérieures à la concentration d'or dans la croûte terrestre, en fait des cibles importantes pour l'exploration et le développement des ressources. Les mécanismes par lesquels un tel hyper-enrichissement se produit sont énigmatiques. La sagesse conventionnelle est que cet enrichissement reflète la saturation et la précipitation de l'or sous forme de cristaux à partir de fluides hydrothermaux. Des expériences en laboratoire et des mesures de systèmes hydrothermaux actifs ont cependant montré que la solubilité et la concentration de ce métal noble dans les fluides minéralisateurs typiques sont, respectivement, exceptionnellement faibles. Par exemple, les concentrations d'or dans les fluides responsables de la minéralisation épithermale sont généralement de l'ordre de 10 à 30 ppb (parties par milliard), ce qui est bien trop faible pour expliquer des concentrations de dizaines de milliers de grammes par tonne d'Au dans les filons de certains gisements. La formation de tels filons à haute teneur par précipitation directe d'or natif ou d'électrum à partir des fluides minéralisants nécessiterait que les fractures restent ouvertes pendant des périodes de temps excessivement longues (par exemple, > 100 000 ans) ou que les flux de fluides soient extraordinaires.

Une solution potentielle au paradoxe de la formation de minerai d'or à très haute teneur, dans un laps de temps géologiquement réaliste, est offerte par le transport physique de l'or à l'état solide sous forme de nanoparticules chargées électriquement (i.e., des suspensions colloïdales) qui floculent pour produire des agrégats d'or. Cette étude examine la minéralisation aurifère des zones Valley of the Kings (VOK) et Eastern Promises (EP) de Brucejack, un vaste gisement d'or-argent épithermal à teneur exceptionnellement élevée dans le district de Stewart-Eskay en Colombie-Britannique, afin d'évaluer cette possibilité. Les images obtenues par microscopie électronique en transmission montrent que : (1) l'or se présente généralement sous la forme de nanocristaux sphériques d'électrum de < 1 à 10 nm contenus dans une matrice de calcite ; et (2) des particules d'électrum plus grandes (100-500 nm), également dans la calcite et composées de centaines de nanoparticules, affichant des orientations diverses de leur réseau cristallin. Ces images fournissent des preuves convaincantes de la présence de suspensions colloïdales d'or (électrum) et de leur floculation.

Pour mieux comprendre comment la floculation se produit dans un système hydrothermal, cette étude examine également les signatures des éléments traces et des isotopes du soufre de la pyrite pré- et, rarement, syn-électrum à Brucejack. La spectrométrie de masse à ions secondaires (SIMS), la spectrométrie de masse à plasma à couplage inductif par ablation laser (LA-ICP-MS) et la spectroscopie de rayons X à dispersion de longueur d'onde par microsonde électronique (EMP-WDS) révèlent que le système hydrothermal de Brucejack a connu une série de changements brusques dans la chimie des fluides, qui ont précédé et finalement coïncidé avec l'apparition d'une minéralisation d'or-argent à très haute teneur. Ces changements, qui comprennent l'apparition de valeurs $\delta^{34}S$ extraordinairement négatives (par exemple, -36,0‰) dans les zones de pré-électrum, aurifère, pyrite arsénifère, suivies de fortes augmentations de $\delta^{34}S$ dans les zones syn-électrum de pyrite sans arsenic, ont été causés par une ébullition vigoureuse et épisodique et l'inondation subséquente du système hydrothermal par l'eau de mer. Cet afflux d'eau de mer a été une étape essentielle dans la création d'une minéralisation bonanza d'électrum en déclenchant l'agrégation de suspensions d'or colloïdal par l'ajout de floculants cationiques et par le refroidissement.

Les analyses LA-ICP-MS, EMP-WDS et SIMS des filons précoces de pyrite à Brucejack ont également révélé que leurs fluides minéralisants à Brucejack étaient d'origine hydrothermale magmatique, comme en témoignent les cœurs des cristaux de pyrite relativement riches en Co et Ni et les des températures relativement élevées estimées par thermométrie d'échange isotopique S pour les paires minérales barytine-pyrite associées. Les cœurs de pyrite avec Co-Ni sont suivis de pyrite a zonation oscillatoire localement colloformes relativement riches en Au et en As et enregistrent une évolution vers des fluides de type épithermique lors du télescopage du système hydrothermal. Une étroite bordure de croissance Co-Ni recouvre généralement les zones oscillatoires As-Au dans les cristaux précoces de pyrite, indiquant une inversion possible du télescopage. Toute cette activité hydrothermale est antérieure à la mise en place des filons épithermaux de quartz-carbonate de qualité bonanza, qui recoupent les filons précoces de pyrite dans tout le gisement. Inspiré par l'observation que les filons épithermaux de quartz-carbonate contiennent généralement de l'or de qualité bonanza là où ces filons recoupent des filons de pyrite antérieures, un modèle est proposé, dans lequel des surfaces chargées sur des zones oscillatoires arsénifères au caractère semi-conducteur de type P dans la pyrite de Stade I déstabilisent électrochimiquement, par pontage cationique, les suspensions d'or colloïdal

circulant dans les conduits épithermales de quartz-carbonate. Cette déstabilisation déclenche la floculation des particules d'or colloïdal et le dépôt d'or à des concentrations bonanza.

La floculation électrochimique de l'or colloïdal par la pyrite arsénifères semi-conductrice de type P offre une nouvelle explication de la façon dont l'or bonanza peut se former tardivement dans les gisements de minerai hydrothermaux, c'est-à-dire après la précipitation des principaux sulfures d'un gisement, sans qu'il soit nécessaire d'invoquer une ébullition ou l'existence de forts gradients physico-chimiques. Le processus a fonctionné en tandem avec un apport d'eau de mer à Brucejack pour produire une importante ressource aurifère à haute teneur.

Frontispiece: Aerial view of the Brucejack deposit showing the location of its main mining (Valley of the Kings) and exploration (Eastern Promises, West, Flow Dome, Shore, Gossan Hill, SG and Golden Marmot) zones. This photograph was taken by the author on August 16, 2012, approximately five years prior to the Brucejack mine entering production.

Table of Contents

List of Figures

List of Tables

Acknowledgements

First and foremost, I wish to express my profound thanks and gratitude to Dr. Anthony E. Williams-Jones for his patient mentorship, enthusiastic encouragement, and, most of all, his sharp sense of wit and humour – all of which have been generously provided over the course of this project. Willy, beyond your supervision, you have inspired me to think 'outside the box' in every facet of life and have shown me the value of cogent scientific writing.

I am also deeply indebted to my original industry supervisor, Dr. Warwick Board (former Vice President of Geology, Pretium Resources Inc.) for, on a cold fall day in 2014, buying into the original idea for the thesis and subsequently giving it your unwavering support throughout your tenure with Pretium. In addition, Warwick, I would like to thank you for sharing your extensive knowledge on the often challenging yet always fascinating geology of the Brucejack deposit, both in the field and during lively discussions in Vancouver and Montreal. Also with Pretium, Dr. Stephanie Wafforn and Barry McDonough are thanked for generously offering their continued support following Warwick's departure. Last but not least from Pretium, Joel Ashburner, Susan Flasha, Sean Tombe, Matt McManus, Octavia Bath, Travis Murphy, Travis Dawson, and all the other mine site geologists whom I had the good fortune of working with are thanked for their support, insightful discussions, guidance, and overall good camaraderie.

At McGill University, Jim Clark and Olga Vasyukova are thanked for their valuable critical comment and helpful suggestions during manuscript preparation. Members of my advisory committee, Dr. Jeanne Paquette in particular, are thanked for always making time to discuss all aspects of my project. I am grateful for the many friendships made with my fellow graduate students, and for the help that they provided with analytical techniques and navigating the department, especially in the early days. At the University of Ottawa, Glenn Poirier is thanked for his expert support and general wizardry with electron microprobe analyses, following the helpful initial microprobe support of Lang Shi at McGill. Dr. Richard Stern at the University of Alberta and Dany Savard and Audrey Lavoie at Université du Québec à Chicoutimi are thanked for their skilled assistance with secondary ion mass spectrometry and laser ablation ICP-MS analyses, respectively.

Finally, I would like to sincerely thank my wife Caroline and my family for always being there for me over the past seven years. Without your steadfast support, generous encouragement, and overall understanding, this thesis would not have been possible.

Preface and Contributions from Authors

This thesis contains three research articles, the first of which has been published in the journal *The Proceedings of the National Academy of Sciences* (Chapter 2); the second has been submitted to the journal *Geology* (Chapter 3); and the third is in preparation for submission to the journal *Economic Geology* (Chapter 4). The research articles all report the results of a study designed to address the fundamental question of how the hyper-enrichment of gold occurs in nature based on evidence amassed from the high-grade Brucejack epithermal Au-Ag deposit in northwestern British Columbia, Canada. Fieldwork for this thesis was carried out over four summers (2016-2019) and included drill core logging, underground- and surface-based geological mapping, and sample collection. Pretium Resources Inc. (Pretium) provided access to the deposit, as well as logistical and geological support during this fieldwork.

The author carried out the sample preparation (rock slab/billet cutting) at McGill university (McGill) and performed the analyses using the following instruments: scanning electron microscope (SEM; McGill, University of Ottawa), electron microprobe (EMP; McGill, University of Ottawa; UOttawa), transmission electron microscope (TEM; McGill), laser ablation-inductively coupled plasma-mass spectrometer (LA-ICP-MS; Université du Québec à Chicoutimi; UQAC), and secondary ion mass spectrometer (SIMS; University of Alberta; UAlberta). Assistance with these instruments was generously provided by Lang Shi (SEM and EMP) and David Liu (TEM) at McGill, Glenn Poirier at UOttawa, Dany Savard and Audrey Lavoie at UQAC, and Richard Stern at UAlberta.

The research articles were written by the author and edited by Anthony Williams-Jones (AWJ), the research supervisor, and James Clark (JC), a research associate with AWJ. AWJ and JC also helped the author interpret the data presented in each of the research articles presented in this thesis. Additional data interpretation and editing assistance were provided by Olga Vasyukova, research associate with AWJ, Warwick Board (WB), former Vice President of Geology for Pretium (Chapter 2), and Richard Stern, managing director of the Canadian Centre for Isotopic Microanalysis (Chapter 3). A modified version of the section entitled "A short history of the Brucejack Au-Ag deposit" in Chapter 1 has previously been published in a research article which the thesis author wrote as a first co-author with WB (see Board et al., 2020, in the Chapter 1 reference list).

CHAPTER 1

Introduction

1.1 General statement

This thesis in economic geology addresses the fundamental question of how the hyper-enrichment of gold occurs in nature. Specifically, by investigating ultra-high-grade mineralisation of the Brucejack epithermal gold-silver deposit in British Columbia, it examines the physicochemical and electrochemical processes that lead to the formation of extreme, 'bonanza'-type accumulations of gold in hydrothermal veins. This chapter: (1) introduces the geology of epithermal deposits and the current problems that affect our understanding of the bonanza gold mineralisation that some of them contain, (2) reviews the evolution of their classification, and (3) provides an overview of the Brucejack area, including a short summary of its exploration and mining history.

1.2 Geology of epithermal gold deposits and motivation for study

The term epithermal was first used by Lindgren (1913) to refer to shallow, relatively low-temperature mineral deposits within a vertically zoned hydrothermal system. Over time, this term has become synonymous with low temperature hydrothermal precious metal deposits formed at shallow depths (i.e., ~100 to 300 °C and 0 to 1,500 m below the paleosurface; John et al., 2018), and descriptors have been added to distinguish several sub-types. Thus, the terms acid-sulphate and adularia-sericite have been used to describe the alteration associated with epithermal deposits proximal to volcanic edifices and those distal from them, respectively (Hayba et al., 1985; Heald et al., 1987). These modifiers have since been supplanted by the terms 'high-sulphidation' and 'low-sulphidation', respectively, which distinguish deposits on the basis of the oxidation state of sulphur in the ore-forming system implied by the sulphide (and sulphate) mineral assemblage (Hedenquist, 1987; Hedenquist and Lowenstern, 1994). Since the early 2000s, a third term, 'intermediate-sulphidation' has been used to refer to epithermal deposits which are characterised by a sulphide mineralogy transitional between that of the high- and low-sulphidation types (Hedenquist et al., 2000; Einaudi et al., 2003; Sillitoe and Hedenquist, 2003). The differences in the mineralogy of these epithermal styles have been attributed to their different geological settings. High-sulphidation epithermal deposits are believed to form from magmatic-hydrothermal fluids, although there is considerable debate over whether these fluids are dominated by liquids or vapours (e.g., Hedenquist et al., 1998; Williams-Jones and Heinrich, 2005). Low-sulphidation epithermal deposits occur distal to magmatic intrusions (which are

commonly host to 'porphyry'-type deposits) or otherwise lack a demonstrable association with magmatic rocks, and form from fluids that are dominantly meteoric (Corbett and Leach, 1998 and references therein). Many low- and intermediate-sulphidation epithermal deposits have characteristics analogous to those of modern geothermal systems (Clark and Williams-Jones, 1990). Intermediate-sulphidation deposits, which are characterised by alteration assemblages similar to those of low-sulphidation (adularia-sericite) deposits, have a distal relationship with magmatic rocks. The fluids forming them are dominantly meteoric but, in some cases, a magmatic component has been recognised (e.g., Vikre, 1989). Although a consensus is emerging that intermediate- and high-sulphidation deposits are the distal and proximal representatives of subduction-related magmatic-hydrothermal systems, there are still many questions to be addressed before it will be possible to develop a comprehensive understanding of the genesis of these deposits.

Epithermal gold deposits are most commonly associated with subduction-related, calc-alkaline to bimodal magmatism in island arc and active continental margin settings (Sawkins, 1972; 1990). In these environments, many epithermal deposits have a close spatial relationship with coeval higher-temperature porphyry copper-gold deposits (Sillitoe and Hedenquist, 2003). Although this spatial and temporal relationship is widely recognised in volcanic arc terranes, a dearth of detailed geological, geochemical and geochronological data has inhibited investigations of the mechanisms controlling their formation and their genetic relationships to porphyry ore-forming magmatic-hydrothermal systems. For example, in Canada, only one integrated, district-scale lithogeochemical and geochronological study has evaluated the source of epithermal gold mineralisation and its possible link to spatially related porphyry deposits (Duuring et al., 2009; Toodoggone district of British Columbia). In the Stewart-Eskay Creek district that hosts Brucejack, numerous geological mapping, geochronological, and, to a lesser extent, geochemical studies have been conducted on many of the major porphyry and porphyry-epithermal systems, including Brucejack and the neighbouring 'supergiant' porphyry Cu-Au deposit Kerr-Sulphurets-Mitchell-Iron Cap (KSM; see Chapter 4). However, the extent to which the epithermal deposits in the district can be placed in the epithermal classification scheme described above, the implications which this classification has for their genesis, and their relationship to spatially related deposits are poorly known.

In addition to uncertainties regarding the classification of epithermal deposits and their relationships with other mineralisation types, a major impediment to the development of robust genetic models for bonanza-style epithermal gold deposits, which can have exceptionally large resources (e.g., Brucejack; 10.7 million oz Au and 62.5 million oz Ag; Tetra Tech, 2020), is our incomplete understanding of the mechanisms of gold transport in epithermal systems in general. If, as is typically assumed, the gold is transported in solution by a hydrothermal fluid at relatively low temperature, then the limited solubility of gold in the putative ore fluid makes it difficult to explain the development of very large, high-grade resources. Although a process like boiling can lead to high grades due to the rapid loss of the ligand (e.g., HS^-) and the accompanying sharp drop in temperature (Williams-Jones et al., 2009), extraordinarily large volumes of fluid are required to account for the mass of metal in large high-grade systems. Based on our knowledge of the geothermal systems with which low-sulphidation systems, are equated, such large volumes of fluid are probably not realistic in the lifespan of a typical porphyry-epithermal deposit (see McLeish et al., 2021 and references therein). Alternatives that need to be considered are: (1) that the temperatures commonly assumed for metal transport greatly underestimate the true temperature because they are based on data that estimate the conditions of deposition; and (2) that transport is not controlled by simple solubility. If the fluid were of magmatic origin (supercritical liquid- or vapour-like), then the gold solubility could be orders of magnitude higher and the volume of fluid required much smaller. Moreover, if the thermal gradient were steep enough, as might be the case with phase separation (boiling), the gold might assume a colloidal form and thereby be available for further transport as nanoparticles in suspension (see Williams-Jones et al., 2009, and reference therein); in such cases, solubility limits associated with conventional models for the transport of gold in solution would not apply.

From a mineral resource standpoint, epithermal gold deposits are an important exploration target because they host a significant portion (~13 %) of the world's total known near-surface gold endowment (Lipson, 2014). Moreover, while ultra-high-grade, or 'bonanza' concentrations of gold occur in many types of hydrothermal deposits, approximately 60 % of Earth's bonanza gold veins occur in epithermal systems (Sillitoe and Hedenquist, 2003). Despite supplying a growing fraction of global gold production and receiving increased scientific attention in recent years, discovery rates for new epithermal gold deposits have been in decline since the 1990s (Kesler and Wilkinson, 2010; Schodde, 2011; Murphy, 2014). The reasons for

this decline are manifold, but a re-occurring issue is that current genetic models, which are essential guides to exploration, still do not satisfactorily explain the formation of many epithermal deposits (e.g., Groves et al., 2003; Cline et al., 2005; Wilkinson, 2013).

1.3 Overview of the Brucejack gold-silver deposit

1.3.1 Geologic framework

This section gives a brief, abstract-level overview of the geology of the Brucejack deposit to provide a framework for the subsequent sections in this chapter, as well as the research findings discussed in Chapters 2 and 3; a comprehensive description and discussion of deposit geology, including supporting references, is offered in Chapter 4.

Brucejack is a large and high-grade (15.7 million tons grading 8.4 g/t Au, 60 g/t Ag, and with individual veins grading up to 41,582 g/t Au in half-metre drill core intervals) intermediate- to low-sulphidation epithermal deposit located in the Stewart-Eskay mining district of northwestern British Columbia, Canada. The deposit is characterised by multi-generational sub-vertical quartz-carbonate-sulphide vein stockworks and subordinate vein breccias hosted primarily within a deformed island arc-related sequence of andesitic to latitic flows, lapilli tuffs, locally derived pyroclastic conglomerate and sandstone, and minor mudstone belonging to the Lower Jurassic Hazelton Group. Regionally, the deposit forms part of the Sulphurets Au-Ag-Cu camp, a 25 km long trend marked by gossans that hosts several world-class Cu-Au-(Mo) porphyry deposits (e.g., Kerr-Sulphurets-Mitchell, Snowfield) along a district scale unconformity between the Hazelton and Upper Triassic Stuhini Groups. Emplacement of the deposit was associated with ca. 183 Ma regional N-S extension and related deep-seated porphyry magmatism, both being late-stage manifestations of the Late Triassic-Early Jurassic development of the Stikine volcanic arc terrane. Nine main zones of mineralisation have been identified at Brucejack (West, Valley of the Kings, Flow Dome, Bridge, Gossan Hill, Shore, SG, Eastern Promises, and Golden Marmot zones; see Frontispiece and Chapter 4). Of these nine zones, only the Valley of the Kings, West, and Eastern Promises zones are, at present, sufficiently explored and drilled to support a mineral reserve estimate and mine plan. High-grade Au-Ag mineralisation in these zones occurs primarily as coarse aggregates of electrum within three intermediate-stage vein phases: (1) electrum-bearing deformed quartz-carbonate ± sericite stockwork veins and breccias, which, in the Valley of the Kings and Eastern Promises, are spatially associated with subvertical stringer quartz veinlets, also

hosting electrum; (2) Zn-Pb-(Cu) quartz-sulphide veins containing common Ag-sulphosalts and electrum; and (3) deformed carbonate ± quartz veins containing abundant orange-coloured, Mn-bearing calcite, and subordinate electrum and lesser Ag-sulphosalts.

1.3.2 Location and access

The Brucejack deposit is located within the Boundary Ranges of the Coast Mountains of northwestern British Columbia (NTS map sheet 104 B/8), 950 km north-northwest of Vancouver, 65 km north of Stewart, and 20 km south of the former Eskay Creek gold mine (Fig. 1.1). The deposit, which at the time of writing, is actively being mined and developed in its Valley of the Kings and West zones (Fig. 1.2; Chapter 4), is accessible via a loose-surface, all-season 65 km road and an 8 km all-season ice road built on the Knipple Glacier (Fig. 1.1) which together link the Brucejack camp to the provincially maintained, paved Highway 37 (Fig. 1.1).

1.3.3 Physiography

The Valley of the Kings zone has a surface extend of approximately 1000 x 600 m and occupies the central portion of a rugged, northeast-sloping alpine plateau located 1 km southwest of Brucejack Lake at approximately 1550 m asl (see Frontispiece photo). Moderate to strongly gossanous, variably silicified, glacially polished, northwest-trending ridges and crags, typically several decametres in scale, punctuate the plateau, which is surrounded and partially obscured by glacial till. Glacial ice covers the southeastern quadrant of the zone. All mineralised vein generations crop out, as do rare hydrothermal breccia and intermediate to mafic dykes (veins and host rocks are described in detail in Chapter 4). Cross-cutting relationships between veins, dykes, faults, alteration, and lithology observed underground are visible on the surface. Deep drilling has indicated that the alteration, mineralisation, and veining in this zone extend to a depth of at least 1,300 m. The mineralisation is open to the east, west, and at depth.

The West zone lies approximately 750 m north of the Valley of the Kings zone along the westernmost reach of Brucejack Lake at approximate 1450 m asl (Fig. 1.2; Chapter 4). From the lake, it extends south to the Brucejack mine camp, west to the Brucejack fault, forming a broadly

Figure 1.1 (next page): Brucejack deposit location map (modified from Pretium Resources Inc. unpublished maps, 2019).

Legend:
- ● Ancillary Facilities
- ■ Aerodrome Beacons
- ⓒ Communication Towers
- Ⓜ Meteorological Station
- ★ Brucejack Gold Mine
- Brucejack Transmission Line M-243 Segment
- Brucejack Transmission Line LOO Segment
- Highway 37 / 37A
- Granduc Road
- Brucejack Access Road (BJAR)
- ✕ BC Hydro Transmission Line
- ✕ Long Lake Transmission Line

1:300,000
UTM Zone 9 (NAD 83)

5 2.5 0 5
Kilometers

9 April 2019
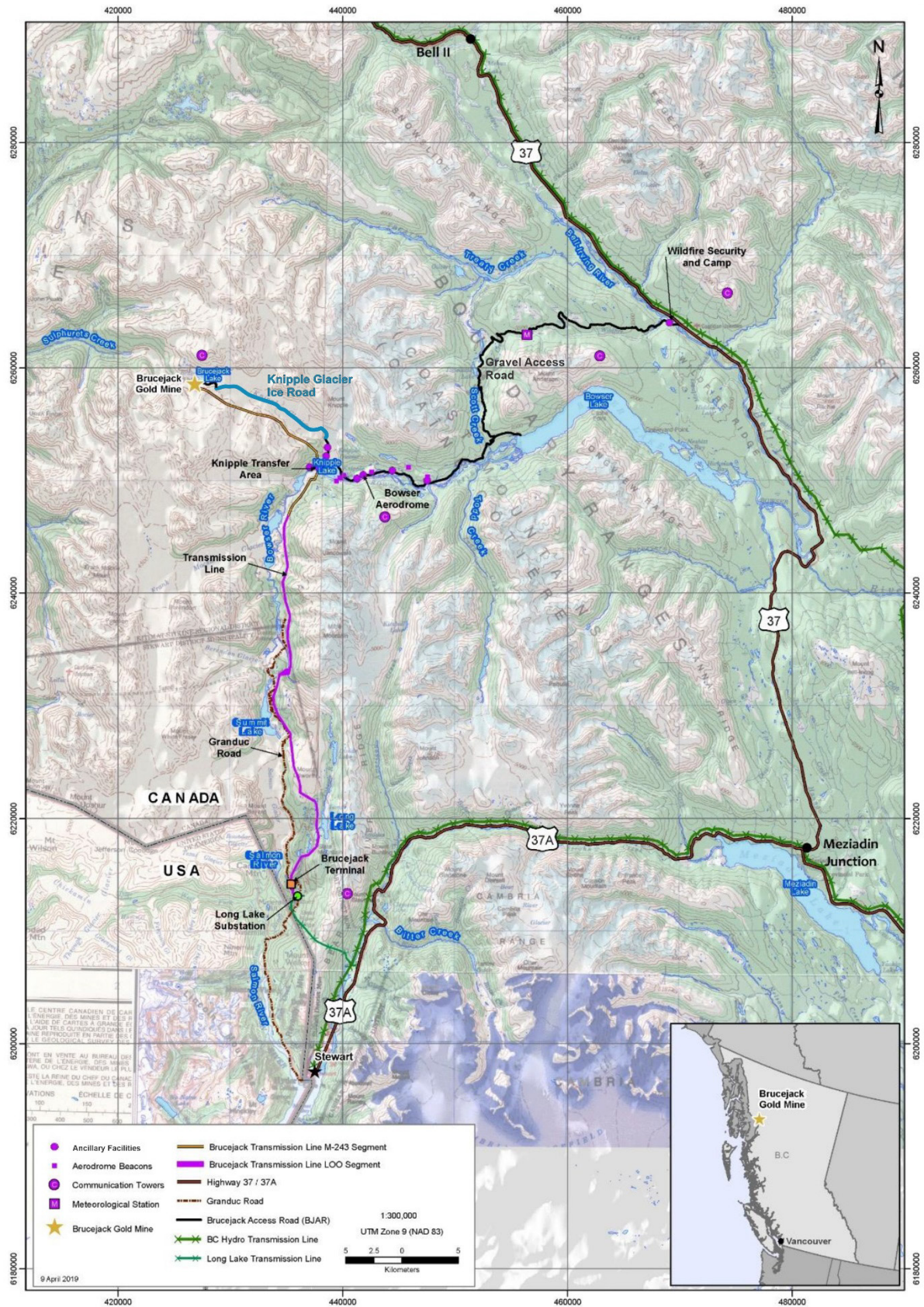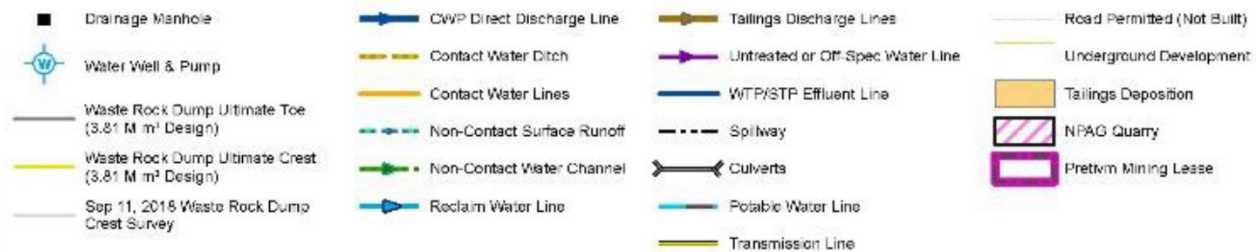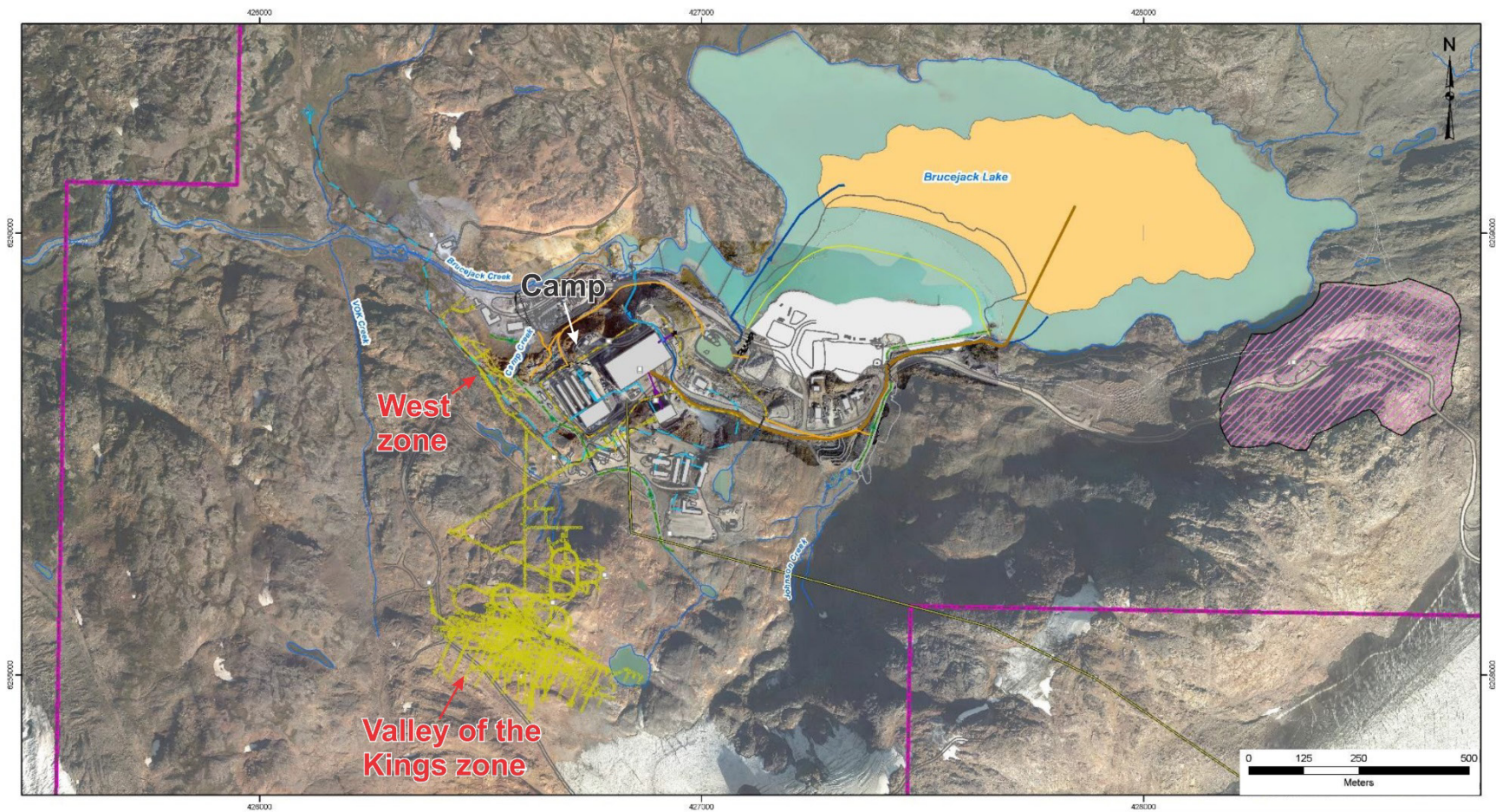
Figure 1.2 (previous page): The Brucejack mine infrastructure showing the location the Valley of the Kings and West zones underground development in plan view (modified from Pretium Resources Inc. unpublished maps, 2019).

circular area approximately 600 m in diameter. Well-developed oxidised pyrite gossans and northwest-trending mineralised vein swarms, including Au-Ag rich quartz stockwork and associated strong wallrock silicification, dominate outcrop exposures. The zone is generally less obscured by till cover than the Valley of the Kings zone and is completely free of glacial ice. Deep drilling by Newhawk Gold Mines Ltd. (see below) demonstrated continuity of the West zone hydrothermal system to at least 650 m below surface; the mineralisation is open to the northwest, southeast, and at depth (Macdonald et al., 1996).

1.3.4 Climate

Climatically, the region is typical of the northern Canadian Coast Mountain ranges. Annual temperatures vary from approximately +25 to -25°C, with wet, winter conditions, typified by heavy annual snow fall (~10 to 15 m at higher elevations and ~2 to 3 m in the valley bottoms) and below-zero temperatures, persisting from early October to late May. Mean temperatures increase rapidly with the onset of spring in early June and south-facing slopes in the Valley of the Kings and West zones usually are free of snow by late June. North-facing slopes may retain some snow year-round. Snow generally returns to higher elevations of the deposit area by mid-September and covers valley bottoms by early November. With the exception of underground research activities, fieldwork is consequently limited to the period from mid-June to early September.

1.4 A short history of the Brucejack gold-silver deposit

Exploration in northwest British Columbia dates back to the Stikine Gold Rush in the early 1860s (Belshaw, 2015), with the earliest known prospecting in the Brucejack Lake area taking place in the 1880s (McPherson, 1994). In about 1885, the Portland Canal and Stewart areas to the south of Brucejack were prospected by placer miners who were leaving the then exhausted Cariboo gold rush, possibly bound for the Yukon (Grove, 1973). Placer gold attracted miners to the Sulphurets creek area immediately west of Brucejack Lake in the 1890s and again in the 1930s, which culminated in a steam-powered Keystone drill being flown in to Sulphurets creek by float plane to test gravels for placer gold in 1933; however, there was no placer production

reported during this period nor were the results of the drilling reported (Bridge et al., 1981). The presence of extensive exposures of gossanous rock in and around upper Sulphurets Creek encouraged prospectors Bruce and Jack Johnstone of Burroughs Bay, Alaska, to explore the area for mineralised vein occurrences in 1935. This led to their discovery of quartz-barite veins near the shores of Brucejack Lake (Kurchkowski, 1988). Small showings of porphyry Cu-Mo and vein-hosted precious metals were subsequently discovered in the Brucejack Lake area between 1935 and 1959 (Bridge and Melnyk, 1983).

Granduc Mines Ltd. staked the area as the Sulphurets property in 1959 and conducted the first formal exploration, including geological mapping, geochemical sampling, geophysical surveying, and limited drilling of known porphyry showings (Payie, 2017). Several mineralised zones, including Snowfield, West, Shore, Galena, and Electrum, were discovered during a period of intensive exploration conducted between 1980 and 1985 by Esso Minerals Canada Ltd., under option from Granduc. Newhawk Gold Mines Ltd. and Lancana Mining Corp optioned the property from Granduc under a three-way joint venture (Newcana JV) in 1985. Newhawk explored the property comprehensively between 1985 and 1994, acquiring a 60% interest in it after buying out Lancana's interest in 1987. The property was officially subdivided into the Sulphside (Sulphurets and Mitchell zones), Snowfield, and Bruceside (Brucejack deposit) properties in 1991. Newhawk acquired 100% ownership of the Snowfield property from Granduc and sold the Sulphside property to Placer Dome Inc. in 1992. In addition to geological mapping, sampling, and geophysical programs, Newhawk completed more than 42,000 m of surface diamond drilling (532 holes), over 5 km of exploratory underground drifting on the West zone (1986-1987), and almost 36,000 m of underground diamond drilling (422 holes) from underground development levels as deep as 1100 m asl (~400 m below surface). Over 40 additional showings were discovered and a mineral reserve of 750,000 tonnes of ore grading 15.4 g/t Au and 678 g/t Ag was estimated for the West zone (Schroeter, 1994). The British Columbia government issued Newhawk a Mine Development Certificate in 1993 but unfavorable market conditions at the time prevented further development.

Silver Standard Resources Inc. acquired Newhawk in 1999, including its 100% interest in Snowfield and 60% interest in the Bruceside properties, and created separate projects for the Snowfield and Brucejack deposits (Board and McNaughton, 2013). The remaining 40% interest

in the Bruceside property was acquired from Black Hawk Mining Inc. (formed following a merger between Granduc and Blackhawk in 1996). Exploration of the Brucejack deposit recommenced in 2009 following Silver Standard's successful exploration of the Snowfield Au-Cu-Mo-Re porphyry deposit. Various base and precious metal showings to the north, west, and south of Brucejack Lake were investigated by mapping, sampling, and 51,500 m of surface diamond drilling (110 holes) was completed during the initial evaluation for a bulk tonnage deposit at Brucejack. In 2010, the intersection of 16,950 g/t Au and 8,700 g/t Ag over a 1.5 m interval resulted in the discovery of the Valley of the Kings zone. Pretium Resources Inc. (Pretium) acquired the Snowfield and Brucejack projects from Silver Standard in December 2010 and focused on defining the Valley of the Kings zone. Detailed surface drilling, mapping and sampling conducted in 2011 and 2012 led to a positive preliminary economic assessment and several mineral resource updates. An underground bulk sample tested mineral resource validity, augmented by additional tightly-spaced underground drilling in 2013. Bulk sample results were deemed positive, with 5,865 oz. Au and 4,950 oz. Ag recovered from 10,302 t rock. Pretium released a positive feasibility study for the Valley of the Kings and West zones in 2014 (Tetra Tech, 2014). Permitting and financing were finalised, and mine construction commenced in 2015. The latter was completed in April 2017 with wet commissioning of the 3,800 tonne/day mill facility taking place in May 2017 followed by the first gold pour in June 2017. As of March 2020, mineral resources (including Measured, Indicated, and Inferred Resources and excluding resources depleted due to production though December 31, 2019) totalled 10.7 million ounces (Moz) gold and 62.5 Moz silver in 32.6 million tonnes (Terra Tech, 2020); the mine surpassed the milestone of 1 Moz gold produced since first gold pour in July of the same year. In March 2022, Newcrest Mining Ltd. acquired Pretium and the Brucejack Mine for $2.8 billion US Dollars.

1.5 Research objectives and thesis structure

Although the geological setting of the Brucejack deposit and the nature of its mineralisation and alteration have been documented by earlier studies (Board and McNaughton, 2013; Greig and Greig, 2013; Tombe, 2015; Harrichhausen, 2016; Tombe et al., 2018; Board et al., 2020), a detailed, geologically integrated genetic model for the gold mineralisation in the deposit has not been developed, nor is it known to what extent, if any, Brucejack is genetically related to

surrounding porphyry deposits such as KSM. In order to develop a comprehensive genetic model for the Brucejack deposit and, by extension, identify key genetic implications for the bonanza-type of hydrothermal gold mineralisation that characterises this and many other epithermal gold deposits, this thesis seeks to address several fundamental issues. These are:

(1) the paragenetic relationships that each of the six vein stages have with high-grade gold mineralisation;

(2) the nature and origin of the hydrothermal fluid in each vein stage;

(3) the physicochemical conditions that were operative during these stages;

(4) the relationship between the epithermal mineralisation and the spatially associated Cu-Au porphyries (if any); and

(5) the physicochemical processes that ultimately controlled the formation of bonanza-grade gold mineralisation.

These objectives have been met by the findings of the three research articles presented in the following three chapters of this manuscript-based thesis. By presenting evidence for the physical transport and flocculation of colloidal gold suspensions at Brucejack, Chapter 2 explains the long-standing paradox of how hydrothermal fluids with low concentrations of gold in solution form bonanza-type gold deposits. Chapter 3 documents extraordinarily intracrystalline $\delta^{34}S$ shifts in Brucejack pyrite, which are used to help constrain the processes associated with, and physicochemical conditions related to, the flocculation of colloidal gold in intermediate- to late-stage ore veins in the deposit. Chapter 4 examines the relationships between the multiple generations of hydrothermal alteration, magmatism and mineralisation at Brucejack, by using a combination of field-based vein mapping, macro- and micro-scale paragenetic observations, major and trace element analyses of electrum and pyrite, and situ sulphur isotope analyses of pyrite and barite; it then uses observations from these methods to construct a novel model for the deposition of bonanza gold in hydrothermal veins through the electrochemical flocculation of colloidal gold suspensions.

These research article chapters are followed by a comprehensive review and discussion of the overarching findings of the thesis, including recommendations for future work (Chapter 5), and concluding remarks addressing the contributions of the thesis to the scientific community (Chapter 6).

References

Belshaw, J.D., 2015, Canadian history: pre-Confederation: BC Open Textbook Project, British Columbia Ministry of Advanced Education, Version 2.3, 600 p.

Board, W.S., and McNaughton, K.C., 2013, The Brucejack high-grade gold project, northwest British Columbia, Canada. NewGenGold Conference, Perth, Australia, Proceedings, p. 177–191. West Perth, Paydirt Pty Ltd.

Board, W.S., McLeish, D.F., Greig, C.J., Bath, O.E., Ashburner, J.E., Murphy, T., and Friedman, R.M., 2020, The Brucejack Au-Ag deposit, northwest British Columbia, Canada: Multistage porphyry to epithermal alteration, mineralization and deposit formation in an island-arc setting, in Sillitoe, R.H., Goldfarb, R.J., Robert, F., and Simmons, S.F., eds., Geology of the World's Major Gold Deposits and Provinces. Society of Economic Geologists Special Publication 23, p. 299–311.

Bridge, D., and Melnyk, W., 1983, 1982 exploration report on the Sulphurets property, Skeena Mining Division, BC. Unpublished report prepared for Esso Minerals Canada Ltd., 91 p.

Bridge, D., 1981, 1980 exploration report on the Sulphurets property, Skeena Mining Division, BC. British Columbia Ministry of Energy, Mines and Petroleum Resources, Geological Branch Assessment Report 18901, 206 p.

Clark, J.R., and Williams-Jones, A.E., 1990, Analogues of epithermal gold–silver deposition in geothermal well scales. Nature, v. 346, p. 644–645.

Cline J.S., Hofstra A.H., Muntean J.L., Tosdal R.M., and Hickey K.A., 2005, Carlin-Type Gold Deposits in Nevada: Critical Geological Characteristics and Viable Models, in Economic Geology 100th Anniversary Volume, p. 451-484.

Corbett, G. J., and Leach, T. M., 1998, Southwest Pacific rim gold-copper systems: structure, alteration, and mineralisation. Society of Economic Geologists Special Publication 6, 237 p.

Duuring, P., Rowins, S. M., McKinley, B. S. M., Dickinson, J. M., Diakow, L. J., Kim, Y-S., and Creaser, R.A., 2009, Examining potential genetic links between Jurassic porphyry Cu-Au-Mo and epithermal Au-Ag mineralization in the Toodoggone district of north-central British Columbia, Canada. Mineralium Deposita, v. 44, p. 463-496.

Einaudi, M.T., Hedenquist, J.W., and Inan, E.E., 2003, Sulfidation state of fluids in active and extinct hydrothermal systems. Transitions form porphyry to epithermal environments in Society of Economic Geologists Special Publication 10, p. 285-312.

Greig, C.J., and Greig, R., 2013, Geology of the Brucejack property: Pretium Resources Inc. Internal company map. Available: https://s1.q4cdn.com/222336918/files/doc_downloads/geology/2013.03.19%20Property%20Geology.pdf.

Grove, E.W., 1973, Detailed Geological Studies in the Stewart Complex, Northwestern British Columbia. Unpublished Ph.D. thesis, McGill University, 434 p.

Groves D.I., Goldfarb R.J., Robert, F., and Hart C.J.R., 2003, Gold Deposits in Metamorphic Belts: Overview of Current Understanding, Outstanding Problems, Future Research, and Exploration Significance. Economic Geology, v. 98, p. 1-29.

Harrichhausen, N.J., 2016, Role of colloidal transport in the formation of high-grade veins at Brucejack, British Columbia. Unpublished M.Sc. thesis, Montreal, McGill University, 103 p.

Hayba, D.O., Bethke, P.M., Heald, P., and Foley, N.K., 1985, Geologic, mineralogic, and geochemical characteristics of volcanic-hosted epithermal precious metal deposits. Reviews in Economic Geology, v. 2, p. 129–167.

Heald, P., Foley, N.K., and Hayba, D.O., 1987, Comparative anatomy of volcanic hosted epithermal deposits: acid-sulphate and adularia-sericite types. Economic Geology, v. 82, p. 1-26.

Hedenquist, J.W., 1987, Mineralization associated with volcanic related hydrothermal systems in the Circum Pacific Basin, in Horn, M.K., ed., Transactions of the 4th circum Pacific energy and mineral resources conference, 17-22 August 1987, Singapore: Tulsa, American Association of Petroleum Geologists, p. 513-523.

Hedenquist, J.W., Arribas, A. Jr., and Reynolds, T.J., 1998, Evolution of an intrusion-centered hydrothermal system: Far Southeast-Lepanto porphyry and epithermal Cu-Mo deposit, Philippines. Economic Geology, v. 93, p. 373–404.

Hedenquist J.W., Arribas A.R., and Gonzalez-Urien G., 2000, Exploration for epithermal gold deposits, in SEG Reviews in Economic Geology 13, p. 245-277.

Heinrich, C.A., 2005, The physical and chemical evolution of low- to medium-salinity magmatic fluids at the porphyry to epithermal transition: a thermodynamic study. Mineralium Deposita, v. 39, p. 864-889.

John, D.A., Vikre, P.G., du Bray, E.A., Blakely, R.J., Fey, D.L., Rockwell, B.W., Mauk, J.L., Anderson, E.D. and Graybeal, F.T., 2018, Descriptive models for epithermal gold-silver deposits Chapter Q of Mineral deposit Models for Resource Assessment. United States Geological Survey, Scientific Investigations Report 2010-5070-Q, 246 p.

Kesler, S.E., and Wilkinson, B.H., 2010, Global hydrothermal gold resources for the next millennium. Society of Economic Geologists, Special Publication 15, p. 5–18.

Kurchkowski, E.R., 1988, Drill report on the Goldwedge property. British Columbia Ministry of Energy, Mines and Petroleum Resources, Geological Branch Assessment Report 16744, 179 p.

Lindgren, W., 1913, Mineral Deposits. McGraw-Hill, New York, 883 p.

Lipson, R., 2014, The Promise and Perils of Porphyry Deposits in the Future of Gold Production. Society of Economic Geologists Newsletter 98, p. 1, 14-21.

Macdonald, A.J., Lewis, P.D., Thompson, J.F.H., Nadaraju, G., Bartsch, R., Bridge. D.J., Rhys, D.A., Roth, T., Kalp, A., Godwin, C.I., and Sinclair, A.J., 1996, Metallogeny of an Early to Middle Jurassic arc, Iskut River area, northwestern British Columbia. Economic Geology, v. 91, p. 1098–1114.

McLeish, D.F., Williams-Jones, A.E., Vasyukova, O.V., Clark, J.R. and Board, W.S., 2021, Colloidal transport and flocculation are the cause of the hyperenrichment of gold in nature. Proceedings of the National Academy of Sciences, v. 118(20), e2100689118.

McPherson, M., 1994, 1994 assessment report on the North Bruce Group, Sulphurets property-Bruceside project, Newhawk Gold Mines Ltd: British Columbia Ministry of Energy, Mines and Petroleum Resources, Geological Branch Assessment Report 23613, 64 p.

Murphy, K., 2014, Fewer discoveries, slowing development weigh on gold industry. In Strategies for Gold Reserves Replacement, SNL Metals & Mining 2014 industry update, Toronto, Canada.

Payie, G.J., 2017, British Columbia Geological Survey MINFILE report no. 104B 193 on the Brucejack area: http://minfile.gov.bc.ca/Summary.aspx?minfilno=104B++193.

Sawkins, F.J., 1972, Sulfide ore deposits in relation to plate tectonics. Journal of Geology, v. 80, p. 377–397.

Sawkins, F.J., 1990, Metal deposits and plate tectonics. Springer-Verlag, Berlin.

Schodde, R., 2011, Recent trends in gold discovery. NewGenGold Conference, Perth, Australia, abstracts with program, p. 1-19.

Schroeter, T.G., 1994, British Columbia mining, exploration, and development 1993 highlights. British Columbia Mineral Exploration Review 1993, British Columbia Geological Survey Information Circular 1994-1, 27 p.

Sillitoe, R.H., and Hedenquist, J. W., 2003, Linkages between volcanotectonic settings, ore-Fluid compositions, and epithermal precious metal deposits, in Volcanic, Geothermal, and Ore-Forming Fluids: Rulers and Witnesses of Processes within the Earth. Society of Economic Geologists Special Publication 23, p. 315-345.

Tetra Tech, 2014, Feasibility study and technical report update on the Brucejack project, Stewart, BC. NI 43-101 Technical Report prepared for Pretium Resources Inc., 460 p.

Tetra Tech, 2020, March 2020 technical report and mineral resources update, Brucejack mine. NI 43-101 Technical Report prepared for Pretium Resources Inc., 383 p.

Tombe, S.P., 2015, Age and origin of the Brucejack epithermal Au-Ag deposit, northwestern British Columbia. M.Sc. thesis, Edmonton, University of Alberta, 201 p.

Tombe, S.P., Richards, J.P., Greig, C.J., Board, W.S., Creaser, R.A., Muehlenbachs, K.A., Larson, P.B., DuFrane, S.A. and Spell, T., 2018, Origin of the high-grade early Jurassic Brucejack epithermal Au-Ag deposits, sulphurets mining Camp, northwestern British Columbia. Ore Geology Reviews, v. 95, p.480-517.

Vikre, P.G., 1989, Fluid-mineral relations in the Comstock Lode. Economic Geology, v. 84, p. 1574-1613.

Wilkinson, J.J., 2013, Triggers for the formation of porphyry ore deposits in magmatic arcs. Nature Geoscience, v. 6, p. 917-925.

Williams-Jones, A.E., and Heinrich, C.A., 2005, Vapor transport of metals and the formation of magmatic-hydrothermal ore deposits. Economic Geology, v. 100, p. 1287–1312.

Williams-Jones, A.E., Bowell, R.J., and Migdisov, A.A., 2009, Gold in solution. Elements, v. 5, p. 281-287.

CHAPTER 2

Colloidal transport and flocculation are the cause of the hyper-enrichment of gold in nature

Preface

Chapter 2 entitled, "Colloidal transport and flocculation are the cause of the hyper-enrichment of gold in nature", provides an overview of the problem of forming ultra-high-grade, or bonanza, hydrothermal gold deposits by the processes of metal dissolution and mineral deposition, i.e., through aqueous complexation and precipitation of crystalline gold. This problem is referred to as, "the high-grade gold ore paradox". The Chapter explores the possibility that the colloidal transport and flocculation of gold might offer a solution to this paradox. The methodology employed to search for evidence of colloidal transport involved making ultrathin (50 to 100 nm) transmission electron microscope (TEM) lamellae (foils) from dendritic clots of electrum sampled from the high-grade Brucejack epithermal Au-Ag deposit. The electrum samples were cut from standard petrographic thin sections and milled down to the desired thickness using a focused ion beam scanning electron microscope (FIB-SEM). The resulting TEM foils were then imaged at ultra-high magnification levels (up to 750,000 x) to resolve and measure atomic lattice fringes in individual and aggregated gold (electrum) nanoparticles and their surrounding calcite matrix. The findings from this TEM imaging are discussed in reference to a proposed model for the formation of bonanza gold occurrences by colloidal gold transport and flocculation.

Abstract

Aqueous complexation has long been considered the only viable means of transporting gold to depositional sites in hydrothermal ore-forming systems. A major weakness of this hypothesis is that it cannot readily explain the formation of ultra-high-grade gold veins. This is a consequence of the relatively low gold concentrations typical of ore fluids (tens of ppb) and the fact that these 'bonanza' veins can contain weight percent-levels of gold in some epithermal and orogenic deposits. Here we present the first direct evidence for a hypothesis that could explain these veins, namely the transport of the gold as colloidal particles and their flocculation in nano-scale calcite veinlets. These gold-bearing nano-veinlets bear a remarkable resemblance to cm-scale ore veins in many hydrothermal gold deposits and give unique insight into the scale-invariability of colloidal flocculation in forming hyper-enriched gold deposits. Using this evidence, we propose a model for the development of bonanza gold veins in high-grade deposits. We argue that gold transport in these systems is largely mechanical and is the result of exceptionally high degrees of supersaturation that preclude precipitation of gold crystals and instead lead to the formation of colloidal particles which flocculate and form much larger masses. These flocculated masses aggregate locally, where they are seismically pumped into fractures to locally form veins composed largely of gold. This model explains how bonanza veins may form from fluids containing ppb concentrations of gold and does not require prior encapsulation of colloidal gold particles in silica gel as proposed by previous studies.

2.1 Introduction

Measurements of gold concentrations in the fluids responsible for epithermal mineralisation and in geothermal fluids, which are considered to be analogues of epithermal ore fluids, are on the order of 10 to 30 ppb (Simmons and Brown, 2006). Moreover, similar concentrations have been calculated for fluids of appropriate composition from the results of experiments designed to determine the speciation of gold in aqueous fluids (Stefánsson and Seward, 2004). Although such concentrations may be sufficient to form veins containing 10's of grams per tonne gold, they are far too low to explain spatially discrete occurrences of ultra-high-grade concentrations which, in some veins, exceed 50 wt.% of gold per tonne on the decimetre scale; these bonanza intervals are commonly accompanied by intervals in the same vein containing < 5 ppm gold (Fig. 2.1). Formation of such bonanza veins by direct precipitation of native gold or electrum from the

ore fluids would require that individual fractures remain open for unreasonably long periods of time (>> 50,000 years[1]; which is a timeframe that exceeds the total lifespan of many porphyry-epithermal deposits[2] and greatly exceeds the estimated ~1,400 years required to seal a 1 m wide vein grading 20 g/t Au in an active geothermal system[3]), or that the fluid flux be extraordinarily high. Indeed, a recent study by Pearce et al. (2015) suggests that the fluid fluxes are typically quite low. They estimated a fluid: rock ratio of ~ 12:1 and concluded from gold solubility considerations that the maximum amount of gold per tonne of rock that could be deposited for this ratio is 20 grams.

The existence of gold colloids has been known since the mid-19th century (Faraday, 1857), and the idea that gold deposits might form from fluids transporting the gold as a colloid (i.e., solid nanoparticles with charged surfaces dispersed in an electrolyte solution) was proposed almost 100 years ago (Boydell, 1924; Frondel, 1938; Cosgrove, 2010). Demonstration, however, that gold can be dissolved in chloride- and bisulphide-bearing aqueous fluids in concentrations of tens and even hundreds of parts per million (Seward, 1973; Gammons and Williams-Jones, 1995; Stefánsson and Seward, 2004;) has led to widely accepted genetic models in which the gold is transported to the site of deposition exclusively as dissolved species, and precipitates in crystalline form (Williams-Jones et al., 2009). Nonetheless, there have been some advocates of colloidal transport, notably Petrovskaya (1973) and Kvasnifsa et al. (1981), who presented textural evidence at millimetre to micron scales in support of a model, in which gold nanoparticles deposit and aggregate to form dendrites. Noting that gold dendrites are commonly hosted by quartz, Saunders (1990, 1994), Herrington and Wilkinson (1993), and Saunders and Schoenly (1995) proposed that the transport of colloidal gold particles was facilitated by the occurrence of flocculated colloidal silica or silica gel. They did not, however, provide direct evidence for the presence of gold colloids.

More recently, Hannington et al. (2016), Gartman et al. (2018), Hannington and Garbe-Schönberg (2019), provided indirect evidence for the existence of gold colloids in hydrothermal fluids. Collectively, these studies detected gold particles ranging from 2 μm to less than 50 nm in diameter in geothermal fluids and seafloor black smokers and showed that the mass of particulate

---

[1] Simmons and Brown (2006)
[2] Buret et al. (2016)
[3] Rowland and Simmons (2012)
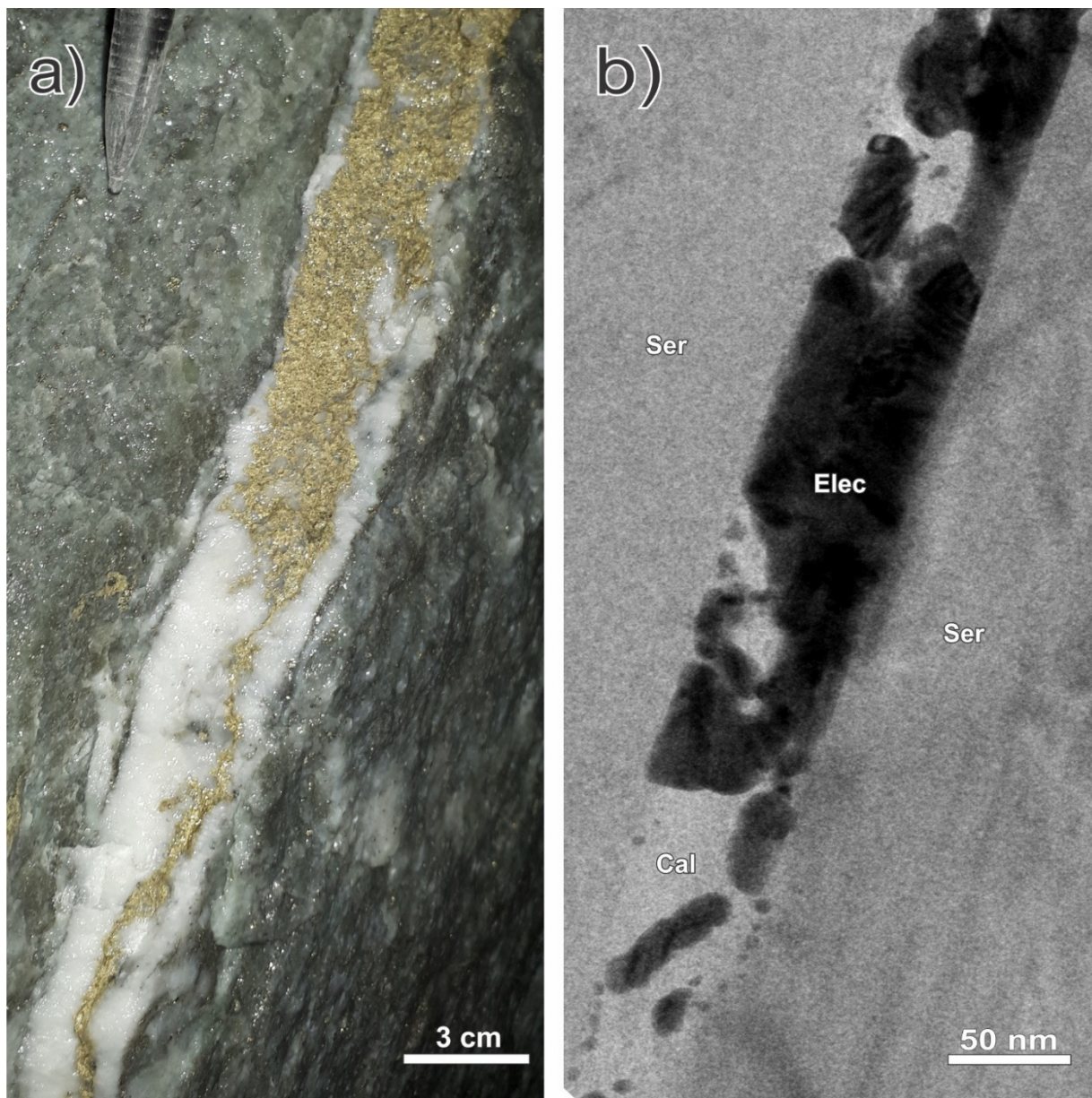
Figure 2.1: Ultra-high-grade (bonanza) electrum mineralisation in (a) a calcite-quartz vein hosted by sericitised crystal tuff in a development face in the underground mine workings, and (b) in a calcite nano-veinlet (bright-field TEM image). The two images emphasise the strong similarity between massive (clotted) electrum at the macro- and nano-scales. Spherical nanoparticles of electrum are evident in the bottom left corner of the nano-veinlet.

and dissolved gold in bulk samples of the fluid greatly exceeds that predicted from solubility calculations. Prokofiev et al. (2000) detected high concentrations of gold in fluid inclusions (up to 6000 ppm Au) in hydrothermal quartz vein samples from the Kola super-deep drill hole, northwest Russia, which they interpreted to represent gold nanoparticles. The only studies that have provided images of colloidal gold particles are those of Harrichhausen (2016), Burke et al.

(2017), and Petrella et al. (2020). These four studies proposed a model of gold concentration similar to that of Saunders (1990) in which visible (cm-) scale gold dendrites in hydrothermal veins are the products of recrystallisation of gold-colloid-bearing amorphous silica. None of these studies have provided direct evidence for colloidal gold flocculation in nano-veinlets and neither have they shown that this phenomenon can potentially occur at the scale of a bonanza-type deposit.

2.2 The Brucejack gold deposit

In order to test for the existence of gold nanoparticles in a fossil hydrothermal system and gain insight into the process by which they could form bonanza gold veins, we have undertaken a transmission electron microscopy (TEM) study of mineralisation from the Brucejack epithermal gold deposit, northwestern British Columbia, Canada. This deposit, which was emplaced near the margin of a long-lived island arc at ~184 Ma (Board et al., 2020), is host to abundant, spatially-restricted occurrences of bonanza grade mineralisation (up to 41,582 g/t Au in a 0.5 m diamond drill core interval (Tombe et al., 2018) in veins with an average thickness of 10 cm (ranging up to a maximum thickness of 2 m). Local concentrations of > 1,000 g/t Au occur in at least three generations of quartz-carbonate-electrum veins over a vertical extent exceeding 1500 m which, from fluid inclusion studies, are interpreted to have developed as a result of boiling and/or fluid mixing (Tombe et al., 2018). The high-grade gold mineralisation occurs typically as 1 to 30 cm diameter/length dense clots comprising micro-veinlets of electrum ($Au_{62}Ag_{38}$, on average (McLeish et al., 2018) and calcite in narrow (1 to 50 cm wide) vein swarms and wider (metre-decametre-scale) quartz-carbonate stockworks and vein breccias. The distribution of electrum clots within the veins is highly irregular; some veins contain many clots in close proximity to each other, such that the veins locally contain over 50 wt% electrum (Fig. 2.1), whereas others contain a single electrum clot. Moreover, within vein swarms, commonly only a single vein contains electrum clots and the others are visibly barren. The wallrock to both the electrum-bearing and barren veins has been affected strongly by extensive, pre-electrum phyllic alteration, which hosts lower grade (< 5 g/t Au) invisible gold in colloform, oscillatory arsenic-rich growth zones in pyrite (McLeish et al., 2018). These rocks, however, do not contain electrum except in rare cases where localised post-mineral deformation sheared electrum along fault planes beyond vein confines.

22

2.3 Methods and results

We prepared five ultra-thin (50 to 100 nm) TEM lamellae from dendritic clots of electrum in two samples from different locations in the Brucejack mine to investigate the nature of the mineralisation at the nanoscale. The TEM lamellae were thinned using the focused ion beam (FIB) milling technique and were centred on areas of electrum in contact with vein-hosted calcite and quartz (see Data Supplement 2.1 for analytical details). Our resulting bright-field TEM images (e.g., Figs. 2.1b and 2.2-2.4) document the existence of numerous dark spheres, ~5 to 15 nm in diameter, which are disseminated in the calcite matrix of 0.5-1cm wide veins or concentrated in calcite-bearing nano-veinlets (< 100 nm wide). In the example illustrated in Figure 2.2a, they occur adjacent to a large grain of electrum and exhibit crystal lattice fringes with a spacing of 2.2 to 2.4 Å (Fig. 2.2b), which is the same as the spacing in the adjacent electrum grain, as well as that of experimentally produced gold and electrum nanoparticles (2.4 and 2.2 Å, respectively (Scott et al., 2012)). Nanoparticles similar in size to those shown in Figure 2.2a are present in all the lamellae and in all cases where lattice fringes could be observed, the lattice spacing was found to be in the range 2.2 to 2.4 Å. There are also larger particles of electrum in all the lamellae, ~30 to 150 nm in diameter (Fig. 2.3a), which consist of multiple 5 to 10 nm-wide domains displaying variable lattice plane orientations (Fig. 2.3b). We interpret these larger particles to be aggregates of nanoparticles, with each nanoparticle having a different lattice plane orientation to that of the adjacent nanoparticles. In all the lamellae, the matrix to the disseminated electrum nanoparticles has a lattice fringe spacing of 3.0 to 3.1 Å, which is the same as that for calcite (~3.0 Å (Zhang et al., 2010)) and distinctly different from that of quartz (~3.4 Å (Levien et al., 1980)). Although quartz was observed in some lamellae, it was not found to contain nanoparticles of electrum.

One of the lamellae, from the contact of a mineralised vein with wallrock, contains electrum nanoparticle-bearing nano-veinlets of calcite (50 to 100 nm wide). These nano-veinlets exploited the cleavage planes of chlorite and sericite (Fig. 2.4a and 2.4b), and are developed along the boundaries between chlorite and quartz crystals or cross-cut the quartz (Fig. 2.4c). The occurs either as isolated particles or aggregates of particles that occupy the full width of the nano-veinlets for distances up to 600 nm (Fig. 2.4a).
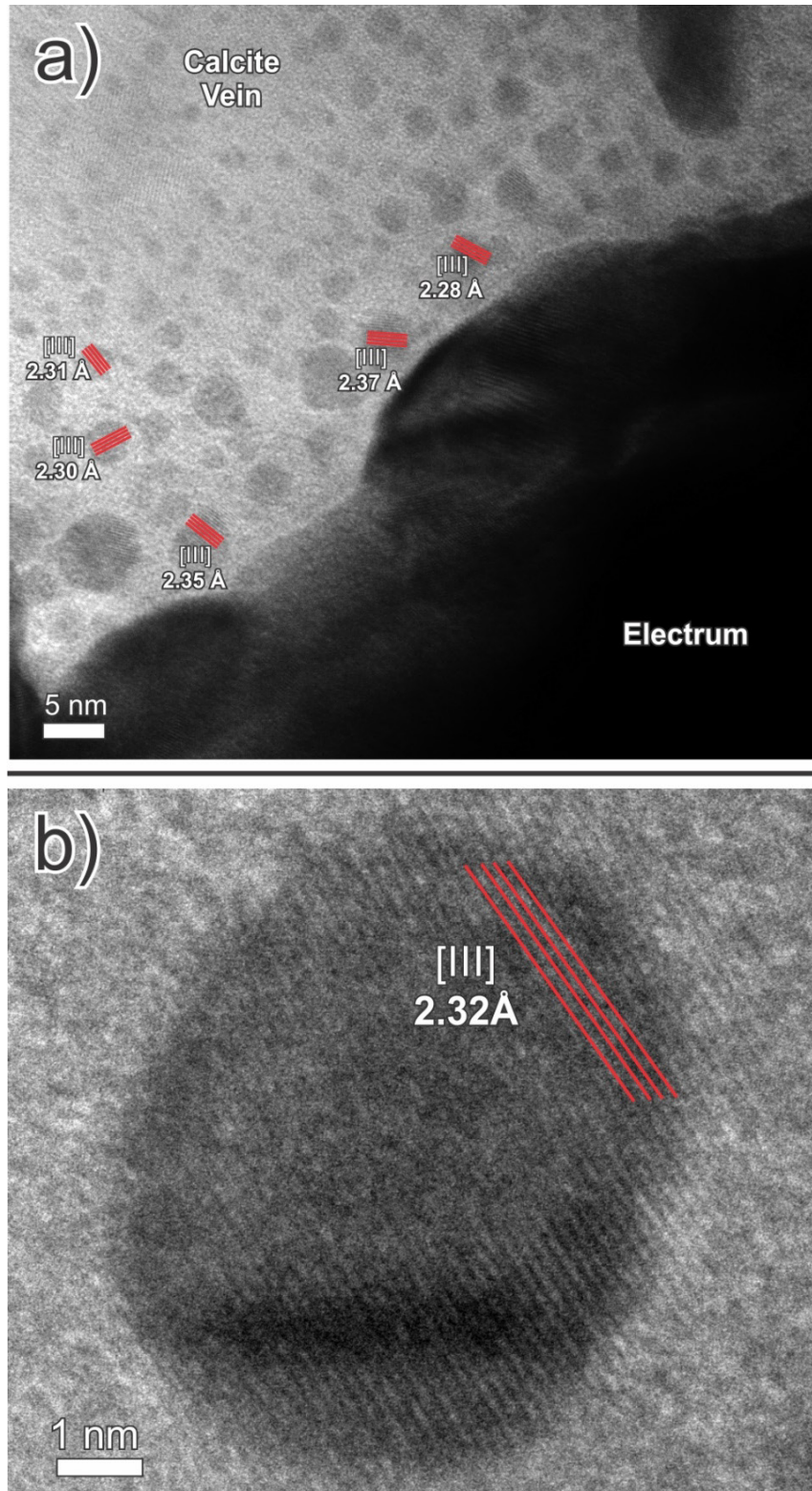
Figure 2.2: Bright-field TEM images of the contact between a large electrum grain and the calcite matrix in a calcite-quartz vein; **(a)** Abundant spherical electrum nanoparticles in calcite; **(b)** An electrum nanoparticle, with a lattice fringe spacing of 2.32 Å.

2.4 Discussion

Although the formation of negatively-charged gold nanoparticles (colloidal gold) and their flocculation has been demonstrated in laboratory experiments (Frondel, 1938; Turkevich et al., 1951; Frens, 1973; Weitz and Oliveria, 1984; Liu et al., 2019), our study is the first to provide direct evidence of the existence of flocculated colloidal-scale gold nanoparticles and document their transport in nanoscale hydrothermal veinlets in a natural system. Specifically, we have shown that isolated, spherical 1-5 nm electrum nanoparticles, identified by their lattice fringe spacing, electron diffraction maxima and EDS spectra (see Chapter 2 Supplementary Information for indexed selected area electron diffraction images and EDS spectra), are common in the Brucejack deposit and that they form aggregates composed of multiple spherical to ovoid sub-particles with unique lattice plane orientations. The irregular shapes exhibited by the larger aggregates are strikingly similar to the dendritic habit displayed by coarse-grained clots of electrum in veins at Brucejack. This mimicry of electrum textures from the nano- to the macro-scale is consistent with the fractal nature of colloidal aggregates observed in experimental studies, as well as in computer simulations of the flocculation of gold colloids (e.g., Witten and Sander, 1981).

Numerous TEM studies of experimentally-grown synthetic crystals (e.g., anatase) have demonstrated that minerals may commonly go through a nanoparticle phase during the incipient stage of crystallisation that accompanies precipitation from solution (e.g., Penn and Banfield, 1998; Hochella et al., 2008). This nanoparticle phase is generally short lived, with crystals continuing to grow beyond this stage by Ostwald ripening. In non-equilibrium systems (e.g., boiling hydrothermal systems in which there is extreme supersaturation due to very steep gradients in physicochemical parameters such as temperature), however, that Ostwald ripening is not a viable mechanism for crystal growth because nucleation rates are too high and growth rates are too low (Penn and Banfield, 1999). In such cases, atoms have insufficient time to organise themselves into crystals and, instead, accumulate in spherical masses to minimise surface area for a given volume. As non-equilibrium environments can persist throughout the evolution of a porphyry-epithermal hydrothermal system (e.g., at boiling / fluid mixing sites), conditions conducive to the formation of metallic nanoparticles may prevail locally for the same duration. The exact location(s) of nanoparticle formation in a hydrothermal system, and the distances over
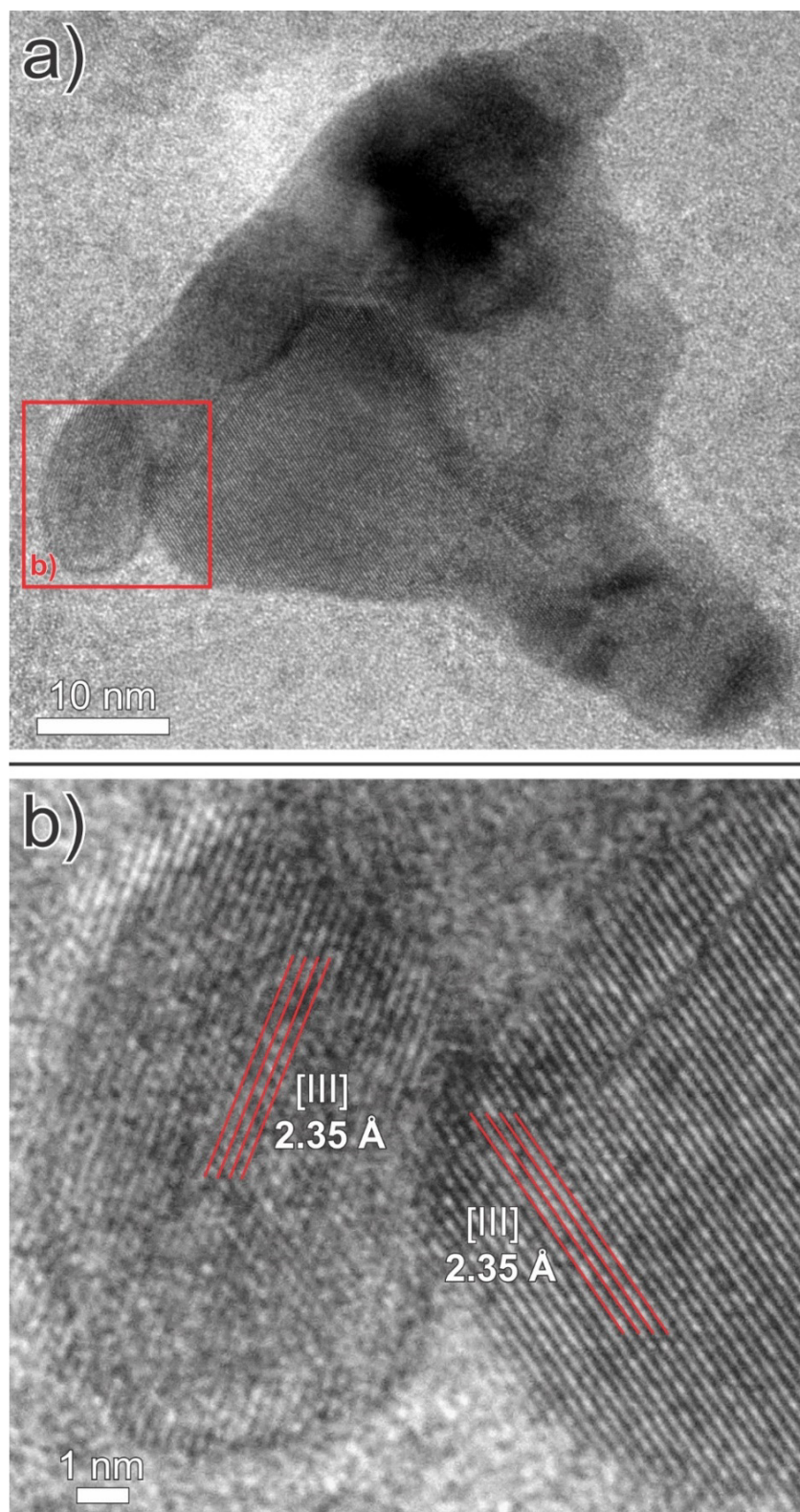
Figure 2.3: (a) A bright-field TEM image of a large electrum nanoparticle**;** (b) An enlargement of the nanoparticle in **(b)** showing that it is composed of numerous, ovoid to spherical nanoparticles with variable lattice plane orientations.
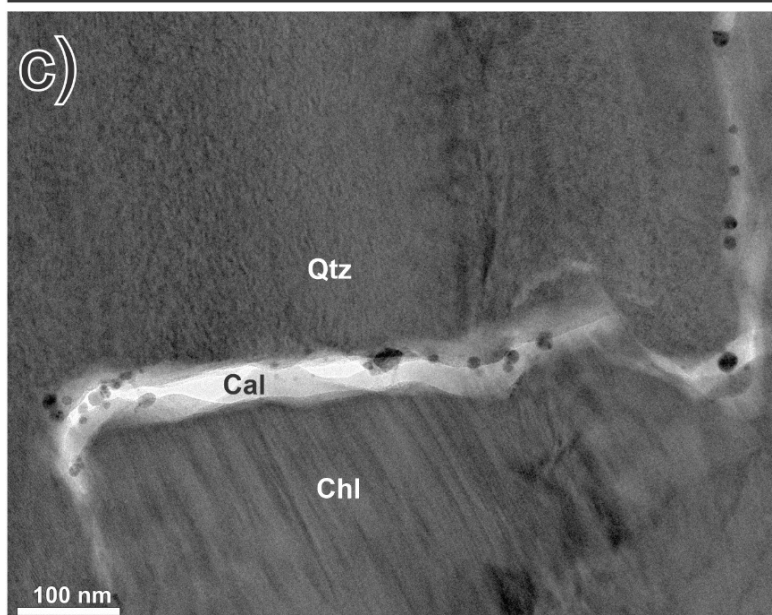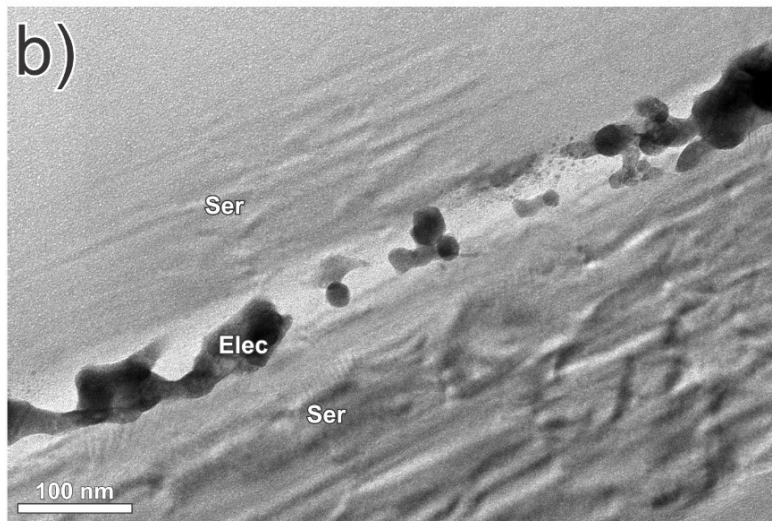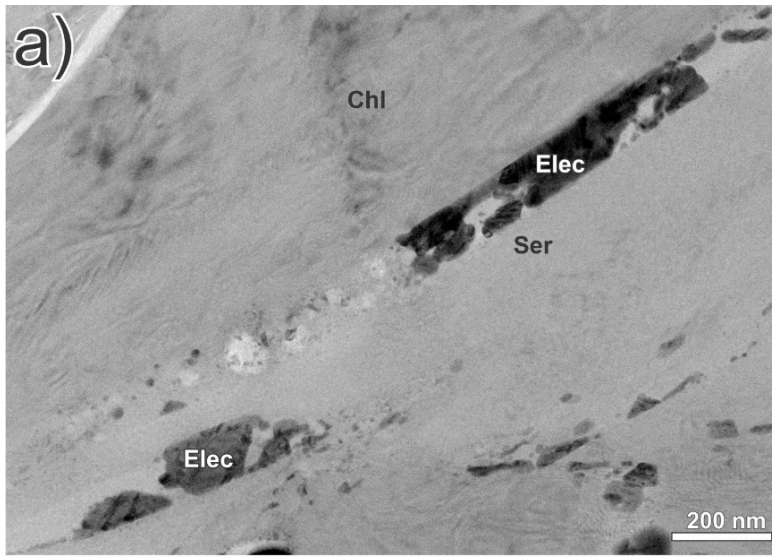
Figure 2.4 (previous page): (a) A bright-field TEM image of electrum nanoparticles (occurring as both flocculated masses and individual nanoparticles) within calcite nano-veinlets that exploited cleavage planes in chlorite and sericite (note: this is a wider field of view version of Figure 2.1b); **(b)** a calcite nano-veinlet containing flocculated and individual spherical electrum nanoparticles that occupies a cleavage plane in sericite; **(c)** electrum nanoparticles in a nano-veinlet of calcite developed along a grain boundary between chlorite and quartz; the nano-veinlet also cuts quartz.

which nanoparticles may be transported in suspension are currently unknown but, for gold nanoparticles, solubility considerations dictate that the nucleation sites are likely to be in the deeper parts of hydrothermal systems (i.e., in the upper-levels of the porphyry environment) where physiochemical conditions permit greater gold solubility yet vigorous, episodic boiling is still possible.

The flocculation of metallic nanoparticles from a hydrothermal fluid can be achieved through boiling, cooling, and/or fluid mixing. Boiling acts in two separate yet reinforcing ways to promote flocculation: (1) the physical effects of boiling increase the collision efficiency of nanoparticles; and (2) boiling-related pH increases lead to the precipitation of minerals containing cationic flocculants (e.g., Al^{3+} and Fe^{3+}), which 'bridge' negatively charged nanoparticles (Iler, 1979; Saunders, 1990). Cooling slows the reduction of Au^+ to Au^0 and decreases the number of nucleation centres for gold nanoparticles, which could lead to the development of larger nanoparticles that flocculate more easily (Frondel, 1938; Madras and McCoy, 2004). The mixing of seawater (see below), which is moderately alkaline (pH 7.5 to 8.5), with an acidic to near-neutral hydrothermal fluid favours the precipitation of cationic flocculants due to the increase in pH, but also adds cationic flocculants (e.g., Na^+) and accelerates cooling, which in turn promotes flocculation (Saunders, 1990). Several lines of evidence suggest that all these processes (boiling, cooling and fluid mixing) were active during the formation of ultra-high-grade gold veins at Brucejack. Tombe et al. (2018), on the basis of a detailed study of fluid inclusions in quartz from two generations of quartz-calcite-electrum veins, concluded that the fluid boiled during vein formation. In addition, the widespread occurrence of hydrothermal breccias and the abundance of auriferous, oscillatory-zoned arsenian pyrite with strongly negative $\delta^{34}S$ signatures (e.g., -36.0‰; Chapter 3) is strong evidence of boiling, which oxidises the fluid by releasing hydrogen, thereby fractionating the heavier isotope into sulphate and the light isotope into reduced sulphur. Similar evidence of boiling has been cited for other

epithermal gold deposits (e.g., Porgera, Papua New Guinea; Peterson and Mavrogenes, 2014) and active geothermal systems (Román et al., 2019). During the final stage of pyrite crystallisation (outer zones of crystals), which was synchronous with electrum flocculation, $\delta^{34}S$ values increased sharply from strongly negative to between +20.0 and +24.0 ‰ (Chapter 3). Significantly, electrum is locally in textural equilibrium with this latest phase of pyrite crystallisation. As the Brucejack deposit was emplaced near the margin of a long-lived island arc in the early Jurassic, and these values, including those of the corresponding fluid, are within the range of those for early Jurassic seawater (~ +15-24‰; Prokoph et al., 2008), we propose that after vigorous, episodic boiling, the hydrothermal ore fluids mixed with seawater. Furthermore, given its close temporal association with electrum deposition, we suggest that this fluid mixing was the principal cause of flocculation and ultimately the reason for the bonanza-style gold mineralisation that characterises the deposit.

We submit, here, a model for the colloidal precipitation, transport and deposition of electrum, which accounts for the extreme concentrations of gold in quartz-carbonate veins at Brucejack. In this model, electrum colloids form in response to boiling of a hydrothermal fluid and are then mechanically transported to sites where they mix with seawater and flocculate. Strong decompression associated with the ascent of fluids from a magma at depth to the shallow crustal level of the Brucejack deposit (≤ 1000 m depth (Tombe et al., 2018)) led to their vigorous boiling. This induced rapid cooling and increases in pH and f_{O_2} that caused extreme supersaturation of gold and the formation of colloidal particles. Whether this boiling also induced flocculation is unknown, though, in principle, the increased particle collision efficiency due to boiling could have promoted the initial flocculation of the electrum nanoparticles (Saunders, 1990). We propose, however, that most of the flocculation occurred in response to the mixing of seawater, which was introduced at a late stage of hydrothermal activity and coincided with electrum mineralisation. This flocculation at numerous, spatially discrete sites spread throughout the deposit, led to the localised clogging of fluid pathways (veins) with massive but sporadically distributed clots of electrum causing the localised hyper-enrichment of gold in the deposit. Seismic pumping resulting from episodic, earthquake-related fault fracturing (Sibson et al., 1975) evidenced by the multi-stage nature of the mineralised veins and hydrothermal breccias at Brucejack (Tombe et al., 2018; Chapter 4), likely helped to circulate flocculated electrum particles through the deposit. By repeatedly clogging the fractures with electrum (as

illustrated in Fig. 2.1b) then unclogging them and introducing new particles, this seismic pumping progressively converted the fractures into hyper-enriched gold veins and was the final and critical driver of bonanza gold ore formation at Brucejack.

Our model offers a simple solution to the long-standing problem of how hydrothermal fluids with low gold concentrations can produce ultra-high grade or bonanza-type gold deposits, a paradox that has not been explained by genetic models involving the in-situ precipitation of crystalline gold, and also does not require the prior encapsulation of colloidal gold particles in silica gel as proposed by some previous studies (e.g., Saunders, 1990, 1994; Herrington and Wilkinson, 1993; and Saunders and Schoenly, 1995; Harrichhausen, 2016; Saunders and Burke, 2017; Burke et al., 2017; Petrella et al., 2020). In addition, boiling-induced colloid formation, followed by colloidal transport to sites of fluid mixing-induced flocculation, may help explain the distribution of high-grade gold mineralisation over vertical extents (e.g., > 1300 m at Brucejack; Chapter 4) that greatly exceed those of the boiling horizons in most fossil hydrothermal systems and their modern geothermal analogues (Clark and Williams-Jones, 1990; Herrington and Wilkinson, 1993). This is because colloid flocculation can occur far from the initial site of colloid formation, whereas the standard boiling model for epithermal deposits requires that phase separation and gold deposition are spatially coincident. We further speculate that the flocculated gold moved through micro- and nano-fractures in the main fluid pathways (which became infilled veins), intermittently clogging these fractures as illustrated in Figure 2.1b, eventually forming the clots of electrum that, on a much larger, visible scale, appear to have clogged the veins that characterise the bonanza mineralisation at Brucejack (Fig. 2.1a). This scenario explains why the massive electrum is texturally late in all the mineralised veins and why the clotted nature of the gold mineralisation, though ubiquitous, is texturally variable throughout the deposit.

In conclusion, the recent discoveries in modern hydrothermal systems of gold nanoparticles that may have formed from colloidal suspensions (Hannington and Garbe-Schönberg, 2019) coupled with our evidence for the colloidal transport of gold in a fossil system, suggest that mechanical enrichment of gold may be a much more widespread phenomenon than has been recognised to date. Indeed, this mineralising process may have occurred in several other types of systems, notably orogenic gold deposits (Voisey et al., 2020), and it may be the key to

understanding the formation of ultra-high grade or bonanza gold deposits in whatever geological environments they may occur.

Acknowledgements

References

Board, W.S., McLeish, D.F., Greig, C.J., Bath, O.E., Ashburner, J.E., Murphy, T., and Friedman, R.M., 2020, The Brucejack Au-Ag deposit, northwest British Columbia, Canada: Multistage porphyry to epithermal alteration, mineralization and deposit formation in an island-arc setting, in Sillitoe, R.H., Goldfarb, R.J., Robert, F., and Simmons, S.F., eds., Geology of the World's Major Gold Deposits and Provinces. Society of Economic Geologists Special Publication 23, p. 299–311.

Boydell, H.C., 1924, The role of colloidal solutions in the formation of mineral deposits. Institution of Mining and Metallurgy Transactions, v. 36, p. 145-337.

Buret, Y., von Quadt, A., Heinrich, C., Selby, D., Wälle, M., and Peytcheva, I., 2016, From along-lived upper-crustal magma chamber to rapid porphyry copper emplacement: reading the geochemistry of zircon crystals at Bajo de la Alumbrera (NW Argentina). Earth and Planetary Science Letters, v. 450, p. 120–131.

Clark, J.R., and Williams-Jones, A.E., 1990, Analogues of epithermal gold-silver deposition in geothermal well scales. Nature, v. 346, p. 644–645.

Faraday, M., 1857, Experimental relations of gold (and other metals) to light. Philosophical Transactions of the Royal Society of London, v. 147, p. 145-181.

Frondel, C., 1938, Stability of colloidal gold under hydrothermal conditions. Economic Geology, v. 33, p. 1-20.

Gartman, A., Hannington, M., Jamieson, J.W., Peterkin, B., Garbe-Schönberg, D., Findlay, A.J., and, Kwasnitschka, T., 2018, Boiling induced formation of colloidal gold in black smoker hydrothermal fluid. Geology, v. 46, p. 39–42.

Hannington, M., Hardardóttir, V., Garbe-Schonberg, D., and Brown, K., 2016, Gold enrichment in active geothermal systems by accumulating colloidal suspensions. Nature Geoscience, v. 9, p. 299–302.

Hannington, M., and Garbe-Schönberg, D., 2019, Detection of gold nanoparticles in hydrothermal fluids. Economic Geology, v. 114, p. 397-400.

Herrington, R., and Wilkinson, J., 1993, Colloidal gold and silica in mesothermal vein systems. Geology, v. 21, p. 539–542.

Hochella, M.F., Lower, S.K., Maurice, P.A., Penn, R.L., Sahai, N., Sparks, D.L., and Twining, B.S., 2008, Nanominerals, mineral nanoparticles, and earth systems. Science, v. 319, p. 1631-1634.

Iler, R.K., 1979, The Chemistry of Silica: Solubility, Polymerization, Colloid and Surface Properties and Biochemistry of Silica: John Wiley & Sons, New York, 896 p.

Levien, L., Prewitt, C.T., and Weidner, D.J., 1980, Structure and elastic properties of quartz at pressure., American Mineralogist 65, p. 920-930.

Liu, W., Chen, M., Yang, Y., Mei Y., Etschmann, B., Brugger, J., and Johannessen, B., 2019, Colloidal gold in sulphur and citrate-bearing hydrothermal fluids: an experimental study. Ore Geology Reviews, v. 114, 103142.

McLeish, D.F., Williams-Jones, A.E., Board, W.S., and Clark, J.R., 2018, Nature and origin of the Brucejack high-grade epithermal gold deposit, northwestern British Columbia (NTS 104B): 2017 update. Geoscience BC Summary of Activities 2017: Minerals and Mining Report 2018-1, p. 31–40.

Pearce, M. A., White, A. J., Fisher, L. A., Hough, R. M., and Cleverley, J. S., 2015, Gold deposition caused by carbonation of biotite during late-stage fluid flow. Lithos, v. 239, p. 114–127.

Penn, R. L., and Banfield, J.F., 1998, Imperfect oriented attachment: dislocation generation in defect-free nanocrystals. Science, v. 281, p. 969-971.

Peterson, E., and Mavrogenes, J.A., 2014, Linking high-grade gold mineralization to earthquake-induced fault-valve processes in the Porgera gold deposit, Papua New Guinea. Geology, v. 42, p. 383–386.

Petrella, L., Thébaud, N., Fougerouse, D., Evans, K., Quadir, Z., and Laflamme, C., 2020, Colloidal gold transport, a key to high-grade gold mineralization? Mineralium Deposita, v. 55, p. 1247-1254.

Prokoph, A., Shields, G.A, and Veizer J., 2008, Compilation and time-series analysis of a marine carbonate δ^{18}O, δ^{13}C, ^{87}Sr/^{86}Sr and δ^{34}S database through Earth history. Earth-Science Reviews, v. 87, p. 113-133.

Rowland, J.V., and Simmons, S.F., 2012, Hydrologic, magmatic, and tectonic controls on hydrothermal flow, Taupo Volcanic Zone, New Zealand: Implications for the formation of epithermal vein deposits. Economic Geology, v.107, p.427-457.

Román, N, Reich, M., Leisen, M., Morata, D., Barra, F., and Deditius, A.P., 2019, Geochemical and micro-textural fingerprints of boiling in pyrite. Geochimica et Cosmochimica Acta, v. 246, p. 60-85.

Saunders, J. A., 1990, Colloidal transport of gold and silica in epithermal precious-metal systems: Evidence from the Sleeper deposit, Nevada. Geology, v. 18, p. 757–760.

Saunders, J.A., 1994, Silica and gold textures in bonanza ores of the Sleeper Deposit, Humboldt County, Nevada: evidence for colloids and implications for epithermal ore-forming processes. Economic Geology, v. 89, p. 628–638.

Saunders, J.A., and Schoenly P.A., 1995, Boiling, colloidal nucleation and aggregation, and the genesis of Bonanza Au-Ag ores of the Sleeper Deposit, Nevada. Mineral Deposita, v. 30, p. 199-210.

Saunders, J.A., and Burke, M., 2017, Formation and aggregation of gold (electrum) nanoparticles in epithermal ores. Minerals, v. 7(9), 163, doi.org/10.3390/min7090163.

Scott, M., Chen, C.-C., Mecklenburg, M., Zhu, C., Xu, R., Ercius, P., Dahmen, U., Regan, B., and Miao, J., 2012, Electron tomography at 2.4-angstrom resolution. Nature, v. 483, p. 444–447.

Seward, T.M., 1973, Thio complexes of gold and the transport of gold in hydrothermal ore solutions. Geochimica et Cosmochimica Acta, v. 37, p. 379-399.

Sibson, R.H., Moore, J.M., and Rankin, A.H., 1975, Seismic pumping — a hydrothermal fluid transport mechanism. Journal of the Geological Society, v. 131, p. 653-659.

Simmons, S. F., and Brown, K. L., 2006, Gold in magmatic hydrothermal solutions and the rapid formation of a giant ore deposit. Science, v. 314, p. 288-291.

Stefánsson, A., and Seward, T. M., 2004, Gold(I) complexing in aqueous sulphide solutions to 500 °C at 500 bar. Geochimica et Cosmochimica Acta, v. 68, p. 4121-4143.

Tombe, S.P., Richards, J.P., Greig, C.J., Board, W.S., Creaser, R.A., Muehlenbachs, K.A., Larson, P.B., Dufrane, S.A., and Spell, T., 2018, Origin of the high-grade Early Jurassic Brucejack epithermal Au-Ag deposits, Sulphurets Mining Camp, northwestern British Columbia. Ore Geology Reviews, v. 95, p. 480-517.

Turkevich, J., Stevenson, P., and Hillier, J. A., 1951, A study of the nucleation and growth process in the synthesis of colloidal gold. Discussions of the Faraday Society, v. 11, p. 55-75.

Voisey, C.R., Willis, D., Tomkins, A.G., Wilson, C.J.L., Micklethwaite, S., Salvemini, F., Bougoure, J., and Rickard, W.D.A., 2020, Aseismic refinement of orogenic gold systems. Economic Geology, v. 115, p. 33–50.

Williams-Jones, A.E., Bowell R.J., and Migdisov, A.A., 2009, Gold in Solution. Elements, v. 5, p. 281-287.

Zhang, F., Xu., H, Konishi, H., and Roden, E.E., 2010, A relationship between d_{104} value and composition in the calcite-disordered dolomite solid-solution series. American Mineralogist, v. 95, p. 1650-1656.

Data Supplement S2.1 – Analytical procedures

The TEM lamellae investigated in this study were prepared with a FEI Helios Nanolab 660 DualBeam focused ion beam scanning electron microscope (FIBSEM; Thermo Scientific, Hillsboro, OR USA) at the Facility for Electron Microscopy Research at McGill University using trench and in situ lift-out techniques. The FIBSEM is equipped with a gallium ion source operating in the accelerating-voltage range 0.5 - 30 keV, a gas injection system (GIS) and an EasyLift Nanomanipulator System.

Prior to inserting a thin section into the Helios, an ex-situ layer of Pt was deposited over the surface using the Leica EM ACE600 sputter coater (Leica Microsystems, Wetzlar, Germany). Areas of the thin section containing Au nanoparticles were identified using the concentric backscatter (CBS) detector at an accelerating voltage of 20 keV and beam current of 0.40 nA. To prevent ion-beam surface damage to the region of interest (ROI) during milling, reduce curtaining effects and strengthen the lamella, an in-situ protective layer of Pt 23-μm long, 3-μm wide and 2-μm thick was deposited using the GIS. Conventional cross-section patterns were used to excavate material from either side of the Pt layer to a depth of ~19 μm. Milling was performed at 30 keV with a stepwise lowering of the ion beam current from 65 nA to 0.79 nA. After thinning a lamella to a thickness of ~1 μm with an ion beam current of 0.79 nA, the lamella was lifted out and attached to a Cu TEM half grid using the EasyLift nanomanipulator. Owing to the large size of the lamella (~23 x 19 μm) and hardness of the sample, the final steps were to thin both sides of the lamella to electron transparency with higher-than-normal beam energy: to ~500 nm using 30 keV and 0.79 nA, to 200 nm using 30 keV and 0.23 nA, and to ~100 nm using 30 keV and 80 pA.

High resolution imaging of the TEM lamellae was performed with a FEI Tecnai G2 F20 STEM (Thermo Scientific, Hillsboro, OR USA) equipped with an EDAX Octane T Ultra W /Apollo XLT2 SDD and TEAM EDS (energy-dispersive X-ray spectroscopy) Analysis System (EDAX, Inc. Mahwah, NJ USA) and a Fischione Instruments Model 3000 Annular Dark Field (ADF) Detector (E.A. Fischione Instruments, Inc., Export, PA USA). The machine was equipped with a Schottky field electron emitter and a TWIN objective lens. The TEM point resolution was 0.27 nm and the line resolution were 0.14 nm. The scanning transmission electron microscope (STEM) high angle annular dark field (HAADF) resolution was 0.3 nm. For STEM, the

collection angle was 57 mrad, and the objective aperture was 100 micron A Gatan Ultrascan 4000 4k x 4k CCD Camera System Model 895 was used for TEM imaging, recording and processing including fast Fourier transformation (FFT) and inverse fast Fourier transformation (IFFT). Images were recorded in bright field mode at an accelerating voltage of 200 kV using the Gatan Model 895 Ultrascan 4000 CCD Camera System (Gatan, Inc., Warrendale, PA USA). STEM was performed by using a HAADF detector operating through the Tecnai imaging and analysis (TIA) interface.

EDAX analysis was supported with an Apollo XLT2 windowless silicon drift detector (SDD) operating through the TIA interface. Point analysis spectra (focussed probe) were recorded with this system.
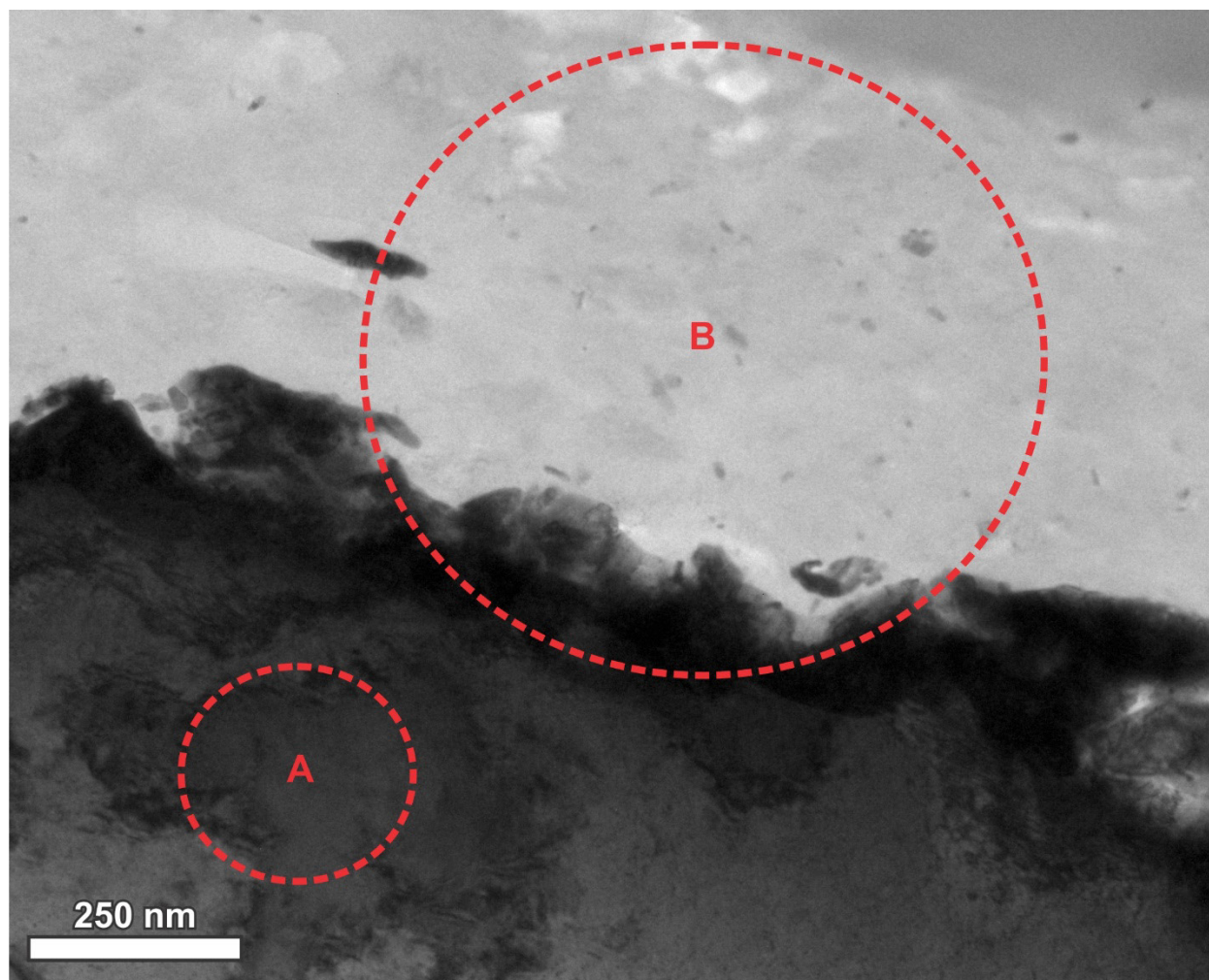
Figure S2.1: A bright field TEM image of the contact between a large electrum grain (lower half of image) and the calcite matrix of the host calcite-quartz vein (upper half of image) showing the source locations (A and B) of SAED images presented in Figures S2 and S3.
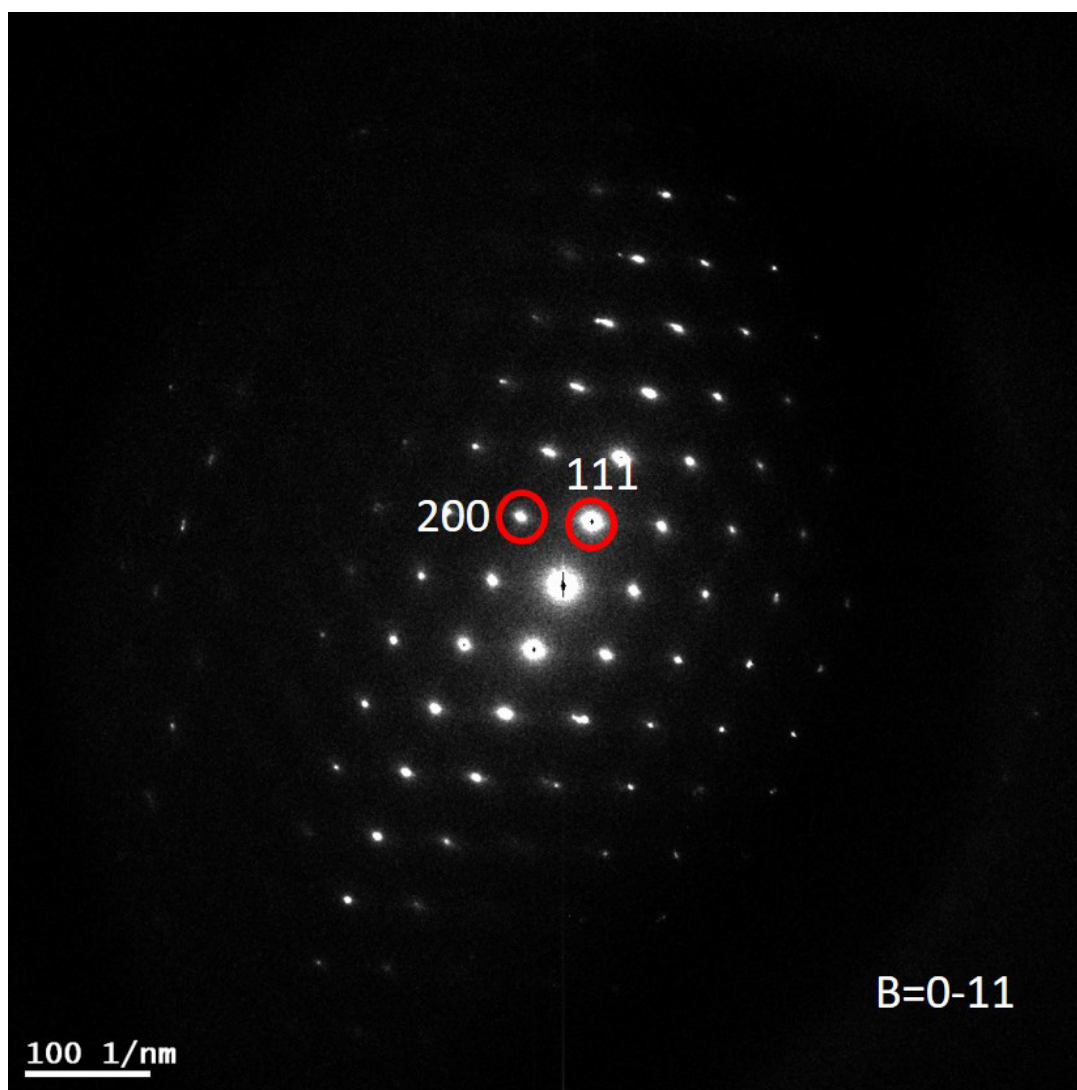
Figure S2.2: A selected area electron diffraction (SAED) image of area A in Figure S1. The diffraction maxima shown here are typical of those for monocrystalline gold. The reflection used to generate the image is (111).
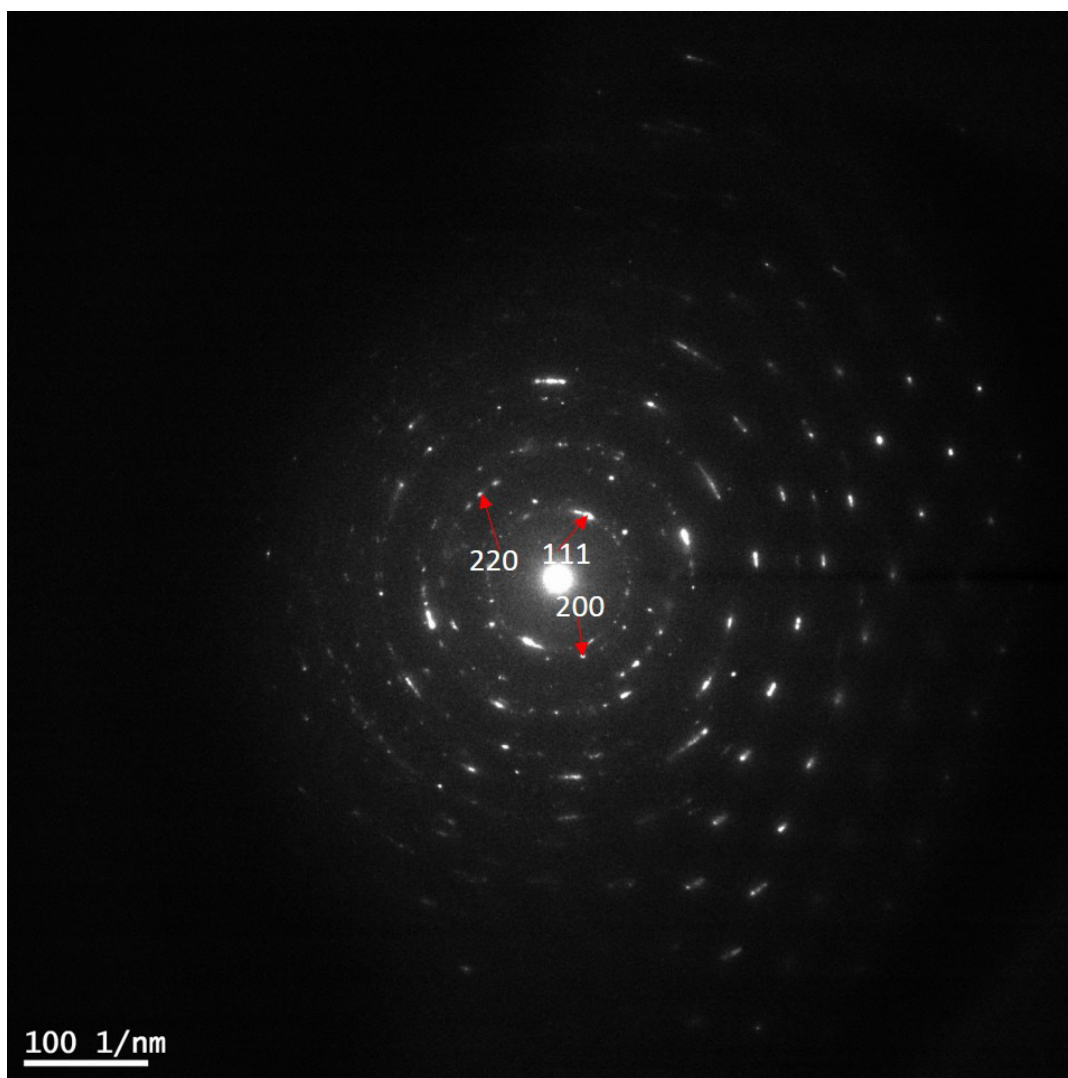
Figure S2.3: A selected area electron diffraction (SAED) image of area B in Figure S1. The diffraction maxima are typical of those for polycrystalline gold and indicate that multiple gold (electrum) crystals are present in the imaged area.
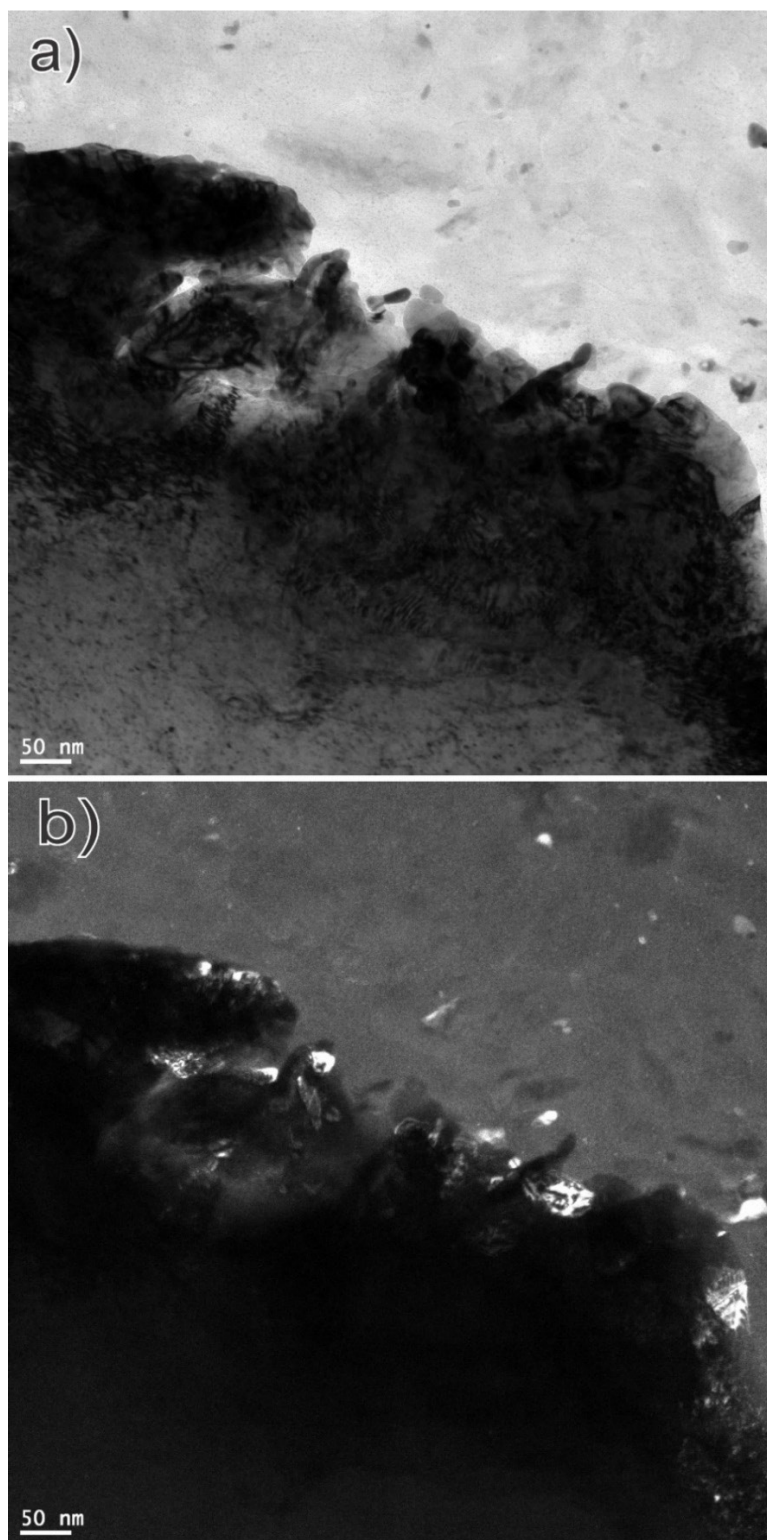
Figure S2.4: (a) bright field and (b) corresponding high-angle angular dark field (HAADF) TEM images of the contact between a large electrum grain (lower left in both images) and the matrix of a calcite vein, which contains nanoparticles of electrum (higher contrast spots in the matrix in the HAADF image).
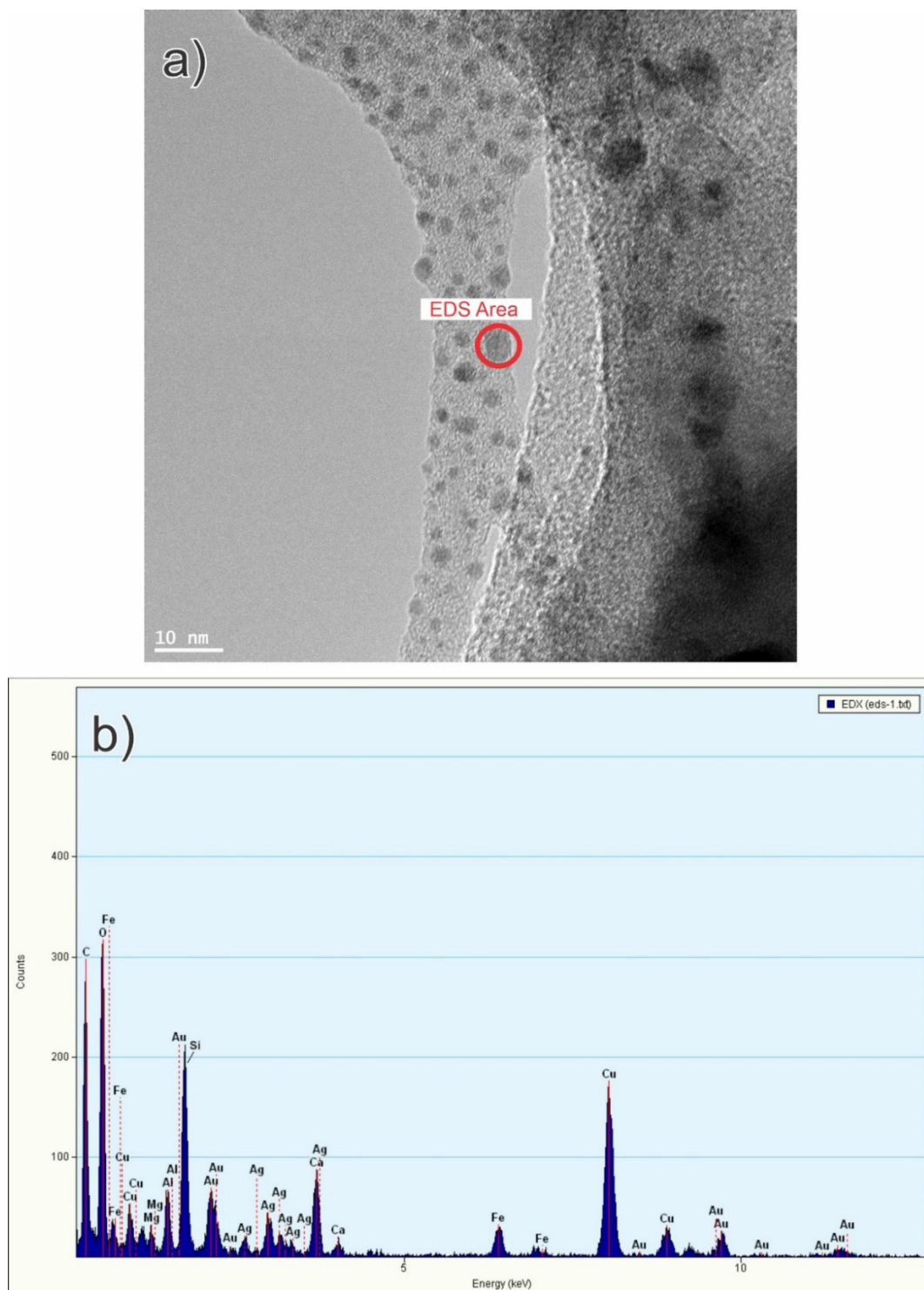
Figure S2.5: (a) bright field TEM image showing gold (electrum) nanoparticles in a calcite-chlorite matrix. (b) Results of an EDS analysis of the circled nanoparticle in the bright field image, confirming that it is electrum. The Cu peaks are artifacts from the instrument. The Ca, C, and O peaks confirm that the matrix material surrounding the nanoparticle is calcite with chlorite (Mg, Fe, Al, and Si peaks).

CHAPTER 3

Extreme shifts in pyrite sulphur isotope compositions reveal the path to bonanza gold mineralisation in the Brucejack deposit, northwestern British Columbia

Preface

The results presented in Chapter 2 demonstrate that gold may be transported in the solid state as nanoparticles (colloids) by hydrothermal fluids to sites where aggregates of gold are deposited through the flocculation of colloidal suspensions. In order to better understand what causes the destabilisation and ultimately flocculation of colloidal suspensions in hydrothermal systems, Chapter 3 entitled, "Extreme shifts in pyrite sulphur isotope compositions reveal the path to bonanza gold mineralisation in the Brucejack deposit, northwestern British Columbia", investigates the trace element and sulphur isotope signatures of pyrite from the high-grade Brucejack epithermal Au-Ag deposit using secondary ion mass spectrometry (SIMS) and electron microprobe wavelength-dispersive X-ray spectroscopy (EMP-WDS) methods. Pyrite is the only sulphide mineral at Brucejack to have formed through every major ore and alteration event in the history of the deposit and therefore provides a unique and uninterrupted record of fluid evolution. The results of the analyses show that pyrite preserves a complex chemical history of fluid evolution that preceded and ultimately coincided with bonanza gold mineralisation; the implications of these findings are discussed in Chapter 3 as they relate to the genetic model presented in Chapter 2.

Abstract

Pyrite is the most common sulphide mineral in hydrothermal ore-forming systems. The ubiquity and abundance of pyrite, combined with its ability to record and preserve a history of fluid evolution in most crustal environments, make it an ideal mineral for studying the genesis of hydrothermal deposits. However, with the exception of boiling, few studies have been able to link changes in pyrite chemistry to hydrothermal ore-forming processes, and, by extension, use pyrite chemistry as a tool for identifying ore-forming events. Here we report the results of high-resolution secondary-ion mass spectrometry and electron microprobe analyses conducted on pyrite from the Brucejack epithermal gold deposit, British Columbia. Our $\delta^{34}S$ and trace element results reveal that the Brucejack hydrothermal system experienced a series of abrupt changes in fluid chemistry which preceded and ultimately coincided with the onset of ultra-high-grade, or 'bonanza', gold-silver mineralisation. We argue that these changes, which include the occurrence of extraordinarily negative $\delta^{34}S$ values (e.g., -36.0‰) in zones of auriferous, arsenian pyrite, followed by sharp increases of $\delta^{34}S$ in syn-electrum zones of non-arsenian pyrite, were caused by vigorous, episodic boiling and subsequent inundation of the hydrothermal system by seawater. We conclude that the influx of seawater was an essential step to forming bonanza-grade electrum mineralisation by triggering, through the addition of cationic flocculants and cooling, the aggregation of colloidal gold suspensions. Our study demonstrates the efficacy of employing high-resolution, in situ analytical techniques to map out individual ore-forming events in a hydrothermal system, and suggests that mixing of seawater with a boiled ore fluid containing colloidal gold is an essential catalyst for bonanza-style mineralisation in epithermal ore-forming systems.

3.1 Introduction

The genesis of spatially restricted, ultra-high-grade 'bonanza' gold in hydrothermal ore deposits has long been enigmatic. Recent research (Burke et al., 2017; Saunders and Burke, 2017; Petrella et al., 2020; Voisey et al., 2020; McLeish et al., 2021) has indicated that the formation of these bonanza occurrences is largely mechanical, involving the transport of gold in the solid-state as colloidal suspensions rather than as a dissolved species. Although the existence of colloidal gold particles is now well established by these studies, the processes that trigger flocculation, i.e., the means by which colloidal particles aggregate to form macroscopic masses of solid gold, have not been demonstrated. Thus, while processes such as boiling, fluid mixing, and reduction have been proposed as possible causes of flocculation (e.g., Saunders 1990; Petrella et al. 2020), evidence that links these processes directly to bonanza-grade gold deposition in a fossil hydrothermal system is lacking.

In order to better understand the controls on flocculation in bonanza-style hydrothermal deposits, we have undertaken a detailed trace element and sulphur isotope study of pyrite from the Brucejack epithermal gold deposit, British Columbia. Pyrite at Brucejack is the only sulphide mineral to have formed through every major ore and alteration event in the paragenesis of the deposit (Harrichhausen, 2016; Tombe et al., 2018). Pyrite thus provides a unique and uninterrupted record of fluid evolution, as well as insight into the physicochemical conditions that governed the flocculation of colloidal gold suspensions at Brucejack.

3.2 The Brucejack Deposit

Brucejack is a large (15.7 million tons grading 8.4 g/t Au, 60 g/t Ag; Shaw, 2020) intermediate- to low-sulphidation Au-Ag epithermal deposit that hosts locally spectacular, bonanza-grade (up to 41,582 g/t Au in a 0.5 m drill core interval) gold mineralisation. The gold occurs in carbonate-quartz vein swarms, fault-fill vein breccias and stockworks in an early Jurassic succession of intermediate to mafic fragmental volcanic, volcaniclastic and argillaceous sedimentary host rocks (Tombe et al., 2018). The deposit was emplaced near the margin of the long-lived Stikinia island arc at ~184 Ma, shortly before it was intruded by a suite of 183 Ma intermediate to mafic dykes (Board et al., 2020). High-grade gold mineralisation occurs typically as 1-30 cm wide clots of calcite-hosted dendritic electrum ($Au_{62}Ag_{38}$), and is commonly in contact with vein- or wallrock-hosted pyrite (McLeish et al., 2018).

45

Most vein-hosted pyrite at Brucejack is cross-cut by high-grade electrum and is therefore believed to have formed during an early, widespread, mainly pre-mineralisation-stage phyllic alteration event (McLeish et al., 2018). Volumetrically minor, late-stage pyrite occurs in textural equilibrium with electrum and is interpreted to have formed during emplacement of the three main electrum-hosting vein stages (Stages III-V; Tombe et al. 2018). Both wallrock- and vein-hosted pyrite exhibit multi-phase growth zoning including: (1) cubic cores with elevated Ni, Se, Sb, Co, Pb and Bi concentrations, surrounded by (2) oscillatory zones containing alternating high/low As ± Au growth bands and locally well-developed colloform textures, and (3) an outermost cubic growth zone that lacks trace-element zonation. Strong similarities in the trace element distributions of the first two growth phases suggest that these components of vein-hosted pyrite were inherited from the wallrocks (McLeish et al., 2018).

3.3 Pyrite and fluid evolution in epithermal ore deposits

Owing to its ability to form over a wide range of physicochemical conditions, its abundance in most fossil hydrothermal systems, and its sensitivity to changes in fluid chemistry, pyrite has become widely recognised as an important monitor of fluid evolution in ore deposits (see Steadman et al., 2021, for a review). Most studies of pyrite in epithermal deposits have focused on trace element distributions (e.g., Börner et al., 2021) and some research has related this distribution and the micro-textural characteristics of pyrite to ore-forming processes such as boiling (e.g., Román et al., 2019). Although a few studies have investigated the intracrystalline isotopic changes that likely accompany, and may be characteristic of, major ore-forming events in porphyry-epithermal (e.g., Peterson and Mavrogenes, 2014) and Carlin-type deposits (e.g., Barker et al., 2009), none have used such data to interpret the occurrence of bonanza gold mineralisation.

3.4 Methods

We sampled pyrite from all three stages of electrum-bearing veins as well as pre-electrum phyllic wallrock alteration from the Brucejack mine to investigate the trace element and $\delta^{34}S$ intra-grain isotopic record that preceded, and eventually coincided with, the formation of high-grade gold mineralisation in the deposit. An initial, qualitative survey of intra-grain compositions was conducted using energy-dispersive X-ray spectroscopy and was followed by the quantitative determination of element concentrations via electron microprobe (EMP) analysis. Sulphur

isotope compositions were subsequently determined in situ by high-resolution secondary ion mass spectrometry (SIMS) analyses. The maximum uncertainty (2σ) for the SIMS δ^{34}S analyses is 0.4 ‰ and typically it is ≤ 0.2 ‰ (see Data Supplements S3.1 for additional analytical details and S3.2 complete results).

3.5 Results

Detailed backscattered electron (BSE) imaging of pyrite from mineralised veins and phyllically altered wallrock indicates that, whereas the previously reported three growth events (see above) are present in samples from all vein stages and wallrock, the intermediate-stage arsenian bands differ significantly from those of the other generations. Pyrite from the Stage V, bonanza-grade Cleopatra vein in the core of the deposit, which has been a major source of gold production, is characterised by arsenian growth bands exhibiting locally well-developed colloform textures that become increasingly chaotic towards the grain rim (Fig. 3.1a). In contrast, pyrite from phyllically altered wallrock directly adjacent to lower grade Stage V veins near the periphery of the deposit display single, broad arsenian growth zones with sharp, euhedral outer limits (Fig. 3.2a). Traverses across these two types of arsenian bands show that they are characterised by different sulphur isotope compositions (Figs. 3.1b-d vs. Fig. 3.2b). In the Cleopatra vein samples, colloform arsenian bands are associated with weakly to extremely negative δ^{34}S shifts (<1‰ to ~16‰ magnitude), whereas the euhedral arsenian bands in peripheral Stage V veins are associated with δ^{34}S values that increase steadily from core to rim (from -1.28 to +23.99‰; Fig. 3.2 transect Y-Y'). Analyses of the colloform and euhedral arsenian bands indicate that the former hosts significant invisible Au (up to 150 ppm), whereas the latter contains no detectable Au ($< \sim 90$ ppm Au).

In addition to the δ^{34}S changes observed in the arsenian growth bands, the SIMS traverses demonstrate that many large intra-grain δ^{34}S shifts, both negative and positive, occur in areas that otherwise lack compositional variation. For example, in the Cleopatra vein, pyrite transect V-V' (Fig. 3.1) exhibits several sharp drops in δ^{34}S in the first 300 µm that do not correlate with compositional changes evident from BSE imaging (Fig. 3.1b), and the outermost (grain rim) analyses show an extremely positive shift in a zone of non-arsenian pyrite. Similar positive shifts occur in the non-arsenian grain rims along traverses U-U' and X-X' (Figs. 3.1b and 1d). Whereas the rim analyses in each traverse in Figure 3.1 yielded variable δ^{34}S values, all traverses reveal
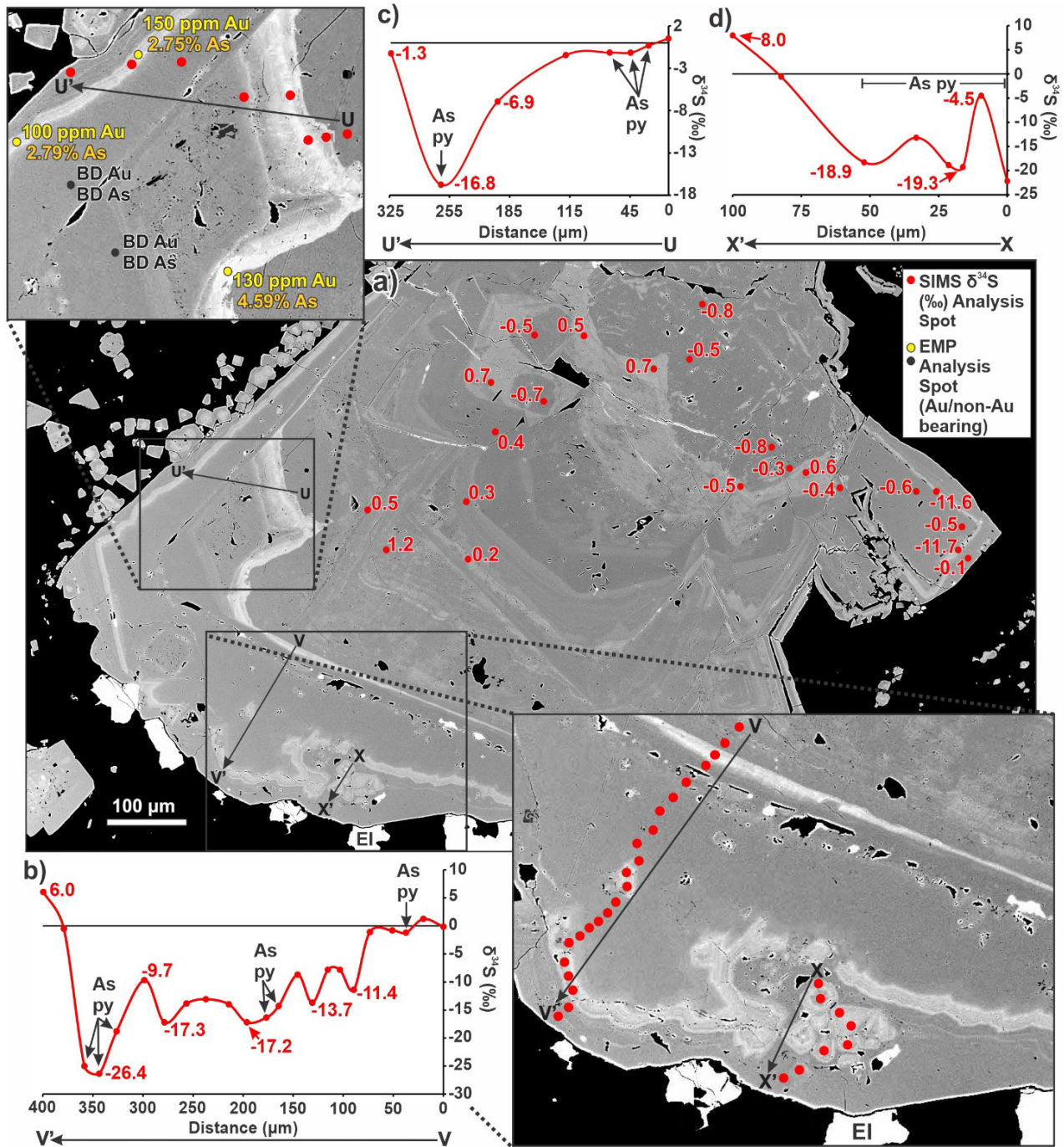
Figure 3.1: (a) A BSE image of pyrite and electrum (El) from the Stage V Cleopatra vein showing complex, multigenerational growth zoning and the location of SIMS δ³⁴S analytical transects U-U', V-V' and X'-X', as well as EMP spot results for Au and As (BD = below detection), and analyses outside of transects. **(b-d)** plots of δ³⁴S vs. distance for transects U-U', V-V' and X'-X', respectively.
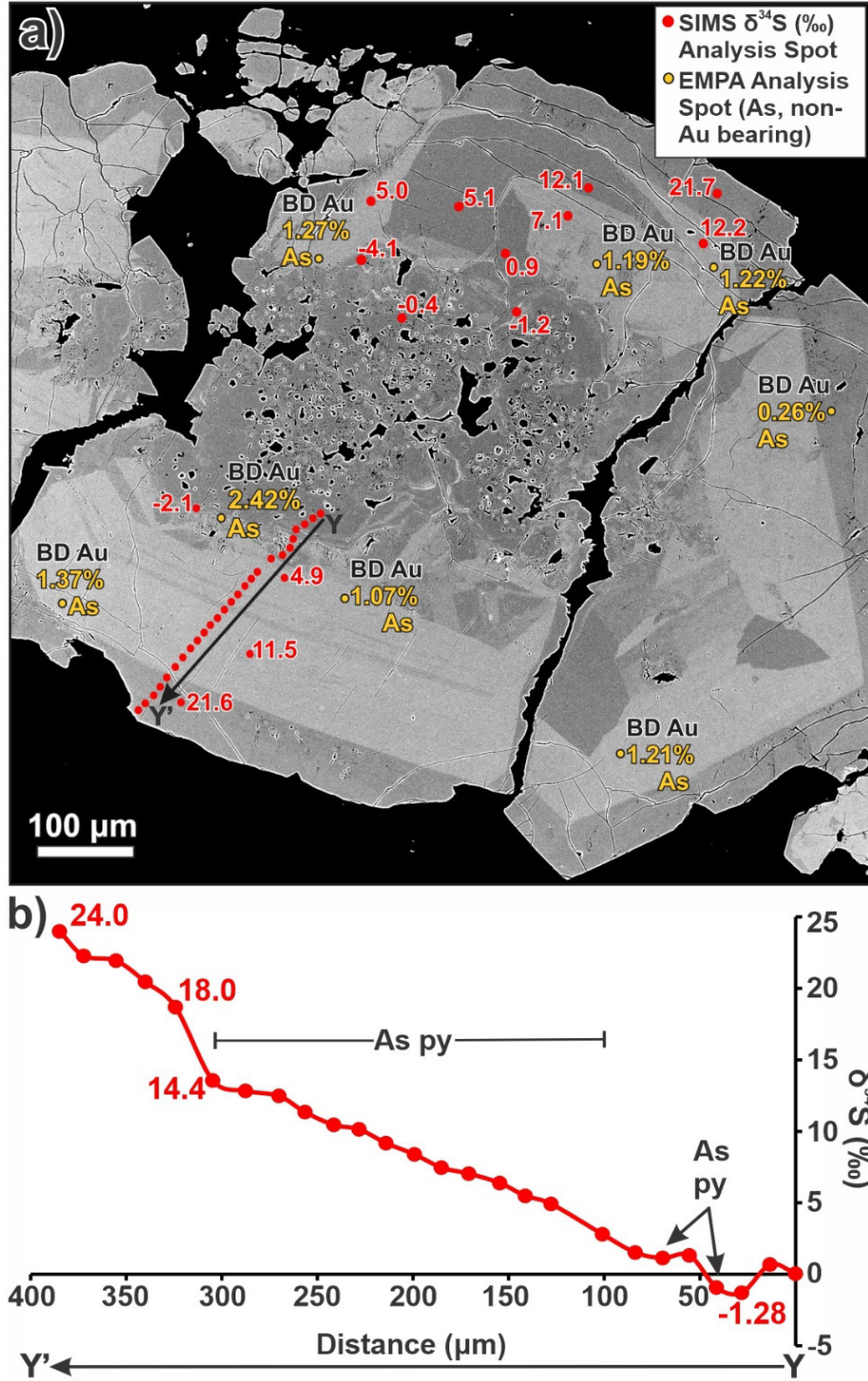
Figure 3.2: (a) A BSE image of a pyrite grain in a Stage V vein from the periphery of the deposit showing SIMS δ^{34}S spots for transect Y-Y', and δ^{34}S and EMP Au and As values for spots analysed outside the transect. **(b)** A plot of δ^{34}S vs. distance for transect Y-Y'.

an extremely positive δ^{34}S shift in the outermost growth zone which, importantly, is in textural equilibrium with high-grade electrum mineralisation (Fig. 3.1a).

In order to further explore the δ^{34}S shifts that led to the formation of electrum mineralisation at Brucejack, a SIMS transect was made across a vein-margin-hosted pyrite grain from a second, Stage V vein in the center of the deposit (Fig. 3.3). Along the transect (Z-Z'; Fig. 3.3a), the vein-margin-parallel growth bands in this grain alternate between broad non-arsenian and narrow arsenian pyrite before terminating in an outer zone consisting of numerous very small (< 20 µm) isolated and agglomerated pyrite crystals. These very small pyrite crystals have cubic to pyritohedron shapes and are in textural equilibrium with electrum. The SIMS transect reveals two inner, non-arsenian zones of pyrite with moderately positive δ^{34}S (+5 to +9‰) signatures, separated by a non-arsenian zone with near-zero δ^{34}S values. Beyond the outer non-arsenian zone, there is a precipitous drop in δ^{34}S values over ~ 50 µm (+8 to -36‰), which coincides initially with a zone of arsenian pyrite and continues outward in non-arsenian pyrite. This is followed by a sharp reversal in δ^{34}S values, which increase by ~30‰ over a distance of ~ 30 µm through both arsenian and non-arsenian zones.

3.6 Discussion

To our knowledge, the δ^{34}S traverses reported in this study record the largest intra-grain variations in sulphur isotope compositions ever identified in a non-biogenic sulphide mineral. For example, the range in δ^{34}S values for a single Brucejack pyrite crystal, from +8.3‰ to -36.0‰ (Fig. 3.3), far exceed the intra-grain variations for hydrothermal pyrite in the Porgera epithermal deposit (Peterson and Mavrogenes, 2014). Furthermore, the most negative δ^{34}S$_{pyr}$ value at Brucejack (-36.0‰; Fig. 3.3a) is substantially lower than both: (1) the lowest δ^{34}S$_{pyr}$ values reported for a porphyry-epithermal ore deposit (Hutchison et al., 2020); and (2) the typical δ^{34}S for pyrite formed during open system bacterial reduction of marine sulphate (Canfield, 2001). The extremely negative values at Brucejack, which are characterised by abrupt changes in pyrite growth, are almost certainly the product of rapid boiling. By vaporising hydrogen, boiling oxidises the hydrothermal fluid and consequently fractionates isotopically heavier sulphur into sulphate and lighter sulphur into reduced sulphur that forms pyrite. This interpretation is supported by the observation that the most negative δ^{34}S values occur in colloform arsenian pyrite, the texture and composition of which (high Au and As concentrations) are typical of
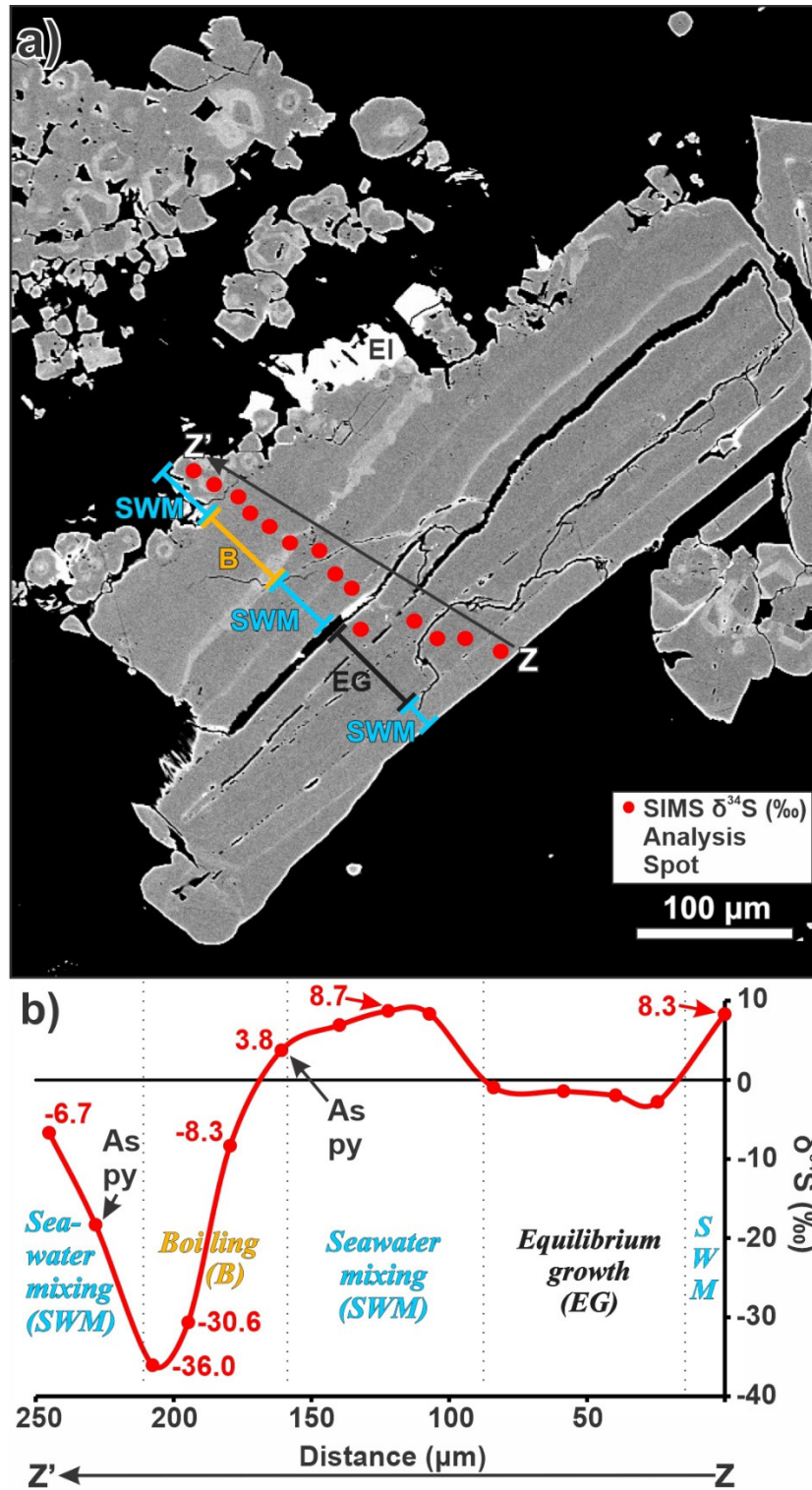
Figure 3.3: (a) A BSE image of a pyrite crystal and adjacent electrum (El) in a Stage V vein from the core of the deposit showing the locations of SIMS δ^{34}S spots for transect Z-Z'. **(b)** A plot of δ^{34}S vs. distance for transect Z-Z'.

boiling-induced pyrite formation (Román et al., 2019). Other hypotheses that have been proposed to explain strongly negative $\delta^{34}S$ values in auriferous, arsenian pyrite are cooling of highly oxidised magmatic fluids and/or extreme disproportionation of SO_2 (Wilson et al., 2007; Peterson and Mavrogenes, 2014). In principle, these hypotheses could explain the very negative $\delta^{34}S$ values observed at Brucejack, but they are not credible because no $\delta^{34}S$ values < -25 ‰ have ever been reported for magmatic hydrothermal systems, even those evolving to very low temperature.

Although the large negative excursion of the pyrite $\delta^{34}S$ values at Brucejack is extraordinary, it is not the most noteworthy finding of this study. Even more surprising are the strongly positive $\delta^{34}S$ shifts that are texturally associated with electrum. They indicate that a process other than boiling must have been operating during bonanza gold deposition. The steady increase in $\delta^{34}S$ values from near zero to ~ +24‰ in the lower grade Stage V peripheral veins (Fig. 3.2) suggests that there was extensive mixing between an originally magmatic-dominant fluid and one with a substantially more positive $\delta^{34}S$ signature. Given that: (1) the Brucejack deposit was emplaced near the edge of an Early Jurassic island arc undergoing widespread denudational extension and/or transtension (Nelson and Kyba, 2014), and (2) Early Jurassic seawater was characterised by $\delta^{34}S$ values of +15 to 24‰ (Prokoph et al., 2008), we propose that this more positive fluid was seawater.

Integrating the Brucejack intra-grain $\delta^{34}S_{pyr}$ record across the deposit reveals a complex interplay of processes leading to, and culminating in, the formation of bonanza gold mineralisation. The cyclical, progressively more negative and extreme shifts in $\delta^{34}S$ values in the ultra-high-grade Cleopatra vein (Fig. 3.1) reflect multiple boiling events which became incrementally more intense over time. This cyclical boiling, which is consistent with a seismic pumping fault-valve model (Sibson et al., 1975), terminated in a singular extreme boiling event that depressed the $\delta^{34}S$ signature by > 17‰ prior to seawater mixing and the onset of the main stage of gold mineralisation. Figure 3.3 demonstrates that pyrite in other high-grade veins, while recording a similarly extreme terminal boiling event followed by a sharp syn-electrum increase in $\delta^{34}S$, preserves an earlier history of the mixing of the ore fluid with seawater unseen by the Cleopatra vein. In transect Z-Z', $\delta^{34}S$ values of pyrite were initially below the range for

equilibrium with Early Jurassic seawater. We speculate that this moderately positive δ^{34}S signature (~ +8.7‰) reflects the initial onset of fault-valve-induced seawater-ore fluid mixing.

In closing, our findings have fundamental implications for the processes by which bonanza-grade hydrothermal gold deposits form, and demonstrate how grain-scale micro-textural and mineral chemical analyses can be used to assess mineralisation processes. Firstly, by establishing the synchronous nature of fluid-mixing and high-grade mineralisation in a deposit where colloidal transport of gold has been identified (McLeish et al., 2021), this study provides direct evidence for syn-mineralisation seawater-mixing, a process which may drive the flocculation of gold nanoparticles (cf. Saunders, 1990). Secondly, contrary to Weatherley and Henley (2013), our results are consistent with the idea that the sulphur isotopic compositions of sulphide minerals record the primary physicochemical changes associated with rapid boiling (flash vaporisation) events. Thirdly, the δ^{34}S transects presented here indicate that, although the occurrence of colloform arsenian pyrite is indeed due to boiling, 'invisible' boiling events in pyrite, i.e., those with no obvious textural or mineral-chemical record, can be relatively common (Fig. 3.1b). Fourthly, our findings highlight the importance of using in situ analytical techniques to resolve stable isotope signatures at the micron-scale; previous studies at Brucejack using whole-grain analytical methods yielded fairly consistent δ^{34}S values for pyrite from mineralised veins, in a narrow range of -1.7 to +0.6‰ (Tombe et al., 2018). Finally, although the EMP data presented here and elsewhere (McLeish et al., 2018) confirm that boiling events were accompanied by significant deposition of gold in the form of auriferous pyrite, the positive, seawater-driven, syn-electrum δ^{34}S shifts in Brucejack pyrite strongly suggest that fluid mixing was the ultimate trigger for high-grade gold mineralisation.

Acknowledgements

References

Barker, S.L.L., Hickey, K.A., Cline, J.S., Dipple, G.M., Kilburn, M.R., Vaughan, J.R., and Longo, A.A., 2009, Uncloaking invisible gold: use of NanoSIMS to evaluate gold, trace elements, and sulfur isotopes in pyrite from Carlin-type gold deposits. Economic Geology, v. 104, p. 897–904.

Board, W.S., McLeish, D.F., Greig, C.J., Bath, O.E., Ashburner, J.E., Murphy, T., and Friedman, R.M., 2020, The Brucejack Au-Ag deposit, northwest British Columbia, Canada: Multistage porphyry to epithermal alteration, mineralization and deposit formation in an island-arc setting, in Sillitoe, R.H., Goldfarb, R.J., Robert, F., and Simmons, S.F., eds., Geology of the World's Major Gold Deposits and Provinces. Society of Economic Geologists Special Publication 23, p. 299–311.

Börner, F., Keith, M., Smith, D.J, Barry, T.L., Neumann, T., and Klemd, R., 2021, Fingerprinting fluid evolution by trace elements in epithermal pyrite, Vatukoula Au-Te deposit, Fiji. Ore Geology Reviews, v. 137, doi: 10.1016/j.oregeorev.2021.104314

Burke, M., Rakovan, J., and Krekeler, M.P.S., 2017, A study by electron microscopy of gold and associated minerals from Round Mountain, Nevada. Ore Geology Reviews, v. 91, p. 708–717.

Canfield, D.E., 2001, Isotope fractionation by natural populations of sulfate-reducing bacteria. Geochimica et Cosmochimica Acta, v. 65, p. 1117–1124.

Harrichhausen, N.J., 2016, Role of colloidal transport in the formation of high-grade gold veins at Brucejack, British Columbia (M.Sc. thesis). McGill University, Montreal, Quebec, 123 p.

McLeish, D.F., Williams-Jones, A.E., Board, W.S. and Clark, J.R., 2018, Nature and origin of the Brucejack high-grade epithermal gold deposit, northwestern British Columbia (NTS 104B): 2017 update. Geoscience BC Summary of Activities 2017: Minerals and Mining Report 2018-1, p. 31–40.

McLeish, D.F., Williams-Jones, A.E., Vasyukova, O.V., Clark, J.R., and Board, W.S., 2021, Colloidal transport and flocculation are the cause of the hyper-enrichment of gold in nature. Proceedings of the National Academy of Sciences, v. 118, doi:10.1073/pnas.2100689118.

Peterson, E., and Mavrogenes, J.A., 2014, Linking high-grade gold mineralization to earthquake-induced fault-valve processes in the Porgera gold deposit, Papua New Guinea. Geology, v. 42, p. 383–386.

Petrella, L., Thébaud, N., Fougerouse, D., Evans, K., Quadir, Z. and Laflamme, C., 2020, Colloidal gold transport, a key to high-grade gold mineralization? Mineralium Deposita, v. 55, p. 1247-1254.

Prokoph, A., Shields, G.A and Veizer J., 2008, Compilation and time-series analysis of a marine carbonate $\delta^{18}O$, $\delta^{13}C$, $^{87}Sr/^{86}Sr$ and $\delta^{34}S$ database through Earth history. Earth-Science Reviews, v. 87, p. 113-133.

Román, N, Reich, M., Leisen, M., Morata, D., Barra, F. and Deditius, A.P., 2019, Geochemical and micro-textural fingerprints of boiling in pyrite. Geochimica et Cosmochimica Acta, v. 246, p. 60-85.

Saunders, J. A., 1990, Colloidal transport of gold and silica in epithermal precious-metal systems: Evidence from the Sleeper deposit, Nevada. Geology, v. 18, p. 757–760.

Saunders, J.A., and Burke, M., 2017, Formation and aggregation of gold (electrum) nanoparticles in epithermal ores. Minerals 7(9), v. 163, doi.org/10.3390/min7090163.

Sibson, R.H., Moore, J.M. and Rankin, A.H., 1975, Seismic pumping — a hydrothermal fluid transport mechanism. Journal of the Geological Society, v. 131, p. 653-659.

Shaw, A., Boese, C., Fraser, C., Ghaffari, H., Jones, I.W.O., Huang, J., Findlater, L., Phifer, M., Herrera, M., Schmitt, R., and Coleman, T., Technical report on the Brucejack Gold Mine, Northwest British Columbia, 2020, available: https://www.sec.gov/Archives/edgar/data/1508844/000119983520000108/ex99-2.htm. Accessed 25 January 2022.

Steadman, J.A., Large, R.R., Olin, P.H., Danyushevsky, L.V., Meffre, S., Huston, D., Fabris, A., Lisitsin, V., and Wells, T., 2020, Pyrite trace element behavior in magmatic-hydrothermal environments: An LA-ICPMS imaging study. Ore Geology Reviews, v. 128, p. 1-20, doi: 10.1016/j.oregeorev.2020.103878.

Tombe, S.P., Richards, J.P., Greig, C.J., Board, W.S., Creaser, R.A., Muehlenbachs, K.A., Larson, P.B., Dufrane, S.A. and Spell, T., 2018, Origin of the high-grade Early Jurassic Brucejack epithermal Au-Ag deposits, Sulphurets Mining Camp, northwestern British Columbia. Ore Geology Reviews, v. 95, p. 480-517.

Voisey, C.R., Willis, D., Tomkins, A.G., Wilson, C.J.L., Micklethwaite, S., Salvemini, F., Bougoure, J. and Rickard, W.D.A., 2020, Aseismic refinement of orogenic gold systems. Economic Geology. v. 115, p. 33–50.

Weatherley, D., and Henley, R.W., 2013, Flash vaporisation during earthquakes evidenced by gold deposits. Nature Geoscience, v. 6, p. 294–298, doi:10.1038/ngeo1759.

Wilson, A.J., Cooke, D.R., Harper, B.J., and Deyell, C.L., 2007, Sulfur isotopic zonation in the Cadia district, southeastern Australia: Exploration significance and implications for the genesis of alkali porphyry gold-copper deposits. Mineralium Deposita, v. 42, p. 465–487, doi:10.1007/s00126-006-0071-9.

Data Supplement S3.1– Analytical methods

Sample selection and petrography

Thirty-one representative polished thin sections from each mineralised vein stage and associated phyllically altered wallrock were selected for study from a comprehensive sample suite (n = 236 samples) collected during the lead author's PhD research on the Brucejack deposit (56° 27.994' N, 130° 11.215' W). The polished thin sections were chosen based on petrographic evidence for pyrite growth zoning as observed in reflected light (e.g., euhedral, inclusion-free grain rims surrounding corroded, inclusion-bearing cores). Four polished thin sections from each mineralised vein stage and associated wallrock were used for in situ trace element and sulphur isotope analyses (by electron microprobe and secondary ion mass spectrometry, respectively; see below) based on growth zoning confirmed by back-scattered electron (BSE) imaging.

Electron Microprobe Wavelength-Dispersive X-ray Spectroscopy (EMP-WDS)

The EMP-WDS analyses of pyrite were performed at the joint University of Ottawa–Canadian Museum of Nature MicroAnalysis Laboratory using a JEOL 8230 SuperProbe with five X-ray wavelength-dispersive spectrometers. Pyrite grains were quantitatively analyzed using the following X-ray lines: As (Lα), Au (Lα), Cu (Kα), Fe (Kα), and S (Kα). A combination of synthetic and natural standards, including Au80Ag20 alloy (Au), cubanite (Cu), GaAs alloy (As) and pyrite (Fe and S), were used for calibration. Microbeam analyses were performed using a beam energy of 20 kV, a 40° takeoff angle, a 2 μm beam diameter and a 200 nA beam current. Counting times for each element were set as follows: As (30 s), Au (200 s), Cu (30 s), Fe (10 s), and S (10 s). Detection limits (2σ) of 100 ppm As, 90 ppm Au, 80 ppm Cu, and 110 ppm Fe, and 70 ppm S were achieved using these operating conditions.

Secondary Ion Mass Spectrometry (SIMS)

SIMS mount preparation and analysis were conducted at the Canadian Centre for Isotopic Microanalysis (CCIM), University of Alberta. Regions of interest 1.5 to 2.5 mm diameter were cored from polished thin-sections, and then cast into two 25 mm epoxy mounts ((M1496, M1548) along with previously polished fragments of the primary CCIM pyrite reference material (S0302A). The mounts were lightly polished to a 0.25-micron finish using diamond pads,

cleaned, and then coated with 20 nm of Au prior to scanning electron microscopy (SEM). SEM characterisation was carried out with a Zeiss EVO MA15 instrument using beam conditions of 20 kV and 3 to 5 nA. A further 80 nm of Au was subsequently deposited on the mounts prior to SIMS analysis.

Sulphur isotope ratios ($^{34}S/^{32}S$) were determined in pyrite using an IMS-1280 multi-collector ion microprobe. Primary beam conditions included the use of 20 keV $^{133}Cs^+$ ions focused to form a probe with diameters of 7 to 10 μm depending on requirements, with beam currents of ~0.2 to 0.6 nA. The primary beam, temporarily increased in intensity, was rastered across a 15 x 15 μm area for 30 s prior to analysis to implant Cs. The normal incidence electron gun was not utilised. Negative secondary ions were extracted through 10 kV potential to the grounded secondary column (Transfer section). Conditions for the Transfer section included an entrance slit width of 80 μm, field aperture of 5 x 5 mm, and a field aperture-to-sample magnification of 100x. Automated tuning of the secondary ions in the Transfer section preceded each analysis. The energy slit was fully open, and both secondary ion species were analyzed simultaneously using Faraday cups for $^{32}S^-$ and $^{34}S^-$ ($^{32}S^-$ in L'2 using $10^{11}\Omega$ amplifier circuits, $^{34}S^-$ in FC2 with $10^{11}\,\Omega$). Exit slit widths of 500 μm and ~270 μm were utilised for ^{32}S and $^{34}S^-$, respectively, that gave nominal mass resolutions of 2000 for $^{32}S^-$ (10% peak height definition) and 3500 for $^{34}S^-$. Faraday cup baselines were measured at the start of the session. Total between-spot analysis time was 200 s.

The analytical protocol involved interspersing analyses of pyrite reference material S0302A ($\delta^{34}S_{VCDT} = 0.0 \pm 0.2$ ‰; R. Stern, unpublished data based upon S-isotope gas source mass spectrometry from several labs) in a 4:1 or 5:1 ratio with unknowns. Pyrite S0302A is homogeneous at the micro-scale. The reference VCDT value utilised for $^{34}S/^{32}S = 0.0441626$ (Ding et al., 2001). Instrumental mass fractionation for $^{34}S^-/^{32}S^-$ was determined for the analytical sessions (IP18020A, IP18020B, IP19028) utilising replicate analyses of S0302A pyrite. The standard deviations of $^{34}S^-/^{32}S^-$ ratios for S0302A were 0.05 to 0.08 ‰ for the sessions, after corrections for time-related IMF drift. Final uncertainties are reported at 95% confidence level (2σ) and propagate within-spot counting errors, between-spot errors to account for spatial and time-correlated (drift) uncertainties (±0.10 ‰ blanket error), and between-session errors that

account for uncertainty in the mean IMF for the session. The total individual spot uncertainties in $\delta^{34}S_{VCDT}$ are typically ±0.2 ‰ (2σ).

Reference Cited

Ding, T., Valkiers, S., Kipphardt, H., De Bièvre, P., Taylor, P. D. P., Gonfiantini, R., and Krouse, R., 2001, Calibrated sulfur isotope abundance ratios of three IAEA sulfur isotope reference materials and V-CDT with a reassessment of the atomic weight of sulfur. Geochimica et Cosmochimica Acta, v. 65, p. 2433–2437. doi:10.1016/S0016-7037(01)00611-1.

Data Supplement S3.2 – Analytical results

Table S3.1: EMP-WDS Results – Figure 3.1

Analysis ID	S WT%	Fe WT%	Cu WT%	Au WT%	As WT%	TOTAL
U_1380x24V3a_pyrite_spot_1	49.98	45.10	0.07	0.013	4.59	99.76
U_1380x24V3a_pyrite_spot_2	53.75	46.66	-	-	-	100.40
U_1380x24V3a_pyrite_spot_3	53.92	46.14	0.01	-	0.03	100.10
U_1380x24V3a_pyrite_spot_4	52.26	44.23	0.16	0.010	2.79	99.45
U_1380x24V3a_pyrite_spot_5	52.41	44.36	0.21	0.015	2.75	99.74

Table S3.2: EMP-WDS Results – Figure 3.2

Analysis ID	S WT%	Fe WT%	Cu WT%	Au WT%	As WT%	TOTAL
SU-021-361a_pyrite_spot_1	52.00	44.94	0.00	0.007	1.37	98.32
SU-021-361a_pyrite_spot_2	52.15	45.26	-	0.001	1.07	98.48
SU-021-361a_pyrite_spot_3	51.36	44.65	0.01	0.007	2.42	98.45
SU-021-361a_pyrite_spot_4	52.19	45.33	-	0.007	1.27	98.80
SU-021-361a_pyrite_spot_5	52.46	44.99	0.01	0.002	1.19	98.65
SU-021-361a_pyrite_spot_6	52.33	45.33	-	0.007	1.22	98.89
SU-021-361a_pyrite_spot_7	53.16	45.36	-	0.002	0.26	98.79
SU-021-361a_pyrite_spot_8	52.10	45.07	-	0.003	1.21	98.39

Table S3.3: SIMS Results – Figure 3.1 – Transect U-U'

Spot Name	$^{34}S/^{32}S$	$\delta^{34}S$ (VCDT)	2σ (‰) inter-session
S5103B_U-U'@1	0.00790	0.52	0.16
S5103B_U-U'@2	0.00745	-0.32	0.15
S5103B_U-U'@3	0.00714	-1.16	0.15
S5103B_U-U'@4	0.00660	-1.15	0.14
S5103B_U-U'@5	0.00803	-1.45	0.17
S5103B_U-U'@6	0.00647	-6.93	0.14
S5103B_U-U'@7	0.01012	-16.76	0.21
S5103B_U-U'@8	0.00645	-1.25	0.14

Table S3.4: SIMS Results – Figure 3.1 – Transect V-V'

Spot Name	$^{34}S/^{32}S$	$\delta^{34}S$ (VCDT)	2σ (‰) inter-session
S5103B_V-V'@1	0.0441560	-0.15	0.15
S5103B_V-V'@2	0.0442170	1.23	0.14
S5103B_V-V'@3	0.0441095	-1.20	0.18
S5103B_V-V'@4	0.0441265	-0.82	0.15
S5103B_V-V'@5	0.0441136	-1.11	0.15
S5103B_V-V'@6	0.0436596	-11.39	0.25
S5103B_V-V'@7	0.0438165	-7.84	0.22
S5103B_V-V'@8	0.0438169	-7.83	0.20
S5103B_V-V'@9	0.0435572	-13.71	0.23
S5103B_V-V'@10	0.0437781	-8.71	0.17
S5103B_V-V'@11	0.0435313	-14.29	0.15
S5103B_V-V'@12	0.0434399	-16.36	0.15
S5103B_V-V'@13	0.0434026	-17.21	0.14
S5103B_V-V'@14	0.0435450	-13.98	0.12
S5103B_V-V'@15	0.0435844	-13.09	0.17
S5103B_V-V'@16	0.0435511	-13.85	0.15
S5103B_V-V'@17	0.0434018	-17.23	0.21
S5103B_V-V'@18	0.0437343	-9.70	0.20
S5103B_V-V'@19	0.0433322	-18.80	0.14
S5103B_V-V'@20	0.0429983	-26.36	0.19
S5103B_V-V'@21	0.0430584	-25.00	0.13
S5103B_V-V'@22	0.0441397	-0.52	0.14
S5103B_V-V'@23	0.0444294	6.04	0.17

Table S3.5: SIMS Results – Figure 3.1 – Transect X-X'

Spot Name	$^{34}S/^{32}S$	$\delta^{34}S$ (VCDT)	2σ (‰) inter-session
S5103B_X-X'@1	0.01306	-22.15	0.26
S5103B_X-X'@2	0.00975	-4.48	0.20
S5103B_X-X'@3	0.00854	-19.28	0.17
S5103B_X-X'@4	0.00886	-18.86	0.18
S5103B_X-X'@5	0.00756	-13.19	0.15
S5103B_X-X'@6	0.00898	-18.28	0.18
S5103B_X-X'@7	0.00572	-0.57	0.12
S5103B_X-X'@8	0.00755	7.98	0.15

Table S3.6: SIMS Results – Figure 3.1 – Eastern Spots

Spot Name	^{34}S/^{32}S	$δ^{34}$S (VCDT)	2σ (‰) inter-session
S5103B_XSE@1	0.00788	0.48	0.16
S5103B_XSE@2	0.00781	1.18	0.16
S5103B_XSE@3	0.00805	0.24	0.17
S5103B_XSE@4	0.00933	0.26	0.19
S5103B_XSE@5	0.00609	0.41	0.13
S5103B_XSE@6	0.00762	0.66	0.16
S5103B_XSE@7	0.00729	-0.65	0.15
S5103B_XSE@8	0.00611	-0.54	0.13
S5103B_XSE@9	0.00808	0.46	0.17
S5103B_XSE@10	0.00684	0.73	0.14
S5103B_XSE@11	0.00845	-0.69	0.17
S5103B_XSE@12	0.00613	-0.77	0.13
S5103B_XSE@13	0.00839	0.48	0.17
S5103B_XSE@14	0.00620	-0.76	0.13
S5103B_XSE@15	0.00702	-0.25	0.15
S5103B_XSE@16	0.00676	0.60	0.14
S5103B_XSE@17	0.00620	-0.04	0.13
S5103B_XSE@18	0.00802	-0.41	0.17
S5103B_XSE@19	0.00619	-3.26	0.13
S5103B_XSE@20	0.00634	-0.57	0.13
S5103B_XSE@21	0.00897	-11.57	0.18
S5103B_XSE@22	0.00695	-0.51	0.14
S5103B_XSE@23	0.01195	-11.68	0.24
S5103B_XSE@24	0.00705	-0.05	0.15

Table S3.7: SIMS Results – Figure 3.2 – Transect Y-Y'

Spot Name	$^{34}S/^{32}S$	$\delta^{34}S$ (VCDT)	2σ (‰) inter-session
S5106B_Y-Y'@1	0.00917	0.05	0.18
S5106B_Y-Y'@2	0.00745	0.69	0.15
S5106B_Y-Y'@3	0.00756	-1.28	0.15
S5106B_Y-Y'@4	0.00823	-0.91	0.17
S5106B_Y-Y'@5	0.00887	1.32	0.18
S5106B_Y-Y'@6	0.00761	1.15	0.15
S5106B_Y-Y'@7	0.00819	1.53	0.17
S5106B_Y-Y'@8	0.01246	2.81	0.25
S5106B_Y-Y'@9	0.00746	4.93	0.15
S5106B_Y-Y'@10	0.01094	5.49	0.22
S5106B_Y-Y'@11	0.01034	6.39	0.21
S5106B_Y-Y'@12	0.00821	7.05	0.17
S5106B_Y-Y'@13	0.01260	7.47	0.25
S5106B_Y-Y'@14	0.00897	8.40	0.18
S5106B_Y-Y'@15	0.01245	9.19	0.25
S5106B_Y-Y'@16	0.00586	10.14	0.12
S5106B_Y-Y'@17	0.00922	10.46	0.19
S5106B_Y-Y'@18	0.01416	11.35	0.28
S5106B_Y-Y'@19	0.00940	12.48	0.19
S5106B_Y-Y'@20	0.00606	12.83	0.12
S5106B_Y-Y'@21	0.01030	13.56	0.21
S5106B_Y-Y'@22	0.01005	18.70	0.20
S5106B_Y-Y'@23	0.00837	20.46	0.17
S5106B_Y-Y'@24	0.01003	21.94	0.20
S5106B_Y-Y'@25	0.00907	22.28	0.18
S5106B_Y-Y'@26	0.00932	23.99	0.19

Table S3.8: SIMS Results – Figure 3.2 – Transect Y-Y' Peripheral Spots

Spot Name	$^{34}S/^{32}S$	$\delta^{34}S$ (VCDT)	2σ (‰) inter-session
S5106B_Y-Y'_PS@1	0.00910	21.60	0.19
S5106B_Y-Y'_PS@2	0.00789	11.51	0.16
S5106B_Y-Y'_PS@3	0.00801	4.85	0.17
S5106B_Y-Y'_PS@4	0.00787	-2.05	0.16

Table S3.9: SIMS Results – Figure 3.2 – Northern Spots

Spot Name	^{34}S/^{32}S	δ^{34}S (VCDT)	2σ (‰) inter-session
S5106B_XSN@1	0.00632	0.93	0.13
S5106B_XSN@2	0.01001	5.05	0.20
S5106B_XSN@3	0.01093	5.07	0.22
S5106B_XSN@4	0.00899	7.06	0.18
S5106B_XSN@5	0.00933	12.05	0.19
S5106B_XSN@6	0.00814	12.20	0.16
S5106B_XSN@7	0.01044	21.74	0.21
S5106B_XSN@8	0.00847	-0.42	0.17
S5106B_XSN@9	0.00771	-4.12	0.16
S5106B_XSN@10	0.00870	-1.22	0.18

Table S3.10: SIMS Results – Figure 3.3 – Transect Z-Z'

Spot Name	^{34}S/^{32}S	δ^{34}S (VCDT)	2σ (‰) inter-session
S5778B1_Z-Z'@1	0.0069	8.32	0.14
S5778B1_Z-Z'@2	0.0074	-2.79	0.15
S5778B1_Z-Z'@3	0.0062	-1.96	0.12
S5778B1_Z-Z'@4	0.0071	-1.43	0.14
S5778B1_Z-Z'@5	0.0087	-0.96	0.17
S5778B1_Z-Z'@6	0.0087	8.36	0.17
S5778B1_Z-Z'@7	0.0086	8.72	0.17
S5778B1_Z-Z'@8	0.0068	6.92	0.14
S5778B1_Z-Z'@9	0.0074	3.75	0.15
S5778B1_Z-Z'@10	0.0064	-8.31	0.13
S5778B1_Z-Z'@11	0.0061	-30.64	0.12
S5778B1_Z-Z'@12	0.0093	-36.06	0.19
S5778B1_Z-Z'@13	0.0075	-18.32	0.15
S5778B1_Z-Z'@14	0.0111	-6.68	0.22

CHAPTER 4

The genesis of the high-grade Brucejack epithermal Au-Ag deposit, northwestern British Columbia: Insights from high-resolution petrographic, trace element and sulphur isotope analyses of pyrite and electrum

Preface

Chapter 4 entitled, "The genesis of the high-grade Brucejack epithermal Au-Ag deposit, northwestern British Columbia: Insights from high-resolution petrographic, trace element and sulphur isotope analyses of pyrite and electrum" builds on the findings of the previous chapter by continuing to explore, and leverage, the extensive fluid history preserved in pyrite from the Brucejack deposit to answer questions about the genesis of bonanza-style hydrothermal gold deposits. Although the overarching goals are similar, Chapter 4 differs from Chapter 3 in that the main focus of the pyrite analyses is to determine the trace element signature of this mineral and place the evolution of this signature in the context of the geology of the deposit, which is described in detail. Detailed macro- and micro-scale paragenetic relationships between the six mineralogically and texturally distinct vein stages (generations) in the deposit are documented and then discussed in reference to the broader fluid evolution findings of the SIMS and EMPA pyrite chemical data presented in Chapter 3 as well as the LA-ICP-MS data presented in this chapter. Sulphur isotope data from SIMS analyses are also presented in this chapter but are used to estimate temperatures of mineralisation in ore-stage veins via barite-pyrite sulphur isotope exchange thermometry rather than elucidate hydrothermal fluid evolution as in Chapter 3. Chapter 4 concludes by presenting, and discussing the implications of the chapter's research findings, particularly the discovery of a novel mechanism for the flocculation of colloidal gold suspensions in hydrothermal systems.

Abstract

It has been long accepted that epithermal gold deposits form as a result of gold precipitation from hydrothermal fluids in which gold is transported mainly as a bisulphide complex and precipitation is most often caused by boiling. A fundamental limitation of this model is that it cannot account for why, in some epithermal deposits, high-grade gold concentrations occur in veins with little to no evidence of co-precipitated sulphide minerals, despite sulfidation being proposed as a prominent precipitation mechanism for hydrothermal gold deposition. A further issue is why, in many epithermal deposits lacking co-precipitated sulphide minerals, evidence for boiling having occurred concurrently with high-grade gold deposition is also absent. To investigate these problems, we have undertaken a detailed petrographic and mineral chemical study of the bonanza-style Brucejack epithermal Au-Ag deposit, northwest British Columbia, Canada, a deposit which lacks evidence for significant syn-mineral sulphidation and boiling.

Our trace element and sulphur isotope results for early (pre-bonanza) pyrite reveal how the Brucejack hydrothermal system evolved in time and space prior to the onset of bonanza mineralisation. The relatively Co-Ni rich cores of pyrite in pre-electrum Stage I veins record the passage of early porphyry-type fluids which evolved to epithermal-type fluids during telescoping of the hydrothermal system, as evidenced by oscillatory, locally colloform pyrite growth zones that mantle the Co-Ni cores and are relatively rich in Au and As. Later, but still during the development of Stage I veins, porphyry-style conditions returned to the system as indicated by narrow but locally well-developed outer (grain rim) Co-Ni growth zones in Stage I pyrite. All of this hydrothermal activity predated the emplacement of the bonanza-grade epithermal Stage III-V carbonate-quartz-electrum veins which, except for volumetrically minor sulphosalt and base metal sulphide minerals in Stage IV veins, largely lack evidence syn-electrum sulphide deposition, and cross-cut Stage I-II veins throughout the deposit. The time between the emplacement of pre-bonanza and syn-bonanza vein stages was brief, as shown by the 182.7 ± 1.0 Ma U-Pb zircon age of syn- to late-mineral trachybasaltic dykes and the 182.6 ± 1.1 Ma U-Pb zircon age of the pre-mineral Andesitic Crystal Tuff. Sulphur isotope exchange thermometry results from pyrite-barite mineral pairs show that the Co-Ni pyrite formed under porphyry conditions whereas bonanza-stage veins formed under lower temperatures characteristic of an epithermal environment.

Noting the close spatial relationship between bonanza gold in Stage III-V veins and pyrite associated with Stage I veins and integrating it with previously documented evidence for the colloidal nature of gold in bonanza-stage veins at Brucejack, we propose a model for the formation of bonanza gold occurrences in the deposit. In this model, charged surfaces on p-type oscillatory arsenian growth zones in Stage I pyrite electrochemically destabilise, through cationic bridging, colloidal gold (gold nanoparticle) suspensions circulating in Stage III-V veins, which ultimately trigger the flocculation of gold colloids on a mass scale and the deposition of gold in bonanza concentrations. This process offers a novel explanation for how bonanza gold may paragenetically late in hydrothermal ore deposits, after the vast majority of sulphide mineral deposition has occurred and without the requirement for phase separation (boiling) or the existence of steep physicochemical gradients.

4.1 Introduction

The mechanisms by which the hyper-enrichment of gold occurs in hydrothermal ore deposits have long been debated, (e.g., Boyle, 1978, 1987; Romberger, 1991; Sillitoe, 1993, 2002; Saunders and Schoenly, 1995; Groves et al., 2003; Richards, 2013; Pokrovski et al., 2015; McLeish et al., 2021). Whereas ultra-high-grade, or 'bonanza' concentrations of gold occur in many types of hydrothermal deposits, approximately 60 % of Earth's bonanza gold veins are hosted in epithermal-type deposits (Sillitoe and Hedenquist, 2003); in these veins, gold is transported mainly as a bisulphide complex, and deposition is considered to occur by precipitation from solution, typically as a result of boiling (White and Hedenquist, 1990). One of the major shortcomings of this model is that it fails to explain why, in some epithermal deposits, high-grade gold concentrations occur in veins with little to no evidence of co-precipitated sulphide minerals, despite sulfidation being proposed as a prominent precipitation mechanism for hydrothermal gold deposition (Williams-Jones et al., 2009), including in many epithermal ore deposits (e.g., Anderson and Eaton, 1990; Richards and Kerrich, 1993; Carrillo Rosúa et al., 2002; John et al., 2003; Kesler et al., 2005; Richards et al., 2006; Voute et al., 2019; Xu et al., 2020). Examples of gold-rich, sulphide-poor veins in epithermal deposits, including Brucejack (Canada; Board et al., 2020), Fruta del Norte (Ecuador; Leary et al., 2016), and Acupan (Philippines; Cooke et al., 1996). Moreover, it is noteworthy that where vein-hosted sulphide minerals are abundant, high-grade gold mineralisation often post-dates most, or in some cases, all generations of sulphide deposition. Late- to post-sulphide gold mineralisation, which typically occurs as electrum or native gold filling fractures in earlier sulphide phases, has been described in a variety of epithermal, orogenic, porphyry, and intrusion-related Au ore-forming environments, including those of the Endeavour 42 (Australia; Henry et al., 2014), Pataz-Parcoy (Peru; Gaboury and Sanchez, 2019; Voute et al., 2019), Didipio (Philippines; Hermo et al., 2022), and Telfer (Australia; Steadman et al., 2021) deposits.

The large (10.7 Moz Au, 62.5 Moz Ag; Tetra Tech, 2020), ca. 183 Ma Brucejack intermediate- to low-sulphidation epithermal deposit in the Stewart-Eskay mineral district of northwestern British Columbia, Canada (Figs. 4.1 and 4.2), is characterised by abundant early sulphides, including pre-ore-stage pyrite-quartz-calcite veins and several generations of syn-ore
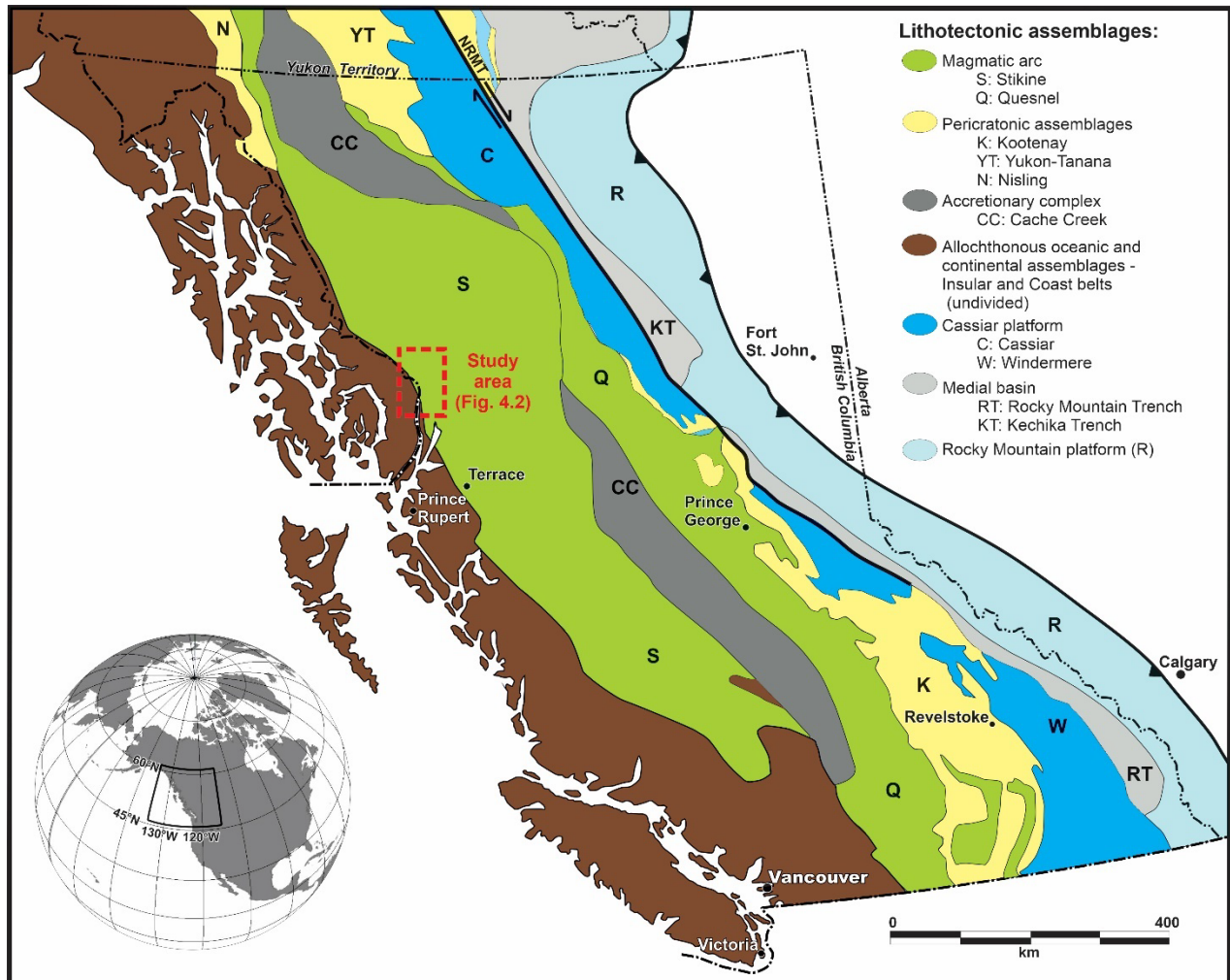
Figure 4.1: Location of the study area shown in terms of the major lithotectonic subdivisions of the Canadian Cordillera (modified after Johnston, 2008). Abbreviation: NRMT, Northern Rocky Mountain Trench (fault).

quartz-calcite-pyrite ± base metal sulphide ± sulphosalt veins, the latter of which host late-stage electrum mineralisation (e.g., as fracture fillings in pyrite; Board et al., 2020). The deposit, which, at present, principally comprises the Valley of the Kings and West zones, also hosts a later generation of sulphide-free calcite-electrum veins that contain localised but spectacular (> 10,000 g/t) bonanza gold (Tombe et al., 2018; McLeish et al., 2021; this study). The deposit therefore provides an opportunity to investigate: (1) the reason(s) why visible gold (electrum) mineralisation is commonly paragenetically late in hydrothermal environments; and (2) the origin of epithermal quartz-carbonate veins that contain extreme concentrations of gold in the absence of co-precipitated sulphide minerals. More generally, Brucejack offers an opportunity to

study the genesis of some of the highest-grade occurrences of epithermal gold mineralisation in the world (up to 41,582 g/t Au in half-metre drill core intervals; Tombe et al. 2018), and explain how high-grade gold mineralisation developed over an extraordinary vertical extent that is unprecedented for an epithermal system (at least 1,300 m in the Valley of the Kings zone; Pretium Resources, 2019).

The controls on the bonanza gold grades, the large metal endowment, and the vertical continuity of the deposit are not fully understood. Recent research has indicated that the mechanical transport of gold in the solid-state as colloidal suspensions, rather than as a dissolved species, combined with the mixing of seawater with a boiled ore fluid, were the essential catalysts for the genesis of Brucejack mineralisation (Chapter 2; Chapter 3). In addition, the superimposition of epithermal mineralisation at Brucejack on and older, genetically unrelated, porphyry and related phyllic alteration may have provided an important (but equivocal) control on the formation of high-grade gold through the early stage sulfidation of wallrocks (Board and Greig, 2014; Tombe et al., 2018).

Although previous studies have identified the mechanisms by which the hyper-enrichment of gold occurred at Brucejack, as well as resolved the general magmatic and hydrothermal history of the deposit, distinguishing the event(s) that were directly responsible for the bonanza gold mineralisation, from those that had only indirect influence on it (e.g., wallrock sulphidation) remains exceedingly difficult. For example, recent work has shown that at least three temporally distinct porphyry intrusions, each with their own associated hydrothermal alteration overprint and low-grade Au-Cu mineralisation, intruded the deposit area in the 10 Myr preceding the emplacement of high-grade veins in the Valley of the Kings (Board et al., 2020). As well, it has been suggested that pre-existing pyrite 'stringer' veins, found in the phyllic alteration halo(s) of one or more of these intrusions acted as an electrochemical trigger for gold deposition (Harrichhausen, 2016).

This paper reports the results of our collective petrographic, trace element, and sulphur isotope thermometric investigation of Brucejack pyrite and associated sulphide and sulphate minerals. By integrating these results with those of previous studies, we develop a genetic model that explains how three key processes, namely, the physical transport of gold as a colloidal suspension, the mixing of seawater with the ore fluid, and the electrochemical interaction

between pyrite and colloidal gold suspensions, generated a hyper-enriched, transitional porphyry-epithermal gold deposit with exceptional vertical extent. In so doing, we also consider the broader evolution of the magmatic-hydrothermal system at Brucejack. The paper concludes by discussing the constraints our investigation places on the physicochemical conditions under which bonanza-grade epithermal mineralisation formed in the deposit and, by extension, similar Au-Ag deposits elsewhere.

4.2 Tectonic setting

The Brucejack deposit is located near the western edge of the Stikine terrane (Stikinia; Fig. 4.1), a paleo-magmatic arc that is considered to have experienced a similar tectono-magmatic evolution to that of the modern-day Philippine archipelago (Marsden and Thorkelson, 1992). In the Brucejack area, Stikinia is bounded by the Cretaceous to Eocene Coast Plutonic Complex to the west and the Middle Jurassic to mid-Cretaceous Bowser Lake Group to the east (Fig. 4.2). Stikinia is thought to have formed during the mid-Palaeozoic in an intra-oceanic arc setting; it is therefore believed to be allochthonous with respect to Laurentia, although the exotic rather than autochthonous nature of its basement rocks is debated (cf. Erdmer et al., 2002; Johnston and Borel, 2007). Volcano-sedimentary rocks of the Late Triassic Stuhini Group and Early Jurassic Hazelton Group represent the principal components of the stratigraphy of Stikinia, and were affected by two distinct episodes of magmatism in the Late Triassic and Early-Middle Jurassic (Macdonald et al. 1996). This magmatism gave rise to numerous porphyry Au-Cu-Mo, epithermal Au-Ag, and intrusion-related Au deposits, which span ~220-186 Ma age range on the terrane-scale (Logan and Mihalynuk, 2014), but are generally thought to be limited to a ~197-188 Ma age range (Kirkham and Margolis, 1995) within the Stewart-Eskay Creek district. Several angular unconformities and disconformities in the host stratigraphy, including a prominent unconformity between the upper Stuhini and basal Hazelton groups, are spatially and temporally associated with this suite of magmatic-hydrothermal deposits (Fig. 4.2; Henderson et al., 1992; Nelson and Kyba, 2014). The unconformities are interpreted to be a product of a tectonically active environment that was likely controlled by a compressional or sinistral transpressional stress regime (Nelson and Colpron, 2007). Overall, the ~220-186 Ma period of porphyry-epithermal deposit emplacement in Stikinia is viewed as genetically comparable to

recent and actively developing metallotects in the southwest Pacific Rim, such as those in Papua New Guinea and the Philippines (Alldrick, 1993; Nelson et al., 2022).

Bracketing Late Triassic and Early-Middle Jurassic magmatic events, porphyry-epithermal-intrusion-related mineralisation and contractional deformation in Stikinia are two back-arc related extensional episodes that gave rise to the 222 Ma Granduc and the 175 Ma Eskay Creek volcanogenic massive sulphide (VMS) deposits (Childe, 1996, 1997). Both deposits are hosted within the Iskut River Formation of the Eskay rift zone (Fig. 4.2), the latter of which transected Stikinia in the mid-Jurassic in response to the collision of Stikinia with the neighbouring arc terrane to the east, Quesnellia, and the related closure of the Cache Creek ocean (Nelson and Colpron, 2007). This collision is believed to have resulted in the termination of magmatism in both arcs and the development of the syn- to post-collisional Bowser Basin, which was filled mainly with marine to locally non-marine clastic sediment shed from the assembled Stikinia-Quesnellia arc and obducted ophiolitic rocks from the Cache Creek ocean (Evenchick et al., 2007; Nelson et al., 2022). In the mid-Cretaceous, accretion of additional outboard terranes of the Insular and Coast belts to the west of Stikinia-Quesnellia imposed renewed contractional deformation on Stikinia and the nascent mid-Cretaceous Coast Plutonic Complex to the west, resulting in the formation of the regional-scale Skeena fold and thrust belt and regionally prominent McTagg anticlinorium (discussed below; Evenchick, 1991; Journeay and Friedman, 1993; Nelson and Kyba, 2014; Febbo et al., 2019a).

4.3 The Stewart-Eskay District

Stretching 70 km north from the town of Stewart to the Eskay Creek deposit in the Unuk River Valley, the Stewart-Eskay district comprises the northern half of a northwest-trending elliptical structural culmination of Lower Jurassic rocks that is exceptionally well-endowed in base and precious metals (Fig. 4.2). A group of prominent porphyry-epithermal and VMS deposits, including Brucejack and nine others (Eskay Creek, Treaty Creek, Kerr-Sulphurets-Mitchell-Iron Cap, Snowfield, Scottie Gold, Granduc, Big Missouri, Silbak-Premier, and Red Mountain) define the Treaty-Stewart mineral trend within the district (Nelson and Kyba, 2014). Collectively, these deposits contain resources of more than 200 Moz of gold and 50 billion pounds of copper, and represent the one of the most well-endowed clusters of hydrothermal ore deposits in the world (Sinclair, 2007; Clarke, 2022).
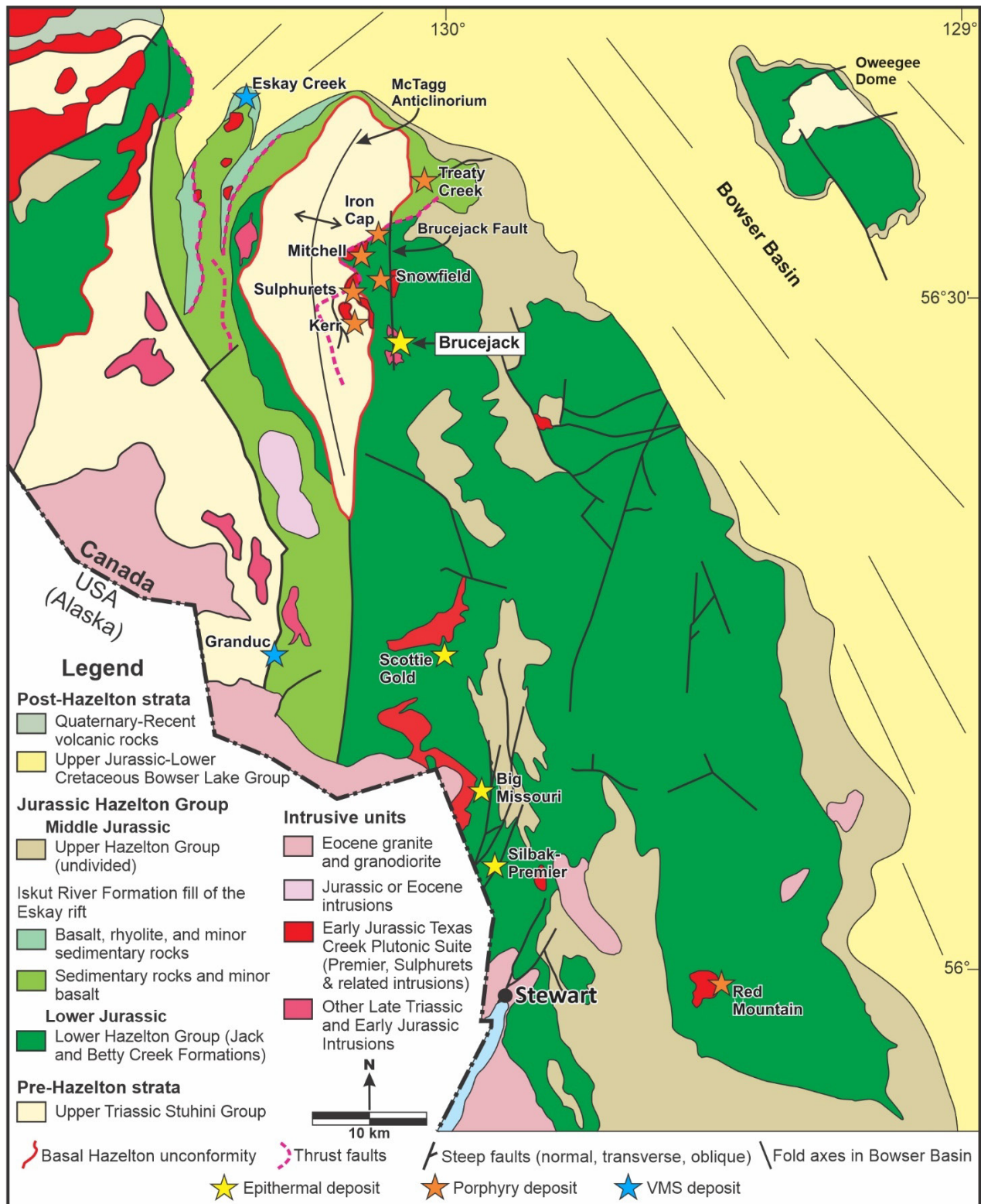
Figure 4.2: Geological map of Stewart–Eskay Creek district showing the location of major porphyry, epithermal and volcanogenic massive sulphide deposits. Modified, in part, after Board et al. (2020), Nelson et al. (2018), and Nelson and Kyba (2014). See text for description of Bowser Lake, Hazelton, and Stuhini Group lithologies.

Structurally, the Stewart-Eskay district is dominated by the mid-Cretaceous McTagg anticlinorium which is cored by volcanic arc and marine sedimentary rocks of the Upper Triassic Stuhini Group and flanked by Lower Jurassic Hazelton Group arc-related volcanic and volcano-sedimentary rocks (Henderson et al., 1992). The basal Hazelton unconformity separates these two stratigraphic packages (Fig. 4.2). Along the eastern limb of the McTagg anticlinorium, the Treaty-Stewart mineral trend closely mirrors the trace of the basal Hazelton unconformity and spatially associated, north-south oriented, extensional to transtensional faults located to the east, suggesting a potential genetic relationship between the unconformity and the mineral trend (Nelson and Kyba, 2014). Stratigraphically, with the exception of porphyry Cu-Au mineralisation that is, in part, hosted by the Stuhini Group at Kerr-Sulphurets-Mitchell-Iron Cap (KSM), all porphyry-epithermal deposits of the trend lie above the unconformity in the lower Hazelton Group.

Within the district, the lower Hazelton Group comprises arkosic sandstone, siltstone, granitoid- to andesite-clast-bearing cobble- to boulder-conglomerate, and local pyroclastic rocks of the ca. 197 Ma Jack Formation, and overlying andesitic to dacitic volcaniclastic rocks and minor volcanic flows, breccias and tuffs of the 197-178 Ma Betty Creek Formation (Nelson et al., 2018). The Betty Creek Formation hosts all the epithermal mineralisation at Brucejack (see below). Several kilometres to the south and east of Brucejack, bimodal volcanic rocks and associated sedimentary facies of the 179 to 173 Iskut River Formation overlie the Betty Creek Formation together with thinly interbedded argillite and laminated felsic tuff of the Bajocian to Callovian Quock Formation, which is considered to be a partial lateral facies equivalent and younger expression of the Iskut River Formation (Nelson et al., 2018; Board et al., 2020). Although these units, which form part of the upper Hazelton group, are not known to host porphyry-epithermal mineralisation, the Iskut River Formation is host to high-grade gold-silver VMS mineralisation at Eskay Creek, and the Quock Formation is stratigraphically important because it forms a visually distinct marker horizon that conformably overlies the Eskay Creek deposit and can be traced regionally (Gagnon et al., 2012). Thinly-bedded tuffaceous beds in the Quock Formation mark the end of Hazelton arc magmatic activity and its highly productive Early Jurassic metallogenic period (Thomson et al., 1986; Gagnon et al., 2012). Siliciclastic strata of the Bowser Lake Group overlie the upper Hazelton Group gradationally to unconformably along the northern end of the district and record rapid denudation and molasse

deposition related to orogenic closure of the Cache Creek ocean (Evenchick and Thorkelson, 2005).

A series of intermediate Early Jurassic porphyry stocks, plugs and subvolcanic intrusions belonging to the 198-188 Ma Texas Creek plutonic suite intruded the Stuhini and Hazelton Group strata along the Treaty-Stewart trend (Fig. 4.2); generally, this plutonic suite is thought to be responsible for ore-forming magmatic-hydrothermal activity in the district (Nelson and Kyba, 2014). The 196-189 Ma Sulphurets and Premier intrusions are the most notable in terms of size and metal endowment, and are genetically related to (and partly host) to the mineralisation of the KSM and Silbak-Premier deposits (Alldrick, 1993; Kirkham and Margolis 1995; Febbo et al., 2019b). A group of younger, 188-179 Ma, dioritic to monzonitic porphyries and mafic dykes intrude the Brucejack deposit area (see below), although intrusive rocks of this age are not recognised elsewhere in the Treaty-Stewart trend nor the Stewart-Eskay district (Nelson et al., 2018). No further magmatism occurred in the district until the early Tertiary when barren granitic to granodioritic plugs and stocks of the 55 Ma Hyder plutonic suite intruded Stuhini and Hazelton Group strata to the west and south of Brucejack (Buddington, 1929; Alldrick, 1993); these intrusions are considered to be satellite plutons of the Eocene Coast Plutonic Complex (Anderson, 1989).

4.4 The Sulphurets Camp and the Premier-Sulphurets intrusions

The Sulphurets Au-Ag-Cu mining camp is centred on the eastern limb of the McTagg anticlinorium and includes the KSM porphyry deposit cluster, the Snowfield porphyry deposit, and the Brucejack epithermal deposit; these are by far the largest and richest Au deposits along the Treaty-Stewart trend (Fig. 4.2). For example, the Mitchell porphyry deposit of the KSM cluster alone contains over 40 Moz Au and is the largest undeveloped Au-Cu deposit in Canada (Febbo et al., 2019a). Brucejack and Snowfield, in comparison, contain resources of 11 and 35 Moz Au respectively, and, with an annual production of approximately 350 koz, Brucejack is currently Canada's fourth largest Au mine (Seabridge Gold Inc., 2020; Pretium Resources Inc., 2020). As noted above, the exceptional metal endowment of the KSM and Snowfield deposits is associated with the Texas Creek Plutonic suite intrusions (Kirkham and Margolis 1995; Febbo et al., 2019b). Historically, due to its proximity to plutons of the Texas Creek Plutonic suite (Fig. 4.2), Brucejack also has been considered as genetically related to Texas Creek magmatism, with

the quartz-carbonate-electrum veins interpreted as either distal epithermal expressions of the KSM porphyries or associated with the Texas Creek-aged Bridge Zone porphyry on the southern margin of the deposit (Fig. 4.3; Davies et al., 1994; Board and McNaughton, 2013). However, the recent finding that epithermal veins at Brucejack were emplaced into rocks as young as 183-182 Ma and cut by dykes of approximately the same age (Board et al., 2020; this study), makes this mineralisation 5-6 Myr younger than the youngest magmatism of the Texas Creek plutonic suite. Brucejack is therefore unlikely to be related to the KSM or Bridge Zone porphyries.

The Premier and Sulphurets intrusions have been studied in detail at KSM (Febbo et al., 2015; Febbo et al., 2019a). The 196-194 Ma alkaline Premier intrusions comprise dykes, sills and stocks of crowded, plagioclase-K-feldspar phyric monzonite to syenite and biotite-pyroxene-hornblende-plagioclase phyric diorite. These intrusions are cut by diorite, monzodiorite and granodiorite plugs, stocks and dykes of the calc-alkaline Sulphurets intrusions (based on cross-cutting relationships in the Mitchell porphyry); the Sulphurets rocks are the product of three stages of 193-190 Ma magmatic-hydrothermal activity. The first two stages were responsible for porphyry Cu-Au mineralisation and widespread potassic, propylitic and phyllic alteration at Mitchell on a scale consistent with a 'supergiant' porphyry deposit (Febbo et al., 2019a). The third stage produced high-sulphidation-type alteration that was telescoped onto earlier potassic alteration and produced widespread Pb-Zn-Bi-Te-Sn-bearing massive pyrite stringer veins. More broadly, the 196-190 Ma Premier and Sulphurets intrusions are interpreted to be genetically associated with widespread and locally intense sericite-pyrite alteration of the upper Stuhini and lower Hazelton Group wallrocks along a 25 km trend that transects the entire Sulphurets camp (Kirkham and Margolis, 1995; Board and Greig, 2014).[4]

Figure 4.3 (next page): Geologic map of the Brucejack area showing the location of the main mineralised zones, labelled numerically: (1) Bridge, (2) Valley of the Kings, (3) Eastern Promises, (4) Flow Dome, (5) West, (6) Gossan Hill, (7) Shore, (8) SG, and (9) Golden Marmot. Lithological units and hydrothermal alteration zones are after Davies et al. (1994), Greig and Greig (2013), Tombe et al. (2018), and Board et al. (2020) with local revisions based on mapping by the authors and unpublished data provided by Pretium Resources Inc. Structural data are from Davies et al. (1994) and Peddle and Johnston (2021).

---

[4] The Premier and Sulphurets intrusions are collectively referred to as the Mitchell intrusions by Kirkham and Margolis (1995) and Board and Greig (2014).
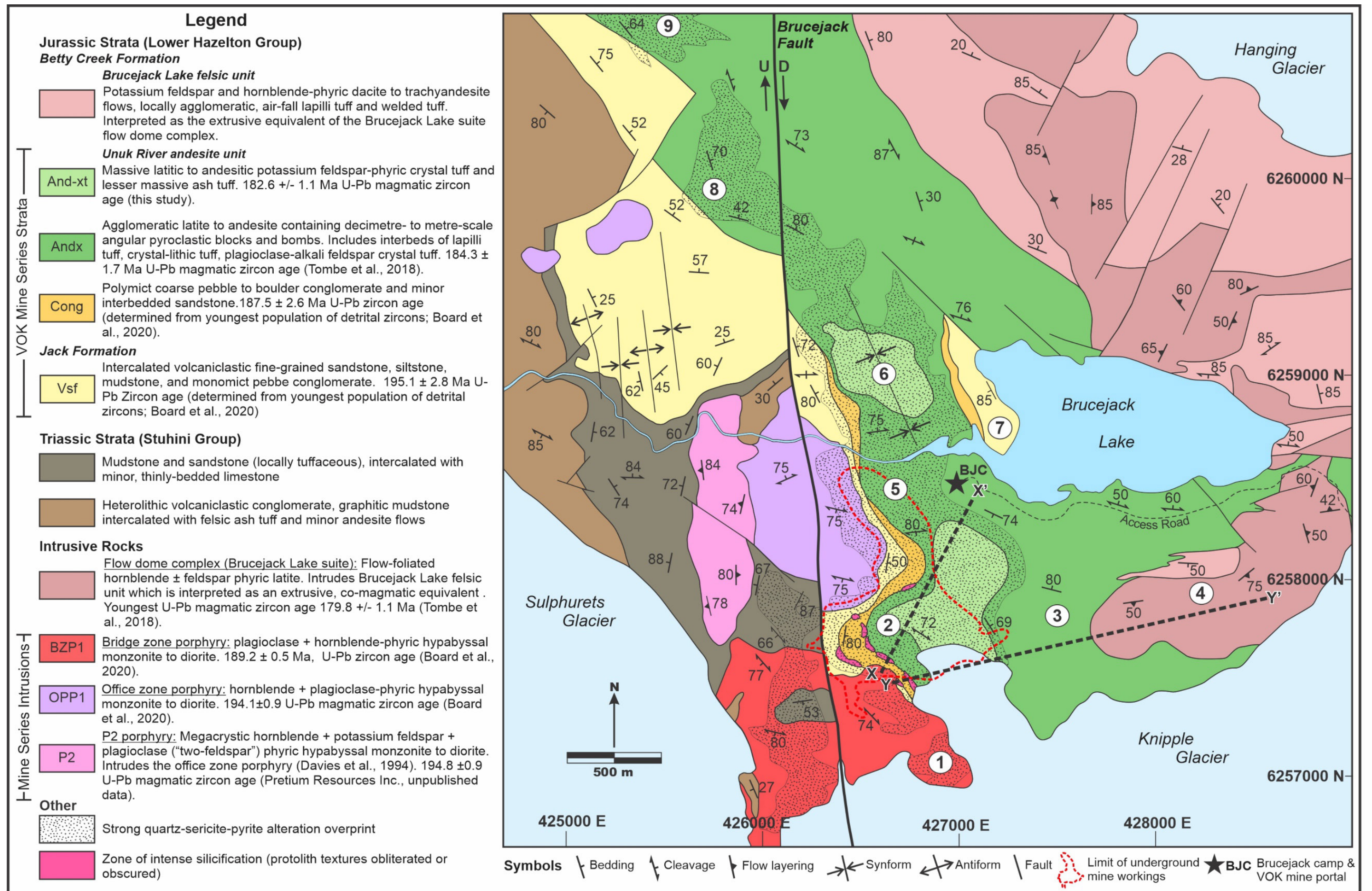
The Sulphurets camp has experienced a complex structural evolution involving multiphase deformation and regional sub-greenschist facies metamorphism (Kirkham and Margolis, 1995). Triassic ductile deformation, manifested by upright, tight to isoclinal folding and the development of an associated subvertical, penetrative pressure solution cleavage, is recorded by rocks of the Stuhini Group in the core of the north-plunging McTagg anticlinorium (Henderson, 1992). These contractional deformation fabrics were interpreted by Greig (2014) as evidence of a major collisional event on a terrane scale in Stikinia. The 203 Ma age of the basal Hazelton unconformity, which truncates tight to isoclinal folds and related cleavage in the Stuhini Group, suggests that orogenesis had ceased by latest Triassic time (Nelson et al., 2018). However, overlying Hazelton Group strata also contain polyphase penetrative deformation fabrics which, while challenging to interpret due to a lack of cross-cutting relationships, may in part evidence renewed, syn-mineral contractional deformation in the Early Jurassic. In the Brucejack area, these fabrics include multidirectional, pressure solution and fracture cleavages and both small- (5-10 cm wavelength) and large-scale (> 100 m wavelength) folds, with the fabric intensity typically proportional to the degree of sericite-chlorite alteration (Peddle and Johnston, 2021). Some studies have concluded that fabric development occurred during two temporally distinct transpressional deformational stages, namely a Jurassic, syn-mineral (~183 Ma) event and a mid-Cretaceous event related to the formation of the Skeena fold and thrust belt (Roach and McDonald, 1992; Margolis, 1993; Board et al., 2020). In contrast, other investigations have assigned all major fabric development in Hazelton Group rocks solely to deformation associated with the mid-Cretaceous event (Alldrick, 1993; Davies et al., 1994; Kirkham and Margolis, 1995; Nelson and Kyba, 2014; Febbo, 2016; Febbo et al., 2019a).

A series of north-trending, steeply dipping faults cut all stratigraphic and intrusive contacts, vein systems, and alteration zones in the Sulphurets camp. The Brucejack fault is the largest and most significant of these faults, with a strike length of over 11 km (Fig. 4.3). Although cross-cutting relationships clearly indicate that the fault is a late structure, Febbo et al. (2019) suggested that it may have originated as a syn-depositional basin-bounding growth fault that was active during the Early Jurassic porphyry-epithermal mineralisation events. A suite of unaltered Cenozoic mafic dykes intrudes the Brucejack fault to the west and north of Brucejack; the dykes show evidence of brittle failure and locally are brecciated along the fault corridor, indicating that the fault was active after emplacement of the deposit (Tombe, 2015). No absolute

79

age determinations are available for the dykes, but they are interpreted to be Cenozoic in age (Tombe et al., 2018). To the west of the Brucejack fault, east- to southeast-directed thrusts and east-verging overturned folds affect the eastern limb of the McTagg anticlinorium (Henderson, 1992). The Sulphurets and underlying Mitchell thrust faults, which offset and juxtapose deeper porphyry-style mineralisation on shallower porphyry-epithermal mineralisation in the KSM porphyry deposit cluster, are the most notable examples of these structures (Kirkham and Margolis, 1995).

4.5 Geology of the Brucejack gold-silver deposit

4.5.1 Mine units (stratified and intrusive host rocks)

The Brucejack deposit lies just east of the basal Hazelton unconformity at the contact between the lowermost sedimentary unit of the Hazelton Group, the Jack Formation, and the overlying andesite to trachyandesite lava flows and volcaniclastic units of the Betty Creek Formation (Figs. 4.2 and 4.3). The contact is interpreted as being paraconformable in the Brucejack area, although in the Valley of the Kings and West zones it is often obscured by intense quartz-sericite-pyrite alteration and is locally intruded by hypabyssal monzonitic to dioritic porphyritic intrusions (the Bridge Zone and Office porphyries, see below; Davies et al., 1994; Peddle and Johnston, 2021). Gold mineralisation in the Valley of the Kings and West zones is hosted by a succession of: (1) volcaniclastic to locally siliciclastic mudstone, siltstone, fine-grained sandstone, and minor monomict pebble conglomerate (mine unit 'Vsf', hereafter Volcanosediment; Fig. 4.4e); (2) polymictic, volcanic clast-bearing coarse pebble to boulder conglomerate and minor sandstone ('Cong', Conglomerate; Fig. 4.4c and d); (3) transitional, epiclastic, medium-grained sandstone ('trans', Transition; Fig. 4.4c) that contains local, texturally-distinct subround volcanically-derived pebbles to cobbles and forms a texturally and chemically distinct marker horizon (low P/Ti); and (4) pyroclastic trachyandesite ('Andx', Andesite; Board et al., 2020; Fig. 4.4b). The overall sequence of mine strata has been correlated with the Unuk River andesite unit of Nelson et al. (2018) based on U-Pb zircon ages of 195 to 184 Ma obtained from magmatic and detrital zircons from within and adjacent to the Brucejack mine (Tombe et al., 2018; Board et al., 2020).

Inclusion of the Volcanosediment mine unit in the Unuk River andesite unit is, however, problematic because mudstone, siltstone and fine-grained sandstone have not been recognised in the Unuk River andesite unit, including in sections mapped by Nelson et al. (2018) near

80
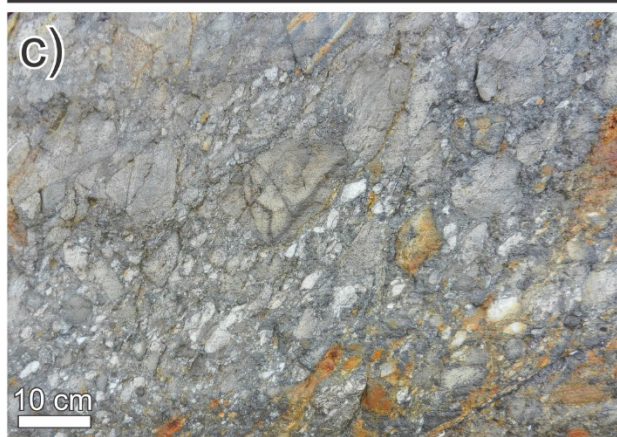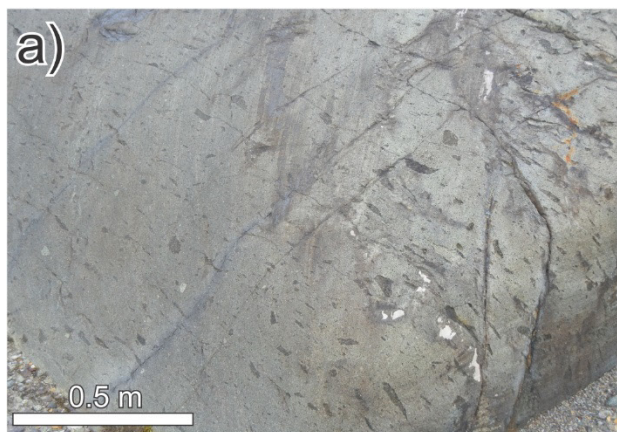
Figure 4.4 (previous page): Representative photographs of Valley of the Kings zone mine units in surface exposures and drill core which, together with pre-mineralisation intrusive rock units (see Fig. 4.5), host the Brucejack deposit. From youngest to oldest (stratigraphically highest to lowest) these are, **(a)** Andesitic Crystal Tuff unit ('And-xt' abbreviated mine series name): massive, fiamme-bearing crystal tuff; **(b)** Fragmental Andesite unit ('Andx'): pyroclastic trachyandesite, containing cm- and dm-scale angular volcanic blocks and bombs; **(c)** Transition unit ('Trans'): epiclastic sandstone that forms a texturally (e.g., subrounded pebbles) and chemically distinct (low P/Ti ratio) marker horizon between the Andesite and Conglomerate units; **(d)** Conglomerate unit ('Cong'): polymict, immature, volcanic clast-bearing conglomerate; and **(e)** Volcano-sedimentary unit ('Vsf'): marine volcaniclastic unit, characterised by (left to right) variable proportions of fine-grained matrix, from clast-supported monomict conglomerate with a fine sandy matrix, to clast-supported conglomerate with a silty matrix, to finely interbedded siltstone and mudstone, and massive mudstone. These units are underlain by well-bedded siltstone and sandstone of the Jack Formation **(f)** and Stuhini Group **(g)** exposed to the west of the deposit area (Fig. 4.3).

Brucejack. Peddle and Johnston (2021) have grouped the Volcanosediment unit with the 197-196 Ma Jack formation, which includes lithologically similar volcaniclastic mudstone, siltstone and sandstone. Given that the U-Pb age of 195.1 ± 2.8 Ma (Board et al., 2020) for the youngest population of detrital zircons in the Volcanosediment unit overlaps with the age of the Jack Formation, we agree with this revised stratigraphy (Fig. 4.3). In addition, and as discussed further below, we define a new, chemically distinct (low Ti/V) andesitic to latitic potassium feldspar-phyric crystal tuff unit ('And-xt', Andesitic Crystal Tuff) that occurs within but is distinct from the Andesite unit because: (1) it lacks pyroclastic fragments, and (2) it is locally in sharp contact with the underlying pyroclastic Andesite where (3) it contains distinct dark grey to black, cm- to locally dm-scale tabular/flattened fiamme at its base (Figs. 4.4a; Pretium Resources Inc., unpublished data).

Bounding the mine sequence strata to the north, west, south, and at depth to the east, are fine-grained plagioclase ± K-feldspar ± hornblende-phyric rocks of the Office, P2, Bridge and Eastern Promises zone porphyries, respectively (Fig. 4.5a-e). Within the immediate mine area, the Office and Bridge zone porphyries display sharp contacts with the stratified rocks of the mine sequence and are interpreted to be monzonitic to dioritic hypabyssal intrusions (Davies et al., 1994; Board et al., 2018; Peddle and Johnston, 2021), although regional mapping campaigns have historically identified them, in part, as andesite, dacite, and latite flows (Kirkham and Margolis, 1995; Greig and Greig, 2013). U-Pb zircon dating of the Office and Bridge zone

Figure 4.5: Representative photographs of Valley of the Kings zone pre-mineralisation intrusive mine units**: (a)** plagioclase ± hornblende phyric (one-feldspar) surface exposure of the Office zone porphyry; **(b)** megacrystic K-feldspar + plagioclase ± hornblende phyric (two-feldspar) exposure of the P$_2$ porphyry; **(c)** phyllically altered plagioclase ± K-feldspar ± hornblende Bridge zone porphyry in drill core; **(d)** propylitically altered plagioclase ± K-feldspar ± hornblende Eastern Promises zone porphyry in drill core, with weak to moderate phyllic overprint; and **(e)** phyllically altered Office zone porphyry in drill core.

porphyries yielded ages of 194.1 ± 0.9 and 189.2 ± 0.5 Ma, respectively (Board et al., 2020). Given that these ages correspond to the oldest rocks in the mine sequence, and their sharp contacts with the Volcanosediment unit, these porphyries are interpreted to have intruded the stratigraphically lowest parts of the sequence (Board et al., 2020). At depth along the eastern limits of the underground mine workings of the Valley of the Kings zone, a recently recognised third fine-grained plagioclase ± K-feldspar ± hornblende-phyric stock, the Eastern Promises zone porphyry, intrudes the Unuk River andesite. Although broadly similar in appearance to the Office and Bridge zone porphyries, this intrusion cuts younger mine series rocks and yielded a considerably younger U-Pb zircon age of 185.9 ± 1.2 Ma (Board et. al, 2020).

The mine sequence strata were intruded by medium-grained, dark olive green to dark grey, weakly altered, syn- to post-mineral dykes (Fig. 4.6), which cut all lithologies in the Jack Formation and the overlying Unuk River andesite unit, as well as most ore-stage veins and the S_1-S_3 penetrative foliation described below. These dykes have previously been classified on the basis of lithogeochemical data as trachybasaltic (Tombe, 2015). They are subplanar, subvertical, generally less than 1.5 m wide, and commonly E-W to NW-SE trending (rarely N-S) with downdip continuations of at least 1,000 m in the Valley of the Kings and at least 450 m in the West zone. Texturally, the dykes are characterised by layered chilled margins and distinct, spherical, largely undeformed, small (< 4 mm), amygdules filled with calcite that increase in abundance towards dyke centres. As documented by Board et al. (2020), these dykes commonly cut mineralised veins, but are spatially coincident with major mineralised vein stockwork zones and appear to have been emplaced along the same structures (Fig. 4.6a). Within mineralised stockwork zones, the dykes both cut the veins and trend parallel to the margins of the zones (see Fig. 4.6a vs. 4.6b). Infrequently, ore-stage veins cut the dykes at low angles along their weakly altered and locally hydrothermally brecciated margins, whereas post-mineral, shallowly-dipping tectonic veins more commonly cross-cut the dykes at high angles (Figs. 4.6c-e). The trachybasaltic dykes, which have a U-Pb zircon age of 182.7 ± 1.0 Ma (Board et al., 2020), are thus interpreted to be late- to post-mineral and provide a minimum age for the high-grade epithermal vein mineralisation and host rocks at Brucejack.

The Brucejack Lake felsic unit overlies the Unuk River andesite and consists of potassium feldspar- and hornblende-phyric dacite to trachyandesite flows, and locally welded
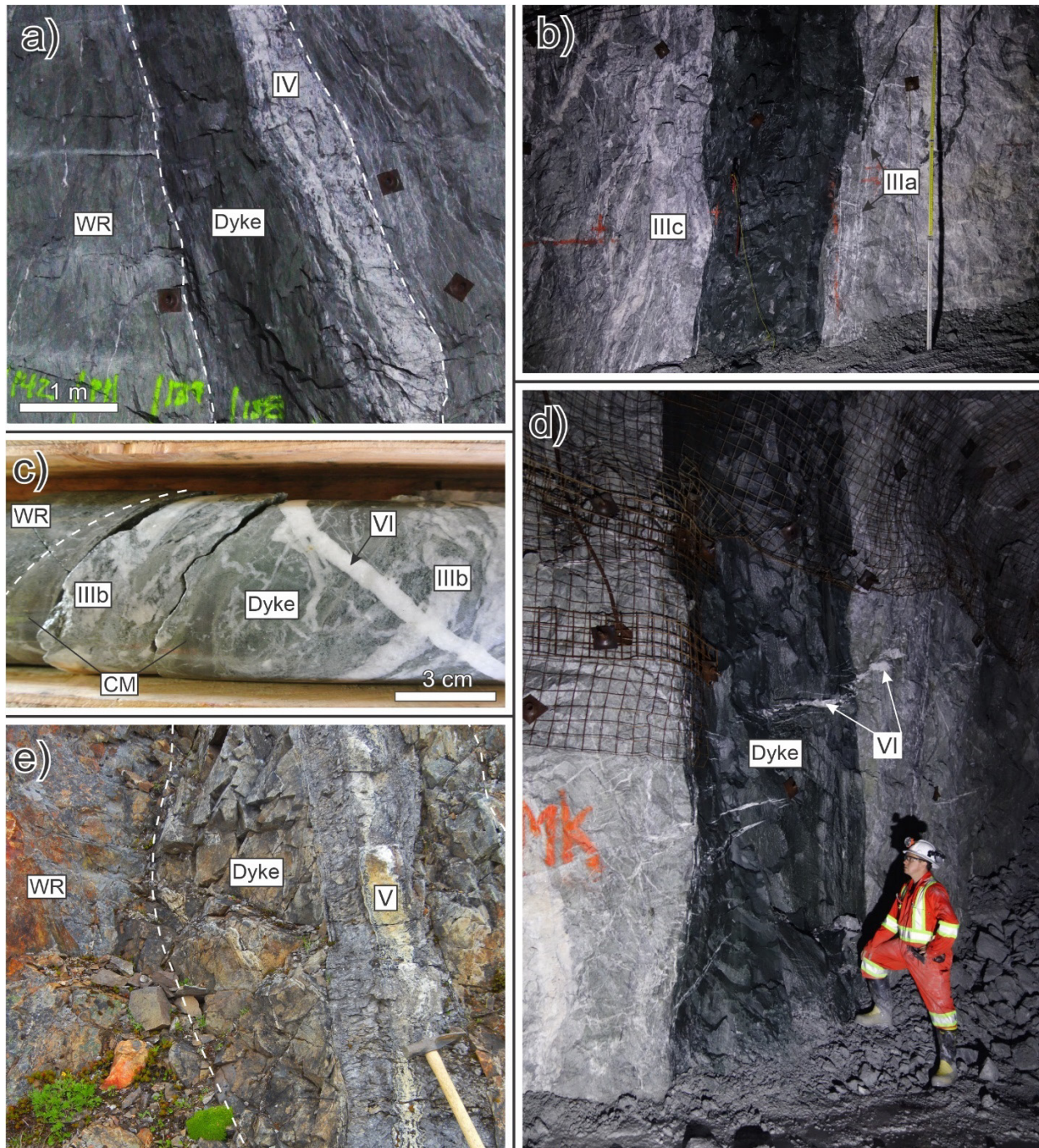
Figure 4.6: Representative photographs of 183 Ma late- to post-mineralisation trachybasaltic dykes in underground and surface exposures and drill core: **(a)** trachybasaltic dyke and a Stage IV vein concordantly exploiting a structural corridor (see below for vein stage descriptions); **(b)** trachybasaltic dyke cutting a four-metre-wide stockwork of Stage IIIc veins in the Domain 13 fault zone (pole at right is 3.5 m long); **(c)** contact between wallrock (WR) and a trachybasaltic dyke in drill core showing chilled margin (CM) and Stage IIIb and VI veins cutting the dyke; **(d)** shallowly dipping, post-ore Stage VI veins cutting a metre-wide trachybasaltic dyke in an underground development face; **(e)** a calcite-rich Stage V vein cutting a trachybasaltic dyke on surface.

air-fall lapilli tuff, cross-stratified crystal tuff, and blocky tuff breccias (Alldrick and Britton, 1988; Davies et al., 1994; Nelson et al., 2018; Fig. 4.7a-c). Volumetrically restricted marine sedimentary rocks and green-weathering massive crystal tuff are intercalated with this succession of otherwise maroon- (hematitic) to beige-weathering volcaniclastic deposits (Macdonald 1993; Fig. 4.7d). The Brucejack Lake felsic unit was intruded by a flow-dome complex which, based on field relationships, is believed to be its intrusive equivalent (Roach and Macdonald, 1992). The complex is composed of a flow-banded and flow-folded plagioclase-K-feldspar phyric latite (Fig. 4.7e-f) that yielded U-Pb zircon ages of 185.6 ± 1.0 and 185.0 ± 1.0 Ma at its base (~1450 m asl; Macdonald, 1993) and 179.8 ± 1.0 Ma at its highest exposed level (~1700 m asl; Tombe et al., 2018). Importantly, with the exception of stratiform hematite alteration, which is generally considered to be a product of subaerial weathering (Britton and Alldrick, 1988), rocks of the Brucejack Lake felsic unit were only altered near its exposed base, where weak to locally moderate phyllic alteration and polyphase hydrothermal quartz-carbonate veining affected porphyritic intrusive rocks of the flow-dome complex (Fig. 4.7a). Higher in the flow dome complex, evidence of phyllic alteration is absent and the rocks are cut only by sporadic tectonic tension-gash veins (Fig. 4.7b) similar to the post-mineral veins described below.

4.5.2 Hydrothermal alteration

At shallow levels (i.e., > 500 m asl mine levels and on surface), metasomatism in the Valley of the Kings and West zones is represented by widespread phyllic alteration (quartz-white mica-pyrite-calcite ± chlorite ± rutile ± apatite) and subordinate silicification. Both alteration types vary in intensity from weak to extreme (i.e., from incipient to complete replacement of the primary minerals), with the degree of alteration generally correlating with Stage I pyrite or Stage II barren quartz vein intensity (Fig. 4.8a-g: see below and Table 4.1 for vein types). This phyllic alteration and silicification affects all units in the mine sequence, with the exception of the 183 Ma trachybasaltic dykes, which are typically only weakly altered to carbonate-sericite-chlorite (Tombe et al. 2018). Locally, there is evidence of a strong lithological control on alteration intensity, including the presence of: (1) metre- to decametre-scale pod-like zones of very strong to complete, dark purple silicification of the Conglomerate unit around its upper and, more commonly, lower contacts, where they extend into the underlying Volcanosedimentary unit (mine unit, 'SIL'; Figs. 4.3, 4.8e); (2) metre-scale, bedding-parallel horizons of massive, coarse-grained, barren pyritization and monomineralic soapy green to greenish grey muscovite (no Cr,
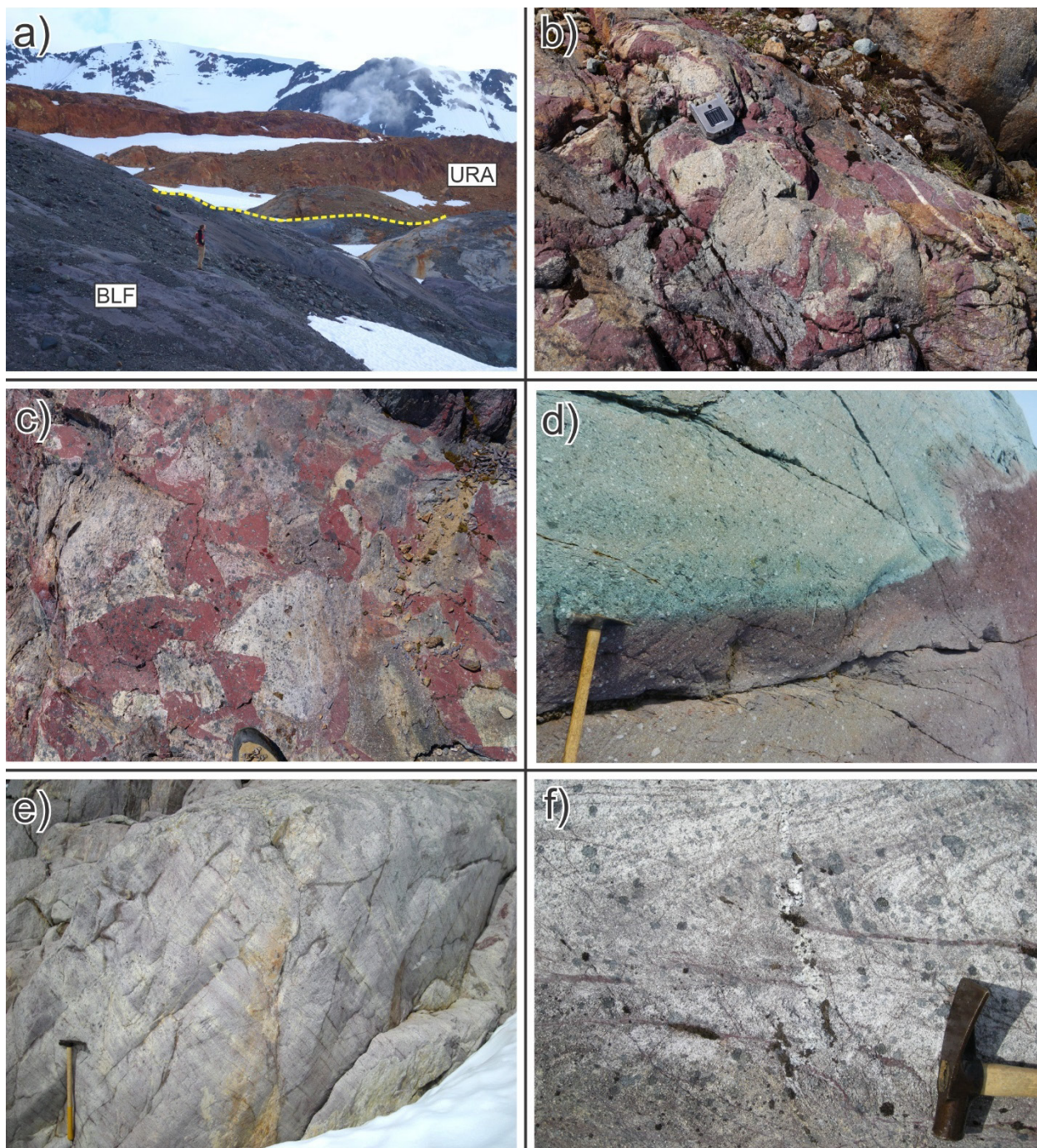
Figure 4.7: Representative photographs of the post-mineralisation extrusive Brucejack Lake felsic unit and intrusive flow dome complex**: (a)** contact between strongly phyllically altered rocks of the Unuk River andesite (URA) and weakly to unaltered rocks of the overlying Brucejack Lake felsic unit (BLF); **(b and c)** breccia of blocky K-feldspar phyric tuff in a hematitic mud matrix – tectonic (tension gash) Stage VI veins are visible in the right of (b); **(d)** contact between maroon- and green-weathered crystal tuff beds; **(e and f)** flow-banding and flow-folding textures in the dacitic to trachyandesitic Brucejack Lake flow dome complex.

V) along the base of the Conglomerate unit below the silica pods and, more rarely, along the upper contact (Fig. 4.8e-f); and (3) centimetre- to metre-scale, barren patches of translucent to pale grey-beige pervasive silicification of the Conglomerate and Volcanosedimentary units, peripheral to barren Stage II quartz stockworks (see below) and possibly genetically related to the silica pods (Fig. 4.8g-h; Board et al., 2020).

Approximately 450 m below the deepest level of current mine development (i.e., ~500 m asl) in the Valley of the Kings Zone, moderate to strong, patchy to locally pervasive, propylitic alteration has been intersected by deep exploration drilling (Pretium Resources Inc., 2019). In the Eastern Promises porphyry this alteration is typically characterised by a partial to complete replacement of the matrix by epidote-chlorite, which gives the rock a mottled appearance, and partial to complete replacement of the feldspar +/- hornblende phenocrysts by epidote > chlorite; this alteration is also commonly associated with chlorite-epidote veinlets with pistachio-green epidote halos (Figs. 4.9a and b). Patchy propylitic alteration also is locally evident in the Volcanosedimentary unit, where it is broadly similar in style, but without the epidote-altered phenocrysts. Phyllic alteration overprinted the propylitic alteration and Stage I pyrite veins (see below) with phyllic alteration halos clearly cross-cutting earlier epidote-chlorite alteration (Fig. 4.10f).

Lithological control on alteration intensity is apparent from the close spatial correlation between intense phyllic alteration (and surface gossans) and the trace of volcanosedimentary and

Figure 4.8 (next page): Surface and drill core photographs of Stage I and II veins (see Figure 4.10 and Table 4.1 for explanation) and related phyllic alteration in the Valley of the Kings zone**.** These two stages formed prior to the emplacement of bonanza-grade Stage III-V veins. **(a)** Complex network of Stage I pyrite stringer veins in a strongly phyllically altered outcrop; **(b)** well-developed quartz-sericite alteration haloes around pyrite-rich medial bands in Stage I veins; **(c)** a Stage I vein with diffuse margins cut by a Stage III a vein; **(d)** a Stage I vein with weakly chloritised margins – pyrite in the adjacent, electrum-bearing (El) Stage III that crosscuts the Stage I vein may have been inherited from the latter vein; **(e)** swarms of fine (mm-width) translucent to white, barren Stage II quartz veins invading the dark grey to dark purple pervasively silicified unit ('Sil') at the base of the Conglomerate unit – these veins cut early, bedding-parallel horizons of massive, coarse-grained, barren hydrothermal pyrite (mpy) and are in turn cut by Stage IIIa and IIIc veins; **(f)** intense sericite alteration (monomineralic soapy green to greenish grey muscovite) marginal to a Stage I vein swarm near the base of the Sil unit in drill core; **(g)** micro-stockwork of translucent Stage II quartz veins in the Sil unit; and **(h)** Stage I, II and VI veins in an intensely silicified area of the Volcanosedimentary unit – note that Stage I and II veins do not penetrate the less permeable mudstone layer on the left whereas the tectonic Stage VI veins penetrate the mudstone.
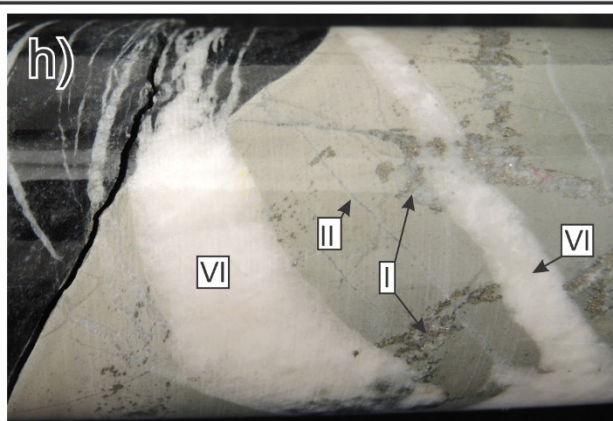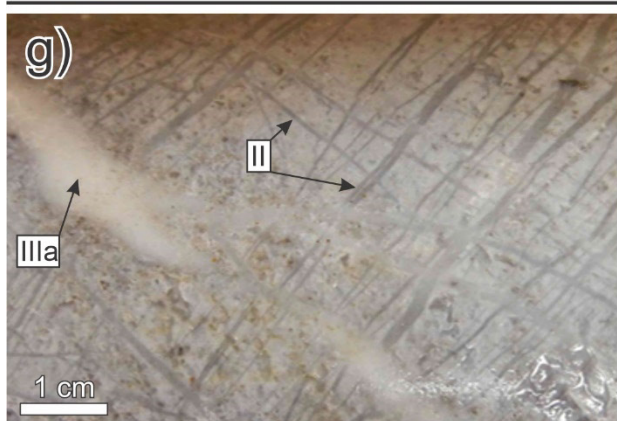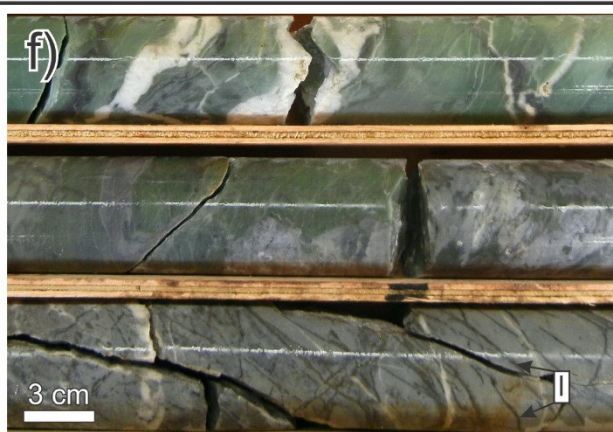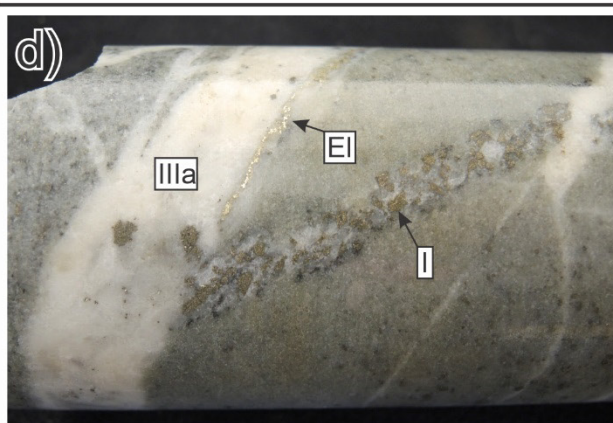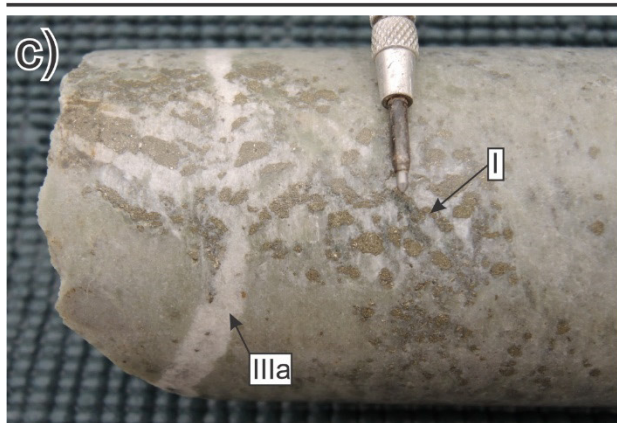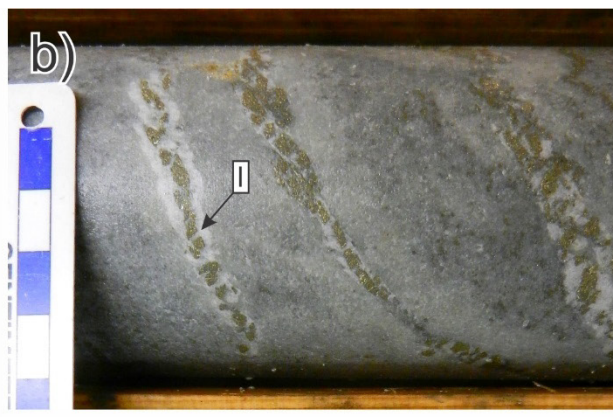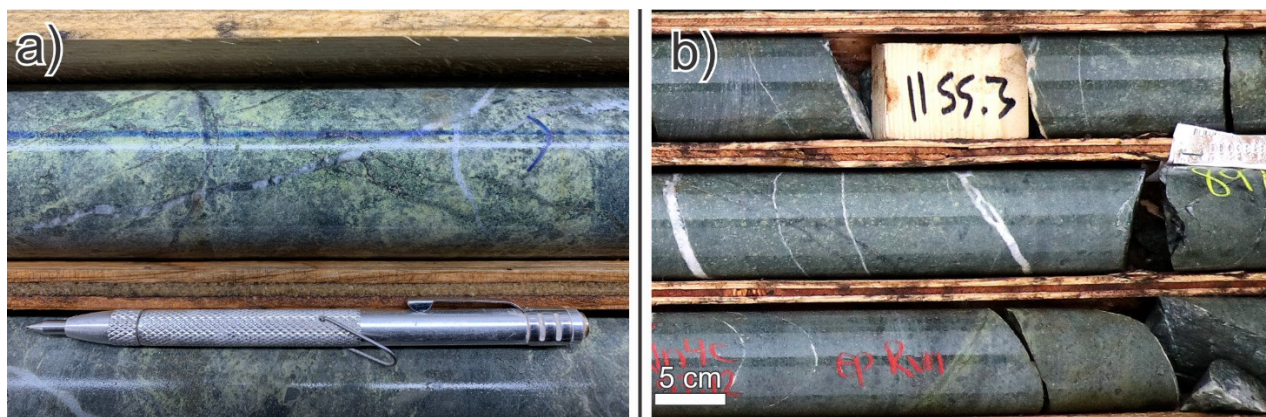
Figure 4.9: Drill core showing characteristic deep (< 500 m asl) moderate to strong propylitic alteration of the Eastern Promises porphyry unit: **(a)** a micro-stockwork of chlorite-pyrite epidote veinlets with pistachio-green epidote halos are cut by later quartz-calcite-chlorite veins; **(b)** partial to complete replacement of feldspar +/- hornblende phenocrysts in the host porphyry matrix by epidote > chlorite – epidote halos, developed around chlorite-pyrite veins, are visible at the bottom of the photograph.

pyroclastic rocks of the Unuk River andesite unit; both the intense phyllic alteration and gossans occur in a broadly overlapping, concave-to-the-west arcuate belt that partially encloses the 194 Ma Office porphyry (Fig. 4.3). All vein stages associated with visible electrum mineralisation, as well as the 183 Ma trachybasaltic dykes, cross-cut zones of intense silicification and pyrite-sericite alteration, indicating that the phyllic and silicic alteration largely predate high-grade epithermal mineralisation (Figs. 4.9c-e; Board et al., 2020). Rhenium-Osmium dating of molybdenite in porphyry-style B-type veins associated with phyllic alteration immediately to the south and north of the Valley of the Kings zone yielded ages of 191.7 ± 0.8 and 191.5 ± 0.8 Ma (Bridge zone) and 189 ± 0.9 Ma (West zone; Tombe et al., 2018), respectively. Collectively, these data imply that the history of alteration in the Valley of the Kings area is complex, involving multiple pulses of magmatic-hydrothermal activity which preceded the high-grade mineralising event that gave rise to the Brucejack deposit.

4.5.3 Mineralisation and veining

Visible Au and Ag mineralisation in the Valley of the Kings and West zones is hosted dominantly in quartz-carbonate veins, stockworks, and breccias, and is characterised by electrum and Ag-bearing sulphosalt minerals (primarily argento-tennantite and argento-tetrahedrite; Table 4.1; Fig. 4.10). Paragenetically early, lower grade (< 5 g/t Au) mineralisation also occurs throughout the Valley of the Kings and possibly the West zone as submicroscopic, 'invisible'

Table 4.1: Vein generations in the Valley of the Kings zone (modified after Tombe et al., 2018 and Board et al., 2020)

Vein stage	Description	Timing	Typical Size	Mineralogy	
				Precious/Base Metals	**Gangue**
I	Discontinuous stringers	Premineral	Thickness: mm Continuity: cm	Invisible Au in Py, tr.Cpy	Py-Qz-Cal-Ser±Chl
II	Discontinuous translucent veinlets		Thickness: mm Continuity: mm		Qz-Py
III	IIIa: sheeted veinlets	Synmineral	Thickness: cm Continuity: dam	El, tr.Sp±Gn±Cpy	Py-Qz-Cal-Dol±Ser±Rt
	IIIb: breccia/flooded zones		Thickness: cm to dm Continuity: m	El, tr.Sp±Gn±Cpy	Py-Qz-Cal-Dol±Ser±Rt
	IIIc: stockwork veins/blow-outs		Thickness: dm to m Continuity: dam to hm	El, tr.Sp±Gn±Cpy, tr.Ag-sulphosalts	Py-Qz-Cal-Dol±Ser±Apy±Rt
IV	Ag-rich base metal sulphide veins		Thickness: cm to dm Continuity: m to dam	Sp-Gn-Cpy-Ag-sulphide+sulphosalts Incl.: acanthite, pyrargyrite, freibergite, polybasite, proustite, argentotennantite, argentotetraderite, pearcite, tr hessite	Py-Qz-Cal-Dol±Ser±Apy±Rt
V	Mn-carbonate veins		Thickness: cm to dm Continuity: m to dam	El, tr.Cpy	Cal±Qz±Py±Rt
VI	Tectonic shear/tension gash veins	Postmineral	Thickness: cm Continuity: cm to m		Qz-Cal-Chl

Note: [1]tr. = trace. Abbreviations; Apy=arsenopyrite, Cal=calcite, Chl=chlorite, Cpy=chalcopyrite, cm=centimeter, dam=decameter, dm=decimeter, Dol=dolomite, El=electrum, Gn=galena, hm=hectometer, m=meter, Py=pyrite, Qz=quartz, Rt=rutile, Ser=sericite (white mica)

| Mineral | Pre-Ore Stage — Mesothermal (porphyry) | | Au-Ag Ore Stage — Epithermal | | | Post-Ore Stage — Tectonic |
	Stage I — Pyrite-quartz ± calcite veins	Stage II — Translucent quartz veins and veinlets	Stage III — Stringer, breccia, and stockwork quartz-calcite veins hosting electrum	Stage IV — Base metal sulphide veins containing Ag-sulphosalts and electrum	Stage V — Calcite dominated veins hosting electrum	Stage VI — Quartz-calcite tectonic shear and tension gash veins
Quartz	solid	solid	solid	solid	dashed	solid
Calcite	dashed		solid	solid	solid	solid
Dolomite			dashed		dashed	
Sericite	solid		dashed	dashed	dashed	
Chlorite	solid					solid
Pyrite	solid		dashed	dashed	dashed	
Rutile			dashed	dashed	dashed	
Chalcopyrite	dashed		dashed	solid	dashed	
Arsenopyrite			dashed	dashed		
Electrum			solid	solid	solid	
Sphalerite		dashed	dashed	solid		
Galena			dashed	solid		
Acanthite		dashed	dashed	solid		
(Ag-) Tetrahedrite			dashed	solid		
(Ag-) Tennantite			dashed	solid		
Pyrargyrite				solid		
Freibergite				solid		
Polybasite				solid		
Proustite				solid		
Pearceite				solid		
Hessite			dashed	solid		

Time →

Figure 4.10: Paragenetic sequence for vein-hosted minerals in the Valley of the Kings zone (modified after Tombe et al., 2018). Solid lines indicate that the listed mineral is prevalent, whereas dashed lines indicate that the listed mineral is present only in trace amounts.

gold within arsenian pyrite stringer veins (Stage I veins), wallrock-hosted disseminated arsenian pyrite, and wallrock-derived arsenian pyrite in quartz-carbonate-electrum veins (McLeish et al., 2018; discussed below). It is uncertain how much this arsenian pyrite contributes to the 11 Moz Au resource at Brucejack, although given that the resource is reported for a cut-off grade of 3.5 g/t Au, its influence is likely small (Board et al., 2020).

Several studies have investigated the paragenetic history of veining in the Valley of the Kings zone (Board and Greig, 2013; Tombe, 2015; Harrichhausen, 2016; Tombe et al., 2018; Board et al., 2020). Six primary vein stages have been recognised by the two most recent studies (Table 4.1). They are: (1) ductilely deformed, variably oriented, locally discontinuous pyrite-quartz ± calcite veins with sericite and, less commonly, weak chlorite alteration halos (Stage I; Fig. 4.8a-d, f and h); (2) white to translucent microcrystalline quartz veins in strongly silicified rocks (Stage II; Fig. 4.8g and h); (3) electrum-bearing quartz-calcite ± dolomite ± sericite veins, which are further subdivided by their mm- to cm-scale sheeted, dm- to m-scale brecciated, and dm- to m-scale stockwork morphologies (Stages IIIa, IIIb, and IIIc respectively; Fig. 4.11); (4) sub-planar to uncommonly anastomosing quartz ± calcite veins containing base metal sulphides (sphalerite, galena, chalcopyrite, arsenopyrite), Ag-sulphosalt (pyrargyrite, argentotetrahedrite, freibergite, polybasite, proustite, argentotennantite, pearceite), acanthite and Ag-rich electrum (Stage IV; Fig. 4.12); (5) sub-planar to planar carbonate ± quartz veins locally containing abundant orange-coloured, Mn-bearing calcite, and electrum (Stage V; Fig. 4.13); and (6) low-angle quartz veins with very rare, remobilised mineralisation filling thrust fault planes and contractional shear zones, and subhorizontal, barren, white quartz tension-gash veins (planar to sigmoidal) with adjacent chlorite alteration (Stage VI; Fig. 4.14).

Stage I and II veins are crosscut by all electrum-bearing vein stages (Stages III to V) and are therefore considered to be pre-ore with respect to bonanza-grade mineralisation. Stage I veins are the only type with alteration (sericite) halos, and are interpreted to be D-type veinlets associated with early porphyry-style alteration (Sillitoe, 2015; Tombe et al., 2018). In addition, Stage I veins are also the only veins that have deformation textures suggestive of their formation in a deeper, mesothermal environment (Board et al., 2020). Stage III to V veins are characterised by complex overprinting relationships and are thus considered to be contemporaneous. Stage VI veins cut all earlier vein generations and trachybasaltic dykes, and were likely emplaced during
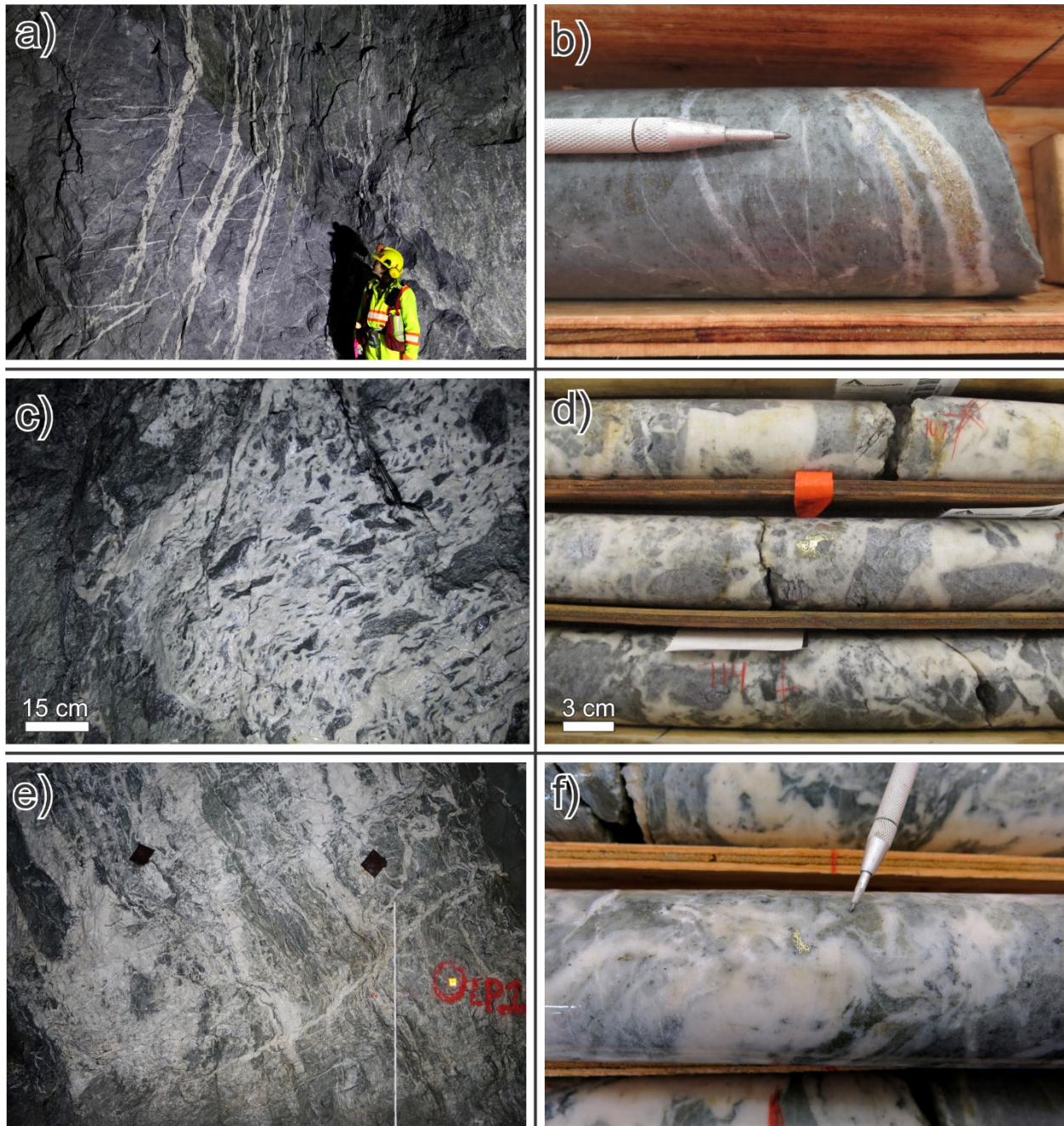
Figure 4.11: Representative drill core and underground photographs of high-grade Stage III veins: **(a)** steeply-dipping sheeted and locally bifurcating Stage IIIa veins in the Sil and Conglomerate units – note that, due to the large rheological contrasts between the units, veins appear to refract as they cross the Sil-Conglomerate contact, indicating that the pervasive silicification of the Sil unit predated vein emplacement; **(b)** bonanza electrum mineralisation in Stage IIIa veins; **(c)** well-developed hydrothermal quartz breccia in a Stage IIIb vein showing characteristic crowded angular wallrock clasts; **(d)** ~ 2 cm wide clot of electrum in a Stage IIIb vein; **(e)** large (> 3 m wide) Stage IIIc vein stockwork with localised quartz flooding (pole at lower right is 1.5 m long); **(f)** 0.5 cm clot of electrum in a Stage IIIc vein.
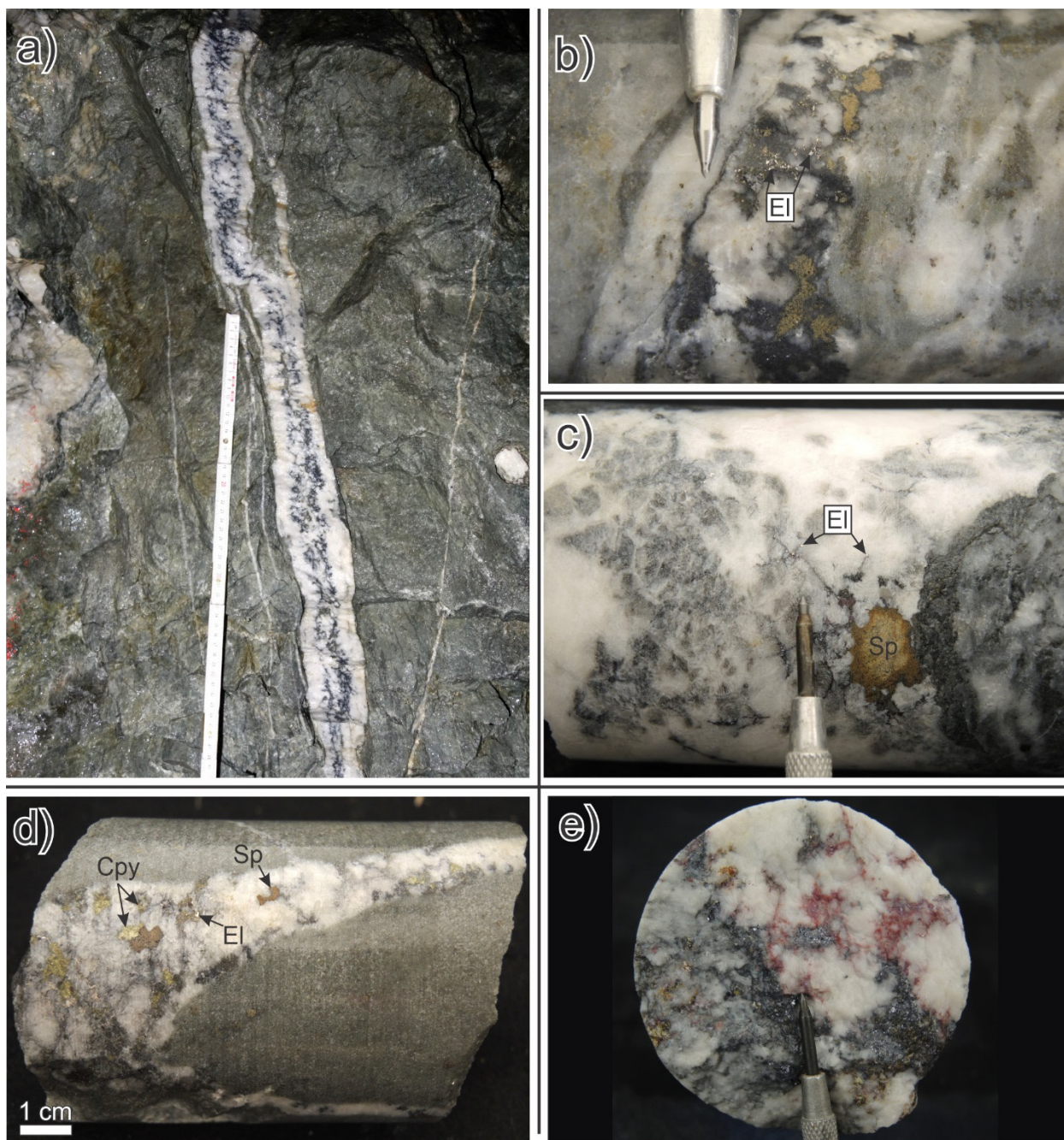
Figure 4.12: Representative drill core and underground photographs of well-mineralised Stage IV veins: **(a)** planar to weakly anastomosing vein with medial band of Ag-sulphosalt + galena + sphalerite (measuring pole is 60 cm long); **(b)** fine-grained Ag-rich electrum intergrown with Ag-sulphosalt minerals and sphalerite; **(c)** very fine-grained Ag-rich electrum hosted in relatively uncommon grey calcite; **(d)** chalcopyrite, sphalerite and fine-grained electrum and Ag-sulphosalt minerals; **(e)** dendritic pyrargyrite, galena, and trace chalcopyrite.
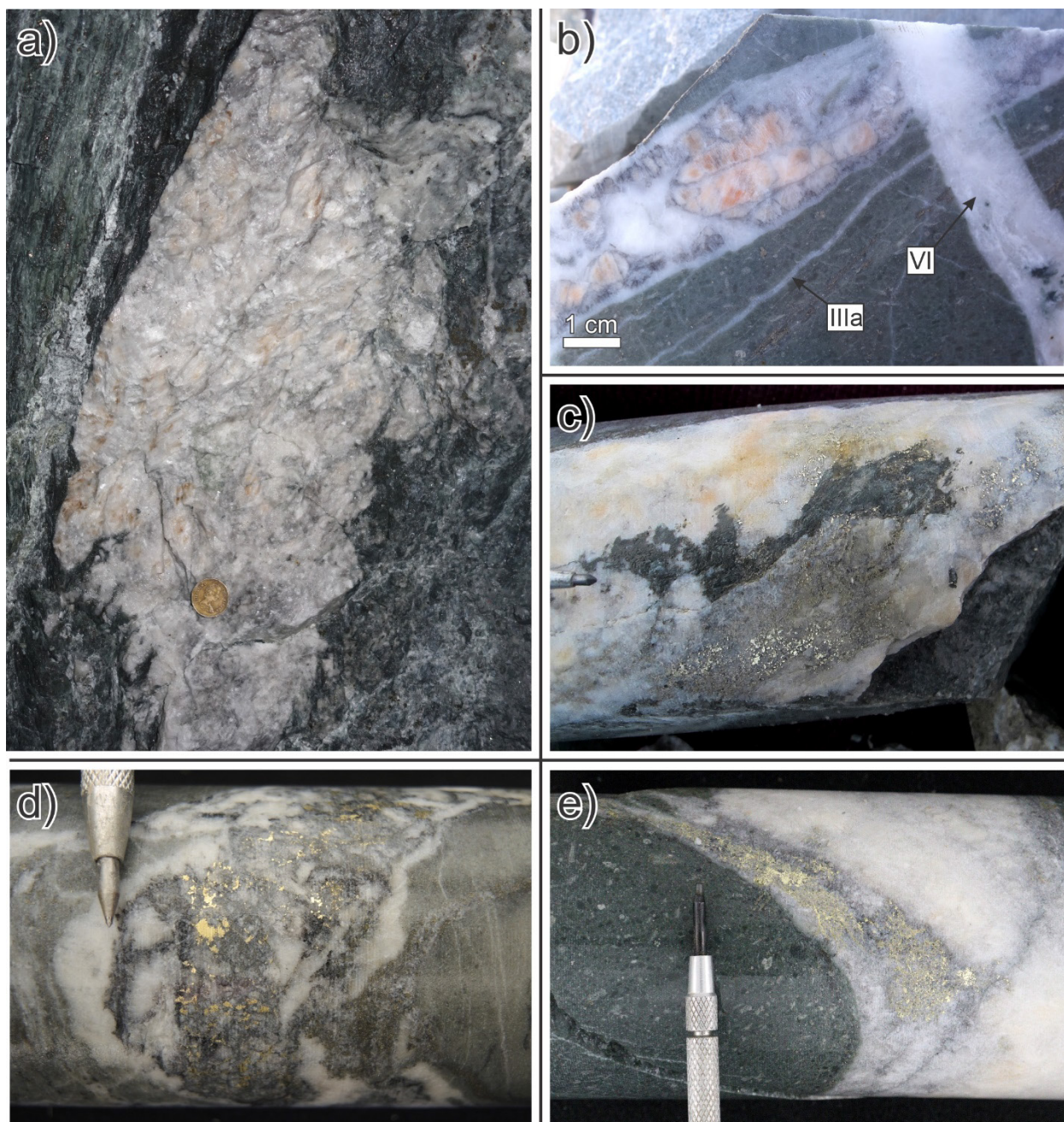
Figure 4.13: Representative drill core and underground photographs of bonanza grade Stage V veins: **(a)** large, dm-scale vein in an underground development face displaying abundant, characteristic pale pink-coloured manganoan calcite – note that vein is composed nearly entirely of calcite and lacks sulphide minerals and quartz; **(b)** Stage V vein with manganoan calcite displaying crustiform banding textures – note that the Stage V vein and the adjacent Stage IIIa vein are crosscut and offset along a Stage VI vein at right of photograph; **(c)** electrum in manganoan calcite-bearing vein; **(d)** electrum in a Stage V grey calcite vein with marginal quartz; **(e)** Stage VI vein with electrum, marginal grey calcite, and medial white calcite – note that the electrum occurs only in the grey calcite.

Figure 4.14: Representative underground and drill core photographs of Stage VI veins: **(a)** a trachybasaltic dyke cut by subhorizontal tension gash veins and a low-angle thrust fault that offsets the dyke; **(b)** narrow, 1-2 cm wide Stage VI vein cutting Stage IIIc and Stage I veins along a low-angle thrust fault that ductilely offsets the Stage IIIc vein; **(c)** abundant subhorizontal, en echelon planar and subvertical sigmoidal, tension-gash veins; **(d)** a cream-coloured Stage VI quartz vein cuts a Stage IV electrum- and Ag-sulphosalt-bearing white quartz vein.

mid-Cretaceous contractional deformation associated with Skeena fold and thrust belt development. In ore-related veins, electrum occurs mainly as fine- to coarse-grained (mm- to cm-scale) dendrites and, less commonly, as massive, cm-scale subhedral clots and aggregates (Fig. 4.15). Where veins have been affected locally by post-mineral, fault-related deformation (see below), electrum also occurs in the form of fine- to medium-grained slickensided sheets (Tombe et al., 2018). Although there is no significant variation in electrum textures among the different vein stages, the chemical composition of the electrum varies considerably, from ~30 to 70 wt% Au, with each stage characterised by a distinctive Au/Ag ratio (McLeish et al., 2018; Data Supplement S4.1). Although a detailed vein paragenesis has not yet been developed for the West zone, it appears to be characterised by a broadly similar sequence of veining and mineralisation, except for a greater abundance of base metal sulphide and silver sulfosalt minerals, and the occurrence of potassium feldspar-quartz veinlets as the earliest vein stage (Board et al., 2020).

With the exception of the base metal sulphide and Ag-sulfosalt mineral-rich Stage IV veins, all electrum-bearing vein generations in the Valley of the Kings zone are characterised by very low sulphide abundances (typically, < 1% total sulphides; Figs. 4.11 and 4.13). Even pyrite, the most common sulphide mineral in the deposit, occurs only in trace amounts in Stage III veins and is rare to absent in Stage V veins. Perhaps most significantly, the highest grade veins in the deposit are effectively devoid of sulphide minerals (Fig. 4.15). Where pyrite occurs in Stage III and V veins, it displays chemical and textural growth zoning indistinguishable from that in the wall rocks, indicating that it was inherited from earlier, wallrock-hosted phyllic alteration, and is xenocrystic (McLeish et al., 2018). There is also no correlation between the modal abundance of pyrite and electrum in Stage III or V veins. Other minerals, including the base metal sulphides and sulphosalts, occur only in trace levels in Stage III veins and are absent from Stage V veins.

Figure 4.15 (next page): Representative photographs of ultra-high-grade Au in drill core from the Valley of the Kings zone: **(a)** Stage V calcite vein in drill hole VU-053 (27,100 ppm Au over 0.5 m) with abundant, dendritic electrum; **(b)**, core in (a) cut along the long axis of the core; **(c)** Stage V calcite vein in VU-125 (10,850 ppm Au over 0.5 m); **(d)** Stage V calcite vein with medial white quartz in VU-346 (17,100 ppm Au over 0.5 m) – drill core is cut to show through-going nature of the electrum; **(e)** Stage IIIb quartz vein in VU-633 (11,650 ppm Au over 0.5 m); **(f)** Stage IIIc quartz-calcite vein in VU-722 (42,100 ppm Au over 0.5); **(g)** Stage IIIc quartz-calcite vein in VU-1631 (3,220 ppm Au over 1.5 m); **(h)** Stage IIIa quartz-calcite vein in SU-084 (5,480 ppm Au over 0.5 m). Note that in all of these bonanza grade occurrences, electrum is not associated with co-precipitated sulphide minerals.

99
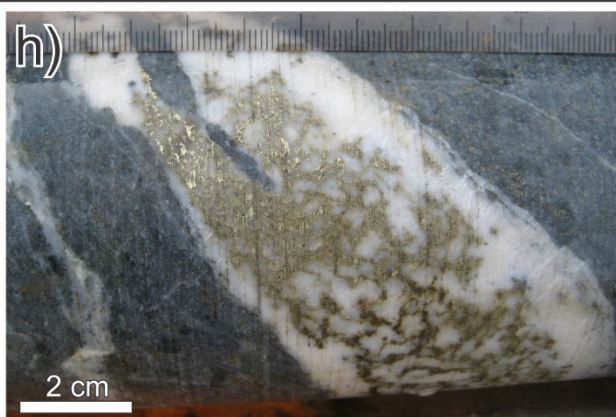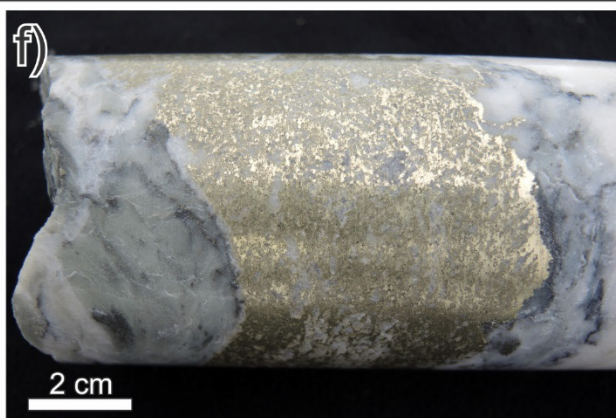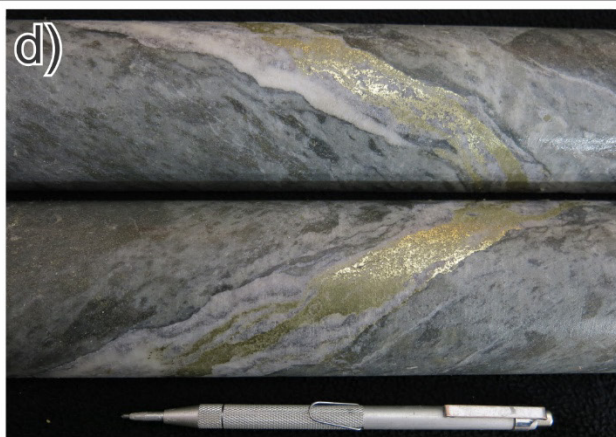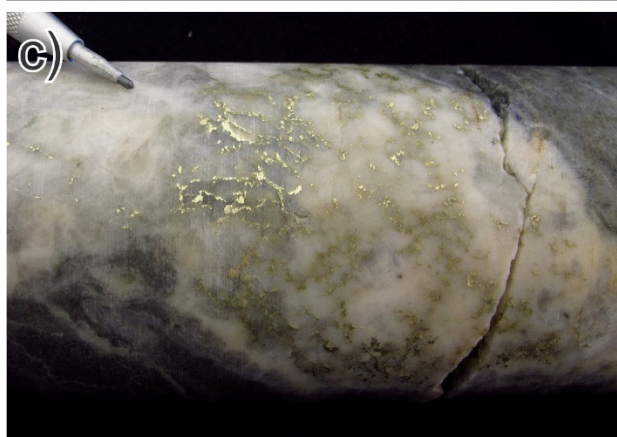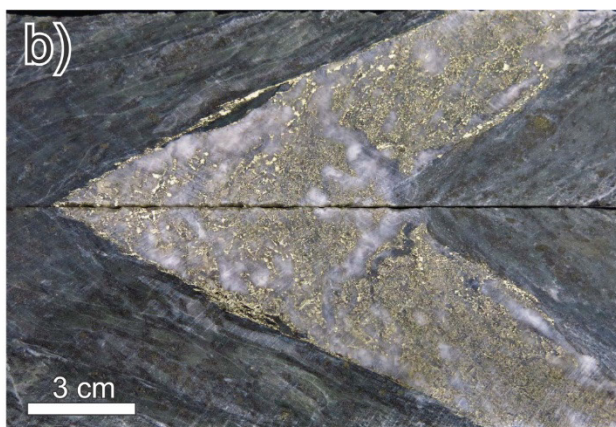
4.5.4 Structure

Mineralised Stage III to V veins generally strike southeast to east-southeast with a steep to vertical dip, although orthogonal north-south and east-west striking subvertical veins occur locally (Tombe et al., 2018). Whilst individual sheeted veins, vein breccias and stockworks occur typically as traceable planar features on a local scale (i.e., they can be followed for 10s to 100s of metres), they anastomose on a broader scale, grading vertically and laterally into one another along fractures, shears, foliation planes, and faults (Fig. 4.16). Stage III to V veins also coalesce along two major east-southeast striking normal faults in the Valley of the Kings zone, the Domain 13 and 20 faults, where they form two important vein corridors between ~5 and 30 m wide (Fig. 4.16). The veins cut two generations of penetrative, east and east-southeast-trending, moderate to steeply dipping, post-phyllic alteration foliation, collectively grouped as S_1-S_2 foliation, and are interpreted to have been emplaced synchronously with the formation of a later, steeply dipping, variably oriented penetrative S_3 foliation developed during a D_3 sinistral transpression event that included localised extension (Board et al., 2020). The complexity of the syn-mineral stress regime and the asymmetrical distribution of strain is further highlighted by a mixture of compressional (shear) and extensional features that occur in the ore-stage veins (Harrichhausen, 2016). Overall, however, deformation textures in each vein stage become progressively weaker from Stage III to V, indicating that mineralisation spanned the waning stages of the D_3 event (Davis, 2017; Tombe et al., 2018). Veins in the West zone were likely emplaced during a similar sinistral transpression event (Roach and Macdonald, 1992). Post-ore deformation in the deposit is variably developed and is largely focused along series of shallow to moderately southwest dipping thrust faults with a top-to-the-northeast sense of movement (Board et al., 2020; Fig. 4.16). Stage VI unmineralised tectonic shear and sub-horizontal tension gash veins are also associated with these faults which, based on $^{40}Ar/^{39}Ar$ muscovite dating, are believed to have formed at ~100 Ma (Tombe et al. 2018).
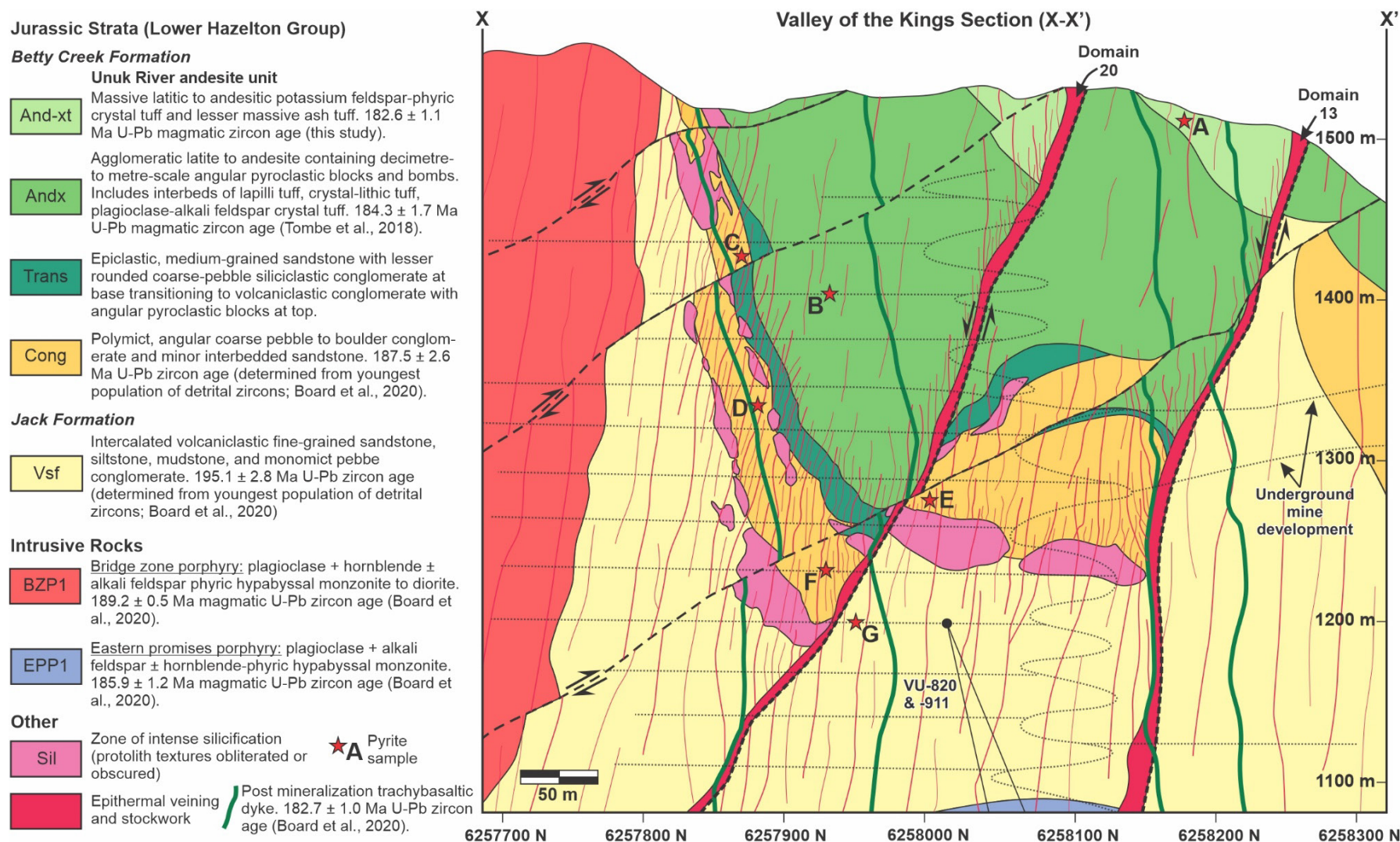
Figure 4.16: Geologic cross-section (X-X' on Fig. 4.3) through the Valley of the Kings zone of the Brucejack deposit showing the location of pyrite samples mapped compositionally by LA-ICP-MS for this study (see Figure 4.25 for element maps). See text for discussion.

4.5.5 Electrum-early pyrite relationships

Notwithstanding the overall low abundance to absence of sulphide minerals in many of the mineralised veins in the Valley of the Kings zone, there appears to be a significant spatial relationship between early-formed hydrothermal pyrite and later electrum. Initial petrographic investigations by Tombe (2015) noted that, as well as free grains, electrum occurs commonly in general association with pyrite, typically as fracture-fillings and microscopic inclusions. Electrum in high grade veins also has been observed to be locally concentrated at sites where Stage I pyrite veins are cross-cut by Stage III to V veins (Harrichhausen, 2016). Both of these studies invoked the pre-sulfidation porphyry alteration model of Heinrich et al. (2004), in which pre-ore sulphidation of Fe-silicate and Fe-oxide wallrock minerals promotes the transport of Au as an aqueous bisulphide complex due to an excess of S over Fe, to explain the apparent spatial relationship between high-grade gold and early phyllic alteration-related pyrite at Brucejack. Harrichhausen (2016) also speculated that charged surfaces on early pyrite may have played a role in mineralisation by attracting suspensions of nanoparticulate gold (i.e., colloids) in the ore-forming fluids. Furthermore, at the neighbouring KSM deposit cluster, Margolis (1993) noted that massive pyrite +/- quartz veins with sericitic alteration halos only contain high-grade gold mineralisation where they are cross-cut and locally infilled by late-stage epithermal Ag-Au-Pb-Zn quartz-barite veins at higher levels of the porphyry system. However, despite the identification of an apparent spatial relationship between epithermal gold and early pyrite at Brucejack and the neighbouring supergiant porphyry deposits, the origin and significance of this relationship, and the potential implications for porphyry-epithermal ore-forming processes in general, remain enigmatic.

4.6 Background: pyrite as a monitor of porphyry-epithermal fluid evolution

Owing to its status as the predominant sulphide mineral in most porphyry-epithermal hydrothermal alteration assemblages (e.g., in phyllic, propylitic, potassic, advanced argillic alteration; Sillitoe, 2010), and its ability to fingerprint subtle changes in fluid chemistry (see Román et al., 2019 for a review), pyrite is well suited to provide a potential monitor for hydrothermal fluid evolution throughout nearly all levels of the porphyry-epithermal environment. Additionally, the incorporation of certain trace elements in pyrite (e.g., Co, Ni, As, Au) has been shown to vary with changing temperature, pH, salinity, fS_2, and redox conditions

(Fleet et al., 1989; Maslennikov et al., 2009; Reich et al., 2013; Keith et al, 2018; Steadman et al., 2021). A temperature-based hierarchy has been proposed for pyrite compositions from fossil black smokers in a VMS deposit in the Southern Urals (Maslennikov et al., 2009). There, high (> 300 °C), intermediate (200-300 °C), and low (150-200 °C) temperature pyrite associations are characterised by elevated concentrations of, respectively: (1) Co, Ni, Cu, Se, Te and Bi, (2) Zn, As, Sb and Sn, and (3) Pb, Sb, Ag, Bi, Au, Tl and Mn. This hierarchy also accords well with trace element signatures and paragenetic trends observed in porphyry-epithermal pyrite, wherein early, higher temperature porphyry-stage pyrite crystals have cores relatively enriched in Co and Ni that are surrounded by lower temperature, paragenetically later As- ± Au-enriched epithermal-stage pyrite overgrowths (Gregory et al., 2013; Reich et al., 2013; Steadman et al., 2021). Studies of strictly porphyry or epithermal deposits (i.e., those that do not exhibit hybrid/overprinting alteration or mineralisation) have found a similar association of elevated Co and Ni with porphyry-type pyrite (e.g., the Mandamah porphyry Cu-Au-Mo deposit, Australia; Steadman et al., 2021) and elevated As and Au with epithermal pyrite (e.g., Yanachoca epithermal Au-Ag deposit, Peru; Deditius et al., 2009).

The application of distinctive intragrain trace element zonation trends in pyrite to understanding the overall evolution and architecture of porphyry-epithermal systems has recently been demonstrated by Sykora et al. (2018) for the supergiant Lihir porphyry-epithermal Au deposit in Papua New Guinea. There, pyrite compositions and zonation patterns document the porphyry to epithermal transition; shallow-level epithermal Au mineralisation was superimposed upon genetically related porphyry-style alteration. Sykora et al. (2018) also documented the occurrence of distinct pyrite textures that are associated with porphyry- and epithermal-type compositional anomalies. These are illustrated in Figure 4.17a, where the characteristic end-member porphyry- and epithermal-stage textures are typified as, respectively: (1) regular, euhedral to subhedral cubic growth zones containing elevated Co and Ni, and (2) irregular subhedral to anhedral, oscillatory zones containing growth bands with locally well-developed colloform textures and elevated As, Mo, Sb, Au, Tl and Pb. These characteristic textures and associated compositional zonation may also occur together in composite grains (Fig. 4.17b), which are interpreted as direct evidence of later, but genetically related epithermal modification of porphyry-stage grains due to telescoping of the hydrothermal system (Sykora et al., 2018).

103
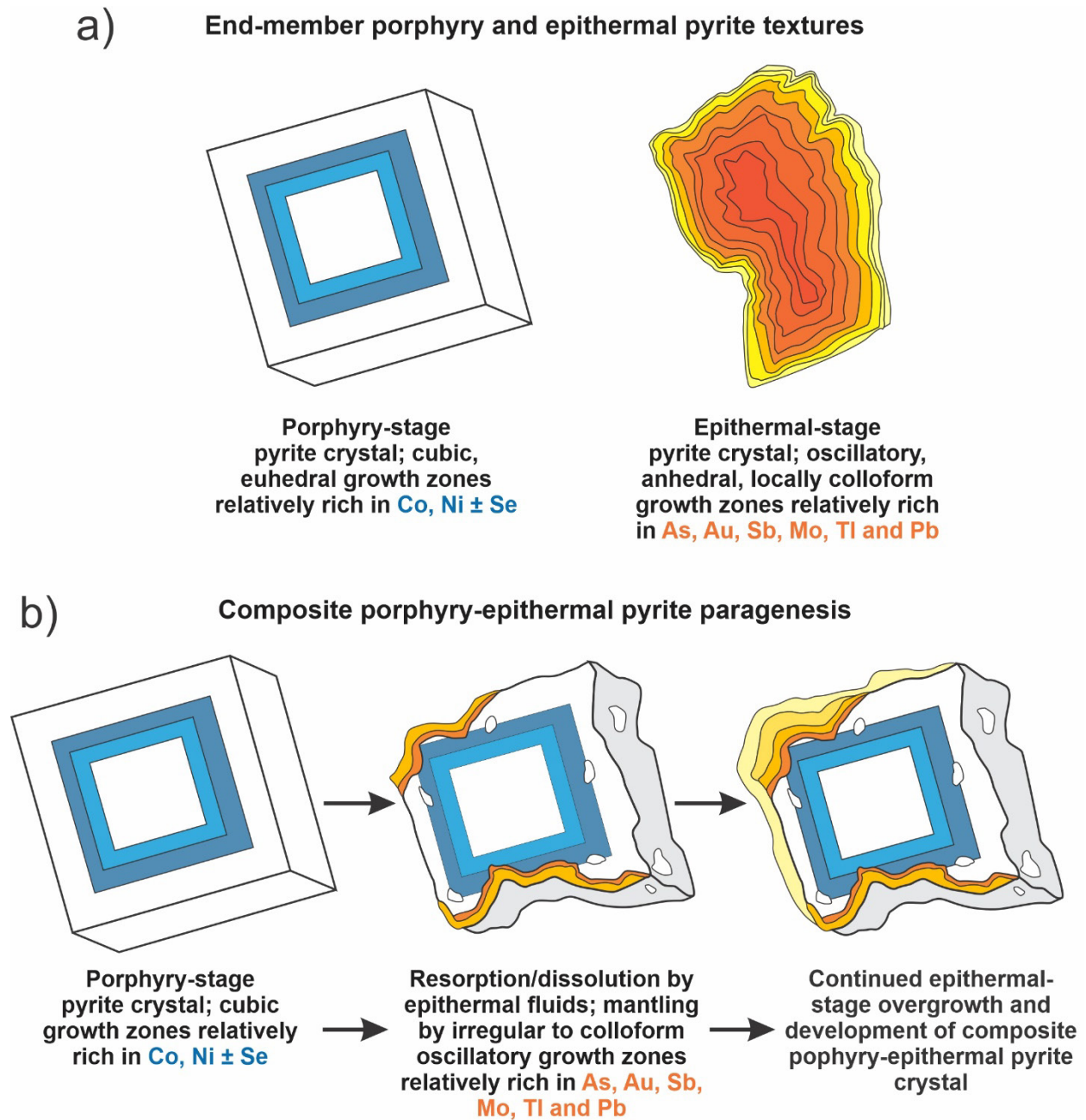
Figure 4.17: Schematic depiction of comparative trace element enrichments and textural intracrystalline growth zonation patterns in pyrite from porphyry, epithermal, and transitional porphyry-epithermal environments (modified after Sykora et al., 2018): **(a)** Porphyry- vs. epithermal-stage pyrite crystals. Porphyry-stage pyrite is characterised by cubically zoned cores, whereas epithermal-stage pyrite has oscillatory zoning; **(b)** composite, porphyry-epithermal pyrite grain cores and rims, illustrating the evolution of an euhedral porphyry-stage crystal, initially relatively rich in Co, Ni ± Se, that was partly dissolved, and then overgrown by rims relatively rich in As, Au, Sb, Mo, Tl, and Pb.

4.7 Methods

To better understand the relationships between the multiple generations of hydrothermal alteration, magmatism and mineralisation at Brucejack, we have undertaken a detailed petrographic and mineral chemical study of pyrite from all stages of mineralised veins and wallrock alteration in the deposit. Using optical microscopy and laser ablation-inductively coupled plasma-mass spectrometry (LA-ICP-MS), we have analysed the trace element and micro-textural characteristics of Brucejack pyrite to: (1) unravel the chemical fingerprints associated with each alteration / mineralisation event leading up to and culminating in bonanza-grade mineralisation in a world-class epithermal gold-silver deposit; (2) elucidate the ore-forming processes that controlled mineralising events, including early, lower grade arsenian pyrite-hosted invisible Au and later, coarse-grained electrum mineralisation; and (3) explore possible linkages between older, porphyry-related pyrite veins and younger high-grade epithermal gold. To better constrain the relationships between Early Jurassic volcano-magmatic activity, hydrothermal alteration, and epithermal mineralisation, we have also conducted a review of the geochronological data for the Brucejack area, including previously unpublished U-Pb zircon ages (Pretium Resources Inc. geochronological database) and have combined this with field checks of sample sites to better document relative age constraints. Lastly, in tandem with our pyrite study, we have performed in situ pyrite-barite sulphur isotope exchange thermometry via high-resolution secondary-ion mass spectrometry (SIMS) to determine the temperature of epithermal- and porphyry-related mineralisation.

4.7.1 Sample collection and optical/electron microscopy

Seventy-two polished thin sections containing representative hydrothermal pyrite from the mineralised vein stages and spatially associated phyllically altered wallrocks were selected for petrographic and mineral chemical study. Sampling was conducted on all accessible levels of underground mine, as well as on surface and drill core. The timing relationships of the vein stages to wallrock features (e.g., pyrite associated with phyllic alteration) were documented during sampling. Emphasis was placed on samples containing coarse-grained electrum in order to evaluate relationships between electrum and pyrite. Petrographic investigations using reflected and transmitted light microscopy documented pyrite growth zoning patterns, and in particular euhedral, inclusion-free rims around corroded, inclusion-bearing crystal cores. Follow-up

petrographic and mineral chemical analyses were conducted using scanning electron microscopy (SEM), electron microprobe wavelength-dispersive X-ray spectroscopy (EMP-WDS), and LA-ICP-MS methods. Mineralised veins containing pyrite in contact with barite were examined by SEM to identify equilibrium textures and assess suitability for in situ, SIMS-based sulphur isotope analyses. A 20 kV accelerating voltage and a high beam current (140-200 nA) were used during SEM analyses to resolve zonation textures in pyrite and barite.

4.7.2 EMPA-WDS analyses

The EMPA-WDS analyses were conducted at the University of Ottawa–Canadian Museum of Nature MicroAnalysis Laboratory using a JEOL 8230 SuperProbe with five X-ray wavelength-dispersive spectrometers. Pyrite was analyzed for As (Lα), Au (Lα), Cu (Kα), Fe (Kα), and S (Kα) using the synthetic and natural standards: Au80Ag20 alloy (Au), cubanite (Cu), GaAs alloy (As), and pyrite (Fe and S). Analyses were performed at 20 kV, 200 nA and a 2 μm beam diameter. Lower (2σ) detection limits of 100 ppm Au and 90 ppm As were achieved using 200 and 30 second peak counting times, respectively.

4.7.3 LA-ICP-MS analyses

Sixteen pyrite grains from sixteen samples were mapped using a Resonetics RESOlution M-50 ArF excimer laser (193 nm) coupled to an Agilent 7900x ICP-MS at the Laboratoire des Matériaux Terrestres of l'Université du Québec à Chicoutimi. Owing to the very low sulphide content of Stage III and V veins, and the propensity for electrum to fill fractures in pyrite (discussed below), which would compromise evaluating lattice-bound or nanoparticulate Au in pyrite, mapping focused on pyrite from Stage I veins (n=15). One Stage III-hosted pyrite grain was also mapped to further test the hypothesis that most vein-hosted pyrite was inherited from Stage I veins and/or phyllically-altered wallrock. The concentrations of ^{27}Al, ^{29}Si, ^{33}S, ^{34}S, ^{44}Ca, ^{47}Ti, ^{51}V, ^{53}Cr, ^{55}Mn, ^{57}Fe, ^{59}Co, ^{60}Ni, ^{63}Cu, ^{65}Cu, ^{66}Zn, ^{72}Ge, ^{74}Ge, ^{75}As, ^{77}Se, ^{82}Se, ^{95}Mo, ^{96}Mo, ^{109}Ag, ^{111}Cd, ^{113}In, ^{115}In, ^{118}Sn, ^{121}Sb, ^{125}Te, ^{128}Te, ^{137}Ba, ^{182}W, ^{184}W, ^{197}Au, ^{200}Hg, ^{202}Hg, ^{203}Tl, ^{204}Pb, ^{205}Tl, ^{206}Pb, ^{207}Pb, ^{208}Pb and ^{209}Bi were measured. Internal standardisation was based on ^{57}Fe using stoichiometric iron values for pyrite. Element-distribution maps (Figs. 4.25 and 4.27) were made by performing a series of line scans across each grain with a beam size of 11–19 μm and a stage speed of 10–20 μm/s. A laser fluence of 13 J/cm2 with a repetition rate of 15 Hz was used for all line scans. A gas blank was measured for 30s before switching on the laser between

each line scan. Silicon was monitored during mapping to check that the ablation signal represented pure sulphide. Standard reference materials used for external calibration were: JB-MSS5, a synthetic FeS crystal provided by J. Brenan, Dalhousie University, containing 50–70 ppm of As, Ag, Bi, Pb, Re, Sb, Se, and Te and 200 ppm Cu (Dare et al., 2010) and used to calibrate for these semimetals; Laflamme Po727, a synthetic FeS crystal provided by Memorial University, doped with 40 ppm of platinum-group elements and Au (Barnes et al., 2008), and used to calibrate for Au; and GSE-1G, a synthetic glass provided by the USGS, doped with 300–600 ppm Ba, Cr, Ge, Mn, Ni, Si, Ti, V, and W (Guillong et al., 2005), and used to calibrate for these elements; and MASS-1, a ZnCuFeS pressed-powder pellet provided by the USGS, doped with 50–70 ppm of most chalcophile elements plus Co, Mo (Wilson et al., 2002), and used to calibrate for the remaining elements. Elements that are present in multiple reference materials were compared and gave similar results. The standard JB-MSS5 was also used as a secondary reference material for intrastandard quality control. Data reduction and map generation were carried out using Iolite for IgorPro software (Paton et al., 2011) for the time-resolved composition of each element. The resulting maps are semiquantitative and indicate element concentrations relative to the calibration standard.

4.7.4 SIMS analyses

Secondary ion mass spectrometry (SIMS) and related sample preparation were carried out at the Canadian Centre for Isotopic Microanalysis (CCIM), University of Alberta. Regions of interest (n=15) 1.5 – 2.5 mm in diameter were cored from polished thin sections mounted on glass. These were cast into a 25 mm epoxy mount together with previously polished fragments of an in-house pyrite reference material (S0302A). The mounts were lightly polished to a 0.25 micron finish using diamond pads, cleaned, and then coated with 10 nm of Au prior to scanning electron microscopy (SEM). SEM characterisation was conducted with a Zeiss EVO MA15 instrument using beam conditions of 20 kV and 3 to 5 nA. A 90 nm film of Au was deposited on the mounts prior to SIMS analyses.

Sulphur isotope ratios (^{34}S/^{32}S) for pyrite were determined using the IMS-1280 multi-collector ion microprobe at CCIM. A primary beam of 20 keV ^{133}Cs+ ions was focused to form a probe with a diameter of 5 to 10 μm depending on the session, and with a beam current of 0.15 to 0.60 nA. The primary beam, temporarily increased in intensity, was rastered across a 15 x 15

µm area for 30 s prior to analysis to implant Cs. Negative secondary ions were extracted through 10 kV potential to the grounded secondary column (Transfer section). Conditions for the Transfer section included an entrance slit width of 80 µm, field aperture of 5 x 5 mm, and a field aperture-to-sample magnification of 100 x. Automated tuning of the secondary ions in the Transfer section preceded each analysis. The energy slit was fully open, and both secondary ion species were analyzed simultaneously using Faraday cups for ^{32}S- and ^{34}S- (^{32}S- in L2 using 1011Ω amplifier circuits, ^{34}S- in FC2 with 1011 Ω). Exit slit widths of 500 µm and ~270 µm were utilised for ^{32}S and ^{34}S-, respectively, that gave nominal mass resolutions of 2000 for ^{32}S- (10% peak height definition) and 3500 for ^{34}S-. Faraday cup baselines were measured at the start of each session. The total between-spot analysis time was 200 s.

The analytical protocol involved interspersing analyses of pyrite reference material S0302A (δ^{34}SVCDT = 0.0 ±0.2 ‰; R. Stern, unpublished data based on S-isotope gas source mass spectrometry) in a 4:1 ratio with the pyrite to be analysed. The reference VCDT value utilised for ^{34}S/^{32}S normalisation was 0.0441626 (Ding et al., 2001). Instrumental mass fractionation for ^{34}S-/^{32}S- was determined from replicate analyses of S0302A pyrite for each session. The standard deviations of ^{34}S-/^{32}S- for S0302A ranged from 0.05 to 0.08 ‰, after small corrections for time-correlated IMF drift. Final uncertainties are reported at the 95% confidence level (2σ) and propagate within-spot counting errors, between-spot errors to account for spatial and time-correlated (drift) uncertainties (±0.10 ‰ blanket error), and between-session errors that account for the uncertainty in the mean IMF for the session. The propagated individual spot uncertainty in δ^{34}SVCDT is typically ±0.15 to 0.20 ‰ (2σ).

The analytical conditions and protocol for barite δ^{34}SVCDT measurements were similar to those for pyrite, but a larger Cs beam of ~15 µm diameter, and a normal incidence electron gun were employed to prevent sample charging. Primary CCIM reference material S0327 barite with a δ^{34}SVCDT of +22.0 ± 0.3‰ (scaled to NBS-127 = +21.1 ‰; R. Stern, unpublished data) was used to measure and track the instrumental mass fractionation. Replicate analyses of S0327 gave standard deviations for ^{34}S-/^{32}S- of ± 0.07 to 0.11 ‰ for individual sessions (IP20030, IP20032A, B, C). The final uncertainty in δ^{34}SVCDT was typically ± 0.25 ‰ for barite.

4.7.5 U-Pb Geochronology Review

Although U-Pb zircon ages for most mine series strata provide important maximum constraints on the age of mineralisation and alteration (Tombe et al., 2018; Board et al., 2020), the age of the recently recognised stratigraphically highest unit, the Andesitic Crystal Tuff, is unknown. The age of this unit is crucial for unravelling the history of hydrothermal pyrite at Brucejack because it is stratigraphically the youngest rock to have been phyllically altered and mineralised; strata of the Brucejack Lake felsic member overlying the eastern portion of the deposit were only hydrothermally altered along their base and are barren. Results from this study, based on previously unpublished dates (Pretium Resources Inc. geochronological database) are reported below and in Data Supplement S4.2 with the U-Pb methodology.

4.8 Results

4.8.1 Macro-scale paragenesis

Cross-cutting relationships indicate that all types of pyrite, including that hosted by Stage I pyrite veins, wallrock-hosted phyllic alteration, and massive, bedding-parallel alteration zones are cut by high-grade epithermal carbonate-quartz-electrum veins (Stages III-V; Fig. 4.18). Moreover, although Stage III-IV veins typically contain only minor pyrite and Stage V veins are commonly sulphide-free, all of the ore-stage Au veins locally host spatially-restricted pyrite that appears to have been derived from the surrounding phyllically altered wallrock. In such cases, pyrite is present in the ore-stage veins either as: (1) individual crystals or aggregates that have been mechanically remobilised from Stage I veins and are cross-cut by ore-stage veins (e.g., Fig 4.8d), or, less commonly, (2) cm-scale xenoliths of phyllically-altered wallrock. In the former, the high-grade vein-hosted pyrite frequently appears to be fractured and locally disaggregated to a greater degree than grains in the adjacent Stage I veins.

Figure 4.18 (next page): Representative underground photographs showing cross-cutting relationships between Stage I pyrite veins and phyllic alteration, including massive, bedding-parallel pyritic alteration zones. **(a-c)** Stage IIIa and IIIc veins cutting massive, bedding-parallel pyritic horizons along the upper margin of the Sil unit; **(d)** Stage IIIa veins cutting a preferentially pyritised clast in the Conglomerate unit; **(e)** ptygmatically folded Stage I vein cut by a Stage IIIa vein; **(f)** chalcopyrite- and Ag-sulphosalt-bearing Stage IV vein cutting Stage I veins with locally well-developed, narrow (1-2 mm) chloritic alteration halos; **(g)** ptygmatic Stage IIIa vein cutting a network of Stage I stringers.
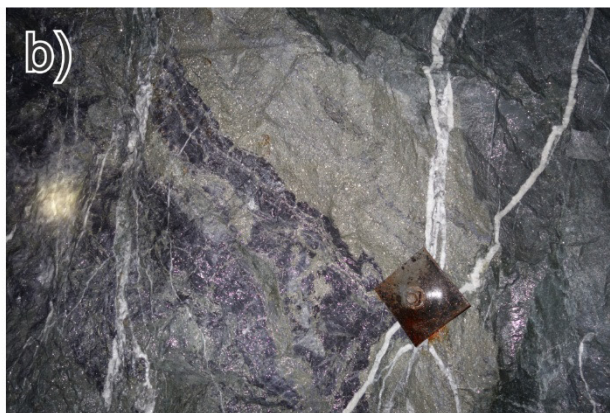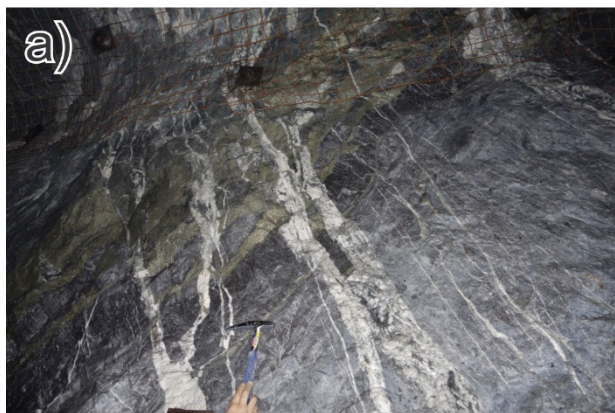
In many of the Stage III-V mineralised veins, there is a close spatial relationship between bonanza gold and pyrite associated with Stage I veins and phyllically-altered wallrock (Fig. 4.19). In particular, electrum is commonly concentrated where Stage III-V veins crosscut Stage I veins or in areas immediately adjacent to preferentially pyritised wallrock (e.g., pyrite-replaced conglomerate clasts, Fig. 4.19b). In the former case, electrum is either completely confined to the cross-cutting area or, sometimes, extends beyond it in Stage III-V veins (possibly indicating the transport direction in these veins). Less frequently, electrum occurs in contact with Stage III-V vein-hosted pyrite crystals that appear to have been inherited from the wallrock or Stage I veins (Fig. 4.19e). Although most of the early occurrences of electrum in contact with pyrite are mm- to cm-scale, blebs to thin wispy bands, larger, dm-scale concentrations of dendritic electrum also occur locally in close association with Stage I veins and pyritised wallrock (Fig. 4.19g).

4.8.2 Micro-scale paragenetic observations

Optical microscope and SEM investigations indicate that pyrite is moderately to heavily fractured and locally disaggregated in ore-stage veins throughout the deposit (Figs. 4.20 and 4.21). In electrum-bearing sectors, intragrain fracture networks are commonly filled partially to completely with electrum. Indeed, backscatter electron (BSE) imaging of pyrite from ore-stage veins shows that this mineral preserves a complex but strikingly uniform history of pre-electrum growth zonation, typically characterised by: (1) an inner, irregular, moderately to strongly

Figure 4.19 (next page): Representative drill core photographs illustrating the close spatial relationship between bonanza gold occurrences in Stage III-V veins and Stage I pyrite veins (including associated pyritic phyllic alteration). **(a)** a 0.5 cm clot of electrum nucleating from pyrite in a Stage I vein where it is crosscut by a Stage IIIa vein – note that the electrum is asymmetrically distributed around the intersection area between the veins, with significantly more electrum occurring in the Stage IIIa vein above the Stage I vein than below it; **(b)** a Stage IIIa vein cross-cutting a phyllically altered clast in the Volcanosediment unit, with abundant mm-scale grains of electrum vein within the strongly pyritised portions of the clast ; **(c)** a narrow, electrum-bearing Stage IIIa vein cross-cutting a Stage I vein– note that electrum in the Stage IIIa vein only occurs in and above the area between the two veins; **(d)** a Stage V vein cross-cutting a Stage I vein with two ~0.5 cm long bands of dendritic electrum nucleating from Stage I pyrite on both sides of the Stage V vein; **(e)** a band of electrum in a Stage IIIb vein nucleating from the edge of a pyrite aggregate in the Stage IIIb – note that the pyrite appears to have been inherited from the adjacent Stage I vein; **(f)** a 0.3 cm clot of electrum plugging a Stage IIIa vein at the intersection of a Stage I vein, ; **(g)** a large (~15 x 3 cm) dendritic aggregate of electrum in a Stage IV vein nucleating from a preferentially pyritised bed or clast in the Volcanosediment unit ; **(h)** a 0.5 cm wide band of dendritic electrum in a Stage IIIa vein nucleating from pyrite in a Stage I vein.
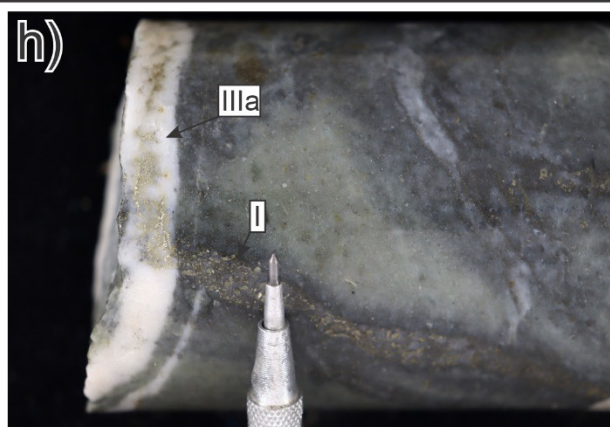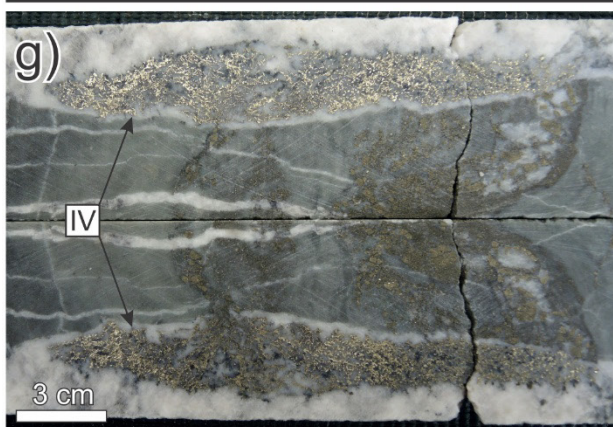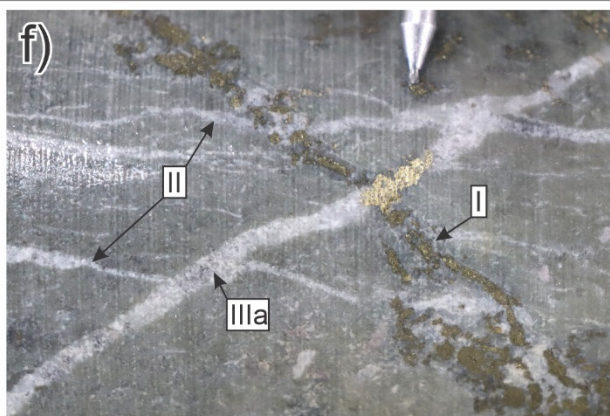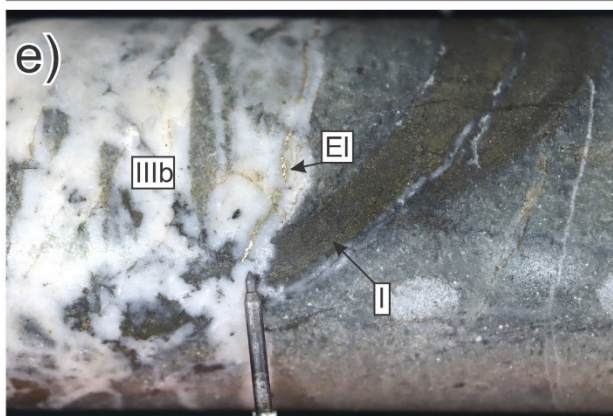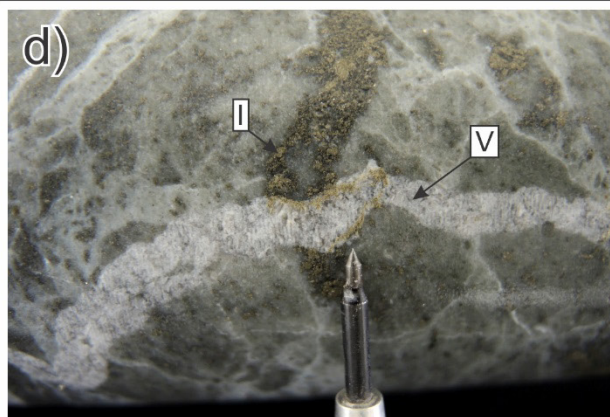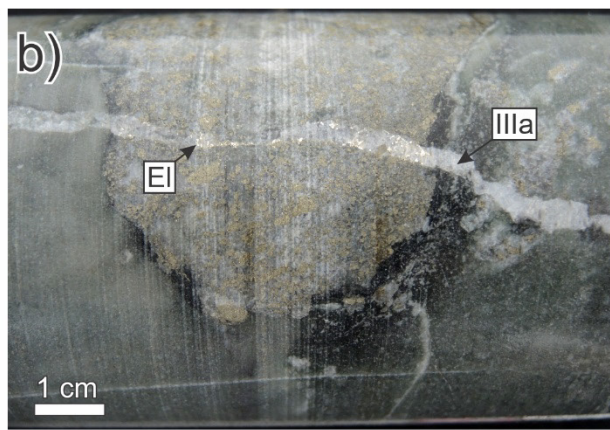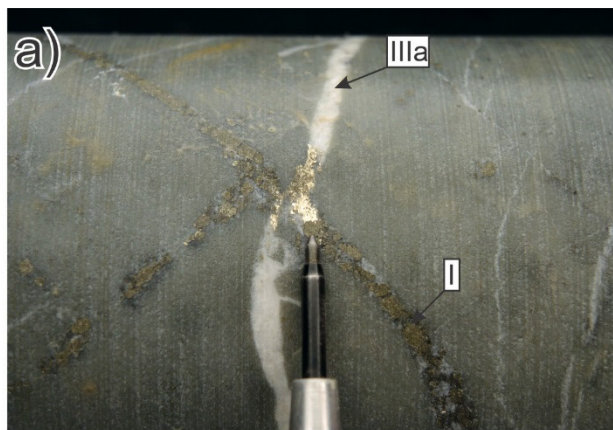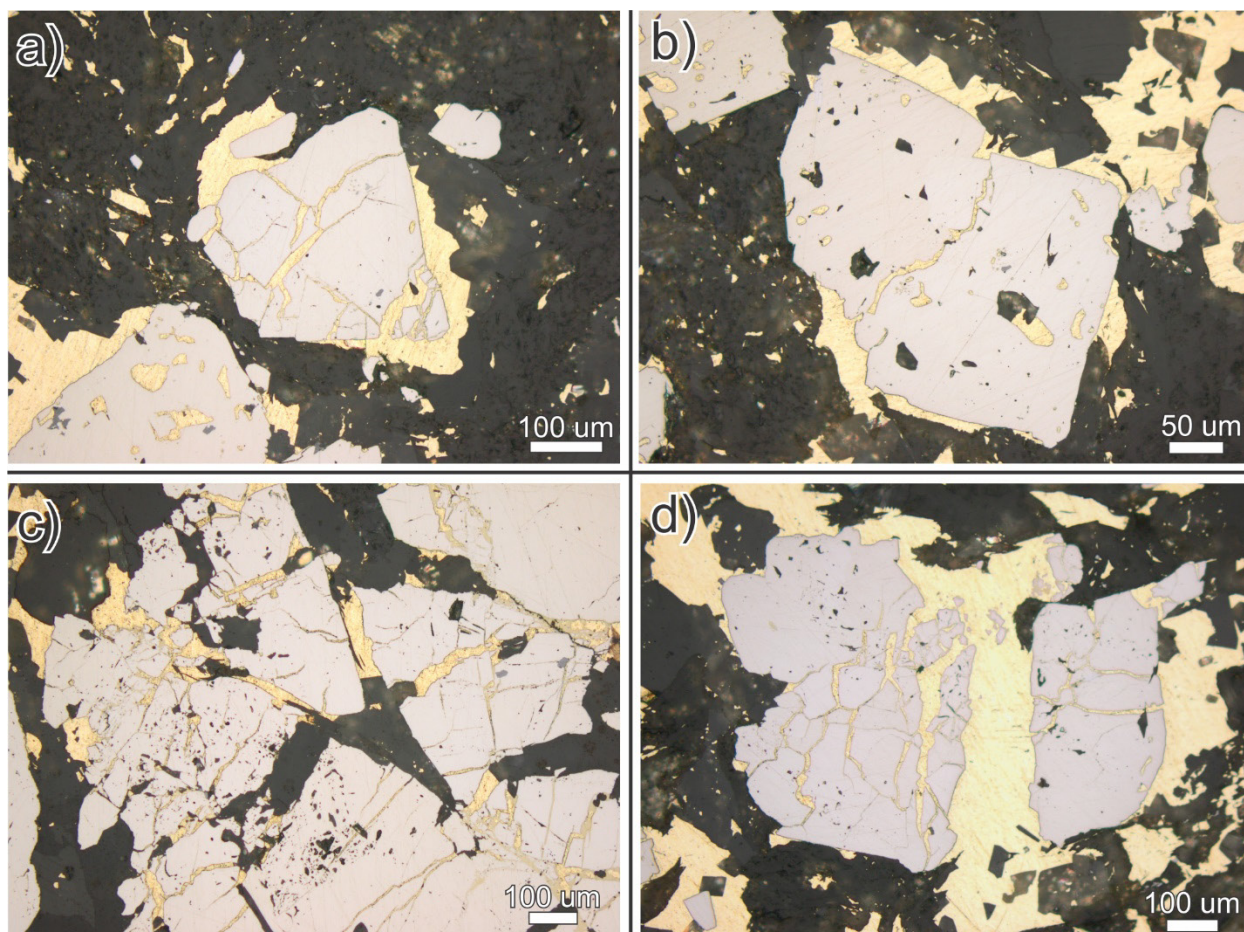
Figure 4.20: Reflected light photomicrographs of electrum filling fractures and nucleating on the surface of pyrite in Stage IIIa (a and b) and IIIb (c and d) veins.

sponge-textured (corroded), anhedral cores that lack compositional contrast; (2) intermediate, oscillatory, locally colloform textured growth rings and layers with variable compositions, and (3) an outer, euhedral, cubic- to pyritohedron-shaped layer that also lacks compositional contrasts (Fig. 4.21). The first two pyrite generations are consistently and clearly cross-cut by electrum-filled fractures, and thus predate electrum mineralisation. The third pyrite generation has a variable timing relationship with respect to electrum; locally, it is cross-cut by electrum (Fig. 4.21c) but, more commonly, the outermost growth zone is in apparent textural equilibrium with electrum (e.g., Fig. 4.21f). This final pyrite generation is also the only growth phase that contains locally abundant, relatively large (> 50 μm) inclusions of electrum (Fig. 4.21c), which are interpreted to coeval with this pyrite generation. In contrast, smaller, < 10-25 μm, electrum inclusions in weakly corroded, oscillatory, variable composition growth bands and sponge-textured cores are interpreted as open-space fillings (Fig. 4.21d). Very rarely, and only in

113
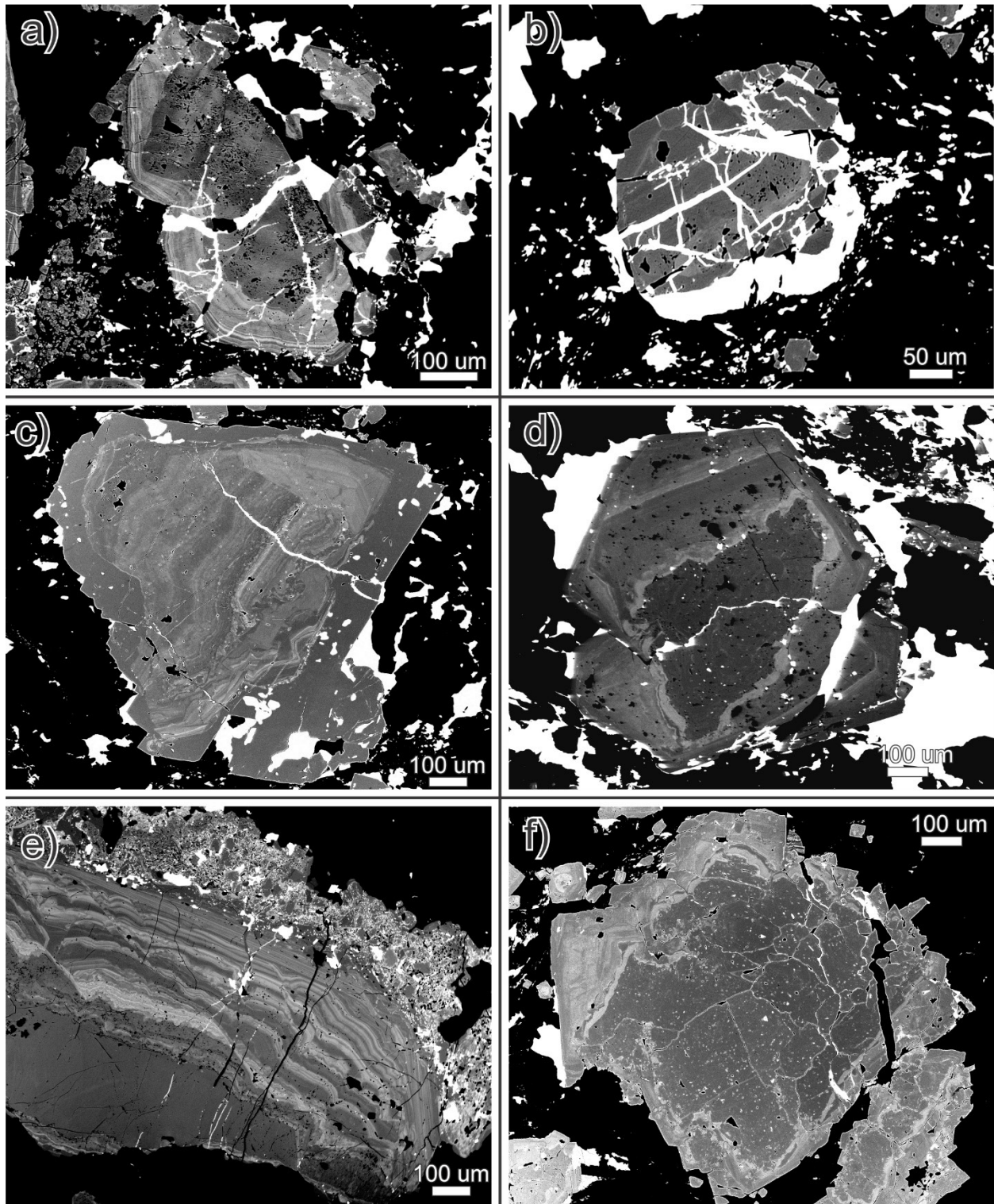
Figure 4.21: Backscattered electron images of pyrite (grey) and electrum (white) from ore-stage veins in the Valley of the Kings zone, showing the complex yet relatively uniform pre-electrum history of pyrite. **(a)** Stage IIIa vein displaying a corroded core of pyrite with well-developed 'sponge' textures, surrounded by oscillatory, colloform textured growth zones of arsenian pyrite; **(b)** Stage IIIb vein with a weakly corroded core of pyrite, surrounded by at least two weakly

114

Figure 4.21 (continued): developed (patchy) growth rings of arsenian pyrite – note that this grain is heavily fractured and invaded by electrum and may be a fragment of an originally larger grain; **(c)** Stage IIIa vein with extensive, oscillatory, arsenian pyrite growth zoning and likely represents a disaggregated fragment of a grain such as shown in (a) – the oscillatory zoning is succeeded by relatively homogenous pyrite; **(d)** Stage V vein with a weakly corroded, anhedral pyrite core that is surrounded by several complete, oscillatory growth rings that become increasingly more euhedral towards the outer margin; **(e)** Stage IV vein with a non-zoned pyrite core surrounded first by a broad area of oscillatory, colloform, zoned arsenian pyrite overgrown by a narrow zone of oscillatory, zoned arsenian pyrite – note the rare syn-electrum pyrite in an outer breccia band; **(f)** Stage V vein with a large, cubic non-arsenian pyrite core displaying weakly corroded margins and surrounded by colloform-textured arsenian oscillatory growth rings – these two generations are cut by electrum along fractures, whereas the outermost non-arsenian euhedral growth bands (left in image) appear to be in textural equilibrium with electrum.

relatively more sulphide-rich Stage IV veins, a fourth pyrite generation occurs as a micro-breccia that hosts electrum at the outermost grain rims (Fig. 4.21e); this electrum is also interpreted to be in textural equilibrium with pyrite.

Backscattered electron imaging of phyllic alteration-related pyrite, whether in Stage I veins or as wallrock-hosted matrix disseminations, shows that they preserve a broadly similar textural history of growth zonation; however, there are some minor variations in grain size and composition (Fig. 4.22). Such similarities further support the interpretation that vein-hosted pyrite was inherited from the wallrocks (McLeish et al., 2018).

4.8.3 EMPA-WDS analyses

In order to quantitatively evaluate major and trace element compositional characteristics associated with the three distinct growth generations, pyrite from Stage I, III and V veins, and phyllic alteration-related wallrock was analysed using EMP-WDS. The Au and As concentrations for core-to-rim transects are shown in Figure 4.23; the other analysed trace elements (Cu, Co, Ni) were below the lower detection limits, except for a few analysis sites that returned weakly anomalous Cu (e.g., 0.21 wt%; see Data Supplement 4.3 for complete results). The oscillatory zones are moderately to strongly enriched in As (~1 to 5 wt.%) and are generally also significantly enriched in Au (100-1920 ppm). Reich et al. (2005) determined the maximum solubility for the solid solution of Au in pyrite and demonstrated that the concentration of Au is directly related to that of As by the linear function $C_{Au} = 0.02 \times C_{As} + 4 \times 10^{-5}$, where C is the
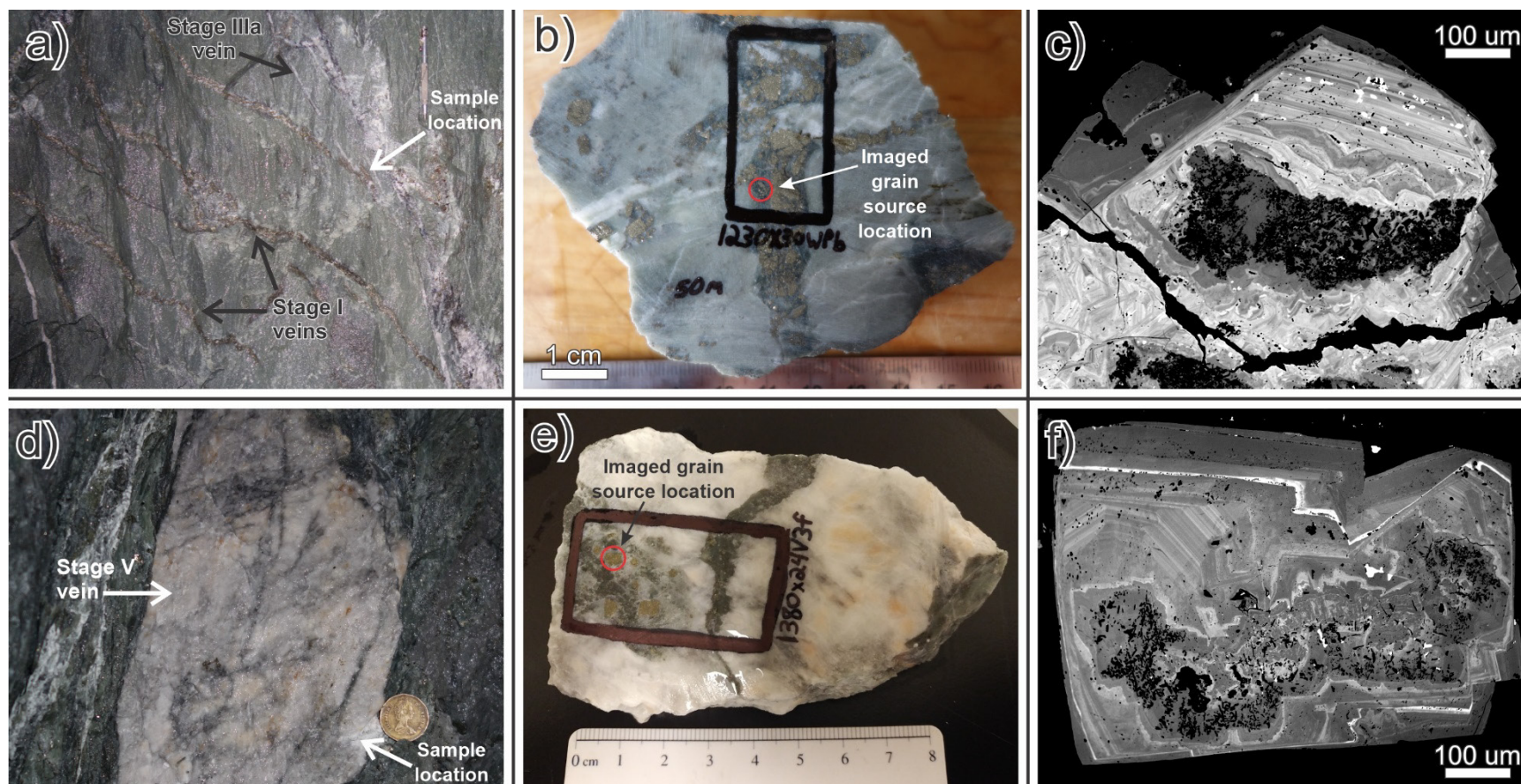
Figure 4.22: Comparison between the growth zonation in pyrite from Stage I veins and that of the wallrock, indicating that they are broadly similar, notwithstanding variations in the size of different growth zones **(a)** Stage I vein showing the pyrite grain imaged in (c); **(b)** location of the imaged pyrite grain in its host Stage I vein; **(c)** BSE image of the Stage I vein pyrite grain in (a); **(d)** wallrock-hosted location for the pyrite grain imaged in (f); **(e)** location of the imaged wallrock-hosted pyrite grain; **(f)** BSE image of the wallrock-hosted pyrite grain in (d).
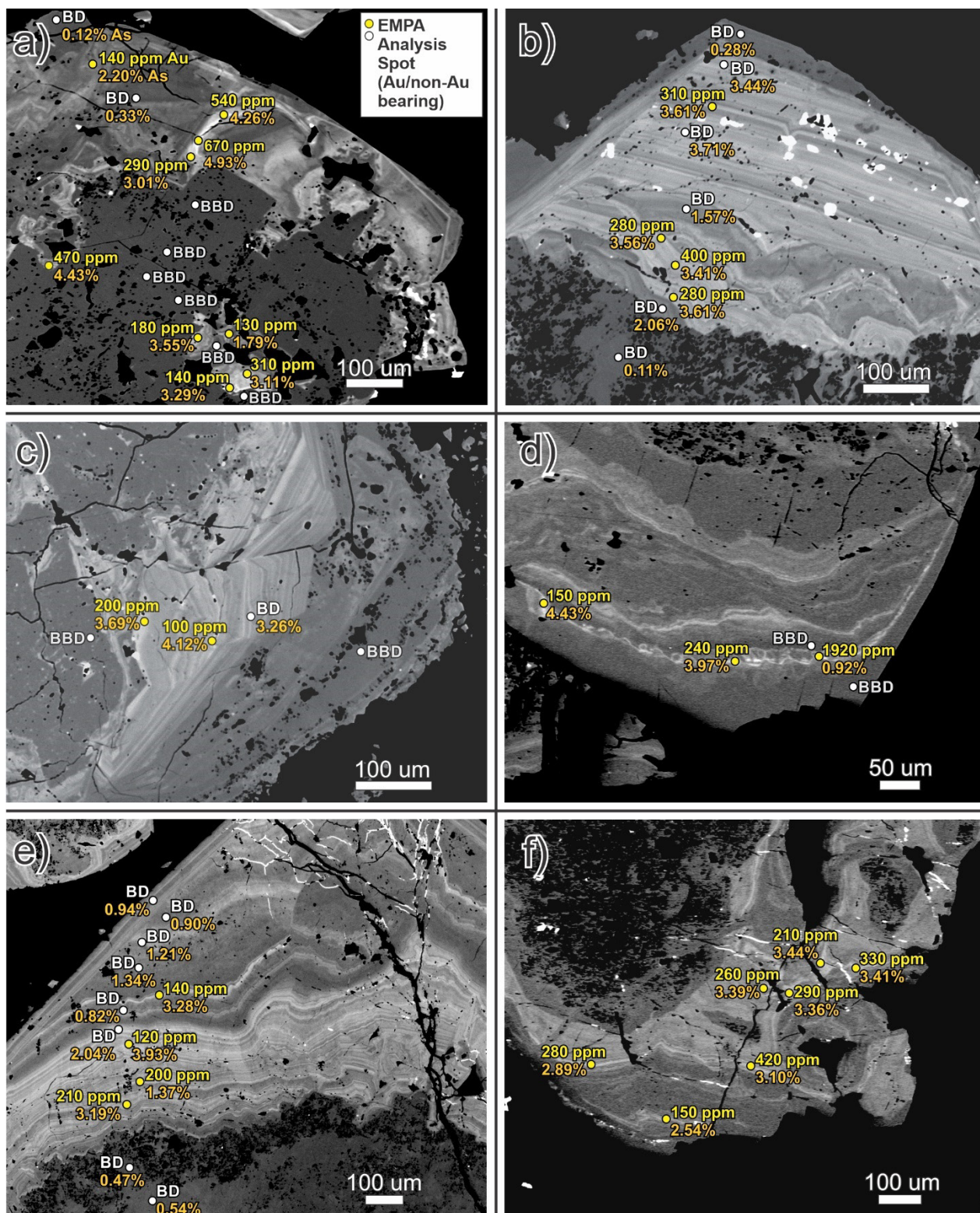
Figure 4.23: Backscattered electron images of pyrite from wallrock and pre-ore and ore-stage veins in the Valley of the Kings and Eastern Promises zones**,** showing EMPA results for Au (yellow) and As (orange). **(a)** matrix-hosted, disseminated pyrite from phyllically altered Eastern Promises zone porphyry; **(b)** Stage I vein-hosted pyrite; **(c)** Stage IV vein-hosted pyrite;

117

Figure 4.23 (continued): (d) Stage V vein-hosted pyrite; **(e)** Stage I vein-hosted pyrite**; (f)** Stage IIIa vein-hosted pyrite. Analyses in yellow yielded Au concentrations above lower detection limit (i.e., ≥ 100 ppm Au) while those in grey were below the lower detection limit ('BD'). Where neither Au nor As were detected, the analysis is labelled 'BBD'.

concentration in moles. The gold is interpreted to occur as submicroscopic (<0.1 μm) inclusions above the limit defined by this function, and below this limit as structurally bound Au atoms in the pyrite lattice (Reich et al., 2005). The Brucejack pyrite displays a broad positive correlation of Au concentration with that of As concentration and, with the exception of a single Stage III pyrite crystal, all the pyrite has compositions that fall below the Au saturation line (Fig. 4.24). This indicates that most of the invisible Au in pyrite at Brucejack is lattice bound and not submicroscopic or nanoparticulate in nature. There are no significant differences between the Au/As ratios of the arsenian pyrite growth bands in wallrock-hosted and those of Stage I-, III-, IV- and V-hosted pyrite. This further supports the hypothesis that pyrite in ore-stage veins was inherited from Stage I veins and/or wallrock.
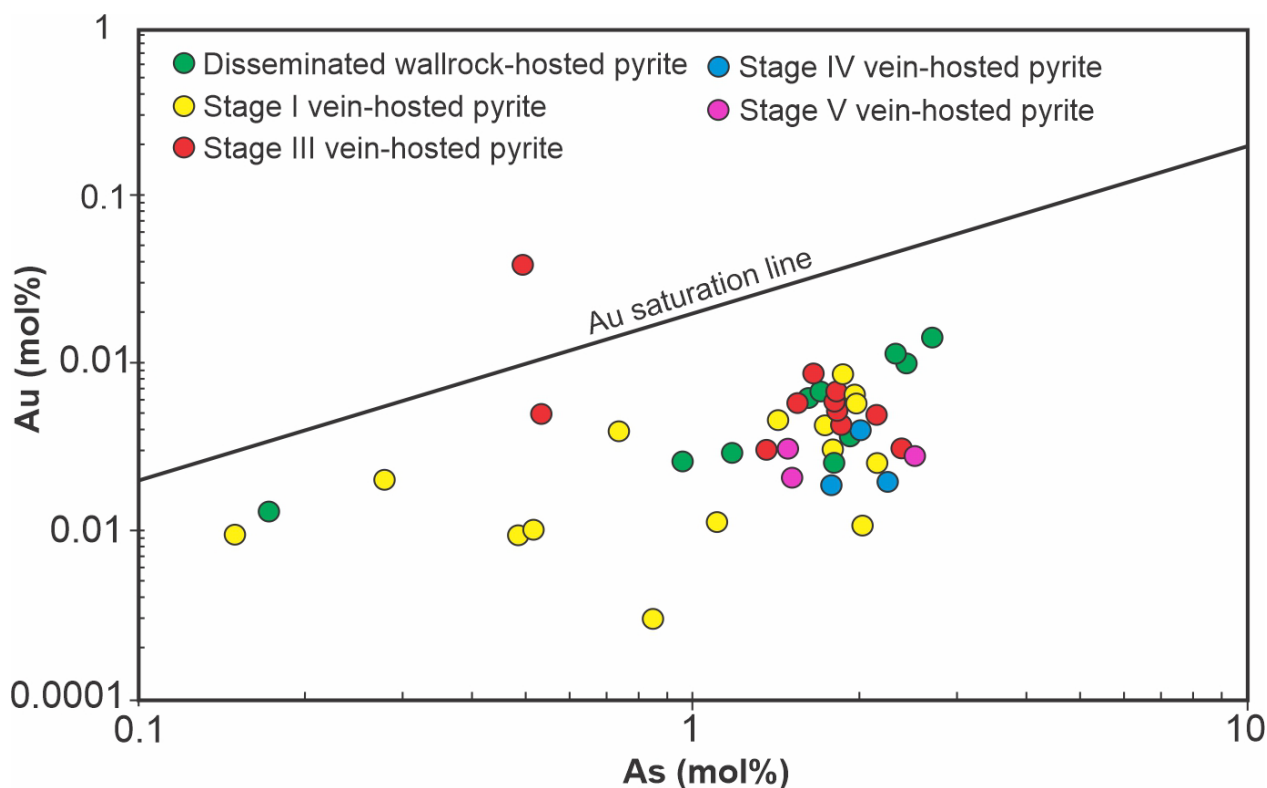
Figure 4.24: Concentration of Au as a function of As concentration in pyrite for crystals shown in Figure 4.23 (recalculated as mol %). The Au saturation limit from Reich et al. (2005) is shown for reference. See text for discussion.

4.8.4 LA-ICP-MS trace element mapping

Maps of Stage I vein pyrite from the Valley of the Kings zone are shown in Figure 4.25 (mapped grains A to G from Section X-X', Fig. 4.16; the section location is shown in Figure 4.3). Although there are variations in the concentration and spatial distribution of ^{59}Co, ^{60}Ni, ^{75}As and ^{197}Au among crystals, a broadly similar zonation, or chemical fingerprint, is characterised by: (1) an inner, cubically- (where less corroded) to irregularly-zoned core with variably high Co and Ni; (2) an intermediate, oscillatory growth zone that is locally colloform and switches rhythmically between comparatively As- and Au-rich bands; and (3) an outer, typically narrow (< 50 μm) rim characterised by euhedral to subhedral growth zones with relatively high Co and Ni concentrations. Some crystals (e.g., D) display thicker, texturally more complex outer zones that include multiple subhedral growth bands with relatively high Co and Ni concentrations. There is clear evidence for pyrite dissolution in the form of locally well-developed resorption (embayed) textures along the contacts between Co- and Ni-rich cores and the innermost oscillatory bands (e.g., C and G).

The pyrite in the mine contrasts texturally with pyrite below the mine. Figures 4.26 and 4.27 show the location and results, respectively, of mapped pyrite samples collected from deep exploration drilling beneath the mine and adjacent Eastern Promises, and Flow Dome zones (drill holes SU-654, VU-820 and VU-911; grains H to M, Section Y-Y'; the section location is shown in Figure 4.3). The pyrite from uppermost part of this deep transect, (Fig. 4.26, H and I) is texturally similar to that mapped in the Valley of the Kings zone, although in some crystals (e.g., Fig. 4.26, H; Flow Dome zone) the intermediate oscillatory growth bands with locally colloform-textured, As- and Au-bearing layers is narrow and has lower As and Au concentrations. At greater depth, As- and Au-bearing oscillatory bands (Fig. 4.26, K and L) are extremely narrow, only partially overgrow the Co- and Ni-rich cores, and have much lower As and Au

Figure 4.25 (next two pages): Laser ablation ICP-MS Co, Ni, As and Au maps for Stage I vein-hosted pyrite from a vertical transect through the Valley of the Kings zone (see Fig. 4.16 for sample locations). BSE images on the left show intracrystalline growth zonation patterns prior to ablation (except for A, which is shown by a post-ablation reflected light image). The column on the right shows the lithology and age of the host rocks from which the pyrite grains were sampled. Lithology colours and mine unit abbreviations are the same as in Figure 4.16.

	VOK Pyrite	^{59}Co Map	^{60}Ni Map	^{75}As Map	^{197}Au Map	Host

A) — LA-ICP-MS Lines — 200 um — 182.6 +/- 1.1 Ma — And-xt

B) — 100 um — 184.3 +/- 1.6 Ma — Andx

C) — 100 um — 187.5 +/- 2.6 Ma — Cong

D) — 100 um

Co (ppm): 0 25 50 75 100
Ni (ppm): 0 25 50 75 100
As (ppm): 0 2000 4000 6000 8000
Au (ppm): 0 10 20 30 40

120

	VOK Pyrite	^{59}Co Map	^{60}Ni Map	^{75}As Map	^{197}Au Map	Host

E) 100 um

F) 100 um

G) 100 um — Map area

187.5 +/- 2.6 Ma — Cong

195.1 +/- 2.8 Ma — Vsf

Co (ppm) 0 25 50 75 100

Ni (ppm) 0 25 50 75 100

As (ppm) 0 2000 4000 6000 8000

Au (ppm) 0 10 20 30 40

Figure 4.26: Long section (Y-Y') through the Valley of the Kings, Eastern Promises, and Flow Dome zones showing the location of pyrite samples mapped by LA-ICP-MS, from deep exploration drill holes (see Figure 4.27 for maps and Figure 4.3 for section location; lithology colours and mine unit abbreviations are the same as in Figure 4.3). Also shown are the sample locations and resulting temperature estimates from sulphur isotope exchange thermometry, as well as the approximate transition from phyllic- to propylitic-dominant wallrock alteration.

Columns (left to right): Deep Exploration Drill Hole Pyrite, ⁵⁹Co Map, ⁶⁰Ni Map, ⁷⁵As Map, ¹⁹⁷Au Map, Host

Rows: H), I), J)

Host: EPP1 — 185.9 +/- 1.2 Ma

Scale bars: 100 um

Color scales:
- Co (ppm): 0 25 50 75 100
- Ni (ppm): 0 25 50 75 100
- As (ppm): 0 2000 4000 6000 8000
- Au (ppm): 0 10 20 30 40

Figure columns (left to right): Deep Exploration Drill Hole Pyrite; ^{59}Co Map; ^{60}Ni Map; ^{75}As Map; ^{197}Au Map; Host

Rows: K), L), M)

Scale bars: 100 um

Color scales:
- Co (ppm): 0, 25, 50, 75, 100
- Ni (ppm): 0, 25, 50, 75, 100
- As (ppm): 0, 2000, 4000, 6000, 8000
- Au (ppm): 0, 10, 20, 30, 40

Host: EPP1, 185.9 +/- 1.2 Ma

124

Figure 4.27 (previous two pages): Laser ablation ICP-MS Co, Ni, As and Au maps for Stage I vein-hosted pyrite from a deep transect beneath the Valley of the Kings, Eastern Promises, and Flow Dome zones (see Fig. 4.26 for sample locations). The BSE images on the left show intracrystalline growth zonation patterns prior to ablation. The column on the right shows the lithology and age of the host rock to the pyrite.

concentrations. The Co- and Ni-bearing cores of all the deeper pyrite (Fig. 4.26, J, K, L and M) are also larger, with more Co- and Ni-rich bands, and lack evidence of dissolution/resorption. Finally, pyrite crystals from the greatest depth (drill holes VU-911 and VU-820, Fig. 4.26, J, ~1300 m below surface, and M, ~1500 m below surface) lack the As- and Au-bearing oscillatory growth bands that characterise all of the shallower pyrite.

4.8.5 SIMS sulphur isotope exchange thermometry

In situ sulphur isotope analyses were conducted on pyrite-barite pairs from three sources: a Stage IIIb vein from the heart of the Valley of the Kings zone, a Stage IV vein from the lower Eastern Promises / Flow Dome Ridge zones, and a quartz-calcite-barite-chalcopyrite vein from deep beneath the Valley of the Kings zone (from drill holes SU-501, SU-657 and VU-2019, respectively; the results shown in Figs. 4.28-4.30, and sample locations in Fig. 4.26). The three samples contain abundant barite in textural equilibrium with pyrite (and, in the case of SU-501, Ag-sulphosalt minerals). The analysed mineral pairs comprise relatively large crystals, except in SU-501 where the pyrite is fine-grained (Fig. 4.28). Electrum is present in the SU-501 and SU-657 vein samples and although it is not in contact with the pyrite-barite pairs, it is hosted by the same carbonate-quartz vein matrix and is interpreted to be coeval with the pyrite-barite pairs. The VU-2019 vein sample, is from a 50 m wide zone of weakly anomalous, deep porphyry-style Au-Cu mineralisation (~30-80 ppb Au, 50-160 ppm Cu) and is associated with pervasive, moderate to locally strong propylitic alteration and sporadic relict potassic alteration of the host Eastern Promises porphyry (Board et al., 2020). Owing to the issue of inheritance of pyrite from the wallrock in ore-stage veins, careful attention was paid to selecting pyrite which, in addition to displaying equilibrium textures indicating synchronous growth with barite (e.g., parallel,

Figure 4.28 (next page): (a and b) Backscattered electron images showing the location of pyrite-barite SIMS analyses used to calculate sulphur isotope exchange temperatures for a Stage IIIb vein from drill hole SU-501 (Valley of the Kings mine workings).
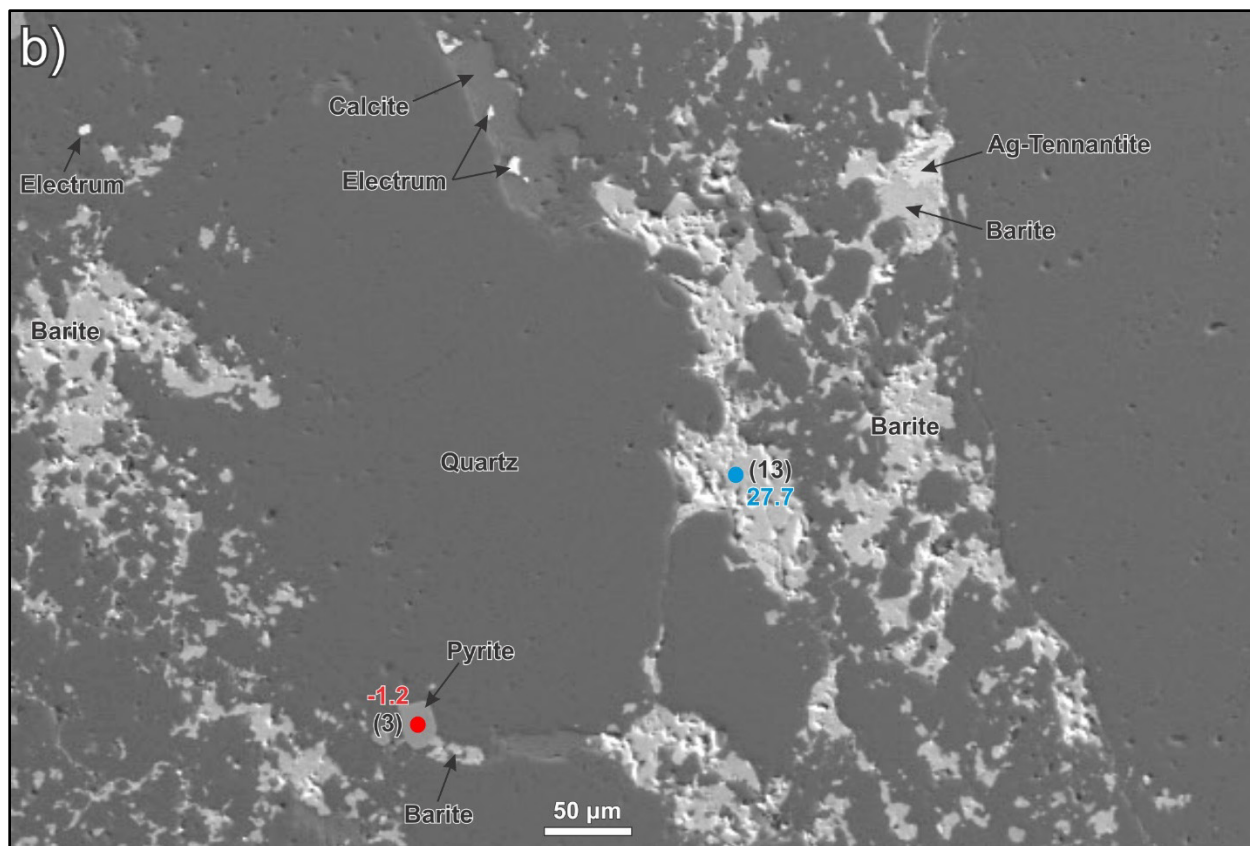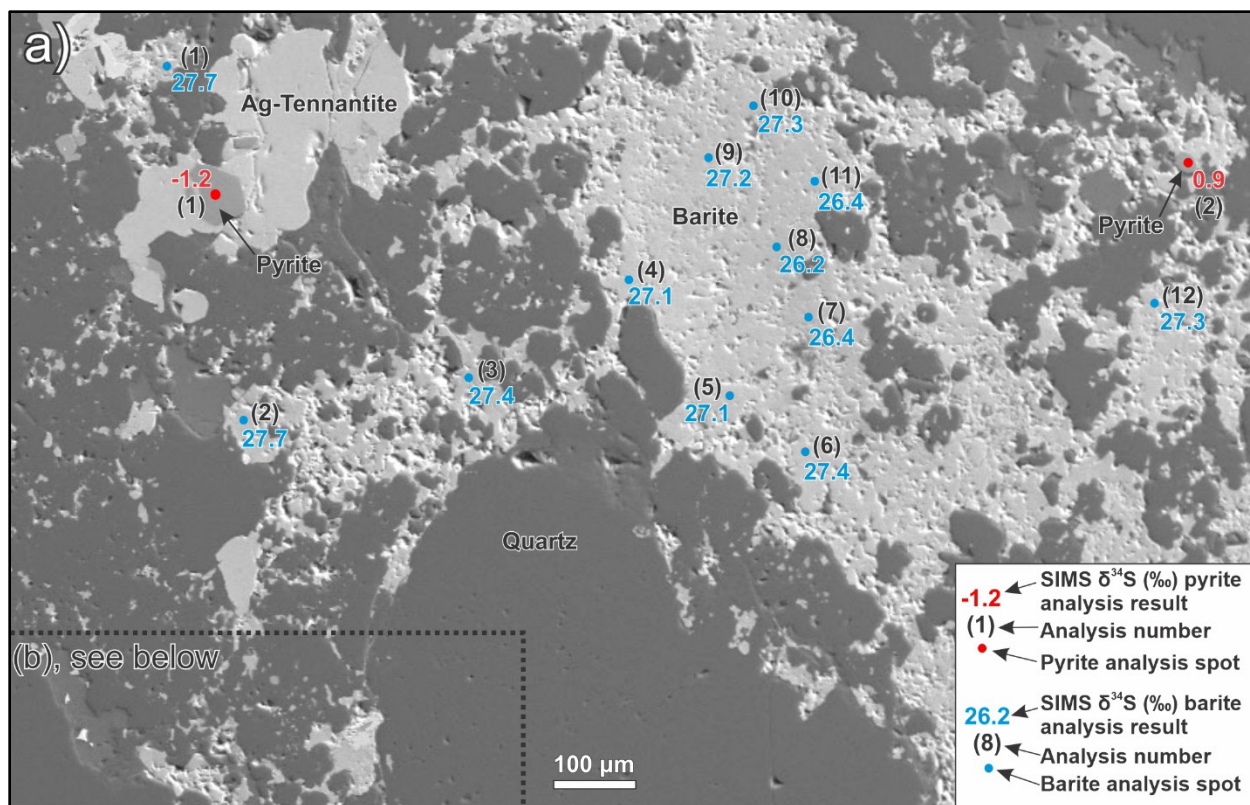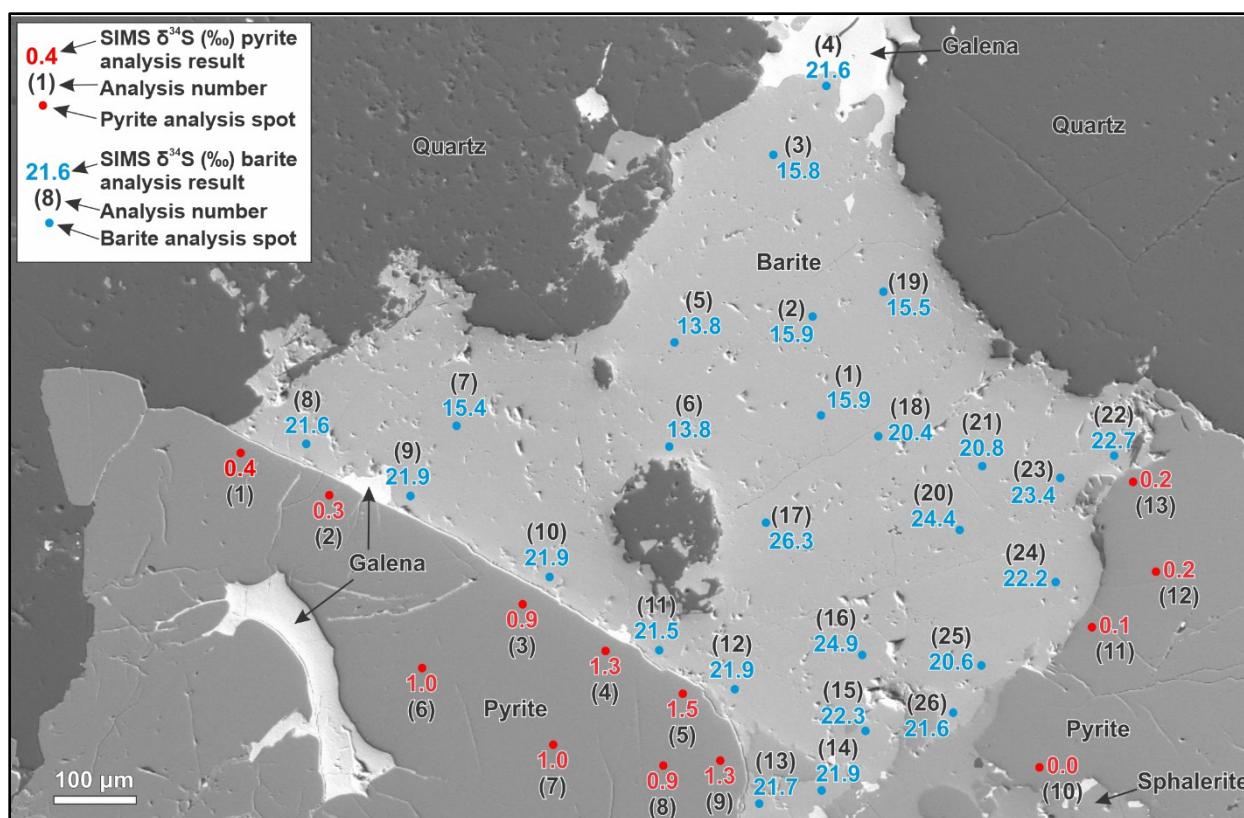
Figure 4.29: Backscattered electron image showing the location of pyrite-barite SIMS analyses used to calculate sulphur isotope exchange temperatures for a deep Stage IV vein from drill hole SU-657 (Eastern Promises/ Flow Dome zones).

euhedral grain boundaries; Fig. 4.29), lacks textures that might indicate a wallrock or Stage I vein origin (e.g., corroded cores and/or oscillatory arsenian growth zoning).

The temperature of the mineralisation (Table 4.2) was estimated using the $\delta^{34}S_{barite}$ and $\delta^{34}S_{pyrite}$ SIMS data and the barite-H_2S and pyrite-H_2S fractionation equations of Ohmoto and Rye (1979). Where pyrite and barite crystals were in direct contact, temperatures were calculated for the individual, spatially associated mineral pairs. An average temperature was calculated for each sample (Table 4.2). In cases where the barite in direct contact with pyrite was not suitable for SIMS analysis due to poor polish (e.g., Fig. 4.30b), proximal barite-pyrite pairs were analysed and the average $\delta^{34}S$ values were used to calculate a temperature. The results indicate that the mineralisation temperature increases with depth, with the SU-501 Valley of the Kings mine sample yielding temperatures approximately 100 and 120 °C cooler than the SU-657 Eastern Promises zone and VU-2019 deep drill hole samples, respectively.
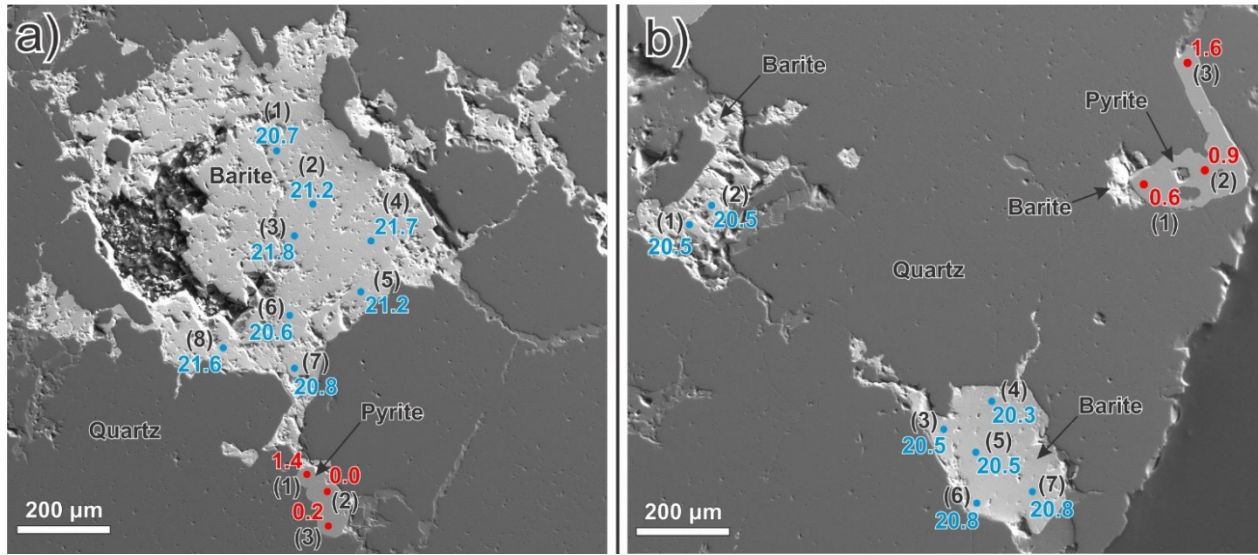
Figure 4.30: (a and b) Backscattered electron images showing the location of pyrite-barite SIMS analyses used to calculate sulphur isotope exchange temperatures for a deep Stage IIIa vein from drill hole VU-2019 (beneath the Valley of the Kings zone).

Table 4.2: Temperature estimates for the Valley of the Kings zone and deep exploration drill hole vein samples using the barite- and pyrite-H2S fractionation equations of Ohmoto and Rye (1979).

	Barite ID in Spot Pair	*Pyrite ID in Spot Pair*	*Barite δ34S (VCDT)*	*Pyrite δ34S (VCDT)*	*Δ Barite-Pyrite δ34S (VCDT)*	*Estimated T crystallisation (°C)*
Sample S501-279a	S501-279a_brt@1	S501-279a_py@1	27.7	-1.2	28.9	188
	S501-279a_brt@12	S501-279a_py@12	27.3	0.9	26.4	215
	S501-279a_brt@5	S501-279a_py@15	27.7	-1.2	28.9	188
					Average T (°C)	**197**
Sample S657-926a	S657-926a_brt@8	S657-926a_py@1	21.6	0.4	21.2	292
	S657-926a_brt@9	S657-926a_py@2	21.9	0.3	21.6	285
	S657-926a_brt@10	S657-926a_py@3	21.9	0.9	21.0	296
	S657-926a_brt@11	S657-926a_py@4	21.5	1.3	20.2	312
	S657-926a_brt@12	S657-926a_py@5	21.9	1.5	20.4	308
	S657-926a_brt@13	S657-926a_py@9	21.7	1.3	20.4	308
	S657-926a_brt@24	S657-926a_py@11	22.2	0.1	22.1	276
	S657-926a_brt@22	S657-926a_py@13	22.7	0.2	22.5	270
					Average T (°C)	**293**
Sample V2019-1202a	V2019-1202a_brt@8	V2019-1202a_py@9	20.8	1.4	19.4	329
	V2019-1202a_brt@1-7	V2019-1202a_py@1-3	20.6	1.0	19.6	325
					Average T (°C)	**327**

4.8.6 U-Pb zircon geochronology – Andesitic Crystal Tuff Mine Unit

The radiometric ages from the Brucejack area includes a previously unpublished U-Pb zircon age of 182.6 ± 1.1 Ma (Pretium Resources Inc. database) for the stratigraphically highest mine series unit, the Andesitic Crystal Tuff. This unit was not included in previous descriptions of the mine stratigraphy (Tombe, 2015; Tombe et al., 2018; Board et al., 2020), which groups this unit with the underlying 184.3 ± 1.7 Ma pyroclastic Andesite. Recent drilling has shown, however, that the top 100 m of the previously defined Andesite consists of a massive, fine-grained crystal tuff which lacks pyroclastic fragments and locally is in sharp contact with the underlying pyroclastic Andesite where it contains well-developed fiamme. This this has led to the recognition of a new mine unit (pers. comm., Pretium Resources Inc., 2022). The Andesitic Crystal Tuff unit sampled for dating is relatively homogeneous and free of pyroclastic and/or lithic fragments, has undergone pervasive phyllic alteration, and is cut by narrow Stage I, IIIa and VI veins. The 182.6 ± 1.1 Ma age (Fig. 4.31) is based on U-Pb isotopic data for nine zircon crystals that cluster
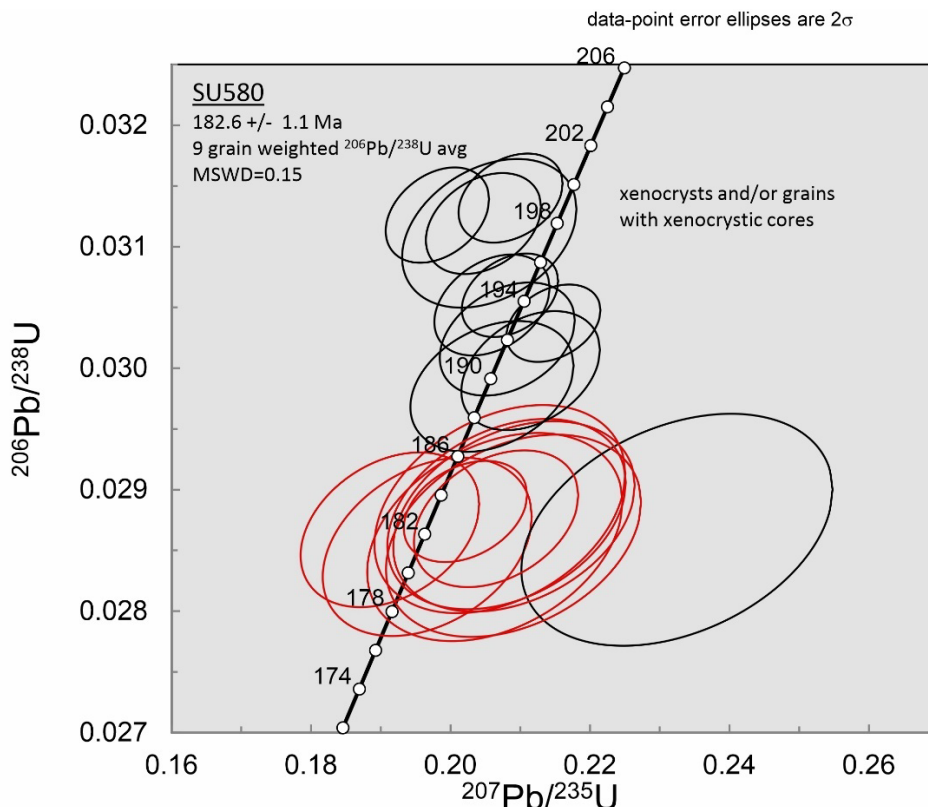
Figure 4.31: Uranium-lead concordia diagram showing age determinations for the Andesitic Crystal Tuff, the stratigraphically highest unit in the mine series to be phyllically altered and locally mineralised with Stage I to V veins. The accepted data (red circles) yield a weighted average ^{206}Pb/^{238}U age of 182.6 ± 1.1 Ma (MSWD = 0.15). Rejected data, interpreted to represent xenocrystic zircons, are shown as black circles.

tightly along concordia (MSWD = 0.15), and are interpreted to represent the crystallisation age of the unit (Fig. 4.31). The remaining ten zircons from the sample yielded older ages that scatter over a range of 183-199 Ma, and are interpreted to be xenocrysts and/or grains with xenocrystic cores.

4.9 Discussion

The spatially discrete, ultra-high-grade gold in epithermal veins at the Brucejack mine are the main source of production and focus of near-mine exploration. In addition to the bonanza concentrations of gold, these veins host gold in the form of coarse (cm- to dm-scale) clots of electrum in a calcite-quartz matrix that is devoid of sulphide minerals which, in other deposits, often complicate gold ore processing and beneficiation (e.g., Vaughan, 2004). The challenges that sulphide minerals pose to gold recoveries in hydrothermal deposits, mainly with respect to refractory gold, are thus a concern in geometallurgical studies, and have been a focus of attention in a wide array of deposits, including epithermal, VMS, porphyry and orogenic types (e.g., Cline, 2001; Arif and Baker, 2004; Petrie et al., 2005; Richards et al., 2006; Asadi et al., 2014; Vikentyev, 2015; Kianinia et al., 2017). In contrast, the coarse nature of gold mineralisation at Brucejack, combined with the simple carbonate-quartz vein mineralogy of its ore-stage veins, are the principal reasons why the mine regularly achieves recoveries of > 95 % by gravity and flotation processing methods (Tetra Tech, 2020).

4.9.1 Implications for the application of classical epithermal ore-forming models at Brucejack

Although the simple mineralogy of most ore-stage veins explains the free-milling, non-refractory, and high-value nature of the gold mineralisation at Brucejack, it also poses a challenge for the accepted solution models that attempt to explain gold transport and deposition. Firstly, given the a priori assumption that vein mineralogy reflects the composition of the hydrothermal fluid, the scarcity of primary sulphide minerals in most of the ultra-high-grade veins at Brucejack, Stage V veins especially, indicates that the fluids forming most of these veins likely had a low S concentration and, by extension, low aHS$^-$ (Stage IV sulphide- and sulphosalt-bearing veins being the exception). Considering that gold is transported in solution as a bisulphide complex under low- to intermediate-sulfidation epithermal conditions (Henley et al., 1984; Williams-Jones et al., 2009), the lack sulphide minerals in textural equilibrium with

130

electrum at Brucejack creates a problem for explaining the hyper-enriched occurrences of gold in the deposit. Secondly, the observations that: (1) the intensity of hydrothermal alteration in the Valley of the Kings zone, particularly the intense phyllic alteration and localised but pervasive silicification (i.e., Sil unit), correlates with the abundance of pre-electrum Stage I veins and (2) electrum-bearing Stage III-V veins cross-cut such alteration, are also difficult to reconcile with typical gold-bisulphide transport models. Most of these models predict that gold deposition occurs chiefly as a result of boiling (e.g., White and Hedenquist, 1990), which fractionates H_2S into the vapour phase and lowers aHS$^-$ in the fluid. Moreover, it has long been known that boiling in epithermal environments is associated with widespread alteration, the dominant minerals (e.g., smectite and. illite) being related to the depth of first boiling (e.g., Buchanan, 1981). Considering that most of the alteration in the Valley of the Kings zone predated the emplacement of the Stage III-V veins, and that Stage III-V veins lack significant alteration haloes, there is no evidence to suggest that boiling caused gold deposition in the bonanza-grade veins. Indeed, the only evidence for boiling in bonanza-grade veins at Brucejack exists in two features that predate the formation of bonanza electrum. The first is the colloform-textured intermediate growth zones of vein-hosted pyrite which, although locally well-developed and associated with boiling-driven negative δ^{34}S shifts (Chapter 3), were clearly inherited from Stage I veins and associated phyllically altered wallrock. Thus, they predate the emplacement of the bonanza-grade veins, as further evidenced by the widespread cross-cutting of these intermediate growth zones by electrum in vein-hosted pyrite (e.g., Fig. 4.21). The second feature is that the high density, liquid-rich aqueous and co-existing low-density vapor-rich fluid inclusions in Stage III and V veins indicative of boiling (Tombe et al., 2018), are hosted in quartz that is not textural equilibrium with and predates the calcite that hosts electrum in these veins (K. Ng, pers. comm., 2022). Taken together, these observations raise a key question regarding the genesis of ultra-high-grade gold: if Gold was not transported by bisulphide complexes and its deposition was not driven by boiling, what process(es) controlled bonanza ore formation at Brucejack?

4.9.2 The electrochemical flocculation of colloidal gold by pyrite

A growing body of evidence suggests that bonanza-style hydrothermal gold deposits are formed by the physical transport of gold as a colloid (i.e., a suspension of $\leq$ 10 nm solid nanoparticles with negatively charged surfaces in an electrolyte solution) rather than by aqueous complexation (Petrovskaya, 1973; Kvasnifsa et al., 1981; Saunders, 1990; Herrington and Wilkinson, 1993;

Saunders and Schoenly, 1995; Hannington et al., 2016; Burke et al., 2017; Saunders and Burke, 2017; Gartman et al., 2018; Hannington and Garbe-Schönberg, 2019; Prokofiev et al., 2020;; Petrella et al.. 2020; McLeish et al., 2021). While there generally is consensus in these studies that colloidal suspensions can explain how gold may be mobilised within hydrothermal systems at concentrations many orders of magnitude greater than those predicted by solubility models, there is little consensus regarding the processes by which colloidal gold suspensions aggregate (i.e., flocculate) to produce ultra-high-grade gold deposits. In addition to being required for the original production of colloidal gold, boiling is the most commonly proposed mechanism to induce flocculation through because it acts in multiple, reinforcing ways to promote flocculation through increasing the collision efficiency of nanoparticles and precipitating minerals containing cationic flocculants such as Al^{3+} and Fe^{3+} (Saunders and Burke, 2017 and refs. therein). However, given some deposits such as Brucejack do not show evidence for boiling being synchronous with bonanza gold deposition, other colloidal processes must also be involved in controlling bonanza gold mineralisation events in hydrothermal systems.

The intimate spatial relationship between later electrum and earlier pyrite (Fig. 4.19) offers insight into a mechanism for the formation of ultra-high-grade gold at Brucejack. The ability of pyrite to electrochemically attract and, through absorption and/or reduction, precipitate Gold on crystal surfaces has been widely documented in laboratory experiments (Sakharova et al., 1975; Hyland and Bancroft, 1989; Mycroft et al., 1995; Maddox et al., 1998; Widler and Seward, 2002; Mikhlin and Romanchenko, 2007). This electrochemical attraction is due to the semiconductive properties of pyrite (Skey, 1871), which can be classified by its n-type (electron donor) or p-type (electron acceptor) characteristics (Shuey, 1975). These characteristics are controlled by impurities in the sulphide structure and, in the case of pyrite, p-type behaviour is caused by the addition of acceptor cations such as As (Pridmore and Shuey, 1976).

Several studies have invoked electrochemical precipitation to explain the close association of native gold with pyrite (Starling et al., 1989; Möller and Kersten, 1994; Gaboury and Sanchez, 2019) and others have used it to explain the occurrence of "invisible" gold in pyrite (e.g., Fleet and Mumin, 1997; den Besten, 1999; Palenik et al., 2004; Reich et al., 2005; Fougerouse et al., 2016). In both cases, the precipitation is interpreted to occur because the pyrite is a p-type semiconductor due to the presence of As, and assumption is made that the gold is transported as either bisulphide or chloride complexes, with deposition occurring via physical

adsorption and/or reduction. However, as has been previously demonstrated, gold was transported at Brucejack as a colloid (McLeish et al., 2021; Chapter 2), which offers an alternate mechanism by which gold may accumulate electrochemically on pyrite surfaces without the direct involvement of a ligand such as HS⁻.

In Figure 4.32, we illustrate a model in which colloidal suspensions of elemental gold in a hydrothermal fluid are attracted to p-type arsenian pyrite surfaces, wherein positive surface charges overcome the negative surface charges of gold nanoparticles, and through cationic coagulation, or 'bridging', cause flocculation of the colloid. According to this model, the flocculated gold is deposited on p-type arsenian pyrite surfaces, thereby explaining the observation that the electrum at Brucejack is commonly concentrated along grain margins or intra-grain fracture networks (Figs. 4.20 and 4.21). Owing to the high conductivity of gold, and the even higher conductivity of Ag (Serway and Jewett, 1998), the p-type electronic characteristics of the pyrite surface that initially induced, or triggered, nucleation (flocculation) of electrum would be transmitted to the gold-fluid interface during deposition of the gold (Jean and Bancroft, 1985; Starling et al., 1989), thereby inducing further flocculation of the gold colloid and ultimately gold (electrum) crystal growth beyond the original pyrite surface. This electrochemical flocculation model for bonanza gold deposition explains why, at Brucejack, many spectacular gold occurrences appear to have been triggered by the intersection of ore-stage veins with pyrite-rich Stage I veins (Fig. 4.19). Given that Stage I veins with intermediate arsenian growth zones have been documented throughout the mine and for ~650 m beneath it (or 1200-1300 m below the top of the Valley of the Kings zone; Figs. 4.25-4.27), the electrochemical flocculation of colloidal gold suspensions by p-type pyrite can also explain the extraordinary vertical extent of the bonanza gold occurrences. It also explains why the lower limit of visible gold occurrences appears to coincide with the loss of well-developed oscillatory zoned arsenian pyrite in Stage I veins with depth (Figs. 4.26 and 4.27).

Figure 4.32 (next page): Schematic model for the formation of bonanza gold deposits through the electrochemical flocculation of colloidal suspensions, shown with macro- and micro-scale images portraying the textural relationship between later gold and earlier Stage I pyrite at Brucejack**. (a)** Drill core photograph demonstrating the macro-scale flocculation 'trigger' relationship between an older pyrite vein and bonanza-grade electrum mineralisation in a younger epithermal quartz-carbonate vein; **(b)** BSE image showing the 'trigger' relationship at a micron scale; **(c)** schematic model portraying the electrochemically-driven accumulation of negatively charged electrum (gold) nanoparticles on the surfaces of p-type arsenian pyrite.

a) Electrum continues to electro-chemically flocculate due to conduction of p-type surface charge to the electrum-fluid interface

Initial flocculation site

b) 100 um

c)

p P-type (As) pyrite	Au deposit
n N-type (non-As) pyrite	e⁻ → Electron flow direction
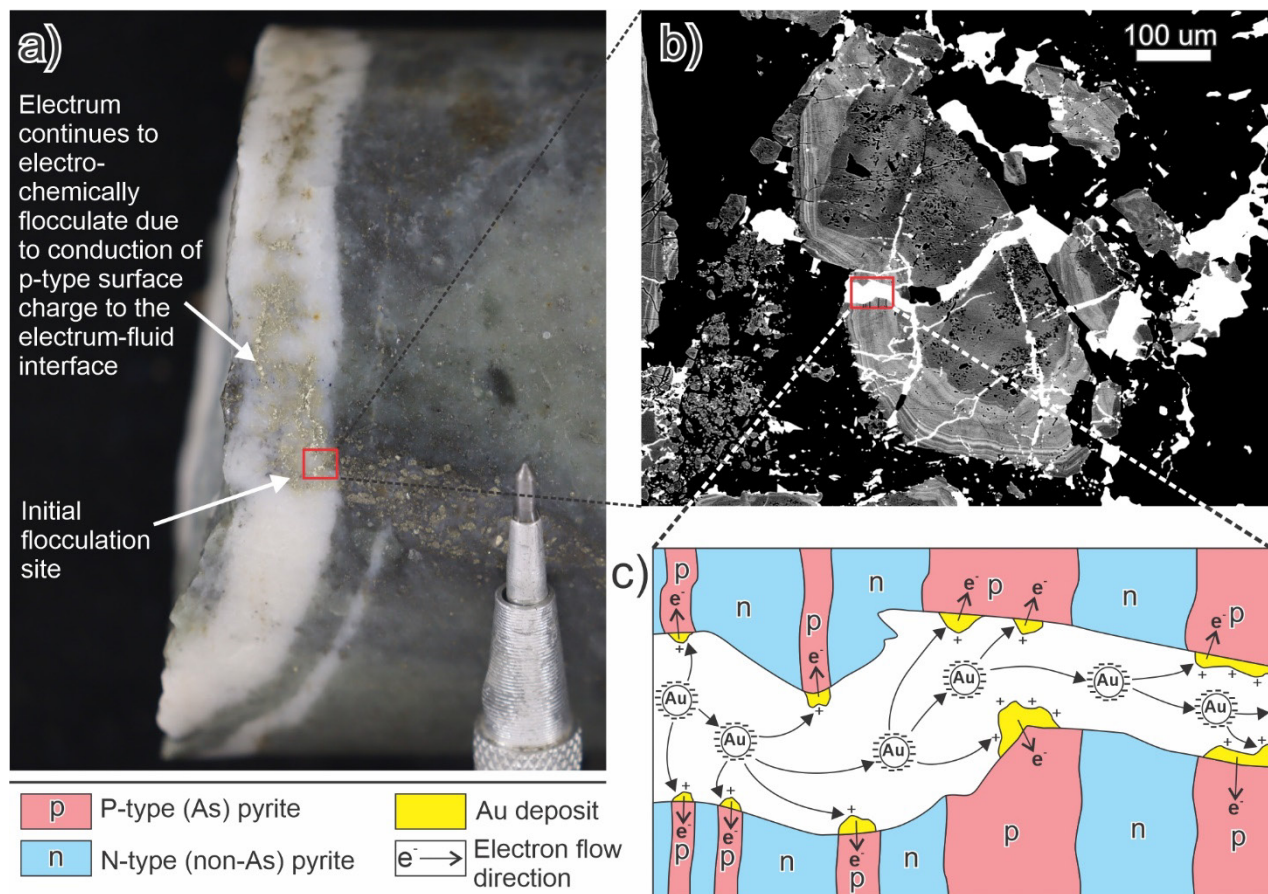
4.9.3 Evolution, age, and source of the Brucejack hydrothermal system

The consistency of the intragrain trace element zonation patterns in Stage I pyrite in the Valley of the Kings zone suggests that these veins share a common history that involved both porphyry and epithermal fluid characteristics. Such pyrite can be classified as "composite" porphyry-epithermal stage pyrite (Sykora et al., 2018; Fig. 4.17) based on the cubic (where not heavily corroded), zoned, Co- and Ni-bearing cores and the surrounding oscillatory zoned, locally colloform mantles that are relatively rich in As and Au. Following the interpretations of Sykora et al. (2018) for Lihir, this zonation suggests that the Brucejack system experienced significant telescoping during its lifetime. In the Valley of the Kings zone, this telescoping was sufficiently profound to create composite zoned pyrite over a vertical distance of at least 1000 m, and up to ~1300 m if the weak As and Au overgrowths in pyrite from deep drill holes (Fig. 4.26) are considered. The deepest pyrite that has been evaluated (Fig. 4.26, J to M, ~1300 to 1500 m below surface) generally lacks oscillatory As-Au zonation and therefore defines a lower limit of

telescoping below the paleo-surface. This limit coincides with the phyllic to propylitic transition, consistent with models that portray the deepest extent of phyllic (sericitic) alteration as the lower limit of telescoping in porphyry-epithermal systems (e.g., Sillitoe, 2010). Intriguingly, all pyrite mapped along the vertical transect (i.e., A to M) are nevertheless characterised by thin (< 50 um), generally weak, but omnipresent, outer growth zones containing Co and Ni. We interpret this to indicate that, following telescoping, a final pulse of porphyry fluids circulated through the veins prior to the cessation of Stage I hydrothermal activity.

Sulphur isotope exchange thermometry temperatures estimated for pyrite-barite pairs in Stage III and IV veins, as well as porphyry-style quartz-calcite-barite-chalcopyrite veins found beneath the VOK, broadly support the transitional porphyry-epithermal deposit architecture described above. In particular, the temperature estimated for the deep porphyry-style veins hosted in propylitic and relict potassic alteration zones beneath the VOK (T = 327 °C) is consistent with them having formed under low- to moderate-temperature porphyry conditions (Meyer and Hemley, 1967; Sillitoe, 2010), whereas the temperature estimated for Stage III veins in the heart of the VOK (T = 197 °C) is characteristic of moderate-temperature epithermal conditions (White and Hedenquist, 1990). The temperature estimated for Stage IV veins in the lower Eastern Promises / Flow Dome Ridge zones (T = 293 °C) suggests that these veins may have formed under transitional porphyry-epithermal conditions which, given their relatively unique base metal sulphide + sulphosalt mineral assemblage, conform to the carbonate-base metal gold class of porphyry-related epithermal systems (Corbett and Leach, 1998).

Pyrite zonation patterns together with U-Pb zircon ages for the syn- to late-mineralisation trachybasaltic dykes, the mine series stratigraphy, and the Eastern Promises porphyry intrusion, indicate that there are important age constraints on, and genetic consequences for, bonanza-grade gold mineralisation. The 182.6 ± 1.1 Ma age reported here for the Andesitic Crystal Tuff, the youngest mine unit, is nearly identical to the 182.7 ± 1.0 Ma age for the trachybasaltic dykes interpreted by Board et al. (2020) as representing a minimum age for mineralisation. The Andesitic Crystal Tuff is characterised by the same intense phyllic alteration and hosts the same Stage I to VI paragenetic sequence of veining as the older, underlying units. Moreover, pyrite zonation in Stage I veins in the Andesitic Crystal Tuff is essentially identical to that of the underlying units. These similarities imply that: (1) the entire sequence of porphyry to epithermal

135

alteration events recorded by Stage I pyrite, as well as the later emplacement of bonanza-grade Stage III to V veins, must have occurred relatively quickly, possibly in a few 100 kyr or less; and (2) all known porphyry intrusions previously proposed as sources for the early, mesothermal (Board et al., 2020) or porphyry "D" type (Sillitoe, 2015) Stage I veins and the bonanza-grade epithermal Stage III-V veins (including the 196-190 Ma Kerr-Sulphurets-Mitchell-Iron Cap porphyries, Board and McNaughton, 2013; and the 185 Ma Eastern Promises P1 porphyry, Board et al., 2020), are too old for their magmas to have been the source of the fluids. Consequently, the source of the hydrothermal fluid(s) responsible for the Brucejack gold mineralisation has yet to be discovered.

4.9.4 Implications for bonanza ore formation in other porphyry-epithermal deposits

The formation of bonanza gold concentrations in porphyry-epithermal systems has been generally attributed to abrupt changes in physicochemical conditions that disrupt solution equilibria and cause extreme supersaturation and rapid gold deposition (Williams-Jones et al., 2009). Such changes are thought to result from three main processes, namely boiling (phase separation), fluid mixing, and/or wallrock sulphidation (Simmons et al., 2020). A major implication of our Brucejack study is that, although steep physicochemical gradients are required to produce colloidal gold in hydrothermal systems, they are not required for the deposition (flocculation) of bonanza gold. Indeed, the conspicuous lack of syn-mineral wallrock alteration (e.g., clay, white mica) and sulphide minerals in ore-related veins at Brucejack indicate that sudden changes in physiochemical conditions did not accompany bonanza gold deposition. Furthermore, the electrochemical flocculation of colloidal gold suspensions by pre-existing p-type sulphide minerals, which can occur independently of physicochemical gradients (i.e., under equilibrium conditions), also explains the enigmas of why: (1) even in bonanza deposits that display abundant evidence for sulphidation (either as sulphide alteration of wallrock or the precipitation of sulphide minerals in ore veins), gold often appears to have formed paragenetically later than the sulphide minerals, and (2) there is also little correlation between gold abundance (grade) and the abundance of sulphide minerals (Romberger, 1992).

Although a few other studies have proposed electrochemical mechanisms for gold deposition in hydrothermal systems that contain significant post-sulphide Au, such as those in the Poderosa-Pataz District, Peru (e.g., Gaboury and Sanchez, 2019), they have all proposed such

mechanisms for the precipitation of gold from solutions in which it is complexed with HS⁻.
Electrochemical destabilisation of Au-bisulphide complexes might explain bonanza gold deposition in these deposits in the absence of boiling, but it does not explain the observed lack of co-precipitated sulphide minerals in such deposits, including Brucejack. This is because the required very high concentration of Au(HS) and/or Au(HS)$_2^-$ in the ore fluid would inevitably lead to at least some sulphide deposition during electrochemically-induced destabilisation of these complexes (i.e., gold precipitation). In contrast, because colloidal transport and electrochemical flocculation of gold can occur independently of bisulphide complexation and/or fluid boiling, our model provides a novel explanation for the paradox of bonanza gold deposition in the absence of both boiling and sulphide precipitation.

Lastly, although it is not known to what extent other metals, beyond gold and silver, might be transported in the colloidal state, there is, in principle, no reason to believe that the p-type pyrite-driven electrochemical flocculation model presented here is limited to triggering the formation of these precious metals. Indeed, while not as common as the widespread occurrences of bonanza-grade electrum mineralisation deposited around Stage I pyrite veins at Brucejack, the recent observation in drill core that bonanza concentrations of sphalerite (Fig. 4.33) can form where Stage IV veins crosscut Stage I veins suggests that similar electrochemical flocculation processes can trigger the deposition of an array of metals in ore-forming hydrothermal systems.

Figure 4.33: Drill core photograph showing bonanza-style accumulations of sphalerite deposited along the surfaces of Stage I vein pyrite crystals where they are crosscut by a Stage IV vein.

4.10 Conclusions

The pyrite chemistry and macro- and micro-scale pyrite-electrum textural relationships at Brucejack provide important insights into how this world-class epithermal gold deposit formed. This includes, including not only the trigger to the deposition of the ultra-high-grade gold mineralisation, but also how the Brucejack hydrothermal system evolved in time and space prior to the onset of bonanza mineralisation. The Co-Ni rich cores of pyrite in Stage I veins record the passage of early mesothermal (porphyry) type fluids which, as evidenced by extensive, intermediate oscillatory, locally colloform pyrite growth zones, evolved to epithermal-type fluids during telescoping of the hydrothermal system. This generated pervasive phyllic alteration, intense local silicification, and the silicification-related Stage II barren quartz veins. Later, but still during the development of Stage I veins, porphyry-style conditions returned to the system as indicated by narrow but locally well-developed outer (grain rim) Co-Ni growth zones in Stage I pyrite. All of this hydrothermal activity predated the emplacement of the bonanza-grade epithermal Stage III-V veins, which cross-cut Stage I-II veins throughout the deposit. The time between the emplacement of pre-bonanza and syn-bonanza vein stages, however, was brief, as shown by the 182.7 ± 1.0 Ma age of syn- to late-mineral trachybasaltic dykes and the 182.6 ± 1.1 Ma post-mineral Andesitic Crystal Tuff. Thus, the entire system, including early pulses of porphyry and pre-bonanza epithermal fluids, had a lifespan of less than a few 100 kyr. This finding has important implications for understanding the evolution of, and exploring in, the Sulphurets camp and Stewart-Eskay District. Whereas previously, the 198-188 Ma Texas Creek plutonic suite was believed to be responsible for all major ore-forming porphyry-epithermal activity along the Treaty-Stewart trend, the large and high-grade gold resource at Brucejack is clearly associated with a significantly (> 5 my) younger porphyry-epithermal system.

Beyond understanding the controls on mineralisation in a deposit-specific context, our findings from Brucejack offer a new model for the formation of bonanza gold veins through the electrochemical flocculation of colloidal gold suspensions. This model builds on previous works which recognised the importance of colloidal gold in forming bonanza gold deposits by proposing a new mechanism for gold colloid flocculation, namely, the mass-scale aggregation of gold nanoparticles and deposition of bonanza gold in hydrothermal ore veins through cationic coagulation, or 'bridging' on pre-existing p-type pyrite. This mechanism offers a novel

explanation for why, in many deposits, bonanza gold forms paragenetically late, either after, or without, sulphide minerals. Moreover, given that it does not require unusual physicochemical conditions and/or (dis)equilibrium conditions, this mechanism may explain bonanza occurrences of gold, and possibly a wealth of other metals, in a large variety of deposit types.

Acknowledgements

References

Alldrick, D.J., 1993, Geology and Metallogeny of the Stewart Mining Camp, Northwestern British Columbia (104B, 103O). British Columbia Ministry of Energy, Mines and Petroleum Resources, British Columbia Geological Survey Bulletin 85, 105 p.

Anderson, R.G., 1989, A stratigraphic, plutonic, and structural framework for the Iskut River map area, northwestern British Columbia, in Current research, part E. Geological Survey of Canada Paper 89-1E, p. 145-154.

Anderson, W.B. and Eaton, P.C., 1990, Gold mineralisation at the Emperor mine, Vatukoula, Fiji. Journal of Geochemical Exploration, v. 36, p. 267-296.

Arif, J., and Baker, T., 2004, Gold paragenesis and chemistry at Batu Hijau, Indonesia: Implications for gold-rich porphyry copper deposits. Mineralium Deposita, v. 39, p. 523−535.

Asadi, H. H., Kianpouryan, S., Lu, Y., and McCuaig, T. C., 2014, Exploratory data analysis and C-A fractal model applied in mapping multi-element soil anomalies for drilling: A case study from Sari-Gunay epithermal gold deposit, NW Iran; Journal of Geochemical Exploration, v. 145, p. 233–245.

Barnes, S.J., Prichard, H.M., Cox, R.A., Fisher, P.C. and Godel, B., 2008, The location of the chalcophile and siderophile elements in platinum-group element ore deposits (a textural,

microbeam and whole rock geochemical study): Implications for the formation of the deposits. Chemical Geology, v. 248, p. 295-317.

Basov, V., 2021, Top 10 largest gold mines in Canada in 2020. Available: https://www.kitco.com/news/2021-03-12/Top-10-largest-gold-mines-in-Canada-in-2020-report.html

den Besten, J., Jamieson, D.N. and Ryan, C.G., 1999, Lattice location of gold in natural pyrite crystals. Nuclear Instruments and Methods in Physics Research Section B: Beam Interactions with Materials and Atoms, v. 152, p. 135-144.

Board, W.B., and Greig, C.J., 2013, Preliminary observations on vein generations at the Brucejack Property, internal company report, 15 p.

Board, W.S., and McNaughton, K.C., 2013, The Brucejack high-grade gold project, northwest British Columbia, Canada. NewGenGold Conference, Perth, Australia, Proceedings, p. 177–191. West Perth, Paydirt Pty Ltd.

Board, W.S., and Greig, C.J., 2014, The Brucejack high grade Au-Ag deposit, northwestern British Columbia, Canada. Geological Society of America Annual Meeting, Vancouver, BC, Abstracts with Programs. Vol. 46, No. 6, p. 589.

Board, W.S., McLeish, D.F., Greig, C.J., Bath, O.E., Ashburner, J.E., Murphy, T., and Friedman, R.M., 2020, The Brucejack Au-Ag deposit, northwest British Columbia, Canada: Multistage porphyry to epithermal alteration, mineralization and deposit formation in an island-arc setting, in Sillitoe, R.H., Goldfarb, R.J., Robert, F., and Simmons, S.F., eds., Geology of the World's Major Gold Deposits and Provinces: Society of Economic Geologists Special Publication 23, p. 299–311.

Boyle, R.W., 1987, History and Genesis of Deposits. Springer, Boston, MA. 676 p.

Boyle, R.W., 1979, The geochemistry of gold and its deposits. Geological Survey of Canada Bulletin 280. 584 p.

Britton, J.M., and D.J. Alldrick, 1988, Sulphurets map area (104A/05W; 104B/08E, 09E), in Geological Fieldwork 1987: British Columbia Ministry of Energy, Mines and Petroleum Resources, British Columbia Geological Survey Paper 1988–1, p. 199-209.

Buchanan, L.J., 1981, Precious metal deposits associated with volcanic environments in the southwest, in Dickson, W.R. and Payne, W.D., eds., Relations of Tectonics to Ore

Deposits in the Southern Cordillera: Arizona Geological Society Digest, v. 14, p. 237-262.

Buddington, A.F., 1929, Geology of Hyder and vicinity Southeastern Alaska. United States Geological Survey, Bulletin 807, 124 p.

Burke, M., Rakovan, J., Krekeler M.P.S., 2017, A study by electron microscopy of gold and associated minerals from Round Mountain, Nevada. Ore Geology Reviews, v. 91, p. 708-717.

Carrillo Rosúa, F.J., Morales Ruano, S. and Fenoll Hach-Alí, P., 2002, The three generations of gold in the Palai–Islica epithermal deposit, southeastern Spain. The Canadian Mineralogist, v. 40, p. 1465-1481.

Childe, F.C., 1996, U-Pb geochronology and Nd and Pb isotope characteristics of the Au-Ag-rich Eskay Creek volcanogenic massive sulfide deposit, British Columbia. Economic Geology, v. 91, p. 1209-1224.

Childe, F.C., 1997, Timing and tectonic setting of volcanogenic massive sulphide deposits in British Columbia: constraints from U-Pb geochronology, radiogenic isotopes, and geochemistry. Unpublished Ph.D. thesis, Vancouver, University of British Columbia, 319 p.

Clarke, G., 2022, Exploration and mining in the Northwest Region, British Columbia. In: Provincial Overview of Exploration and Mining in British Columbia, 2021. British Columbia Ministry of Energy, Mines and Low Carbon Innovation, British Columbia Geological Survey Information Circular 2022-01, p. 43-65.

Cline, J.S., 2001, Timing of gold and arsenic sulfide mineral deposition at the Getchell Carlin type gold deposit, north-central Nevada. Economic Geology, v. 96, p. 75–90.

Cooke, D.R., McPhail, D.C. and Bloom, M.S., 1996, Epithermal gold mineralization, Acupan, Baguio District, Philippines; geology, mineralization, alteration, and the thermochemical environment of ore deposition. Economic Geology, v. 91, p. 243-272.

Corbett, G J and Leach, T M, 1998, Southwest Pacific Rim gold-copper systems: structure, alteration, and mineralization. Society of Economic Geologists Special Publication 6, 237 p.

Dare, S.A., Barnes, S.J. and Prichard, H.M., 2010. The distribution of platinum group elements (PGE) and other chalcophile elements among sulfides from the Creighton Ni–Cu–PGE sulfide deposit, Sudbury, Canada, and the origin of palladium in pentlandite. Mineralium Deposita, v. 45, p. 765-793.

Davies, A.G.S., Lewis, P.D. and Macdonald, A.J., 1994, Stratigraphic and structural setting of the mineral deposits in the Brucejack Lake area, northwestern British Columbia, in Current Research 1994-A, Geological Survey of Canada, p. 37–43.

Davis, B., 2017, Foliation history and development of N-S structures at Brucejack: Field visit observation report. Unpublished report prepared for Pretium Resources Inc. by OREFIND, 32 p.

Deditius, A.P., Utsunomiya, S., Ewing, R.C., Chryssoulis, S.L., Venter, D. and Kesler, S.E., 2009, Decoupled geochemical behavior of As and Cu in hydrothermal systems. Geology, v. 37, p. 707-710.

Ding, T., Valkiers, S., Kipphardt, H., De Bièvre, P., Taylor, P. D. P., Gonfiantini, R., and Krouse, R., 2001, Calibrated sulfur isotope abundance ratios of three IAEA sulfur isotope reference materials and V-CDT with a reassessment of the atomic weight of sulfur. Geochimica et Cosmochimica Acta, v. 65, p. 2433–2437.

Erdmer, P., Moore, J.M., Heaman, L., Thompson, R.I., Daughtry, K.L. and Creaser, R.A., 2002, Extending the ancient margin outboard in the Canadian Cordillera: record of Proterozoic crust and Paleocene regional metamorphism in the Nicola horst, southern British Columbia. Canadian Journal of Earth Sciences, v. 39, p. 1605-1623.

Evenchick, C.A., 1991, Geometry, evolution, and tectonic framework of the Skeena fold belt, north central British Columbia. Tectonics, v. 10, p. 527-546.

Evenchick, C.A. and Thorkelson, D.J., 2005, Geology of the Spatsizi River map area, north-central British Columbia. Geological Survey of Canada Bulletin 577, 276 p.

Evenchick, C.A., McMechan, M.E., McNicoll, V.J., and Carr, S.D., 2007, A synthesis of the Jurassic–Cretaceous tectonic evolution of the central and southeastern Canadian Cordillera: Exploring links across the orogen. Geological Society of America Special Paper 433, p. 117-145.

Febbo, G.E., Kennedy, L.A., Savell, M., Creaser, R.A. and Friedman, R.M., 2015, Geology of the Mitchell Au-Cu-Ag-Mo porphyry deposit, northwestern British Columbia, Canada, in

Geological Fieldwork 2014, BC Ministry of Energy and Mines, BC Geological Survey, Paper 2015-1, p. 59–86.

Febbo, G.E., 2016, Structural evolution of the Mitchell Au-Cu-Ag-Mo porphyry deposit, northwestern British Columbia. Unpublished M.Sc. thesis, Vancouver, University of British Columbia, 328 p.

Gaboury, D. and Oré Sanchez, C., 2020, Electrochemical gold precipitation to explain extensive vertical and lateral mineralization in the world-class Poderosa-Pataz district, Peru. Terra Nova, v. 32, p. 97-107.

Febbo, G.E., Kennedy, L.A., Nelson, J.L., Savell, M.J., Campbell, M.E., Creaser, R.A., Friedman, R.M., van Straaten, B.I., and Stein, H.J., 2019a, The evolution and structural modification of the supergiant Mitchell Au-Cu porphyry, northwestern British Columbia. Economic Geology, v. 114, p. 303-324.

Febbo, G.E., Friedman, R.M., Kennedy, L.A., and Nelson, J.L., 2019b, U-Pb geochronology of the Mitchell deposit, northwestern British Columbia: British Columbia Ministry of Energy, Mines and Petroleum Resources, British Columbia Geological Survey GeoFile 2019-03, 8 p.

Fleet, M.E., Maclean, P.J., and Barbier J., 1989, Oscillatory-zoned As-bearing pyrite from strata-bound and stratiform gold deposits: an indicator of ore fluid evolution. Economic Geology Monograph 6, p. 356–362.

Fleet, M.E., and Mumin, A.H., 1997, Gold-bearing arsenian pyrite and marcasite and arsenopyrite from Carlin Trend gold deposits and laboratory synthesis. American Mineralogist, v. 82, p. 182-193.

Fougerouse, D., Micklethwaite, S., Tomkins, A.G., Mei, Y., Kilburn, M., Guagliardo, P., Fisher, L.A., Halfpenny, A., Gee, M., Paterson, D. and Howard, D.L., 2016, Gold remobilisation and formation of high grade ore shoots driven by dissolution-reprecipitation replacement and Ni substitution into auriferous arsenopyrite. Geochimica et Cosmochimica Acta, 178, p. 143-159.

Gagnon, J.-F., Barresi, T., Waldon, J.W.F., Nelson, J.L., Poulton, T.P., and Cordey, F., 2012, Stratigraphy of the upper Hazelton Group and the Jurassic evolution of Stikinia, British Columbia: Canadian Journal of Earth Sciences, v. 49, p. 1027–1052.

Gartman, A., Hannington, M., Jamieson, J.W., Peterkin, B., Garbe-Schönberg, D., Findlay, A.J., and Kwasnitschka, T., 2018, Boiling induced formation of colloidal gold in black smoker hydrothermal fluids. Geology, v. 46, p. 39–42.

Gregory, M.J., Lang, J.R., Gilbert, S., and Hoal, K.O., 2013, Geometallurgy of the Pebble porphyry copper-gold-molybdenum deposit, Alaska: Implications for gold distribution and paragenesis. Economic Geology, v. 108, p. 463-482.

Greig, C.J., 2014, Latest Triassic–earliest Jurassic contractional deformation, uplift and erosion in Stikinia, NW BC. Geological Society of America Abstracts with Programs, v. 46, no. 6, p. 588.

Greig, C.J., and Greig, R., 2013, Geology of the Brucejack property: Pretium Resources Inc. Internal company map. Available: https://s1.q4cdn.com/222336918/files/doc_downloads/geology/2013.03.19%20Property%20Geology.pdf.

Groves, D.I., Goldfarb, R.J., Robert, F., and Hart, C.J., 2003, Gold deposits in metamorphic belts: overview of current understanding, outstanding problems, future research, and exploration significance. Economic Geology, v. 98, p. 1-29.

Guillong, M., Hametner, K., Reusser, E., Wilson, S.A. and Günther, D., 2005, Preliminary characterisation of new glass reference materials (GSA-1G, GSC-1G, GSD-1G and GSE-1G) by laser ablation-inductively coupled plasma-mass spectrometry using 193 nm, 213 nm and 266 nm wavelengths. Geostandards and Geoanalytical Research, v. 29, p. 315-331.

Hannington, M., Hardardóttir, V., Garbe-Schonberg, D. Brown, K., 2016, Gold enrichment in active geothermal systems by accumulating colloidal suspensions. Nature Geoscience, v. 9, p. 299–302.

Hannington, M., and Garbe-Schönberg, D, 2019, Detection of gold nanoparticles in hydrothermal fluids. Economic Geology, v. 114, p. 397-400.

Harrichhausen, N.J., 2016, Role of colloidal transport in the formation of high-grade veins at Brucejack, British Columbia. Unpublished M.Sc. thesis, Montreal, McGill University, 103 p.

Heinrich, C.A., Driesner, T., Stefánsson, A., and Seward, T.M., 2004, Magmatic vapor contraction and the transport of gold from the porphyry environment to epithermal ore deposits. Geology, v. 32, p. 761-764.

Henderson, J.R., Kirkham, R.V., Henderson, M.N., Payne, J.G., Wright, T.O., and Wright, R.L., 1992, Stratigraphy and structure of the Sulphurets area, British Columbia. Current research. Geological Survey of Canada Paper 92, p. 323-332.

Henley, R.W., Truesdell, A.H., and Barton, P.B., 1984, Fluid-mineral equilibria in hydrothermal systems. Society of Economic Geologists, Reviews in Economic Geology, v. 1, 267 p.

Henry, A.D., McInnes, P., and Tosdal, R.M., 2014, Structural evolution of auriferous veins at the Endeavour 42 gold deposit, Cowal mining district, NSW, Australia. Economic Geology, v. 109, p. 1051-1077.

Hermo, M.I., Balangue-Tarriela, M.I.R., Takahashi, R., Gabo-Ratio, J.A., and Frias, S.M., 2022, Mineralization styles and ore-forming conditions of the quartz-fragment-rich breccia (QBX) at the Didipio alkalic porphyry Cu-Au deposit, Nueva Vizcaya, Philippines. Ore Geology Reviews, v. 143, 104724.

Herrington, R., and Wilkinson, J., 1993, Colloidal gold and silica in mesothermal vein systems. Geology, v. 21, p. 539–542.

Hyland, M.M., Bancroft, G.M., 1989, An XPS study of gold deposition at low temperatures on sulphide minerals: reducing agents. Geochimica et Cosmochimica Acta, v. 53, p. 367-372.

Jean, G.E. and Michael, B.G., 1985, An XPS and SEM study of gold deposition at low temperatures on sulphide mineral surfaces: Concentration of gold by adsorption/reduction. Geochimica et Cosmochimica Acta, v. 49, p. 979-987.

John, D.A., Hofstra, A.H., Fleck, R.J., Brummer, J.E., and Saderholm, E.C., 2003, Geologic setting and genesis of the Mule Canyon low-sulfidation epithermal gold-silver deposit, north-central Nevada. Economic Geology, v. 98, p. 425-463.

Johnston, S.T., 2008, The cordilleran ribbon continent of North America. Annual Review of Earth and Planetary Sciences, v. 36, p. 495-530.

Johnston, S.T., and Borel, G.D., 2007, The odyssey of the Cache Creek terrane, Canadian Cordillera: Implications for accretionary orogens, tectonic setting of Panthalassa, the

Pacific superwell, and break-up of Pangea. Earth and Planetary Science Letters, v. 253, p. 415-428.

Journeay, J.M., and Friedman, R.M., 1993, The Coast Belt thrust system: evidence of Late Cretaceous shortening in southwest British Columbia. Tectonics, v. 12, p. 756-775.

Keith, M., Smith, D.J., Jenkin, G.R., Holwell, D.A., and Dye, M.D., 2018, A review of Te and Se systematics in hydrothermal pyrite from precious metal deposits: Insights into ore-forming processes. Ore Geology Reviews, 96, p. 269-282.

Kesler, S.E., Campbell, I.H., Smith, C.N., Hall, C.M., and Allen, C.M., 2005, Age of the Pueblo Viejo gold-silver deposit and its significance to models for high-sulfidation epithermal mineralization. Economic Geology, v. 100, p. 253-272.

Kianinia, Y., Khalesi, M.R., Seyedhakimi, A., and Soltani, F., 2017, Flotation of mercury from the tailings of the Agh-Darreh gold processing plant, Iran; Journal of the Southern African Institute of Mining and Metallurgy, v. 117, p. 83-88.

Kirkham, R.V., and Margolis, J., 1995, Overview of the Sulphurets area, northwestern British Columbia. Porphyry deposits of the northwestern Cordillera, Canadian Institute of Mining, Metallurgy, and Petroleum, Special Publication 46, p. 473-483.

Kvasnifsa, N.V., Kuznetsov, Y. A., and Latysh, I. K., 1981, Crystal morphology of native gold from some ore regions of the Ukraine. International Geology Review, v. 23, p. 227-232.

Leary, S., Sillitoe, R.H., Stewart, P.W., Roa, K.J., and Nicolson, B.E., 2016, Discovery, geology, and origin of the Fruta del Norte epithermal gold-silver deposit, southeastern Ecuador. Economic Geology, v. 111, p. 1043-1072.

Logan, J.M. and Mihalynuk, M.G., 2014, Tectonic controls on early Mesozoic paired alkaline porphyry deposit belts (Cu-Au±Ag-Pt-Pd-Mo) within the Canadian Cordillera. Economic Geology, v. 109, p. 827-858.

Macdonald, A.J., Lewis, P.D., Thompson, J.F., Nadaraju, G., Bartsch, R., Bridge, D.J., Rhys, D.A., Roth, T., Kaip, A., Godwin, C.I. and Sinclair, A.J., 1996, Metallogeny of an early to middle Jurassic arc, Iskut river area, northwestern British Columbia. Economic Geology, v. 91, p. 1098-1114.

Maddox, L.M., Bancroft, G.M., Scaini, M.J. and Lorimer, J.W., 1998, Invisible gold:
Comparison of Au deposition on pyrite and arsenopyrite. American Mineralogist, v. 83,
p. 1240-1245.

Marsden, H. and Thorkelson, D.J., 1992, Geology of the Hazelton volcanic belt in British
Columbia: Implications for the Early to Middle Jurassic evolution of
Stikinia. Tectonics, v. 11, p. 1266-1287.

Margolis, J., 1993, Geology and intrusion-related copper-gold mineralization, Sulphurets, British
Columbia: Ph.D. Dissertation, Eugene, OR, University of Oregon, 394 p.

Maslennikov, V.V., Maslennikova, S.P., Large, R.R., and Danyushevsky, L.V., 2009, Study of
trace element zonation in vent chimneys from the Silurian Yaman-Kasy volcanic-hosted
massive sulfide deposit (Southern Urals, Russia) using laser ablation-inductively coupled
plasma mass spectrometry (LA-ICPMS). Economic Geology, v. 104, p. 1111-1141.

McLeish, D.F., Williams-Jones, A.E., and Board, W.S., 2017, Nature and origin of the Brucejack
high-grade epithermal gold deposit, northwestern British Columbia (NTS 104B), in
Geoscience BC Summary of Activities 2016, Geoscience BC, Report 2017-1, p. 223-232.

McLeish, D.F., Williams-Jones, A.E., Board, W.S., and Clark, J.R., 2018, Nature and origin of
the Brucejack high-grade epithermal gold deposit, northwestern British Columbia (NTS
104B): 2017 update, in Geoscience BC Summary of Activities 2017: Minerals and
Mining, Geoscience BC, Report 2018-1, p. 31-40.

McLeish, D.F., Williams-Jones, A.E., Vasyukova, O.V., Clark, J.R., and Board, W.S., 2021,
Colloidal transport and flocculation are the cause of the hyperenrichment of gold in
nature. Proceedings of the National Academy of Sciences, 118(20), e2100689118.

Meyer, C., and Hemley, J.J., 1967, Wall rock alteration, in Barnes, H.L., ed., Geochemistry of
hydrothermal ore deposits, New York, Holt, Rinehart and Winston, p. 166−235.

Mikhlin, Y.L., and Romanchenko, A.S., 2007, Gold deposition on pyrite and the common sulfide
minerals: An STM/STS and SR-XPS study of surface reactions and Au nanoparticles.
Geochimica et Cosmochimica Acta, v. 71, p. 5985-6001.

Möller, P., and Kersten, G., 1994, Electrochemical accumulation of visible gold on pyrite and
arsenopyrite surfaces. Mineralium Deposita, v. 29, p. 404-413.

Mycroft, J.R., Bancroft, G.M., McIntyre, N.S., and Lorimer, J.W., 1995, Spontaneous deposition of gold on pyrite from solutions containing Au (III) and Au (I) chlorides. Part I: A surface study. Geochimica et Cosmochimica Acta, v. 59, p. 3351-3365.

Nelson, J.L., Colpron, M., and Goodfellow, W.D., 2007, Tectonics and metallogeny of the British Columbia, Yukon and Alaskan Cordillera, 1.8 Ga to the present. Mineral deposits of Canada: a synthesis of major deposit-types, district metallogeny, the evolution of geological provinces, and exploration methods: Geological Association of Canada, Mineral Deposits Division, Special Publication 5, p. 755-791.

Nelson, J.L., and Kyba, J., 2014, Structural and stratigraphic control of porphyry and related mineralization in the Treaty Glacier–KSM–Brucejack–Stewart trend of northwestern Stikinia, in Geological Fieldwork 2013: British Columbia Ministry of Energy, Mines and Petroleum Resources, British Columbia Geological Survey Paper 2014–1, p. 111-140.

Nelson, J., Waldron, J., van Straaten, B., Zagorevski, A., and Rees, C., 2018, Revised stratigraphy of the Hazelton Group in the Iskut River region, northwestern British Columbia: Geological Fieldwork 2017, British Columbia Ministry of Energy, Mines and Petroleum Resources, British Columbia Geological Survey Paper 2018-1, p. 15-38.

Nelson, J.L., van Straaten, B., and Friedman, R., 2022, Latest Triassic–Early Jurassic Stikine–Yukon-Tanana terrane collision and the onset of accretion in the Canadian Cordillera: Insights from Hazelton Group detrital zircon provenance and arc–back-arc configuration. Geosphere, v. 18, p. 670-696.

Ohmoto, H., and Rye, R.O., 1979, Isotopes of sulfur and carbon, in: Barnes, H.L. (Ed.), Geochemistry of hydrothermal ore deposits, 2nd ed. Wiley, New York, p. 509-567.

Palenik, C.S., Utsunomiya, S., Reich, M., Kesler, S.E., Wang, L. and Ewing, R.C., 2004, "Invisible" gold revealed: Direct imaging of gold nanoparticles in a Carlin-type deposit. American Mineralogist, 89(10), p. 1359-1366.

Paton, C., Hellstrom, J., Paul, B., Woodhead, J. and Hergt, J., 2011, Iolite: Freeware for the visualisation and processing of mass spectrometric data. Journal of Analytical Atomic Spectrometry, v. 26, p. 2508-2518.

Peddle, C., and Johnston, S.T., 2021, Review of the structural geology of the Brucejack intermediate-sulphidation epithermal deposit, northwestern British Columbia (NTS

104B), in Geoscience BC Summary of Activities 2020: Minerals, Geoscience BC, Report 2021-01, p. 29–40.

Petrella, L., Thébaud, N., Fougerouse, D., Evans, K., Quadir, Z., and Laflamme, C., 2020, Colloidal gold transport, a key to high-grade gold mineralization? Mineralium Deposita, v. 55, p. 1247-1254.

Petrie, B.S., Craw D., and Ryan, C.G., 2005, Geological controls on refractory ore in an orogenic gold deposit, Macraes mine, New Zealand. Mineralium Deposita, v. 40, p. 45-58.

Petrovskaya, N.V., 1973, Samorodnoe Zoloto (Native Gold), Moscow: Nauka, 347 p.

Pokrovski, G.S., Kokh, M.A., Guillaume, D., Borisova, A.Y., Gisquet, P., Hazemann, J.L., Lahera, E., Del Net, W., Proux, O., Testemale, D., and Haigis, V., 2015, Sulfur radical species form gold deposits on Earth. Proceedings of the National Academy of Sciences, v. 112, p. 13484-13489.

Pretium, 2020, Brucejack reserve summary. Available : https://www.pretivm.com/brucejack/reserves-and-resources/default.aspx

Pridmore, D.F., and Shuey, R.T., 1976, The electrical resistivity of galena, pyrite, and chalcopyrite. American Mineralogist, v. 61, p. 248-259.

Reich, M., Kesler, S.E., Utsunomiya, S., Palenik, C.S., Chryssoulis, S.L., and Ewing, R., 2005, Solubility of gold in arsenian pyrite. Geochemica et Cosmochimica Acta, v. 69, p. 2781-2796.

Reich, M., Deditius, A., Chryssoulis, S., Li, J.W., Ma, C.Q., Parada, M.A., Barra, F., and Mittermayr, F., 2013, Pyrite as a record of hydrothermal fluid evolution in a porphyry copper system: A SIMS/EMPA trace element study. Geochimica et Cosmochimica Acta, v. 104, p. 42-62.

Richards, J.P. and Kerrich, R., 1993, The Porgera gold mine, Papua New Guinea; magmatic hydrothermal to epithermal evolution of an alkalic-type precious metal deposit. Economic Geology, v. 88, p. 1017-1052.

Richards, J.P., Wilkinson, D., and Ullrich, T., 2006, Geology of the Sari Gunay epithermal gold deposit, northwest Iran. Economic Geology, v. 101, p. 1455–1496.

Richards, J.P., 2013, Giant ore deposits formed by optimal alignments and combinations of geological processes. Nature geoscience, v. 6, p. 911-916.

Roach, S., and Macdonald, A.J., 1992, Silver-gold vein mineralization, West zone, Brucejack Lake, northwestern British Columbia (104B/8E), in Geological Fieldwork 1991: British Columbia Ministry of Energy, Mines and Petroleum Resources, British Columbia Geological Survey Paper 1992–1, p. 503-512.

Román, N., Reich, M., Leisen, M., Morata, D., Barra, F., and Deditius, A.P., 2019, Geochemical and micro-textural fingerprints of boiling in pyrite. Geochimica et Cosmochimica Acta, v. 246, p. 60-85.

Romberger, S., 1992, A model for bonanza gold deposits. Geoscience Canada, v. 19, p. 63-72.

Saunders, J. A., 1990, Colloidal transport of gold and silica in epithermal precious-metal systems: Evidence from the Sleeper deposit, Nevada. Geology, v. 18, p. 757–760.

Saunders, J.A., and Schoenly, P.A., 1995, Boiling, colloid nucleation and aggregation, and the genesis of bonanza Au-Ag ores of the Sleeper deposit, Nevada. Mineralium Deposita, v. 30, p. 199-210.

Saunders, J.A., and Burke, M., 2017, Formation and aggregation of gold (electrum) nanoparticles in epithermal ores. Minerals, v. **7**, 163, doi.org/10.3390/min7090163.

Seabridge Gold, 2020, Snowfield estimated mineral resources. Available: https://www.seabridgegold.com/press-release/seabridge-completes-acquisition-of-snowfield-property-from-pretivm

Serway, R.A., and Jewett, J.W., 1998, Principles of physics (Vol. 1). Fort Worth, TX. Saunders College Publishing, 601 p.

Sillitoe, R. H., 1993, Giant and bonanza gold deposits in the epithermal environment: Assessment of potential genetic factors, in Whiting B. H., Mason R., and Hodgson C. J. eds., Giant Ore Deposits, Society of Economic Geologists Special Publication 2, p. 125-156.

Sillitoe, R.H., 2002, Some metallogenic features of gold and copper deposits related to alkaline rocks and consequences for exploration. Mineralium Deposita, v. 37, p. 4-13.

Sillitoe, R.H., and Hedenquist, J. W., 2003, Linkages between volcanotectonic settings, ore-Fluid compositions, and epithermal precious metal deposits, in Volcanic, Geothermal, and Ore-Forming Fluids: Rulers and Witnesses of Processes within the Earth. Society of Economic Geologists Special Publication 23, p. 315-345.

Sillitoe, R.H., 2010, Porphyry copper systems. Economic geology, v. 105, p. 3-41.

Sillitoe, R.H., 2015, Comments on geology and exploration potential of the Brucejack gold-silver deposit and environs, British Columbia, Canada, unpublished report prepared for Pretium Resources Inc., 16 p.

Simmons, S.F., Tutolo, B.M., Barker, S.L.L., Goldfarb, R.J., and Robert, F., 2020, Hydrothermal gold deposition in epithermal, Carlin, and orogenic deposits. Society of Economic Geologists Special Publication 23, p. 823-845.

Sinclair, W.D., 2007, Porphyry deposits. Mineral deposits of Canada: A synthesis of major deposit-types, district metallogeny, the evolution of geological provinces, and exploration methods. Geological Association of Canada, Mineral Deposits Division, Special Publication, 5, p. 223-243.

Sakharova, M.S., Batrakova, Yu.A., Ryakhovskaya S.K., 1975, Investigation of electrochemical interactions between sulfides and Au-bearing solution. Geochemistry International, v.12, p. 84-89.

Shuey, R.T., 1975, Semiconducting ore minerals. Elsevier, Amsterdam. 415 p.

Skey, W., 1871, On the electromotive power of metallic sulfides. New Zealand Institute Transactions and Proceedings, v. 3, p. 232-236.

Starling, A., Gilligan, J.M., Carter, A.H.C., Foster, R.P., and Saunders, R.A., 1989, High-temperature hydrothermal precipitation of precious metals on the surface of pyrite. Nature, v. 340, p. 298-300.

Steadman, J.A., Large, R.R., Olin, P.H., Danyushevsky, L.V., Meffre, S., Huston, D., Fabris, A., Lisitsin, V., and Wells, T., 2021, Pyrite trace element behavior in magmatic-hydrothermal environments: An LA-ICPMS imaging study. Ore Geology Reviews, v. 128, doi: 10.1016/j. oregeorev.2020.103878

Sykora, S., Cooke, D.R., Meffre, S., Stephanov, A.S., Gardner, K., Scott, R., Selley, D., and Harris, A.C., 2018, Evolution of pyrite trace element compositions from porphyry style and epithermal conditions at the Lihir gold deposit: Implications for ore genesis and mineral processing: Economic Geology, v. 113, p. 193-208.

Tetra Tech, 2020, March 2020 technical report and mineral resources update, Brucejack mine: NI 43-101 Technical Report prepared for Pretium Resources Inc., 383 p.

Thomson, R.C., Smith, P.L., and Tipper, H.W., 1986, Lower to Middle Jurassic (Pliensbachian to Bajocian) stratigraphy of the northern Spatsizi area, north-central British Columbia. Canadian Journal of Earth Sciences, v. 23, p. 1963-1973.

Tombe, S.P., 2015, Age and origin of the Brucejack epithermal Au-Ag deposit, northwestern British Columbia: M.Sc. thesis, Edmonton, University of Alberta, 201 p.

Tombe, S.P., Richards, J.P., Greig, C.J., Board, W.S., Creaser, R.A., Muehlenbachs, K.A., Larson, P.B., DuFrane, S.A., and Spell, T., 2018, Origin of the high-grade early Jurassic Brucejack epithermal Au-Ag deposits, sulphurets mining Camp, northwestern British Columbia. Ore Geology Reviews, v. 95, p. 480-517.

Vaughan, J. P., 2004, The process mineralogy of gold: The classification of ore types; JOM, Metals and Materials Society, v. 56, p. 46-48.

Vikentyev, I.V., 2015, Invisible and microscopic gold in pyrite: methods and new data for massive sulfide ores of the Urals. Geology of Ore Deposits, v. 57, p. 237–265.

Voute, F., Hagemann, S.G., Evans, N.J., and Villanes, C., 2019, Sulfur isotopes, trace element, and textural analyses of pyrite, arsenopyrite and base metal sulfides associated with gold mineralization in the Pataz-Parcoy district, Peru: implication for paragenesis, fluid source, and gold deposition mechanisms. Mineralium Deposita, v. 54, p. 1077-1100.

White, N.C. and Hedenquist, J.W., 1990, Epithermal environments and styles of mineralization: variations and their causes, and guidelines for exploration. Journal of Geochemical Exploration, 36(1-3), p. 445-474.

Widler, A.M., and Seward, T.M., 2002, The adsorption of gold (I) hydrosulphide complexes by iron sulphide surfaces. Geochimica et Cosmochimica Acta, v. 66, p. 383-402.

Williams-Jones, A.E., Bowell, R.J., and Migdisov, A.A., 2009. Gold in solution. Elements, v. 5, p. 281-287.

Wilson, S.A., Ridley, W.I., and Koenig, A.E., 2002, Development of sulfide calibration standards for the laser ablation inductively-coupled plasma mass spectrometry technique. Journal of Analytical Atomic Spectrometry, v. 17, p. 406-409.

Xu, N., Wu, C.L., Li, S.R., Xue, B.Q., He, X., Yu, Y.L., and Liu, J.Z., 2020, LA-ICP-MS in situ analyses of the pyrites in Dongyang gold deposit, Southeast China: Implications to the gold mineralization. China Geology, v. 3, p. 230-246.

Data Supplement S4.1– EMPA electrum analyses

A large number of EMPA-WDS analyses of electrum were performed at the McGill University Electron Microprobe Laboratory and the joint University of Ottawa - Canadian Museum of Nature MicroAnalysis Laboratory using JEOL 8900 and JEOL 8230 SuperProbe instruments, respectively. Both instruments are equipped with five X-ray wavelength dispersive spectrometers and, with limited exceptions, identical operating conditions were used at both facilities. Electrum grains were quantitatively analysed for Ag (Lα), Au (Mα), Hg (Lα; Mβ in Ottawa), and Te (Lβ) using the following synthetic and natural standards: Au60Ag40 alloy (Au and Ag), cinnabar (Hg), and native Te (Te; Sb_2Te_3 in Ottawa). Microbeam analyses were performed using a beam energy of 20 keV, a 40 degrees takeoff angle, a 5 μm beam diameter, and a 30 nA beam current (40 nA current in Ottawa). Duplicate EMPA-WDS spot tests were done on select electrum grains at both facilities and no significant difference in results were observed.

Gold and silver results from the EMPA-WDS analyses of electrum are shown in Figure S4.1 and in the analytical results table below. The Au:Ag ratio of the electrum appears to vary considerably with vein type and no significant variation in the Au:Ag ratio of electrum is observed within individual samples. Analyses were taken across electrum grains (rim-core-rim) for both quartz-carbonate-matrix-hosted and pyrite-inclusion–hosted electrum with no obvious Au:Ag differences observed. No tellurium was detected in the electrum; moderately levels of mercury (< 3.1 wt %) were found locally, generally in electrum samples with a high silver content (40-60 wt %) from Stage IV veins. The regular, systematic variation in the Au:Ag ratio of the electrum with vein type was confirmed with some overlap observed between vein types. Three Stage IV samples in which electrum occurs in textural equilibrium with galena and sphalerite (SU-312, SU-322, and SU-580) yielded gold values significantly lower than in Stage IV veins where no textural equilibrium was observed between electrum and base metal sulphide mineralisation. Three-dimensional imaging of the electrum chemistry results showed that there was no significant spatial control on electrum chemistry.
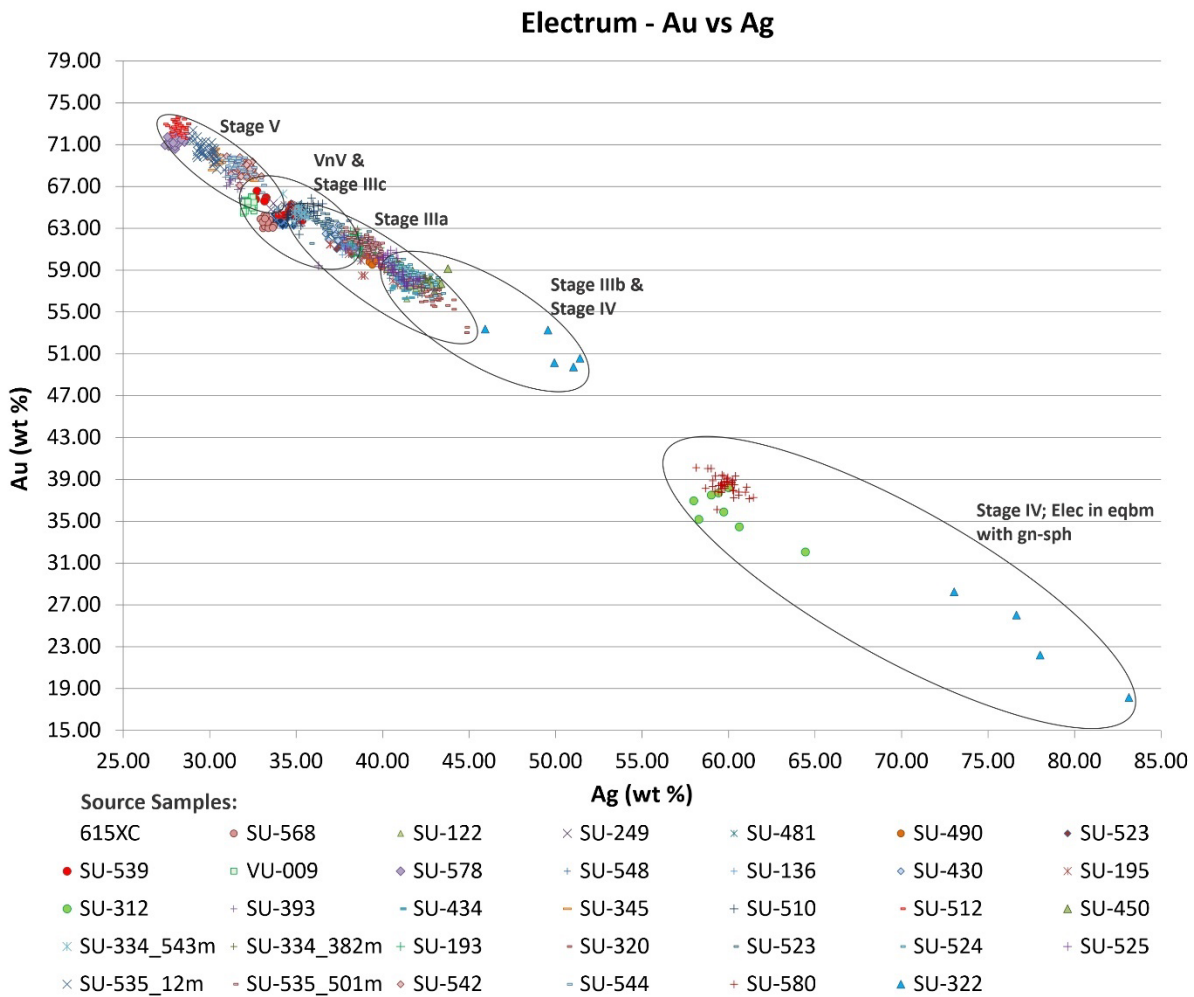
Figure S4.1: Gold and silver concentrations in Brucejack Valley of the Kings zone electrum based on EMPA-WDS analyses.

Table S4.1: Electron microprobe wavelength-dispersive X-ray spectroscopy electrum chemistry analysis results

Analysis Spot ID	Ag (wt%)	Hg (wt%)	Au (wt%)	Te (wt%)	Total
Sample 615XC1					
Electrum-615XC1-10-1	33.83	0.005	64.02	0.000	97.86
Electrum-615XC1-10-2	34.40	0.095	63.34	0.000	97.84
Electrum-615XC1-1-1	34.86	0.125	63.27	0.000	98.26
Electrum-615XC1-2-1	34.06	0.196	63.47	0.062	97.79
Electrum-615XC1-3-1	34.29	0.183	63.46	0.051	97.98
Electrum-615XC1-3-2	34.22	0.000	63.26	0.035	97.52
Electrum-615XC1-4-1	33.83	0.142	63.95	0.052	97.97
Electrum-615XC1-4-2	34.16	0.220	63.68	0.000	98.06
Electrum-615XC1-4-3	33.74	0.000	63.67	0.000	97.41
Electrum-615XC1-5-vlg-1	34.14	0.110	63.72	0.044	98.01
Electrum-615XC1-5-vlg-4	34.12	0.233	63.81	0.000	98.16
Electrum-615XC1-6-1	34.29	0.222	64.12	0.000	98.63
Electrum-615XC1-6-2	34.48	0.307	63.94	0.000	98.73
Electrum-615XC1-7-1	33.91	0.000	64.02	0.048	97.98
Electrum-615XC1-8-1	34.12	0.042	64.25	0.097	98.51
Electrum-615XC1-8-2	33.97	0.115	63.66	0.000	97.75
Electrum-615XC1-9-1	33.75	0.202	64.33	0.000	98.28
Electrum-615XC1-9-2	34.09	0.000	63.75	0.000	97.84
Sample S568-422a					
Electrum-S568-1-1	33.09	0.988	63.01	0.000	97.09
Electrum-S568-1-2	33.16	0.740	64.22	0.000	98.12
Electrum-S568-1-3	33.47	0.966	63.82	0.047	98.30
Electrum-S568-2-1	33.20	0.982	63.18	0.000	97.36
Electrum-S568-2-2	33.72	0.892	63.24	0.000	97.85
Electrum-S568-3-1	33.31	1.080	63.54	0.000	97.93
Electrum-S568-3-2	32.94	1.140	63.90	0.010	97.99
Electrum-S568-3-3	33.40	0.950	63.02	0.000	97.37
Electrum-S568-4-1	33.21	1.010	63.98	0.032	98.23
Electrum-S568-4-2	33.28	1.130	64.17	0.000	98.58
Electrum-S568-5-1	33.34	0.990	63.60	0.022	97.95
Electrum-S568-5-2	33.06	1.100	63.61	0.039	97.81
Sample S122-215a					
Electrum-SU122-1-1	42.15	0.280	57.85	0.000	100.28
Electrum-SU122-1-10-1	42.15	0.105	57.01	0.000	99.27
Electrum-SU122-1-10-2	42.02	0.305	56.99	0.000	99.32
Electrum-SU122-1-11	42.26	0.119	57.35	0.000	99.73
Electrum-SU122-1-2	42.08	0.171	57.31	0.000	99.56
Electrum-SU122-1-3	41.92	0.219	57.25	0.062	99.45
Electrum-SU122-1-4	42.28	0.396	56.85	0.000	99.53
Electrum-SU122-1-5	41.80	0.266	57.46	0.000	99.53

Analysis Spot ID	Ag (wt%)	Hg (wt%)	Au (wt%)	Te (wt%)	Total
Electrum-SU122-1-6	42.08	0.252	57.57	0.000	99.90
Electrum-SU122-1-7	41.40	0.318	56.26	0.024	98.00
Electrum-SU122-1-8-inc-by-cpy	41.15	0.067	57.52	0.024	98.76
Sample S249-116a					
Electrum-SU249-1-1	35.22	0.262	63.75	N/A	99.23
Electrum-SU249-2-1	34.75	0.084	64.18	N/A	99.02
Electrum-SU249-2-2	35.10	0.000	63.74	N/A	98.84
Electrum-SU249-3-1	33.55	0.319	64.81	N/A	98.68
Electrum-SU249-3-2	33.69	0.181	65.39	N/A	99.26
Electrum-SU249-4-1	34.37	0.249	65.15	N/A	99.77
Electrum-SU249-4-2	33.90	0.000	65.01	N/A	98.91
Electrum-SU249-5-1	34.59	0.192	64.24	N/A	99.02
Electrum-SU249-5-2	35.16	0.061	63.52	N/A	98.74
Sample S481-186					
Electrum-SU481-10-1	37.37	0.103	61.90	0.025	99.40
Electrum-SU481-11-1	38.16	0.127	61.31	0.000	99.60
Electrum-SU481-11-2	38.22	0.117	61.17	0.000	99.51
Electrum-SU481-11-3-light	38.03	0.159	60.79	0.000	98.98
Electrum-SU481-16-1	36.84	0.155	62.29	0.078	99.36
Electrum-SU481-18-1	37.57	0.040	61.13	0.021	98.76
Electrum-SU481-18-2	37.52	0.318	61.65	0.058	99.55
Electrum-SU481-19-1	37.97	0.224	61.15	0.000	99.34
Electrum-SU481-19-2-light	37.20	0.027	62.04	0.000	99.27
Electrum-SU481-20-1	38.34	0.072	61.34	0.038	99.79
Electrum-SU481-20-2	37.57	0.168	62.09	0.011	99.84
Electrum-SU481-21-1	36.88	0.000	62.21	0.000	99.09
Electrum-SU481-22-1	37.78	0.120	62.34	0.019	100.26
Electrum-SU481-23-1	38.18	0.000	61.12	0.015	99.32
Electrum-SU481-9-1	37.91	0.415	61.56	0.026	99.91
Electrum-SU481-9-2	38.52	0.291	61.86	0.000	100.67
Electrum-SU481-9-3	37.45	0.282	62.58	0.000	100.31
Sample S490-364a					
Electrum-SU490-1-1	39.11	0.249	60.53	N/A	99.89
Electrum-SU490-1-2	39.55	0.041	60.23	N/A	99.82
Electrum-SU490-1-3	39.06	0.230	60.62	N/A	99.91
Electrum-SU490-2-1Pinc	39.23	0.169	59.78	N/A	99.18
Electrum-SU490-3-1Pinc	39.40	0.000	59.52	N/A	98.92
Electrum-SU490-4-1	39.02	0.305	60.44	N/A	99.77
Electrum-SU490-5-1	39.61	0.000	59.87	N/A	99.48
Electrum-SU490-6-1	39.88	0.111	60.27	N/A	100.26
Electrum-SU490-7-1	39.94	0.146	59.36	N/A	99.45

Analysis Spot ID	Ag (wt%)	Hg (wt%)	Au (wt%)	Te (wt%)	Total
Sample S523-313a					
Electrum-SU523-1-1rim	37.95	0.218	61.15	N/A	99.32
Electrum-SU523-1-2rim	38.56	0.375	60.96	N/A	99.90
Electrum-SU523-1-3rim	38.91	0.490	60.43	N/A	99.83
Electrum-SU523-1-4rim	37.35	0.245	61.01	N/A	98.61
Electrum-SU523-1-5rim	37.87	0.341	61.66	N/A	99.87
Electrum-SU523-1-6rimsphal	38.62	0.512	60.48	N/A	99.61
Electrum-SU523-2-1smallinc	38.21	0.384	60.46	N/A	99.05
Electrum-SU523-4-1	37.44	0.234	61.70	N/A	99.37
Electrum-SU523-4-2	37.49	0.488	61.26	N/A	99.24
Electrum-SU523-5-1	37.79	0.241	61.81	N/A	99.84
Electrum-SU523-5-2	37.83	0.426	61.60	N/A	99.86
Sample S539-509a					
Electrum-SU539-1-1	33.97	0.177	64.32	N/A	98.47
Electrum-SU539-1-2	34.30	0.053	64.28	N/A	98.63
Electrum-SU539-1-3	34.72	0.120	65.03	N/A	99.87
Electrum-SU539-14-1	35.28	0.187	64.35	0.000	99.82
Electrum-SU539-14-3	35.41	0.042	64.32	0.000	99.77
Electrum-SU539-15-1	34.81	0.274	65.01	0.021	100.11
Electrum-SU539-15-2	35.36	0.374	64.41	0.054	100.20
Electrum-SU539-15-3	35.27	0.000	64.84	0.032	100.14
Electrum-SU539-16-1	34.92	0.311	64.20	0.000	99.43
Electrum-SU539-16-2	34.74	0.053	65.02	0.064	99.88
Electrum-SU539-17-1	34.73	0.085	65.28	0.017	100.11
Electrum-SU539-18-1	34.87	0.062	65.16	0.000	100.09
Electrum-SU539-19-1	35.36	0.083	63.80	0.000	99.24
Electrum-SU539-20-1	34.69	0.432	64.74	0.000	99.86
Electrum-SU539-2-1	34.59	0.262	64.70	N/A	99.55
Electrum-SU539-2-2	34.69	0.276	64.87	N/A	99.84
Electrum-SU539-2-3	35.06	0.000	64.56	N/A	99.62
Electrum-SU539-3-1	34.85	0.148	64.86	N/A	99.86
Electrum-SU539-5-1	33.26	0.086	65.95	N/A	99.30
Electrum-SU539-5-2	33.21	0.146	65.73	N/A	99.09
Electrum-SU539-5-3	32.73	0.199	66.56	N/A	99.49
Electrum-SU539-5-4	33.17	0.083	65.62	N/A	98.87
Electrum-SU539-5-5	32.66	0.104	65.79	N/A	98.55
Sample V009-36a					
Electrum-VU009-1-1	32.14	0.000	65.09	0.035	97.27
Electrum-VU009-1-2	31.95	0.048	64.46	0.057	96.52
Electrum-VU009-2-1	32.09	0.000	64.64	0.032	96.76
Electrum-VU009-3-1ue	32.04	0.056	65.72	0.049	97.87
Electrum-VU009-3-2c	31.95	0.103	64.63	0.000	96.68
Electrum-VU009-3-3be	32.28	0.000	65.21	0.016	97.51

Analysis Spot ID	Ag (wt%)	Hg (wt%)	Au (wt%)	Te (wt%)	Total
Electrum-VU009-4-1	32.58	0.000	65.20	0.000	97.78
Electrum-VU009-4-2c	32.42	0.000	66.04	0.000	98.46
Electrum-VU009-4-3be	32.20	0.052	65.30	0.000	97.55
Electrum-VU009-5-1s	32.56	0.075	64.66	0.049	97.34
Electrum-VU009-5-2s	32.49	0.120	65.99	0.102	98.70
Electrum-VU009-6-vlg-1	32.45	0.000	64.96	0.000	97.41
Electrum-VU009-6-vlg-2	32.13	0.110	65.55	0.000	97.79
Electrum-VU009-6-vlg-3	32.19	0.117	65.61	0.031	97.95
Electrum-VU009-6-vlg-4	31.96	0.166	65.54	0.019	97.69
Electrum-VU009-6-vlg-5	32.57	0.000	65.48	0.016	98.07
Electrum-VU009-7-1pyeqbm	32.23	0.101	65.32	0.050	97.70
Electrum-VU009-7-2pyeqbm	32.21	0.063	65.55	0.000	97.82
Sample S578-14a					
Electrum-S578-14a-1-1	27.63	0.847	70.87	0.079	99.43
Electrum-S578-14a-1-2	27.42	0.946	70.95	0.000	99.32
Electrum-S578-14a-1-3	28.08	0.949	71.58	0.000	100.61
Electrum-S578-14a-2-1	28.21	0.954	71.68	0.012	100.86
Electrum-S578-14a-2-2	27.88	0.372	71.85	0.000	100.10
Electrum-S578-14a-3-1	27.66	1.190	71.40	0.012	100.26
Electrum-S578-14a-3-2	27.70	0.833	71.14	0.000	99.67
Electrum-S578-14a-4-1-vfg	27.74	0.512	71.61	0.000	99.86
Electrum-S578-14a-5-1	27.57	0.667	71.74	0.019	100.00
Electrum-S578-14a-5-2	27.90	0.967	71.11	0.000	99.98
Electrum-S578-14a-6-1	27.96	0.982	72.02	0.000	100.96
Electrum-S578-14a-6-2	28.16	0.880	71.42	0.000	100.46
Electrum-S578-14a-7-1	28.07	0.374	71.59	0.000	100.03
Electrum-S578-14a-7-2	28.14	0.431	71.77	0.055	100.40
Electrum-S578-14a-7-3	28.01	0.720	70.58	0.096	99.41
Electrum-S578-14a-8-1-vlg	28.00	0.580	70.83	0.007	99.42
Electrum-S578-14a-8-2-vlg	28.55	0.763	71.25	0.000	100.56
Electrum-S578-14a-8-3-vlg	28.47	0.507	71.75	0.000	100.73
Electrum-S578-14a-8-4-vlg	28.20	0.309	71.68	0.008	100.20
Electrum-S578-14a-8-5-vlg	28.20	0.663	71.10	0.027	99.99
Electrum-S578-14a-9-1-vfg	28.07	0.116	71.19	0.010	99.39
Electrum-S578-14a-11-1-vfg	28.07	0.811	71.59	0.005	100.48
Electrum-S578-14a-12-1	27.89	0.609	71.17	0.000	99.67
Electrum-S578-14a-12-2	28.36	0.981	71.51	0.000	100.85
Sample S548-306a					
Electrum-S548-306a-1-1	40.59	0.574	59.01	0.000	100.17
Electrum-S548-306a-1-2	41.12	0.335	58.27	0.000	99.73
Electrum-S548-306a-1-3	40.81	0.427	58.13	0.090	99.46
Electrum-S548-306a-1-4	41.14	0.510	58.06	0.000	99.71

Analysis Spot ID	Ag (wt%)	Hg (wt%)	Au (wt%)	Te (wt%)	Total
Electrum-S548-306a-2-1	40.97	0.354	58.71	0.000	100.03
Electrum-S548-306a-2-2	41.23	0.510	58.49	0.118	100.35
Electrum-S548-306a-2-3	40.91	0.160	58.74	0.000	99.81
Electrum-S548-306a-2-4	41.09	0.097	58.29	0.000	99.48
Electrum-S548-306a-2-5	42.26	0.352	57.79	0.057	100.46
Electrum-S548-306a-3-1	41.00	0.275	58.58	0.000	99.86
Electrum-S548-306a-3-2	41.13	0.031	58.26	0.000	99.42
Electrum-S548-306a-4-1	41.35	0.334	58.74	0.000	100.42
Electrum-S548-306a-4-2	40.82	0.000	57.86	0.000	98.68
Electrum-S548-306a-4-3	41.51	0.204	57.08	0.000	98.79
Electrum-S548-306a-5-1-vlg	41.75	0.568	58.19	0.000	100.51
Electrum-S548-306a-5-2-vlg	41.19	0.037	57.72	0.046	98.99
Electrum-S548-306a-5-3-vlg	41.53	0.246	57.91	0.000	99.69
Electrum-S548-306a-5-4-vlg	41.36	0.086	58.41	0.000	99.86
Electrum-S548-306a-5-5-vlg	41.06	0.572	58.50	0.056	100.19
Electrum-S548-306a-5-6-vlg	41.99	0.000	58.03	0.000	100.02
Electrum-S548-306a-6-2	41.01	0.314	57.97	0.079	99.37
Electrum-S548-306a-6-3	41.89	0.198	57.56	0.013	99.66
Electrum-S548-306a-7-1-vfg	40.45	0.382	57.06	0.000	97.89
Electrum-S548-306a-8-1-vfg	41.16	0.000	57.99	0.000	99.15
Electrum-S548-306a-9-1-vfg	40.42	0.126	58.24	0.000	98.79
Electrum-S548-306a-10-1-vfg	42.04	0.442	56.65	0.000	99.13
Sample S136-228a					
Electrum-S136-228a-1-1	38.19	0.762	61.00	0.000	99.95
Electrum-S136-228a-1-2	38.25	0.851	61.45	0.000	100.55
Electrum-S136-228a-1-3	38.65	0.381	61.81	0.000	100.84
Electrum-S136-228a-2-1-dark	38.85	0.564	61.00	0.037	100.45
Electrum-S136-228a-2-2	38.27	0.857	60.85	0.069	100.05
Electrum-S136-228a-2-3-light	38.29	1.010	61.81	0.034	101.14
Electrum-S136-228a-3-1	38.69	0.791	59.90	0.000	99.38
Electrum-S136-228a-4-1	38.24	0.733	61.32	0.000	100.29
Electrum-S136-228a-4-2	38.53	0.883	60.52	0.000	99.93
Electrum-S136-228a-4-3	38.65	0.681	61.46	0.000	100.79
Electrum-S136-228a-4-4	38.47	0.930	61.22	0.000	100.62
Electrum-S136-228a-5-1	37.86	0.729	61.67	0.000	100.26
Electrum-S136-228a-5-2	38.03	0.561	61.35	0.000	99.94
Electrum-S136-228a-5-3	37.78	0.500	61.24	0.000	99.52
Electrum-S136-228a-5-4	37.90	0.752	61.20	0.000	99.85
Electrum-S136-228a-5-5	37.98	0.218	61.45	0.000	99.65
Electrum-S136-228a-5-6	37.74	0.572	61.75	0.000	100.06
Electrum-S136-228a-6-1	37.65	0.860	61.30	0.000	99.81
Electrum-S136-228a-6-2	37.80	0.709	62.14	0.000	100.65

Analysis Spot ID	Ag (wt%)	Hg (wt%)	Au (wt%)	Te (wt%)	Total
Electrum-S136-228a-6-3	38.05	1.100	62.39	0.000	101.54
Electrum-S136-228a-6-4	37.85	0.576	61.17	0.000	99.60
Electrum-S136-228a-6-5	38.21	1.320	61.08	0.000	100.61
Electrum-S136-228a-7-1	37.81	0.789	62.11	0.052	100.76
Electrum-S136-228a-7-2	37.98	0.283	61.81	0.000	100.07
Electrum-S136-228a-7-3	37.93	0.467	61.83	0.000	100.23
Electrum-S136-228a-8-1	38.52	0.700	61.33	0.000	100.55
Electrum-S136-228a-8-2	37.84	0.437	60.99	0.000	99.27
Electrum-S136-228a-9-1	38.26	0.613	61.04	0.000	99.91
Electrum-S136-228a-9-2	37.67	0.778	60.49	0.000	98.94
Electrum-S136-228a-10-1-vfg	38.22	0.346	62.04	0.000	100.61
Electrum-S136-228a-11-1-vfg	39.16	0.200	61.73	0.060	101.15
Electrum-S136-228a-12-1-vfg	38.24	0.411	61.40	0.000	100.05
Electrum-S136-228a-13-1-vfg	38.63	0.189	60.94	0.000	99.76
Electrum-S136-228a-14-1-vfg	39.35	0.695	60.18	0.087	100.31
Electrum-S136-228a-15-1	37.64	0.376	61.99	0.000	100.01
Electrum-S136-228a-15-2	37.77	0.779	62.30	0.063	100.91
Electrum-S136-228a-15-3	37.81	0.948	62.08	0.000	100.84
Sample S430-136a					
S430-136a_1_N-S	37.07	N/A	62.89	N/A	100.55
S430-136a_1_N-S	36.65	N/A	63.24	N/A	100.52
S430-136a_1_N-S	36.70	N/A	62.49	N/A	99.76
S430-136a_1_N-S	37.24	N/A	62.65	N/A	100.51
S430-136a_1_N-S	37.20	N/A	62.36	N/A	100.06
S430-136a_2_N-S	36.89	N/A	61.87	N/A	99.27
S430-136a_2_N-S	37.45	N/A	63.32	N/A	101.31
S430-136a_2_N-S	36.86	N/A	63.36	N/A	100.87
S430-136a_2_N-S	37.15	N/A	62.92	N/A	100.70
S430-136a_2_N-S	37.25	N/A	62.36	N/A	100.26
S430-136a_3_E-W_Py	37.43	N/A	61.84	N/A	99.99
S430-136a_3_E-W_Py	38.68	N/A	61.68	N/A	100.88
S430-136a_3_E-W_Py	38.64	N/A	60.68	N/A	100.03
S430-136a_3_E-W_Py	38.92	N/A	60.64	N/A	100.15
Sample S195-194a					
SU-195-194a_1	38.07	N/A	60.95	N/A	99.97
SU-195-194a_1	36.96	N/A	61.47	N/A	99.31
SU-195-194a_1	36.99	N/A	61.47	N/A	99.35
SU-195-194a_2	38.93	N/A	60.38	N/A	100.29
SU-195-194a_2	38.76	N/A	59.92	N/A	99.52
SU-195-194a_2	38.37	N/A	60.63	N/A	99.95
SU-195-194a_2	39.03	N/A	60.35	N/A	100.33

Analysis Spot ID	Ag (wt%)	Hg (wt%)	Au (wt%)	Te (wt%)	Total
SU-195-194a_2	39.03	N/A	61.55	N/A	101.51
SU-195-194a_3	38.83	N/A	60.46	N/A	100.22
SU-195-194a_3	39.26	N/A	60.24	N/A	100.64
SU-195-194a_3	39.52	N/A	60.91	N/A	101.30
SU-195-194a_3	38.67	N/A	61.71	N/A	101.27
SU-195-194a_4_DVM	38.04	N/A	60.53	N/A	99.50
SU-195-194a_4_DVM	38.96	N/A	58.49	N/A	98.57
SU-195-194a_4_DVM	38.80	N/A	58.50	N/A	98.30
SU-195-194a_4_DVM	40.29	N/A	58.98	N/A	100.37
SU-195-194a_5_DVM	40.87	N/A	57.57	N/A	99.59
SU-195-194a_6_DVM	40.60	N/A	57.98	N/A	99.67
Sample S312-456a					
SU-312-456a_2	59.72	N/A	35.89	N/A	97.11
SU-312-456a_2	57.98	N/A	36.96	N/A	96.53
SU-312-456a_2	58.99	N/A	37.51	N/A	98.09
SU-312-456a_5	60.00	N/A	38.20	N/A	99.93
SU-312-456a_5	64.43	N/A	32.06	N/A	97.68
SU-312-456a_6	59.42	N/A	37.71	N/A	98.77
SU-312-456a_6	58.28	N/A	35.18	N/A	95.05
SU-312-456a_6	60.61	N/A	34.47	N/A	96.76
Sample S393-76a					
SU-393-76a_1	31.23	N/A	68.33	N/A	100.03
SU-393-76a_1	31.10	N/A	68.20	N/A	99.78
SU-393-76a_1	30.92	N/A	67.92	N/A	99.23
SU-393-76a_1	31.20	N/A	67.87	N/A	99.51
SU-393-76a_1	31.47	N/A	67.94	N/A	99.84
SU-393-76a_2	31.83	N/A	65.88	N/A	98.07
SU-393-76a_2	31.85	N/A	66.79	N/A	98.97
SU-393-76a_2	31.67	N/A	67.14	N/A	99.15
SU-393-76a_2	32.01	N/A	68.10	N/A	100.48
SU-393-76a_2	31.98	N/A	67.95	N/A	100.42
SU-393-76a_3	31.24	N/A	68.52	N/A	100.28
SU-393-76a_3	31.24	N/A	67.54	N/A	99.21
SU-393-76a_3	31.63	N/A	68.15	N/A	100.08
SU-393-76a_3	31.76	N/A	67.38	N/A	99.56
SU-393-76a_4	31.64	N/A	68.50	N/A	100.55
SU-393-76a_4	31.31	N/A	67.90	N/A	99.60
SU-393-76a_4	31.33	N/A	68.55	N/A	100.27
SU-393-76a_4	30.92	N/A	68.57	N/A	99.98
SU-393-76a_4	31.10	N/A	68.83	N/A	100.50
SU-393-76a_5	31.48	N/A	67.73	N/A	99.80

Analysis Spot ID	Ag (wt%)	Hg (wt%)	Au (wt%)	Te (wt%)	Total
SU-393-76a_5	31.13	N/A	68.05	N/A	99.68
SU-393-76a_5	31.20	N/A	67.22	N/A	99.18
SU-393-76a_5	31.18	N/A	67.64	N/A	99.76
SU-393-76a_5	31.54	N/A	68.19	N/A	100.53
SU-393-76a_6	31.11	N/A	67.43	N/A	99.26
SU-393-76a_6	30.98	N/A	67.07	N/A	98.69
SU-393-76a_6	31.62	N/A	66.72	N/A	98.99
Sample S434-29a					
SU-434-29a_1	41.30	N/A	57.77	N/A	99.89
SU-434-29a_1	41.31	N/A	57.11	N/A	99.18
SU-434-29a_1	41.53	N/A	56.39	N/A	98.64
SU-434-29a_1	41.69	N/A	57.61	N/A	100.04
SU-434-29a_1	41.43	N/A	57.58	N/A	99.75
SU-434-29a_2	41.14	N/A	56.30	N/A	98.41
SU-434-29a_2	40.43	N/A	57.25	N/A	98.51
SU-434-29a_2	41.26	N/A	57.37	N/A	99.35
SU-434-29a_2	41.47	N/A	57.69	N/A	99.98
SU-434-29a_2	41.56	N/A	57.32	N/A	99.65
SU-434-29a_3	40.50	N/A	57.51	N/A	98.70
SU-434-29a_3	41.28	N/A	58.52	N/A	100.67
SU-434-29a_3	41.00	N/A	57.71	N/A	99.33
SU-434-29a_3	41.49	N/A	58.28	N/A	100.49
SU-434-29a_3	41.70	N/A	57.31	N/A	99.73
SU-434-29a_4	41.73	N/A	56.82	N/A	99.41
SU-434-29a_4	41.58	N/A	58.41	N/A	100.73
SU-434-29a_4	42.01	N/A	58.26	N/A	100.96
SU-434-29a_4	42.09	N/A	58.70	N/A	101.58
SU-434-29a_4	41.89	N/A	58.70	N/A	101.47
SU-434-29a_5_DVM	40.73	N/A	58.32	N/A	99.90
SU-434-29a_5_DVM	40.68	N/A	58.13	N/A	99.55
SU-434-29a_5_DVM	41.12	N/A	58.60	N/A	100.56
SU-434-29a_5_DVM	41.13	N/A	57.74	N/A	99.77
SU-434-29a_6_DVM	41.35	N/A	57.63	N/A	99.77
SU-434-29a_6_DVM	41.28	N/A	57.93	N/A	100.06
SU-434-29a_6_DVM	41.10	N/A	57.05	N/A	98.99
Sample S345-162a					
SU-345-162a_1	32.58	N/A	67.53	N/A	100.60
SU-345-162a_2	31.94	N/A	68.26	N/A	100.55
SU-345-162a_2	32.11	N/A	68.21	N/A	100.74
SU-345-162a_2	32.29	N/A	67.67	N/A	100.32
SU-345-162a_2	32.16	N/A	68.48	N/A	100.93

Analysis Spot ID	Ag (wt%)	Hg (wt%)	Au (wt%)	Te (wt%)	Total
SU-345-162a_2	32.18	N/A	68.45	N/A	101.12
SU-345-162a_4	30.64	N/A	69.34	N/A	100.43
SU-345-162a_4	30.33	N/A	69.91	N/A	100.50
SU-345-162a_4	30.15	N/A	68.57	N/A	99.09
SU-345-162a_4	30.02	N/A	69.60	N/A	99.99
SU-345-162a_4	30.40	N/A	69.19	N/A	99.81
SU-345-162a_5	30.25	N/A	70.18	N/A	100.82
SU-345-162a_5	30.26	N/A	70.43	N/A	101.02
SU-345-162a_5	30.70	N/A	69.31	N/A	100.35
SU-345-162a_5	30.78	N/A	69.52	N/A	100.66
SU-345-162a_5	30.52	N/A	69.15	N/A	100.02
SU-345-162a_6	30.26	N/A	69.03	N/A	99.68
SU-345-162a_6	30.41	N/A	70.03	N/A	100.84
SU-345-162a_6	30.27	N/A	70.59	N/A	101.18
SU-345-162a_6	30.35	N/A	70.60	N/A	101.26
SU-345-162a_6	30.55	N/A	70.02	N/A	101.00
Sample S510-201a					
SU-510-201a_electrum_1	34.51	N/A	64.27	N/A	99.42
SU-510-201a_electrum_1	34.70	N/A	64.61	N/A	99.93
SU-510-201a_electrum_1	34.97	N/A	64.47	N/A	100.02
SU-510-201a_electrum_1	35.28	N/A	63.25	N/A	99.42
SU-510-201a_electrum_1	35.78	N/A	64.61	N/A	101.04
SU-510-201a_electrum_1	35.25	N/A	64.18	N/A	100.13
SU-510-201a_electrum_2	34.66	N/A	64.58	N/A	99.87
SU-510-201a_electrum_2	35.01	N/A	63.84	N/A	99.62
SU-510-201a_electrum_2	35.19	N/A	64.48	N/A	100.36
SU-510-201a_electrum_2	35.27	N/A	65.22	N/A	101.10
SU-510-201a_electrum_2	34.57	N/A	64.32	N/A	99.55
SU-510-201a_electrum_2	35.17	N/A	64.59	N/A	100.51
SU-510-201a_electrum_3	34.47	N/A	64.04	N/A	99.08
SU-510-201a_electrum_3	35.21	N/A	65.17	N/A	101.12
SU-510-201a_electrum_3	35.20	N/A	64.55	N/A	100.38
SU-510-201a_electrum_3	35.24	N/A	63.86	N/A	99.71
SU-510-201a_electrum_3	35.07	N/A	64.33	N/A	100.20
SU-510-201a_electrum_3	35.50	N/A	64.03	N/A	100.15
SU-510-201a_electrum_4	33.99	N/A	64.79	N/A	99.44
SU-510-201a_electrum_4	34.69	N/A	65.34	N/A	100.64
SU-510-201a_electrum_4	34.39	N/A	65.19	N/A	100.23
SU-510-201a_electrum_4	34.77	N/A	63.91	N/A	99.40
SU-510-201a_electrum_4	35.18	N/A	62.43	N/A	98.17
SU-510-201a_electrum_NA_5	35.89	N/A	65.87	N/A	102.45
SU-510-201a_electrum_NA_5	35.98	N/A	65.37	N/A	102.07

Analysis Spot ID	Ag (wt%)	Hg (wt%)	Au (wt%)	Te (wt%)	Total
SU-510-201a_electrum_NA_5	35.44	N/A	64.96	N/A	101.09
SU-510-201a_electrum_NA_5	35.42	N/A	64.77	N/A	100.95
SU-510-201a_electrum_NA_5	36.04	N/A	64.68	N/A	101.39
SU-510-201a_electrum_NA_5	36.21	N/A	63.67	N/A	100.59
SU-510-201a_electrum_NA_6	36.01	N/A	65.11	N/A	101.82
SU-510-201a_electrum_NA_6	36.13	N/A	63.77	N/A	100.63
SU-510-201a_electrum_NA_6	36.27	N/A	65.24	N/A	102.15
SU-510-201a_electrum_NA_6	35.65	N/A	64.92	N/A	101.26
SU-510-201a_electrum_NA_6	36.02	N/A	64.42	N/A	101.17
SU-510-201a_electrum_NA_6	35.89	N/A	64.44	N/A	101.05
SU-510-201a_electrum_NA_6	35.66	N/A	65.13	N/A	101.37
SU-510-201a_electrum_NA_7	36.53	N/A	65.36	N/A	102.64
SU-510-201a_electrum_NA_7	36.21	N/A	64.23	N/A	101.11
SU-510-201a_electrum_NA_7	36.02	N/A	64.59	N/A	101.31
SU-510-201a_electrum_NA_7	35.58	N/A	64.55	N/A	100.84
SU-510-201a_electrum_NA_7	35.32	N/A	65.30	N/A	101.20
Sample 512-365a					
SU-512-365a_electrum_1	28.01	N/A	73.08	N/A	101.39
SU-512-365a_electrum_1	28.08	N/A	72.87	N/A	101.47
SU-512-365a_electrum_1	27.68	N/A	72.58	N/A	100.56
SU-512-365a_electrum_1	27.88	N/A	73.34	N/A	101.64
SU-512-365a_electrum_1	27.45	N/A	72.80	N/A	100.61
SU-512-365a_electrum_1	27.98	N/A	72.88	N/A	101.20
SU-512-365a_electrum_2	28.24	N/A	72.84	N/A	101.47
SU-512-365a_electrum_2	27.85	N/A	72.59	N/A	100.75
SU-512-365a_electrum_2	28.11	N/A	73.09	N/A	101.69
SU-512-365a_electrum_2	28.13	N/A	72.43	N/A	100.89
SU-512-365a_electrum_2	28.11	N/A	72.19	N/A	100.71
SU-512-365a_electrum_2	28.07	N/A	72.77	N/A	101.17
SU-512-365a_electrum_NA_3	27.68	N/A	72.18	N/A	100.24
SU-512-365a_electrum_NA_3	27.87	N/A	73.16	N/A	101.33
SU-512-365a_electrum_NA_3	27.74	N/A	72.25	N/A	100.32
SU-512-365a_electrum_NA_3	27.77	N/A	73.40	N/A	101.56
SU-512-365a_electrum_NA_3	28.06	N/A	73.63	N/A	102.16
SU-512-365a_electrum_NA_4	27.81	N/A	72.71	N/A	100.87
SU-512-365a_electrum_NA_4	27.35	N/A	72.96	N/A	100.68
SU-512-365a_electrum_NA_4	27.78	N/A	71.80	N/A	100.00
SU-512-365a_electrum_NA_4	28.13	N/A	72.41	N/A	100.83
SU-512-365a_electrum_NA_4	28.50	N/A	72.68	N/A	101.61
SU-512-365a_electrum_NA_4	28.19	N/A	72.86	N/A	101.44
SU-512-365a_electrum_NA2_5	28.42	N/A	73.44	N/A	102.19
SU-512-365a_electrum_NA2_5	28.16	N/A	71.92	N/A	100.38

Analysis Spot ID	Ag (wt%)	Hg (wt%)	Au (wt%)	Te (wt%)	Total
SU-512-365a_electrum_NA2_5	28.02	N/A	73.38	N/A	101.74
SU-512-365a_electrum_NA2_5	28.02	N/A	72.35	N/A	100.74
SU-512-365a_electrum_NA2_5	28.52	N/A	72.39	N/A	101.22
SU-512-365a_electrum_NA2_5	28.58	N/A	72.07	N/A	100.96
SU-512-365a_electrum_NA2_6	28.35	N/A	72.59	N/A	101.34
SU-512-365a_electrum_NA2_6	28.28	N/A	72.10	N/A	100.83
SU-512-365a_electrum_NA2_6	28.67	N/A	72.99	N/A	102.12
SU-512-365a_electrum_NA2_6	28.62	N/A	71.59	N/A	100.55
SU-512-365a_electrum_NA2_6	28.36	N/A	71.69	N/A	100.42
Sample S450-255a					
SU-450-255a_electrum_1	41.42	N/A	58.32	N/A	100.25
SU-450-255a_electrum_1	40.64	N/A	58.83	N/A	99.80
SU-450-255a_electrum_1	40.69	N/A	59.52	N/A	100.61
SU-450-255a_electrum_1	40.77	N/A	59.68	N/A	100.80
SU-450-255a_electrum_1	40.98	N/A	59.59	N/A	100.98
SU-450-255a_electrum_1	40.79	N/A	59.92	N/A	100.92
SU-450-255a_electrum_1	41.07	N/A	59.44	N/A	101.04
SU-450-255a_electrum_1	41.03	N/A	58.90	N/A	100.31
SU-450-255a_electrum_2	40.28	N/A	59.16	N/A	99.75
SU-450-255a_electrum_2	40.88	N/A	59.62	N/A	100.78
SU-450-255a_electrum_2	41.15	N/A	59.43	N/A	100.95
SU-450-255a_electrum_2	41.73	N/A	58.94	N/A	101.20
SU-450-255a_electrum_2	43.20	N/A	57.98	N/A	102.13
SU-450-255a_electrum_3	41.98	N/A	57.82	N/A	100.36
SU-450-255a_electrum_3	42.43	N/A	58.21	N/A	101.14
SU-450-255a_electrum_3	42.28	N/A	57.82	N/A	100.91
SU-450-255a_electrum_3	42.79	N/A	58.18	N/A	101.74
SU-450-255a_electrum_3	43.78	N/A	59.15	N/A	103.55
SU-450-255a_electrum_4	42.99	N/A	56.96	N/A	100.73
SU-450-255a_electrum_4	41.58	N/A	57.57	N/A	99.60
SU-450-255a_electrum_4	42.71	N/A	57.87	N/A	101.03
SU-450-255a_electrum_4	42.84	N/A	57.60	N/A	101.33
SU-450-255a_electrum_4	43.38	N/A	57.72	N/A	101.94
Sample S327-21a					
Electrum-S327-21a-1-1	40.73	0.696	58.60	0.000	100.03
Electrum-S327-21a-1-2	40.75	0.411	58.63	0.000	99.79
Electrum-S327-21a-1-3	40.64	0.345	59.31	0.000	100.30
Electrum-S327-21a-1-4	40.73	0.778	59.13	0.000	100.64
Electrum-S327-21a-1-5	40.65	0.631	59.05	0.000	100.33
Electrum-S327-21a-1-6	40.41	0.993	59.09	0.000	100.49
Electrum-S327-21a-1-7	40.54	0.761	59.02	0.012	100.33

Analysis Spot ID	Ag (wt%)	Hg (wt%)	Au (wt%)	Te (wt%)	Total
Electrum-S327-21a-1-8	40.73	0.345	58.62	0.000	99.70
Electrum-S327-21a-1-9	40.43	0.417	59.77	0.000	100.62
Electrum-S327-21a-2-1	40.52	0.784	58.35	0.047	99.70
Electrum-S327-21a-2-2	40.43	0.739	58.59	0.022	99.78
Electrum-S327-21a-2-3	40.38	0.696	59.01	0.011	100.10
Electrum-S327-21a-2-4	40.17	0.366	59.39	0.000	99.93
Electrum-S327-21a-2-5	40.39	1.220	59.29	0.000	100.90
Electrum-S327-21a-2-6	40.08	0.477	59.54	0.000	100.10
Electrum-S327-21a-3-1	40.72	0.012	59.09	0.000	99.82
Electrum-S327-21a-3-2	40.90	0.742	58.86	0.000	100.50
Electrum-S327-21a-3-3	40.35	0.371	59.04	0.000	99.76
Electrum-S327-21a-3-4	40.39	0.479	59.15	0.000	100.02
Electrum-S327-21a-3-5	39.85	0.484	59.49	0.000	99.82
Electrum-S327-21a-4-1	40.22	0.782	59.78	0.000	100.78
Electrum-S327-21a-4-2	40.46	1.390	59.33	0.000	101.18
Electrum-S327-21a-4-3	40.43	0.517	59.83	0.000	100.78
Electrum-S327-21a-4-4	39.39	0.435	60.39	0.000	100.22
Electrum-S327-21a-4-5	39.60	0.380	60.18	0.000	100.16
Electrum-S327-21a-4-6	40.26	0.334	58.64	0.000	99.23
Electrum-S327-21a-5-1	39.38	0.787	59.71	0.000	99.88
Electrum-S327-21a-5-2	40.34	0.000	59.33	0.000	99.67
Electrum-S327-21a-5-3	40.53	0.921	59.31	0.000	100.76
Electrum-S327-21a-5-4	40.46	0.417	58.74	0.000	99.62
Electrum-S327-21a-5-5	40.69	0.684	59.46	0.000	100.83
Electrum-S327-21a-6-2-pyinc	40.00	1.170	59.16	0.000	100.33
Electrum-S327-21a-7-1-pyinc	40.20	0.669	58.54	0.000	99.41
Electrum-S327-21a-7-2-pyinc	40.14	0.728	59.38	0.000	100.25
Electrum-S327-21a-8-1-pyinc	40.71	0.967	58.83	0.000	100.51
Electrum-S327-21a-9-1-pyinc	40.43	0.337	59.75	0.000	100.52
Electrum-S327-21a-10-1-pyinc	39.92	0.582	59.06	0.000	99.56
Electrum-S327-21a-11-1-pyinc	40.21	0.896	59.66	0.000	100.77
Electrum-S327-21a-12-1	44.23	0.942	54.67	0.000	99.84
Electrum-S327-21a-12-2	43.51	0.139	56.64	0.000	100.29
Electrum-S327-21a-12-3	43.59	0.103	56.70	0.013	100.41
Electrum-S327-21a-12-4	42.77	0.457	56.09	0.000	99.32
Electrum-S327-21a-12-5	42.73	0.542	57.08	0.039	100.39
Electrum-S327-21a-13-1	43.67	0.671	55.05	0.016	99.41
Electrum-S327-21a-13-2	43.50	0.687	56.48	0.021	100.69
Electrum-S327-21a-13-3	43.41	1.170	56.66	0.000	101.24
Electrum-S327-21a-13-4	43.66	1.030	57.03	0.000	101.72
Electrum-S327-21a-14-1-pyinc	43.66	1.080	56.01	0.000	100.75
Electrum-S327-21a-15-1-pyinc	44.04	0.444	55.74	0.010	100.23
Electrum-S327-21a-15-2-pyinc	44.56	0.712	55.61	0.000	100.88

166

Analysis Spot ID	Ag (wt%)	Hg (wt%)	Au (wt%)	Te (wt%)	Total
Sample S322-31a					
Electrum-S322-31a-1-1-light	49.93	0.366	50.16	0.000	100.46
Electrum-S322-31a-1-2-dark	73.04	0.777	28.26	0.000	102.08
Electrum-S322-31a-1-3-dark	78.01	0.822	22.21	0.000	101.04
Electrum-S322-31a-1-4-light	45.93	0.663	53.37	0.000	99.96
Electrum-S322-31a-1-5-dark	83.14	0.395	18.15	0.000	101.69
Electrum-S322-31a-2-1-light	51.41	0.430	50.59	0.000	102.43
Electrum-S322-31a-2-4-light	49.56	0.694	53.28	0.000	103.53
Electrum-S322-31a-2-5-light	51.03	0.708	49.76	0.024	101.52
Electrum-S322-31a-2-6-dark	76.64	0.077	26.03	0.000	102.75
Electrum-S322-31a-2-7-dark	73.39	0.335	21.79	0.000	95.52
Sample S334-543a					
Electrum-S334-543a-1-1	34.96	0.436	64.14	0.000	99.54
Electrum-S334-543a-1-2	35.51	0.036	64.20	0.000	99.75
Electrum-S334-543a-2-1	35.46	0.000	64.45	0.000	99.91
Electrum-S334-543a-2-2	35.69	0.015	64.08	0.000	99.79
Electrum-S334-543a-3-1	34.91	0.300	64.51	0.000	99.72
Electrum-S334-543a-3-2	35.32	0.448	64.21	0.014	99.99
Electrum-S334-543a-3-3	35.56	0.000	64.62	0.000	100.18
Electrum-S334-543a-4-1	35.10	0.341	65.16	0.029	100.63
Electrum-S334-543a-4-2	35.14	0.000	64.96	0.000	100.10
Electrum-S334-543a-5-1	35.55	0.000	64.27	0.000	99.82
Electrum-S334-543a-6-1	34.24	0.190	66.30	0.000	100.73
Electrum-S334-543a-6-2	33.91	0.000	64.68	0.000	98.59
Electrum-S334-543a-7-1	35.18	0.152	64.78	0.000	100.11
Electrum-S334-543a-7-2	35.21	0.295	64.30	0.011	99.82
Electrum-S334-543a-8-1	35.32	0.156	65.00	0.000	100.48
Electrum-S334-543a-8-2	35.51	0.305	64.19	0.011	100.02
Electrum-S334-543a-9-1	34.94	0.206	64.86	0.042	100.05
Electrum-S334-543a-9-2	35.29	0.373	64.17	0.000	99.83
Electrum-S334-543a-10-1	34.97	0.000	65.14	0.037	100.15
Electrum-S334-543a-10-2	34.88	0.000	63.49	0.000	98.37
Sample S334-382a					
Electrum-S334-382a-1-1	42.50	0.381	57.82	0.000	100.70
Electrum-S334-382a-1-2	42.51	0.240	58.05	0.000	100.80
Electrum-S334-382a-1-3	42.70	0.053	58.19	0.000	100.94
Electrum-S334-382a-1-4	42.42	0.259	58.44	0.000	101.12
Electrum-S334-382a-1-5	43.01	0.119	57.77	0.000	100.90
Electrum-S334-382a-2-1	42.97	0.000	57.24	0.007	100.22
Electrum-S334-382a-3-1	43.07	0.263	57.01	0.067	100.41

167

Analysis Spot ID	Ag (wt%)	Hg (wt%)	Au (wt%)	Te (wt%)	Total
Electrum-S334-382a-4-1	42.29	0.306	57.62	0.000	100.22
Electrum-S334-382a-4-2	42.41	0.300	58.16	0.000	100.87
Electrum-S334-382a-4-3	42.95	0.318	57.79	0.013	101.07
Electrum-S334-382a-4-4	42.67	0.624	57.20	0.044	100.54
Electrum-S334-382a-4-5	43.28	0.000	57.27	0.000	100.55
Electrum-S334-382a-5-1	41.61	0.248	58.24	0.000	100.10
Electrum-S334-382a-5-2	42.35	0.205	58.45	0.006	101.01
Electrum-S334-382a-5-3	42.18	0.074	58.04	0.000	100.29
Electrum-S334-382a-5-4	41.81	0.755	58.41	0.017	100.99
Electrum-S334-382a-5-5	41.81	0.140	58.22	0.000	100.17
Electrum-S334-382a-6-1	40.46	0.000	59.83	0.000	100.29
Electrum-S334-382a-6-2	41.14	0.305	59.33	0.000	100.78
Electrum-S334-382a-6-3	40.88	0.267	59.85	0.000	101.00
Electrum-S334-382a-6-4	40.52	0.119	59.61	0.000	100.25
Electrum-S334-382a-7-1	42.16	0.976	58.16	0.020	101.32
Electrum-S334-382a-7-2	42.49	0.623	58.32	0.008	101.44
Electrum-S334-382a-7-3	42.43	0.260	57.28	0.000	99.97
Electrum-S334-382a-7-4	42.78	0.000	58.11	0.000	100.89
Sample S193-674a					
Electrum-S193-674a-1-1	38.54	0.044	62.87	0.000	101.45
Electrum-S193-674a-1-2	38.73	0.264	61.90	0.000	100.89
Electrum-S193-674a-1-3	38.98	0.108	60.69	0.000	99.78
Electrum-S193-674a-1-4	38.66	0.000	60.43	0.000	99.09
Electrum-S193-674a-2-1	38.74	0.654	61.40	0.000	100.79
Electrum-S193-674a-2-2	38.87	0.127	61.90	0.000	100.90
Electrum-S193-674a-2-3	39.67	0.219	61.32	0.000	101.21
Electrum-S193-674a-3-2	38.44	0.000	61.83	0.000	100.27
Electrum-S193-674a-3-3	38.82	0.303	61.33	0.000	100.45
Electrum-S193-674a-4-1	38.78	0.345	61.86	0.006	100.99
Electrum-S193-674a-4-2	39.15	0.453	62.13	0.000	101.73
Electrum-S193-674a-4-3	38.76	0.000	60.91	0.000	99.67
Electrum-S193-674a-5-1	38.15	0.167	62.75	0.000	101.07
Electrum-S193-674a-5-2	38.40	0.513	62.03	0.028	100.97
Electrum-S193-674a-5-3	38.25	0.117	61.57	0.000	99.94
Electrum-S193-674a-5-4	38.36	0.000	60.35	0.000	98.71
Electrum-S193-674a-5-1	38.38	0.700	62.37	0.000	101.45
Electrum-S193-674a-5-2	38.58	0.610	62.52	0.000	101.71
Electrum-S193-674a-5-3	38.40	0.000	62.45	0.000	100.85
Electrum-S193-674a-5-4	38.29	0.000	62.36	0.000	100.65
Electrum-S193-674a-5-5	38.89	0.045	61.61	0.000	100.55
Electrum-S193-674a-6-1	39.31	0.466	61.24	0.000	101.02
Electrum-S193-674a-6-2	39.78	0.088	60.26	0.018	100.15

Analysis Spot ID	Ag (wt%)	Hg (wt%)	Au (wt%)	Te (wt%)	Total
Electrum-S193-674a-6-3	39.86	0.000	61.16	0.000	101.02
Electrum-S193-674a-7-1	39.38	0.000	61.00	0.000	100.38
Electrum-S193-674a-7-2	39.57	0.636	60.64	0.000	100.85
Electrum-S193-674a-7-3	38.16	0.403	62.25	0.000	100.81
Electrum-S193-674a-7-4	38.61	0.000	62.28	0.000	100.89
Electrum-S193-674a-7-5	38.53	0.372	61.93	0.000	100.83
Electrum-S193-674a-7-6	38.86	0.000	61.63	0.000	100.49
Electrum-S193-674a-7-7	39.05	0.312	61.34	0.000	100.70
Sample S320-10a					
Electrum-S320-10a-1-1	43.13	0.666	57.10	0.000	100.90
Electrum-S320-10a-1-2	42.39	0.678	56.92	0.000	99.99
Electrum-S320-10a-1-3	42.36	1.060	57.45	0.000	100.87
Electrum-S320-10a-1-4	42.97	0.744	56.59	0.000	100.30
Electrum-S320-10a-1-5	42.68	1.010	56.56	0.031	100.28
Electrum-S320-10a-2-1	42.45	0.931	57.56	0.000	100.94
Electrum-S320-10a-2-2	41.73	0.853	58.44	0.000	101.02
Electrum-S320-10a-2-3	44.00	0.790	56.16	0.000	100.95
Electrum-S320-10a-3-1-gal-eqbm	42.94	0.243	56.19	0.000	99.37
Electrum-S320-10a-3-2-gal-eqbm	42.75	1.130	56.03	0.000	99.91
Electrum-S320-10a-4-1	42.88	0.531	56.58	0.000	99.99
Electrum-S320-10a-4-2	42.13	1.240	55.97	0.000	99.34
Electrum-S320-10a-5-1	44.75	1.070	53.03	0.000	98.85
Electrum-S320-10a-5-2	43.12	1.210	56.11	0.000	100.44
Electrum-S320-10a-5-3	42.89	0.737	55.52	0.000	99.15
Electrum-S320-10a-6-1	43.65	0.767	55.63	0.036	100.08
Electrum-S320-10a-6-2	44.77	0.978	53.54	0.024	99.31
Electrum-S320-10a-7-1	44.01	0.486	55.25	0.023	99.77
Electrum-S320-10a-7-2	43.06	1.240	56.22	0.000	100.52
Electrum-S320-10a-8-1	42.56	0.419	57.14	0.021	100.14
Electrum-S320-10a-8-2	43.25	0.902	56.27	0.042	100.46
Electrum-S320-10a-9-1	42.78	0.627	55.66	0.000	99.07
Electrum-S320-10a-10-1	42.37	1.090	56.04	0.000	99.50
Electrum-S320-10a-10-2	42.46	0.854	56.48	0.000	99.79
Electrum-S320-10a-11-1	42.22	0.987	57.49	0.043	100.74
Electrum-S320-10a-12-1	40.95	0.492	58.48	0.000	99.92
Electrum-S320-10a-12-2	41.80	0.710	57.38	0.000	99.89
Electrum-S320-10a-12-3	41.46	0.636	58.08	0.000	100.18
Electrum-S320-10a-13-1	43.19	0.665	56.69	0.000	100.55
Electrum-S320-10a-13-2	43.14	0.735	56.36	0.000	100.24
Sample S523-313a					
Electrum-S523-313a-1-1	37.53	0.000	63.05	0.000	100.58

169

Analysis Spot ID	Ag (wt%)	Hg (wt%)	Au (wt%)	Te (wt%)	Total
Electrum-S523-313a-1-2	36.40	0.000	63.48	0.000	99.88
Electrum-S523-313a-1-3	37.76	0.000	62.23	0.000	99.99
Electrum-S523-313a-1-4	36.55	0.000	63.20	0.000	99.75
Electrum-S523-313a-1-5	37.92	0.000	63.73	0.000	101.65
Electrum-S523-313a-3-1	36.54	0.000	62.92	0.000	99.46
Electrum-S523-313a-3-2	36.77	0.000	63.88	0.000	100.65
Electrum-S523-313a-3-3	36.80	0.000	62.50	0.000	99.30
Electrum-S523-313a-3-4	36.86	0.000	62.55	0.000	99.41
Electrum-S523-313a-3-5	35.79	0.000	61.56	0.000	97.35
Electrum-S523-313a-3-6	37.53	0.000	63.40	0.000	100.93
Electrum-S523-313a-3-7	39.09	0.000	62.69	0.000	101.78
Electrum-S523-313a-6-1	36.81	0.000	62.79	0.000	99.60
Electrum-S523-313a-6-2	37.57	0.000	62.68	0.000	100.25
Electrum-S523-313a-6-3	36.88	0.000	63.72	0.000	100.60
Electrum-S523-313a-6-4	37.92	0.000	61.82	0.000	99.74
Electrum-S523-313a-7-1	36.42	0.000	64.42	0.000	100.84
Electrum-S523-313a-7-2	36.10	0.000	63.87	0.000	99.97
Electrum-S523-313a-7-3	36.73	0.000	63.43	0.000	100.16
Electrum-S523-313a-8-1	36.90	0.000	63.37	0.000	100.27
Electrum-S523-313a-8-2	36.00	0.000	63.81	0.000	99.81
Electrum-S523-313a-8-3	35.58	0.000	64.33	0.000	99.91
Electrum-S523-313a-8-4	36.78	0.000	63.72	0.000	100.50
Electrum-S523-313a-8-5	37.18	0.909	63.68	0.000	101.77
Electrum-S523-313a-9-1	37.39	0.000	63.26	0.000	100.65
Electrum-S523-313a-9-2	35.75	0.000	64.06	0.000	99.81
Electrum-S523-313a-9-3	36.43	0.000	63.22	0.000	99.65
Electrum-S523-313a-10-1	36.52	0.000	63.67	0.000	100.19
Electrum-S523-313a-10-2	36.08	0.000	63.55	0.000	99.63
Electrum-S523-313a-10-3	36.83	0.000	62.62	0.000	99.45
Electrum-S523-313a-11-1	36.70	0.308	64.37	0.000	101.38
Electrum-S523-313a-11-2	36.43	0.000	63.24	0.000	99.67
Electrum-S523-313a-11-3	36.68	0.308	63.96	0.000	100.95
Electrum-S523-313a-11-4	36.74	0.000	63.66	0.000	100.40
Electrum-S523-313a-11-5	37.16	0.000	62.24	0.000	99.40
Electrum-S523-313a-12-1	36.27	0.000	64.75	0.000	101.02
Electrum-S523-313a-12-2	36.58	0.000	63.05	0.000	99.63
Electrum-S523-313a-12-3	36.26	0.000	63.63	0.000	99.89
Sample S524-124a					
Electrum-S524-124a-1-1	41.52	0.181	58.88	0.000	100.58
Electrum-S524-124a-1-2	41.45	0.000	59.16	0.000	100.61
Electrum-S524-124a-1-3	40.68	0.000	59.13	0.000	99.81
Electrum-S524-124a-2-1	40.85	0.000	59.35	0.000	100.20

Analysis Spot ID	Ag (wt%)	Hg (wt%)	Au (wt%)	Te (wt%)	Total
Electrum-S524-124a-2-2	40.79	1.210	59.35	0.000	101.35
Electrum-S524-124a-2-3	41.47	0.000	59.53	0.000	101.00
Electrum-S524-124a-2-4	40.66	0.000	59.60	0.000	100.26
Electrum-S524-124a-3-1	41.06	0.000	59.16	0.000	100.22
Electrum-S524-124a-3-2	41.14	0.000	59.04	0.000	100.18
Electrum-S524-124a-3-	40.93	0.911	58.71	0.000	100.55
Electrum-S524-124a-3-4	41.06	0.000	59.30	0.000	100.36
Electrum-S524-124a-4-1	40.27	0.000	58.61	0.000	98.88
Electrum-S524-124a-4-	41.09	0.524	60.06	0.000	101.67
Electrum-S524-124a-4-3	40.21	0.000	60.09	0.000	100.30
Electrum-S524-124a-5-1	40.55	0.438	60.00	0.000	100.99
Electrum-S524-124a-5-2	40.87	0.000	59.35	0.000	100.22
Electrum-S524-124a-3	41.30	0.000	59.38	0.000	100.68
Electrum-S524-124a-5-4	40.96	0.000	59.65	0.000	100.61
Electrum-S524-124a-6-1	40.37	0.055	60.33	0.000	100.76
Electrum-S524-124a-6-2	40.49	0.000	59.56	0.000	100.05
Electrum-S524-124a-6-3	40.02	0.000	59.71	0.000	99.73
Electrum-S524-124a-6-4	40.31	0.000	59.81	0.000	100.12
Electrum-S524-124a-7-1	40.41	0.000	60.21	0.000	100.62
Electrum-S524-124a-7-2	40.27	0.000	59.39	0.000	99.66
Electrum-S524-124a-7-3	40.71	0.000	59.21	0.000	99.92
Electrum-S524-124a-8-1	41.46	0.353	58.48	0.000	100.29
Electrum-S524-124a-8-2	41.91	0.267	58.67	0.000	100.85
Electrum-S524-124a-8-3	42.21	0.000	58.74	0.000	100.95
Electrum-S524-124a-8-4	41.19	0.138	58.71	0.000	100.04
Electrum-S524-124a-dark-9-1	41.20	0.000	58.36	0.000	99.56
Electrum-S524-124a-dark-9-2	41.50	0.000	58.79	0.000	100.29
Electrum-S524-124a-dark-9-3	40.81	0.000	57.87	0.000	98.68
Electrum-S524-124a-dark-10-1	41.79	0.000	58.49	0.000	100.28
Electrum-S524-124a-dark-10-2	40.68	0.954	58.46	0.000	100.09
Electrum-S524-124a-dark-10-3	41.13	0.052	59.31	0.000	100.49
Electrum-S524-124a-dark-10-4	41.47	0.052	58.50	0.000	100.02
Electrum-S524-124a-11	40.87	0.227	58.57	0.000	99.67
Electrum-S524-124a-11-2	41.21	0.000	59.13	0.000	100.34
Electrum-S524-124a-11-3	42.39	0.000	57.63	0.000	100.02
Electrum-S524-124a-11	41.23	0.224	58.32	0.000	99.77
Electrum-S524-124a-11-5	41.82	0.000	58.92	0.000	100.74
Electrum-S524-124a-11-6	41.71	0.000	58.79	0.000	100.50
Electrum-S524-124a-12-1	43.08	0.000	58.28	0.000	101.36
Electrum-S524-124a-12-6	42.93	0.000	57.56	0.000	100.49
Electrum-S524-124a-12-7	42.95	0.000	57.79	0.000	100.74
Electrum-S524-124a-12-8	43.39	0.000	56.76	0.000	100.15
Electrum-S524-124a-13-1	42.93	0.000	57.61	0.000	100.54

171

Analysis Spot ID	Ag (wt%)	Hg (wt%)	Au (wt%)	Te (wt%)	Total
Electrum-S524-124a-13	41.66	0.897	58.27	0.000	100.83
Electrum-S524-124a-13-3	42.71	0.000	56.27	0.000	98.98
Electrum-S524-124a-13-4	42.94	0.000	56.56	0.000	99.50
Electrum-S524-124a-14-1	42.18	0.182	58.11	0.000	100.47
Electrum-S524-124a-14-2	42.66	0.000	58.57	0.000	101.23
Electrum-S524-124a-14-3	41.53	0.700	57.80	0.000	100.03
Electrum-S524-124a-14-4	41.92	0.000	57.76	0.000	99.68
Sample S525-49a					
Electrum-S525-49a-1-1	42.24	1.170	57.37	0.000	100.78
Electrum-S525-49a-1-2	42.96	0.000	57.09	0.000	100.05
Electrum-S525-49a-1-3	42.27	0.484	56.76	0.000	99.52
Electrum-S525-49a-2-1	41.45	0.000	57.49	0.000	98.94
Electrum-S525-49a-2-2	41.43	0.000	57.56	0.000	98.99
Electrum-S525-49a-2-3	41.59	0.354	58.35	0.000	100.29
Electrum-S525-49a-3-1	42.04	0.000	57.99	0.000	100.03
Electrum-S525-49a-3-2	41.78	0.000	58.00	0.000	99.78
Electrum-S525-49a-3-3	41.14	0.000	58.63	0.000	99.77
Electrum-S525-49a-3-4	41.28	0.000	57.91	0.000	99.19
Electrum-S525-49a-4-1	40.10	0.000	59.29	0.000	99.39
Electrum-S525-49a-4-5	41.21	0.000	58.12	0.000	99.33
Electrum-S525-49a-4-6	41.94	0.138	58.10	0.000	100.18
Electrum-S525-49a-5-1	40.65	0.000	58.83	0.000	99.48
Electrum-S525-49a-5-2	42.36	0.121	58.23	0.000	100.71
Electrum-S525-49a-light-6-1	40.14	0.000	60.35	0.000	100.49
Electrum-S525-49a-light-6-2	40.01	0.000	59.93	0.000	99.94
Electrum-S525-49a-light-6-3	39.98	0.000	60.44	0.000	100.42
Electrum-S525-49a-light-6-4	40.28	0.000	60.43	0.000	100.71
Electrum-S525-49a-light-7-1	38.75	0.000	61.76	0.000	100.51
Electrum-S525-49a-light-7-2	39.28	0.000	61.36	0.000	100.64
Electrum-S525-49a-light-7-3	39.15	0.000	61.77	0.000	100.92
Electrum-S525-49a-light-8-1	40.35	0.000	59.71	0.000	100.06
Electrum-S525-49a-light-8-2	39.77	0.000	60.18	0.000	99.95
Electrum-S525-49a-light-8-3	41.18	0.000	58.89	0.000	100.07
Electrum-S525-49a-light-9-1	37.85	0.000	61.01	0.000	98.86
Electrum-S525-49a-light-9-2	39.26	0.000	60.75	0.000	100.01
Electrum-S525-49a-light-9-3	38.77	0.000	62.17	0.000	100.94
Electrum-S525-49a-light-9-4	38.50	0.000	61.74	0.000	100.24
Electrum-S525-49a-light-9-5	37.78	0.000	62.12	0.000	99.90
Electrum-S525-49a-11-1	41.37	0.484	57.76	0.000	99.61
Electrum-S525-49a-11-2	41.25	0.225	57.44	0.000	98.92
Electrum-S525-49a-11-3	40.94	0.000	58.01	0.000	98.95
Electrum-S525-49a-11-4	42.11	0.000	58.19	0.000	100.30

Analysis Spot ID	Ag (wt%)	Hg (wt%)	Au (wt%)	Te (wt%)	Total
Electrum-S525-49a-11-5	41.77	0.000	57.59	0.000	99.36
Sample S525-50a					
Electrum-S525-50a1-1	40.29	0.481	60.60	0.000	101.37
Electrum-S525-50a-1-2	39.99	0.000	59.55	0.000	99.54
Electrum-S525-50a-1-3	40.58	0.000	59.07	0.000	99.65
Electrum-S525-50a-2-1	40.67	0.000	59.52	0.000	100.19
Electrum-S525-50a-2-3	40.93	0.000	58.43	0.000	99.36
Electrum-S525-50a-2-4	40.53	0.000	59.04	0.000	99.57
Electrum-S525-50a-3-1	40.30	0.481	58.98	0.000	99.76
Electrum-S525-50a-3-2	39.84	0.309	59.35	0.000	99.50
Electrum-S525-50a-6-1	38.98	0.308	60.81	0.000	100.10
Electrum-S525-50a-6-2	39.57	0.000	61.34	0.000	100.91
Electrum-S525-50a-6-3	39.57	0.000	61.71	0.000	101.28
Electrum-S525-50a--7-1	39.72	0.000	60.26	0.000	99.98
Electrum-S525-50a-8-1	39.47	0.000	60.18	0.000	99.65
Electrum-S525-50a-8-2	39.79	0.000	59.69	0.000	99.48
Electrum-S525-50a-dark-10-1	36.30	0.000	59.43	0.000	95.73
Electrum-S525-50a-dark-12-1	40.48	0.000	60.91	0.000	101.39
Electrum-S525-50a-dark-12-2	40.80	0.000	60.71	0.000	101.51
Electrum-S525-50a-dark-12-3	40.60	0.000	58.80	0.000	99.40
Electrum-S525-50a-dark-13-1	39.74	0.000	60.43	0.000	100.17
Electrum-S525-50a-dark-13-2	40.07	0.000	60.24	0.000	100.31
Electrum-S525-50a-dark-14-1	40.54	0.000	59.43	0.000	99.97
Electrum-S525-50a-dark-14-2	40.75	0.000	58.77	0.000	99.52
Electrum-S525-50a-dark-15-1	40.89	0.052	60.11	0.000	101.05
Electrum-S525-50a-dark-15-2	39.85	0.523	60.42	0.000	100.79
Sample S535-12a					
Electrum-S535-12a-dark-1-1	30.28	0.000	70.56	0.000	100.84
Electrum-S535-12a-dark-1-2	30.58	0.000	69.56	0.000	100.14
Electrum-S535-12a-dark-2-1	30.87	0.000	68.58	0.000	99.45
Electrum-S535-12a-dark-3-1	30.40	0.000	69.78	0.000	100.18
Electrum-S535-12a-dark-3-2	30.25	0.000	69.15	0.000	99.40
Electrum-S535-12a-dark-3-3	30.39	0.000	68.66	0.000	99.05
Electrum-S535-12a-dark-4-1	29.78	0.000	71.30	0.000	101.08
Electrum-S535-12a-dark-4-2	29.04	0.000	72.38	0.000	101.42
Electrum-S535-12a-dark-5-1	30.23	0.000	69.21	0.000	99.44
Electrum-S535-12a-dark-5-2	29.46	0.000	70.74	0.000	100.20
Electrum-S535-12a-dark-5-3	29.75	0.000	70.70	0.000	100.45
Electrum-S535-12a-6-1	29.32	0.000	71.15	0.000	100.47
Electrum-S535-12a-6-2	30.12	0.000	71.20	0.000	101.32
Electrum-S535-12a-6-3	29.57	0.000	71.27	0.000	100.84

Analysis Spot ID	Ag (wt%)	Hg (wt%)	Au (wt%)	Te (wt%)	Total
Electrum-S535-12a-7-1	29.30	0.000	69.76	0.000	99.06
Electrum-S535-12a-7-2	31.00	0.000	69.72	0.000	100.72
Electrum-S535-12a-7-3	30.34	0.000	69.34	0.000	99.68
Electrum-S535-12a-8-1	30.21	0.000	69.65	0.000	99.86
Electrum-S535-12a-8-2	30.16	0.000	70.67	0.000	100.83
Electrum-S535-12a-8-3	29.65	0.000	69.90	0.000	99.55
Electrum-S535-12a-8-4	30.21	0.000	70.42	0.000	100.63
Electrum-S535-12a-8-6	29.43	0.000	70.64	0.000	100.07
Electrum-S535-12a-9-1	29.25	0.000	70.00	0.000	99.25
Electrum-S535-12a-9-2	28.85	0.000	71.45	0.000	100.30
Electrum-S535-12a-9-3	29.29	0.000	71.75	0.000	101.04
Electrum-S535-12a-9-4	28.99	0.000	71.84	0.000	100.83
Electrum-S535-12a-9-5	29.04	0.000	71.39	0.000	100.43
Electrum-S535-12a-10-1	30.07	0.000	70.40	0.000	100.47
Electrum-S535-12a-10-2	30.13	0.000	69.93	0.000	100.06
Electrum-S535-12a-10-3	30.40	0.000	69.40	0.000	99.80
Electrum-S535-12a-11-1	29.30	0.000	70.37	0.000	99.67
Electrum-S535-12a-11-2	29.55	0.000	70.17	0.000	99.72
Electrum-S535-12a-11-3	29.60	0.000	70.17	0.000	99.77
Electrum-S535-12a-11-4	29.48	0.000	70.84	0.000	100.32
Electrum-S535-12a-12-1	29.55	0.000	70.40	0.000	99.95
Electrum-S535-12a-12-2	30.26	0.000	70.20	0.000	100.46
Electrum-S535-12a-12-3	29.85	0.000	69.86	0.000	99.71
Electrum-S535-12a-12-4	30.04	0.000	70.04	0.000	100.08
Sample S535-501a					
Electrum-S535-501a-1-1	38.67	0.000	61.72	0.000	100.39
Electrum-S535-501a-1-2	38.68	0.222	61.44	0.000	100.34
Electrum-S535-501a-1-3	37.95	0.000	62.02	0.000	99.97
Electrum-S535-501a-1-4	38.16	0.000	62.09	0.000	100.25
Electrum-S535-501a-1-5	37.71	0.000	61.75	0.000	99.46
Electrum-S535-501a-2-1	37.76	0.000	63.07	0.000	100.83
Electrum-S535-501a-2-2	37.49	0.000	62.50	0.000	99.99
Electrum-S535-501a-2-3	37.80	0.000	62.74	0.000	100.54
Electrum-S535-501a-3-1	38.45	0.000	61.79	0.000	100.24
Electrum-S535-501a-3-2	38.23	0.392	62.14	0.000	100.76
Electrum-S535-501a-3-3	37.91	0.732	62.14	0.000	100.78
Electrum-S535-501a-3-4	38.38	0.000	62.92	0.000	101.30
Electrum-S535-501a-4-1	38.12	0.136	61.98	0.000	100.24
Electrum-S535-501a-4-2	38.93	0.000	62.33	0.000	101.26
Electrum-S535-501a-4-3	38.75	0.000	61.99	0.000	100.74
Electrum-S535-501a-4-4	38.96	0.000	62.38	0.000	101.34
Electrum-S535-501a-nda-5-1	39.72	0.000	60.44	0.000	100.16

Analysis Spot ID	Ag (wt%)	Hg (wt%)	Au (wt%)	Te (wt%)	Total
Electrum-S535-501a-nda-5-2	39.50	0.000	61.33	0.000	100.83
Electrum-S535-501a-nda-5-3	38.97	0.478	60.74	0.000	100.19
Electrum-S535-501a-nda-6-1	38.86	0.000	60.85	0.000	99.71
Electrum-S535-501a-nda-6-2	38.98	0.000	61.17	0.000	100.15
Electrum-S535-501a-nda-6-3	39.12	0.000	60.69	0.000	99.81
Electrum-S535-501a-nda-6-4	39.03	0.051	61.50	0.000	100.58
Electrum-S535-501a-nda-7-1	39.79	0.043	60.80	0.000	100.63
Electrum-S535-501a-nda-7-2	38.92	0.000	61.04	0.000	99.96
Electrum-S535-501a-nda-8-1	39.30	0.000	61.23	0.000	100.53
Electrum-S535-501a-nda-8-2	39.44	0.000	61.66	0.000	101.10
Electrum-S535-501a-nda-8-3	39.36	0.000	60.26	0.000	99.62
Electrum-S535-501a-nda-8-4	39.05	0.000	60.91	0.000	99.96
Electrum-S535-501a-nda-9-1	39.22	0.000	62.16	0.000	101.38
Electrum-S535-501a-nda-9-2	38.96	0.000	61.44	0.000	100.40
Electrum-S535-501a-nda-9-3	38.86	0.000	61.87	0.000	100.73
Electrum-S535-501a-nda-9-4	38.43	0.000	61.75	0.000	100.18
Electrum-S535-501a-nda-9-5	38.77	0.000	61.42	0.000	100.19
Electrum-S535-501a-nda-10-1	39.65	0.000	61.24	0.000	100.89
Electrum-S535-501a-nda-10-2	39.27	0.000	61.42	0.000	100.69
Electrum-S535-501a-nda-10-3	38.87	0.000	61.47	0.000	100.34
Electrum-S535-501a-nda-11-1	38.43	0.000	61.80	0.000	100.23
Electrum-S535-501a-nda-11-2	38.32	0.000	61.67	0.000	99.99
Electrum-S535-501a-nda-11-3	38.93	0.000	62.23	0.000	101.16
Electrum-S535-501a-nda-11-4	39.21	0.000	61.78	0.000	100.99
Electrum-S535-501a-nda-11-5	39.21	0.000	62.07	0.000	101.28
Electrum-S535-501a-nda-11-6	39.46	0.000	61.42	0.000	100.88
Electrum-S535-501a-nda-11-7	38.02	0.000	62.61	0.000	100.63
Electrum-S535-501a-nda-11-9	38.55	0.000	61.73	0.000	100.28
Electrum-S535-501a-nda-11-10	38.37	0.000	62.82	0.000	101.19
Electrum-S535-501a-nda-12-1	39.35	0.000	61.65	0.000	101.00
Electrum-S535-501a-nda-12-3	39.71	0.000	61.51	0.000	101.22
Electrum-S535-501a-nda-12-4	39.74	0.000	61.06	0.000	100.80
Electrum-S535-501a-nda-13-1	39.34	0.000	60.82	0.000	100.16
Electrum-S535-501a-nda-13-2	39.35	0.000	61.07	0.000	100.42
Electrum-S535-501a-nda-13-3	39.51	0.479	61.59	0.000	101.58
Electrum-S535-501a-nda-14-1	39.86	0.051	61.59	0.000	101.50
Electrum-S535-501a-nda-14-2	38.60	0.043	61.70	0.000	100.34
Electrum-S535-501a-15-1	38.29	0.000	62.51	0.000	100.80
Electrum-S535-501a-15-2	38.36	0.000	61.83	0.000	100.19
Electrum-S535-501a-15-3	38.54	0.000	61.41	0.000	99.95
Electrum-S535-501a-15-4	38.28	0.000	62.57	0.000	100.85

Sample S542-271a

Analysis Spot ID	Ag (wt%)	Hg (wt%)	Au (wt%)	Te (wt%)	Total
Electrum-S542-271a-1-1	31.25	0.000	68.17	0.000	99.42
Electrum-S542-271a-1-2	31.66	0.000	68.75	0.000	100.41
Electrum-S542-271a-1-3	31.92	0.000	69.25	0.000	101.17
Electrum-S542-271a-1-4	31.74	0.000	67.99	0.000	99.73
Electrum-S542-271a-2-1	31.00	0.000	69.90	0.000	100.90
Electrum-S542-271a-2-2	31.51	0.000	69.54	0.000	101.05
Electrum-S542-271a-2-3	31.75	0.000	69.83	0.000	101.58
Electrum-S542-271a-2-4	31.81	0.000	68.91	0.000	100.72
Electrum-S542-271a-2-5	31.73	0.000	67.12	0.000	98.85
Electrum-S542-271a-2-6	31.86	0.000	68.65	0.000	100.51
Electrum-S542-271a-2-7	32.29	0.000	68.10	0.000	100.39
Electrum-S542-271a-3-1	31.46	0.000	68.76	0.000	100.22
Electrum-S542-271a-3-2	31.94	0.000	68.79	0.000	100.73
Electrum-S542-271a-3-3	32.30	0.000	68.76	0.000	101.06
Electrum-S542-271a-3-4	31.93	0.000	69.45	0.000	101.38
Electrum-S542-271a-3-5	32.54	0.000	68.71	0.000	101.25
Electrum-S542-271a-4-1	32.70	0.000	68.03	0.000	100.73
Electrum-S542-271a-4-2	32.35	0.000	68.20	0.000	100.55
Electrum-S542-271a-4-3	31.65	0.000	68.64	0.000	100.29
Electrum-S542-271a-5-1	32.03	0.000	69.30	0.000	101.33
Electrum-S542-271a-5-2	31.74	0.000	69.29	0.000	101.03
Electrum-S542-271a-5-3	32.14	0.000	69.23	0.000	101.37
Electrum-S542-271a-5-4	32.33	0.000	68.78	0.000	101.11
Electrum-S542-271a-5-5	32.12	0.000	68.95	0.000	101.07
Electrum-S542-271a-6-1	32.36	0.000	69.10	0.000	101.46
Electrum-S542-271a-6-2	32.49	0.000	69.40	0.000	101.89
Electrum-S542-271a-6-3	31.79	0.000	68.87	0.000	100.66
Electrum-S542-271a-6-4	31.77	0.000	69.20	0.000	100.97
Electrum-S542-271a-6-5	33.00	0.000	68.00	0.000	101.00
Electrum-S542-271a-7-1	31.53	0.000	68.77	0.000	100.30
Electrum-S542-271a-7-2	31.80	0.000	68.10	0.000	99.90
Electrum-S542-271a-7-light-3	32.25	0.000	68.74	0.000	100.99
Electrum-S542-271a-7-light-4	32.15	0.000	68.88	0.000	101.03
Electrum-S542-271a-7-6	32.49	0.000	68.51	0.000	101.00
Electrum-S542-271a-7-7	32.46	0.000	68.15	0.000	100.61
Electrum-S542-271a-8-1	32.11	0.000	69.10	0.000	101.21
Electrum-S542-271a-8-2	32.01	0.000	68.63	0.000	100.64
Electrum-S542-271a-8-3	32.01	0.000	68.85	0.000	100.86
Electrum-S542-271a-8-4	32.47	0.000	68.59	0.000	101.06
Electrum-S542-271a-9-1	32.11	0.000	68.08	0.000	100.19
Electrum-S542-271a-9-2	31.84	0.000	69.02	0.000	100.86
Electrum-S542-271a-9-3	31.75	0.000	68.76	0.000	100.51
Electrum-S542-271a-9-4	31.83	0.000	67.97	0.000	99.80

Analysis Spot ID	Ag (wt%)	Hg (wt%)	Au (wt%)	Te (wt%)	Total
Electrum-S542-271a-10-1	31.62	0.000	69.28	0.000	100.90
Electrum-S542-271a-10-2	32.25	0.000	69.30	0.000	101.55
Electrum-S542-271a-10-3	32.34	0.000	68.66	0.000	101.00
Electrum-S542-271a-10-4	31.74	0.000	69.11	0.000	100.85
Electrum-S542-271a-10-5	32.14	0.000	69.07	0.000	101.21
Electrum-S542-271a-10-6	32.15	0.000	67.91	0.000	100.06
Sample S544-23a					
Electrum-S544-23a-1-1	32.43	0.000	68.83	0.000	101.26
Electrum-S544-23a-1-2	32.91	0.000	66.42	0.000	99.33
Electrum-S544-23a-1-3	33.01	0.000	67.13	0.000	100.14
Electrum-S544-23a-2-1	32.43	0.000	68.17	0.000	100.60
Electrum-S544-23a-2-2	32.00	0.000	67.93	0.000	99.93
Electrum-S544-23a-2-3	32.46	0.000	68.82	0.000	101.28
Electrum-S544-23a-2-4	32.22	0.000	68.38	0.000	100.60
Electrum-S544-23a-3-1	31.81	0.000	68.61	0.000	100.42
Electrum-S544-23a-3-2	31.85	0.000	68.48	0.000	100.33
Electrum-S544-23a-3-3	32.84	0.000	67.61	0.000	100.45
Electrum-S544-23a-4-1	31.29	0.000	69.50	0.000	100.79
Electrum-S544-23a-4-2	31.69	0.000	69.31	0.000	101.00
Electrum-S544-23a-4-4	31.70	0.000	68.80	0.000	100.50
Electrum-S544-23a-4-5	31.48	0.000	69.14	0.000	100.62
Electrum-S544-23a-5-1	31.59	0.000	69.66	0.000	101.25
Electrum-S544-23a-5-2	31.30	0.000	69.58	0.000	100.88
Electrum-S544-23a-5-3	30.93	0.000	68.97	0.000	99.90
Electrum-S544-23a-5-4	31.32	0.000	68.88	0.000	100.20
Electrum-S544-23a-5-5	31.04	0.000	69.80	0.000	100.84
Electrum-S544-23a-5-6	30.81	0.000	69.52	0.000	100.33
Electrum-S544-23a-6-1	31.08	0.000	68.79	0.000	99.87
Electrum-S544-23a-6-2	31.10	0.000	69.37	0.000	100.47
Electrum-S544-23a-6-3	31.14	0.000	69.51	0.000	100.65
Electrum-S544-23a-6-4	31.27	0.000	68.76	0.000	100.03
Electrum-S544-23a-7-1	31.49	0.000	69.72	0.000	101.21
Electrum-S544-23a-7-2	31.54	0.000	69.71	0.000	101.25
Electrum-S544-23a-7-3	31.22	0.000	67.91	0.000	99.13
Electrum-S544-23a-8-1	31.23	0.000	69.84	0.000	101.07
Electrum-S544-23a-8-2	31.04	0.000	69.74	0.000	100.78
Electrum-S544-23a-8-3	31.54	0.000	69.43	0.000	100.97
Electrum-S544-23a-9-1	31.26	0.000	69.69	0.000	100.95
Electrum-S544-23a-9-2	31.37	0.000	69.06	0.000	100.43
Electrum-S544-23a-9-3	30.91	0.000	67.98	0.000	98.89
Electrum-S544-23a-10-1	31.90	0.000	69.75	0.000	101.65
Electrum-S544-23a-10-2	31.78	0.000	68.48	0.000	100.26

Analysis Spot ID	Ag (wt%)	Hg (wt%)	Au (wt%)	Te (wt%)	Total
Electrum-S544-23a-10-3	31.32	0.000	68.06	0.000	99.38
Sample S580-321a					
Electrum-S580-321a-3-1	59.57	1.460	37.75	0.000	98.78
Electrum-S580-321a-3-2	59.77	1.150	38.51	0.000	99.43
Electrum-S580-321a-3-3	60.33	1.950	38.48	0.000	100.76
Electrum-S580-321a-3-4	61.19	2.220	37.15	0.000	100.56
Electrum-S580-321a-3-5	61.43	2.210	37.27	0.000	100.91
Electrum-S580-321a-3-6	60.60	1.290	37.79	0.000	99.68
Electrum-S580-321a-3-7	61.04	1.320	38.27	0.000	100.63
Electrum-S580-321a-3-8	60.30	1.770	37.91	0.000	99.98
Electrum-S580-321a-3-9	60.59	1.020	37.51	0.000	99.12
Electrum-S580-321a-3-10	60.97	0.936	37.78	0.000	99.69
Electrum-S580-321a-4-1	59.08	1.460	38.32	0.000	98.86
Electrum-S580-321a-4-2	60.40	0.978	39.33	0.000	100.71
Electrum-S580-321a-4-3	59.95	0.758	38.63	0.000	99.34
Electrum-S580-321a-4-4	59.09	0.669	38.87	0.000	98.63
Electrum-S580-321a-5-1	59.62	1.770	38.45	0.000	99.84
Electrum-S580-321a-5-2	59.62	1.290	38.45	0.000	99.36
Electrum-S580-321a-6-1	58.80	1.500	40.05	0.000	100.35
Electrum-S580-321a-6-2	58.13	1.110	40.13	0.000	99.37
Electrum-S580-321a-6-3	59.00	1.680	40.05	0.000	100.73
Electrum-S580-321a-7-1	59.78	0.141	38.18	0.000	98.10
Electrum-S580-321a-7-2	59.60	0.000	38.54	0.000	98.14
Electrum-S580-321a-7-3	58.67	3.080	38.15	0.000	99.90
Electrum-S580-321a-7-4	59.41	1.680	37.84	0.000	98.93
Electrum-S580-321a-7-5	59.78	1.200	38.35	0.000	99.33
Electrum-S580-321a-8-1	59.91	2.210	39.05	0.000	101.17
Electrum-S580-321a-8-2	59.71	0.000	39.31	0.000	99.02
Electrum-S580-321a-8-3	60.25	1.290	38.90	0.000	100.44
Electrum-S580-321a-8-4	59.43	1.200	38.41	0.000	99.04
Electrum-S580-321a-8-5	59.33	1.330	36.12	0.000	96.78
Electrum-S580-321a-9-1	59.58	1.110	38.62	0.000	99.31
Electrum-S580-321a-9-2	59.66	0.888	38.13	0.000	98.68
Electrum-S580-321a-9-3	60.18	1.940	38.63	0.000	100.75
Electrum-S580-321a-10-1	60.30	1.770	37.24	0.000	99.31
Electrum-S580-321a-10-2	59.21	1.680	37.87	0.000	98.76
Electrum-S580-321a-10-3	60.25	1.110	37.96	0.000	99.32
Electrum-S580-321a-11-1	60.19	0.932	38.72	0.000	99.84
Electrum-S580-321a-11-2	59.53	0.932	38.41	0.000	98.87
Electrum-S580-321a-11-3	60.23	1.460	38.52	0.000	100.21
Electrum-S580-321a-dark-12-1	59.23	1.240	39.35	0.000	99.82
Electrum-S580-321a-dark-12-2	59.75	1.410	38.76	0.000	99.92

Data Supplement S4.2– U-Pb zircon geochronology by LA-ICP-MS

Part 1 – Methods

Mineral separations were done at the Pacific Centre for Isotopic and Geochemical Research (PCIGR) at the University of British Columbia, using conventional crushing, pulverizing, and wet shaking table concentration methods, followed by heavy liquid and magnetic separation.

Uranium-lead analyses were carried out using laser ablation (LA) ICP-MS methods. Analyses were done using a New Wave UP-213 laser ablation system and a ThermoFinnigan Element2 single collector, double-focusing, magnetic sector ICP-MS. The data acquisition and reduction protocol employed at the PCIGR has been described by Tafti et al. (2009), and is briefly summarised below. The best quality zircons were handpicked from the heavy mineral concentrate and mounted in an epoxy puck along with several grains of the 337 Ma Plešovice zircon standard (Sláma et al., 2007) and a 197 Ma in-house zircon monitor, and brought to a very high polish. The surface of the mount was washed for 10 minutes with dilute nitric acid and rinsed in ultraclean water prior to analysis. High quality portions of each grain, free of alteration, inclusions, or cores, were selected for analysis. Line scans rather than spot analyses were employed in order to minimize elemental fractionation during the analyses (Košler et al., 2008). Backgrounds were measured with the laser shutter closed for ten seconds, followed by data collection with the laser firing for approximately 29 seconds. The time-resolved signals were analyzed using GLITTER software (Van Achterbergh et al., 2001; Griffin et al., 2008), which automatically subtracts background measurements, propagates all analytical errors, and calculates isotopic ratios and ages. Corrections for mass and elemental fractionation were made by bracketing analyses of unknown grains with replicate analyses of the Plešovice zircon standard.

A typical analytical session at the PCIGR consists of four analyses of the standard zircon, followed by two analyses of the 197 Ma in-house zircon monitor, four analyses of unknown zircons, two standard analyses, four unknown analyses, etc., and finally two analyses of the in-house monitor and four standard analyses. Final interpretation and plotting of the analytical results employs ISOPLOT software (Ludwig, 2003). The amount of radiogenic ^{207}Pb in young zircons is extremely low; hence, counting errors are correspondingly high, and calculated errors for ^{207}Pb/^{235}U and ^{207}Pb/^{206}Pb ages are also high. Interpreted ages for the

samples dating in this study are based on a weighted average of the individual calculated $^{206}Pb/^{238}U$ ages. The amount of measured ^{204}Pb in all but a very small number of the analyses generated during the study is negligible, so no correction was made for contained common Pb.

References cited

Griffin, W.L., Powell, W.J., Pearson, N.J. and O'Reilly, S.Y., 2008, Glitter: Data reduction software for laser ablation ICP-MS; *In* Sylvester, P.J. (ed.), Laser Ablation ICP-MS in the Earth Sciences: Current Practices and Outstanding Issues, Mineralogical Association of Canada Short Course Series, Short Course 40, Vancouver, B.C., p. 308-311.

Košler, J., Forst, L., Sláma, J., 2008, Lamdate and Lamtool: spreadsheet-based data reduction for laser ablation ICP-MS; *In* Sylvester, P.J. (ed.), Laser Ablation ICP-MS in the Earth Sciences: Current Practices and Outstanding Issues, Mineralogical Association of Canada Short Course Series, Short Course 40, Vancouver, B.C., p. 315-317.

Ludwig, K., 2003, Isoplot/Ex, version 3: A geochronological toolkit for Microsoft Excel: Berkeley, California, Geochronology Center, Berkeley.

Sláma, J., J., Košler, J., Condon, D.J. Crowley, J.L., Gerdes, A., Hanchar, J.M., Horstwood, M.S.A., Morris, G.A., Nasdala, N., Norberg, N., Schaltegger, U., Schoene, B., Tubrett, M.N. and Whitehouse, M.J., 2007, Plešovice zircon — A new natural reference material for U–Pb and Hf isotopic microanalysis, Chemical Geology, v. 249, p. 1-35.

Tafti, R., Mortensen, J.K., Lang, J.R., Rebagliati, M. and Oliver, J.L., 2009, Jurassic U-Pb and Re-Os ages for newly discovered Xietongmen Cu-Au porphyry district, Tibet: Implications for metallogenic epochs in the southern Gangdese Belt; Economic Geology, v. 104, p. 127–136

Van Achterbergh, E., Ryan, C.G., Jackson, S.E. and Griffin, W.L., 2001, Data reduction software for LA-ICP-MS: appendix; *In* Sylvester, P.J. (ed.), Laser Ablation –ICP-Mass Spectrometry in the Earth Sciences: Principles and Applications, Mineralogical Association of Canada Short Course Series, Ottawa, Ontario, Canada, v. 29, p. 239-243.

Part 2 – Results

Table S4.2: LA-ICP-MS U-Pb zircon analysis results

Age estimates with 1 sigma uncertainty (Ma) | Isotopic Ratios with absolute errors

Zircon No.	$^{207}Pb/^{235}U$ Ma	$^{207}Pb/^{235}U$ +/- 1σ Error	$^{206}Pb/^{238}U$ Ma	$^{206}Pb/^{238}U$ +/- 1σ Error	$^{207}Pb/^{206}Pb$ Ma	$^{207}Pb/^{206}Pb$ +/- 1σ Error	$^{207}Pb/^{235}U$ Ratio	$^{207}Pb/^{235}U$ 1σ Error	$^{206}Pb/^{238}U$ Ratio	$^{206}Pb/^{238}U$ 1σ Error	Rho	$^{207}Pb/^{206}Pb$ Ratio	$^{207}Pb/^{206}Pb$ 1σ Error	Th/U Ratio
SU5801-1	197.5	2.3	192.8	0.82	240.2	26.82	0.2148	0.0028	0.0304	0.0001	0.33	0.0510	0.0006	0.1996
2	177.7	4.46	182.2	1.63	102.5	58.63	0.1913	0.0052	0.0287	0.0003	0.33	0.0481	0.0012	0.1808
3	192	3.33	192.1	1.17	153.2	40.48	0.2082	0.0040	0.0302	0.0002	0.33	0.0491	0.0009	0.1268
4	190.5	6.3	181.8	2.22	270.2	74.4	0.2064	0.0075	0.0286	0.0004	0.34	0.0517	0.0017	0.1294
5	182.3	5.2	181.3	1.88	200.2	65.24	0.1967	0.0061	0.0285	0.0003	0.34	0.0501	0.0014	0.1937
6	212.2	7.52	182.2	2.45	424.5	77.04	0.2325	0.0091	0.0287	0.0004	0.35	0.0553	0.0020	0.1563
7	192.8	5.94	182.9	2.04	142.3	70.74	0.2091	0.0071	0.0288	0.0003	0.33	0.0489	0.0015	0.1524
8	191.1	6.18	183.3	2.17	231.4	73.27	0.2071	0.0074	0.0288	0.0004	0.34	0.0508	0.0017	0.1508
9	191.9	5.87	183	2.02	138.8	70.23	0.2080	0.0070	0.0288	0.0003	0.33	0.0488	0.0015	0.1492
10	192.7	6.27	181.9	2.15	207.4	73.96	0.2090	0.0075	0.0286	0.0003	0.33	0.0503	0.0016	0.1344
11	194.8	3.4	190.4	1.23	253	39.79	0.2115	0.0041	0.0300	0.0002	0.35	0.0513	0.0009	0.1801
12	186.9	3.05	183.1	1.07	199.4	37.71	0.2021	0.0036	0.0288	0.0002	0.33	0.0501	0.0008	0.1362
13	183.5	2.57	198.4	0.97	105	32.91	0.1981	0.0030	0.0313	0.0002	0.33	0.0481	0.0007	0.1571
14	192.3	2.37	194.3	0.86	175.2	28.51	0.2085	0.0028	0.0306	0.0001	0.34	0.0496	0.0006	0.1988
15	189.1	2.84	198	1.08	193.6	34.64	0.2047	0.0034	0.0312	0.0002	0.33	0.0500	0.0008	0.2112
16	190.7	4.05	182.8	1.43	255.4	48.3	0.2066	0.0048	0.0288	0.0002	0.34	0.0513	0.0011	0.187
17	190.2	2.84	193.8	1.05	176.4	34.54	0.2060	0.0034	0.0305	0.0002	0.34	0.0496	0.0007	0.1722
18	189.8	4.3	197.5	1.58	181.7	52.3	0.2056	0.0051	0.0311	0.0003	0.32	0.0497	0.0011	0.1461
19	190.2	4.02	189.6	1.4	154.2	49.14	0.2060	0.0048	0.0299	0.0002	0.32	0.0491	0.0011	0.1288
20	192.4	2.56	199.3	0.96	168.5	30.62	0.2086	0.0031	0.0314	0.0002	0.33	0.0494	0.0007	0.1953

Counts /sec, background corrected

Zircon No.	^{202}Hg	^{204}Pb	^{206}Pb	^{207}Pb	^{208}Pb	^{232}Th	^{235}U	^{238}U
SU5801-1	0	0	21932	1109	2505	58782	2796	291687
2	58	0	15005	715	1450	38583	2023	211379
3	40	33	10242	498	776	17505	1296	136776
4	26	2	13360	684	1047	24636	1794	188636
5	0	0	18589	923	1791	51486	2540	263197
6	21	14	13564	743	1215	30152	1730	191162
7	85	0	26828	1299	2145	57912	3361	376628
8	0	35	14825	745	1145	31622	1948	207694
9	54	30	19871	960	1573	41979	2497	278835
10	50	0	12253	610	922	23461	1577	173024
11	100	20	19341	981	1897	47404	2508	260725
12	100	3	12361	612	936	23830	1638	173375
13	44	0	17131	815	1458	35152	2224	221520
14	1	0	24529	1203	2609	65034	3117	324043
15	3	0	16227	802	1816	44874	2117	210344
16	33	24	15860	804	1774	42081	2105	222966
17	0	0	17149	841	1696	39507	2205	227213
18	0	9	11693	574	929	22419	1509	151955
19	0	33	9754	473	718	17186	1241	132142
20	7	9	25083	1225	2748	63688	3171	323008

Data Supplement S4.3– EMPA pyrite analyses

Table S4.3: complete results for the EMPA-WDS pyrite analyses reported in Section 4.8.3.

Analysis Spot ID	S wt%	Fe wt%	Cu wt%	Au wt%	As wt%	Total
Sample V911-592						
VU-911-592_pyrite_1	54.35	46.46	-	-	0.12	100.94
VU-911-592_pyrite_2	52.42	45.84	0.01	0.014	2.20	100.47
VU-911-592_pyrite_3	54.04	46.31	-	0.007	0.33	100.67
VU-911-592_pyrite_4	50.57	45.06	0.02	0.054	4.26	99.96
VU-911-592_pyrite_5	49.92	44.83	0.02	0.067	4.93	99.76
VU-911-592_pyrite_6	51.38	45.67	0.01	0.029	3.00	100.08
VU-911-592_pyrite_7	54.24	46.74	-	0.003	-	100.98
VU-911-592_pyrite_8	54.37	46.48	0.00	0.009	-	100.86
VU-911-592_pyrite_9	54.30	46.69	-	0.007	-	101.00
VU-911-592_pyrite_10	54.08	46.69	0.00	0.008	-	100.78
VU-911-592_pyrite_11	51.10	45.41	0.01	0.018	3.55	100.10
VU-911-592_pyrite_12	53.89	46.32	-	-	0.20	100.41
VU-911-592_pyrite_13	52.60	45.85	0.01	0.013	1.79	100.28
VU-911-592_pyrite_14	51.50	45.42	0.02	0.031	3.11	100.08
VU-911-592_pyrite_15	51.21	45.33	0.01	0.013	3.29	99.86
VU-911-592_pyrite_16	50.20	44.89	0.01	0.047	4.43	99.57
Sample 1200x22V0a						
U_1200X22V0a_pyrite_1	53.59	46.49	-	-	0.19	100.27
U_1200X22V0a_pyrite_2	52.12	46.08	0.00	0.006	2.06	100.26
U_1200X22V0a_pyrite_3	50.75	45.65	0.01	0.028	3.61	100.04
U_1200X22V0a_pyrite_4	51.02	45.56	0.01	0.040	3.41	100.04
U_1200X22V0a_pyrite_5	50.54	45.44	0.06	0.029	3.56	99.63
U_1200X22V0a_pyrite_6	52.19	45.83	0.01	0.001	1.57	99.60
U_1200X22V0a_pyrite_7	50.60	45.45	0.03	0.005	3.71	99.80
U_1200X22V0a_pyrite_8	50.86	45.64	0.03	0.031	3.53	100.09
U_1200X22V0a_pyrite_9	50.81	45.54	0.03	0.000	3.44	99.82
U_1200X22V0a_pyrite_10	53.32	46.49	-	0.005	0.28	100.10
Sample 1410x17WPa						
U_1410x17WPa_pyrite_1	53.45	46.67	0.00	-	-	100.12
U_1410x17WPa_pyrite_2	50.64	45.58	0.01	0.020	3.69	99.95
U_1410x17WPa_pyrite_3	50.29	45.37	-	0.010	4.12	99.79
U_1410x17WPa_pyrite_4	50.96	45.53	0.00	0.009	3.26	99.76
U_1410x17WPa_pyrite_5	53.52	46.55	0.02	0.008	-	100.10

Analysis Spot ID	S wt%	Fe wt%	Cu wt%	Au wt%	As wt%	Total
Sample 1200x22WPa						
1200X22WPa_pyrite_1	53.13	46.46	-	0.010	0.52	100.12
1200X22WPa_pyrite_2	53.13	46.34	-	-	0.47	99.95
1200X22WPa_pyrite_3	50.91	45.61	0.01	0.021	3.19	99.74
1200X22WPa_pyrite_4	52.34	46.05	-	0.020	1.37	99.77
1200X22WPa_pyrite_5	50.27	45.38	0.01	0.012	3.93	99.59
1200X22WPa_pyrite_6	51.78	45.96	-	-	2.04	99.78
1200X22WPa_pyrite_7	52.76	46.09	-	-	0.82	99.67
1200X22WPa_pyrite_8	50.76	45.48	0.00	0.014	3.28	99.53
1200X22WPa_pyrite_9	52.34	46.15	0.00	-	1.34	99.84
1200X22WPa_pyrite_10	52.45	46.08	0.01	-	1.21	99.75
1200X22WPa_pyrite_11	52.63	46.10	0.00	0.005	0.90	99.64
1200X22WPa_pyrite_12	52.50	45.96	-	0.005	0.94	99.41
Sample S195-194a						
SU-195-194a_pyrite_1	50.81	45.82	0.01	0.024	3.97	100.63
SU-195-194a_pyrite_2	50.88	46.16	0.01	0.015	4.43	101.50
SU-195-194a_pyrite_3	52.42	45.70	0.11	0.192	0.92	99.34
SU-195-194a_pyrite_4	54.33	48.58	-	-	0.01	102.92
SU-195-194a_pyrite_5	54.25	47.45	-	0.000	-	101.69
SU-195-194a_pyrite_6	51.03	46.53	0.02	0.021	3.44	101.03
SU-195-194a_pyrite_7	51.24	46.70	0.01	0.033	3.41	101.39
SU-195-194a_pyrite_8	51.41	46.61	0.02	0.029	3.36	101.43
SU-195-194a_pyrite_9	51.37	46.65	0.02	0.026	3.39	101.45
SU-195-194a_pyrite_10	51.53	46.62	0.02	0.042	3.10	101.30
SU-195-194a_pyrite_11	52.02	46.52	0.01	0.015	2.54	101.11
SU-195-194a_pyrite_12	51.81	46.61	0.02	0.028	2.89	101.35
Sample 1380x24V3a						
U_1380x24V3a_pyrite_1	49.98	45.10	0.07	0.013	4.59	99.76
U_1380x24V3a_pyrite_2	53.75	46.66	-	-	-	100.40
U_1380x24V3a_pyrite_3	53.92	46.14	0.01	-	0.03	100.10
U_1380x24V3a_pyrite_4	52.26	44.23	0.16	0.010	2.79	99.45
U_1380x24V3a_pyrite_5	52.41	44.36	0.21	0.015	2.75	99.74

CHAPTER 5

Discussion

5.1 Comprehensive findings and contributions to the scientific community

The macro-, micro-, and nano-scale textural and petrographic observations, the trace element and isotope mineral chemical data and the detailed paragenetic analysis conducted during this study have resulted in major advances in our understanding of how bonanza-style hydrothermal gold deposits form. These advances are described in the following paragraphs.

Over the past half century, a general conclusion of geochemical investigations of gold-enriched fossil hydrothermal systems and their active geothermal counterparts has been that precious metal concentrations, no matter how extraordinary, are controlled by simple solubility (Helgeson and Garrels, 1968; Krupp and Seward, 1987; Sillitoe and Hedenquist, 2003; Williams-Jones et al., 2009; Zhu et al., 2011; Simmons et al., 2020). However, because of the low concentration of Au(I) complexes in hydrothermal fluids (Simmons and Brown, 2006), this conclusion has been challenged. In particular, some researchers have questioned the idea that simple dissolution and precipitation can account for the gold observed in ultra-high-grade, or 'bonanza', gold deposits (Chapter 2 and references therein), especially in lower temperature hydrothermal systems where both the measured and modelled concentration of gold in the hydrothermal fluids are at the level of parts per billion (Seward 1973; Gammons and Williams-Jones, 1995; Heinrich et al., 2004; Stefánsson and Seward, 2004; Zezin et al., 2011; Hurtig and Williams-Jones, 2014). Several papers have therefore recently proposed, and presented indirect evidence for, the physical transport of gold in the solid state as nanoparticles (colloids), in hydrothermal systems (Hannington et al., 2016; Gartman et al., 2018; Hannington and Garbe-Schönberg, 2019; Petrella et al., 2020).

This study builds on earlier research and provides new insight into how bonanza-type hydrothermal gold deposits may form providing: (1) the first direct evidence of the formation of colloidal gold particles and their flocculation in nano-scale hydrothermal calcite veinlets in a fossil hydrothermal system; and (2) detailed mechanisms to explain the formation of enigmatic, extraordinarily high concentrations of gold and silver in some hydrothermal ore-forming systems. The novel, nano-scale transmission electron microscope (TEM) analysis of electrum mineralisation from the Brucejack epithermal gold deposit has found evidence for the widespread existence of gold-silver (electrum) nanoparticles hosted in nano-scale veinlets (50-100 nm wide) in this fossil hydrothermal system. The nanoparticles of electrum are observed to

occur as both individual, ~5 nm diameter spheres, in which the gold is clearly identified by its 2.35 Å lattice fringe (lattice plane spacing), as well as larger, ~30-150 nm-diameter particles. Significantly, the larger particles commonly consist of multiple ~ 5 nm-wide domains, with adjacent domains displaying different crystal lattice plane orientations. This composite nature displayed by the larger particles is interpreted to indicate that they are flocculated aggregates of multiple, originally separate colloidal particles of gold. Using this evidence, the study develops a model for the formation of ultra-high-grade gold veins in fossil hydrothermal systems in which gold transport is mechanical and results from an exceptionally high degree of boiling-induced supersaturation. This supersaturation precludes precipitation of gold crystals and instead leads to the formation of colloidal particles which, with fluid evolution, e.g., pH change and electrolyte addition, flocculate to form much larger masses of solid gold.

In order to better understand how flocculation occurs in a hydrothermal system, this study has leveraged the unique array of properties of hydrothermal pyrite, namely its ubiquity and abundance, as well as its ability to record and preserve a history of fluid evolution for a wide range of physicochemical conditions, to use it as a geochemical tracer and elucidate the evolution of the hydrothermal fluids. Whereas these properties have been recognised since at least the 1950s, the intricacy of the intracrystalline chemical record of pyrite has been appreciated only recently (e.g., Peterson and Mavrogenes, 2014). The combination of high-resolution in situ techniques employed by this study, including secondary ion mass spectrometry (SIMS), laser ablation-inductively coupled plasma-mass spectrometry (LA-ICP-MS) and electron microprobe wavelength-dispersive X-ray spectroscopy (EMP-WDS), has further advanced our understanding of the potential complexity of information stored in the intracrystalline chemical record of pyrite by: (1) documenting the largest and finest scale intra-grain variations in sulphur isotope compositions ever identified in a non-biogenic sulphide mineral, and (2) providing the first example of the use of intracrystalline sulphur isotope data to interpret the occurrence of ultra-high-grade (bonanza) gold mineralisation in a hydrothermal system. Specifically, the high-resolution (5-10 μm) SIMS analyses have revealed several extraordinary decreases in $\delta^{34}S$ values (e.g., +8 to -36‰) over remarkably short distances (< 75 μm). These decreases are commonly associated with growth bands of arsenian, auriferous (invisible gold-bearing) pyrite, as determined by electron microprobe analyses, and are followed by sharp, large positive reversals in $\delta^{34}S$ values (e.g., + 30‰ over a distance of < 30 μm) in

pyrite that is in textural equilibrium with high-grade gold (electrum) mineralisation. These extreme changes in $\delta^{34}S$ values have been interpreted by this study to indicate that repeated episodes of vigorous boiling affected the hydrothermal system at Brucejack prior to its inundation by Jurassic seawater. This influx of seawater was an essential step in creating bonanza electrum mineralisation, which involved triggering the aggregation of colloidal gold suspensions through the addition of cationic flocculants and cooling. The findings of this part of the study are thus innovative in that they demonstrate the efficacy of employing high-resolution, in situ SIMS, LA-ICP-MS, and EMP-WDS techniques to map individual ore-forming events in a hydrothermal system. They are also provocative in that they suggest that fluid mixing, rather than boiling, was the ultimate trigger for bonanza-grade gold mineralisation in a hydrothermal system.

LA-ICP-MS mapping and SIMS analysis of hydrothermal pyrite by this study have also revealed that the early mineralising fluids at Brucejack were of magmatic hydrothermal (porphyry) origin, and that these fluids evolved over time to become epithermal-type fluids during telescoping of the hydrothermal system. This finding, when considered in conjunction with the results of the macro- and micro-scale paragenetic and nano-scale TEM analyses of hydrothermal veins in the deposit, have led to the identification of a previously unrecognised process by which bonanza gold may form in a hydrothermal system, namely the electrochemical flocculation of gold colloids by semiconductive p-type As-pyrite. This process stands out amongst the currently favoured processes for bonanza gold formation from hydrothermal fluids in that it does not require the existence of a steep physiochemical gradient or unusual disequilibrium conditions (cf. Simmons et al., 2020 for review). The process also offers a novel explanation for why, in many deposits, bonanza gold is paragenetically late, forming either after, or without, sulphide minerals.

5.2 Recommendations for future studies

Although our geological understanding of the Brucejack deposit, including the means by which its high-grade gold ores formed, its present mineralisation and alteration characteristics, and the overall chemical and temporal evolution of its hydrothermal fluids, have been advanced by this study, several fundamental knowledge gaps remain regarding the genesis of the deposit. These most notably are, in short:

(1) the physical and chemical conditions favouring the precipitation and/or flocculation of the ultra-high-grade mineralisation currently being mined in the VOK and West zones;

(2) the origin of hyper-enriched gold bearing fluids which gave rise to high-grade gold mineralisation in the VOK and West zones; and

(3) the genetic and temporal relationships between the hydrothermal events responsible for the different stages of alteration and gold mineralisation throughout the deposit, including occurrences of spatially-discrete, 'nuggety' ultra-high-grade gold mineralisation, as well as disseminated low grade gold mineralisation.

More specifically, while this study has demonstrated that high-grade gold in the Valley of the Kings (VOK) zone of the deposit was transported and deposited from a carbonate-rich fluid that contained gold in a nanoparticle (colloidal) state, rather than the dissolved state, our understanding of colloidal transport of gold at Brucejack is imperfect. Evidence for the existence of gold colloids at Brucejack has been found, to date, only in a relatively small number of samples and many questions remain regarding the extent to which colloidal processes were operational both within in the VOK and in satellite ore zones such as the West, Bridge, Shore, Gossan Hill and Golden Marmot zones. Beyond the issue of high-grade gold transport and deposition, the source(s) of the hyper-enriched gold-bearing fluids that gave rise to the high-grade gold mineralisation in the VOK and West zone are still very much equivocal. Exploratory deep drilling beneath the VOK, West, and Flow Dome Zones by Pretium in 2019 and early 2020 provided several significant clues that a potential porphyry source for the VOK and West zone epithermal mineralisation may lie much closer to the present mine workings than previously proposed (i.e., < 1 km radius vs. the > 5 km radius proposed by Board and McNaughton, 2013), but a genetic relationship between the extensive porphyry-style alteration encountered beneath the VOK and West zone and the epithermal mineralisation currently being mined has not yet been established, nor has the source of the porphyry-style alteration been found. Moreover, the genetic relationship between the VOK and its satellite ore zones is unclear.

In order to address these three knowledge gaps and better understand the overall evolution and hydrothermal alteration and mineralisation architecture of the Brucejack deposit, several detailed studies need to be carried out to build on the findings of this study. The first

would be a detailed transmission electron microscope (TEM) investigation of a broad suite of samples from the mine representing all generations of veins carrying bonanza-style mineralisation (Stages III to V). Such a study would help determine the extent to which colloidal transport and deposition of gold was involved in the formation of ultra-high-grade ores in the VOK (i.e., was it the principal mechanism, or simply a complementary mechanism to classical solution transport and precipitation of gold?). The results of this study could help refine a genetic model for mineralisation in the VOK and, by providing a clearer understanding of the physicochemical controls on high-grade vein formation, help guide exploration.

It is recommended that any future TEM study be complemented by a separate but complementary stable and radiogenic isotope study (C, O, H, S and Pb) of pyrite, calcite, and Zn-Pb sulphides associated with the electrum mineralisation to elucidate the sources of the mineralising fluids, metals and sulphur in the VOK and West zones, as well as in any genetically associated brownfields exploration targets being explored by the company that potentially are genetically-related (e.g., the West, Bridge, Shore, and Gossan Hill, and Golden Marmot zones). By determining the chemical (major and trace element composition, salinity, and pH) and physical (pressure, temperature) conditions under which gold was transported by the epithermal system(s) represented by each of these mining/exploration targets, a more accurate and robust genetic model for the Brucejack deposit as a whole will be developed.

A third study would be an integrated field and laboratory investigation focused on gaining a better understanding of the gold-silver mineralisation and hydrothermal alteration characteristics of the West zone and deep VOK exploration drill cores. Identification and classification of important epithermal and porphyry-style mineralisation and alteration textures would be carried out on mineralised samples using optical and scanning electron microscope (SEM) techniques. In addition, isotopic analyses of key ore and hydrothermal alteration minerals would be carried out using a combination of thermal ionisation mass spectrometry (TIMS) and ICP-MS methods; whole-rock analyses would be conducted using X-ray fluorescence (XRF) and ICP-MS; and mineral compositions would be analysed using the electron microprobe analyser (EMPA) and LA-ICP-MS. As the West zone continues to be developed by the company, additional field-based alteration and mineralisation mapping both underground and on surface would help improve our understanding of the chemical changes that accompanied alteration and

mineralisation, as well as improve understanding of the timing of alteration events relative to gold mineralisation in the West zone. Temperature information should be sought from stable isotope data as part of this study, and mineralogical observations should be integrated with existing geochronological and thermobarometric data, in an effort to better understand the evolution of the deposit in pressure-temperature-time (P-T-t) space. Important exploration vectors could be developed from this work, that among other things could test the validity of the much speculated upon genetic link between the VOK and West zone epithermal mineralisation and porphyry-style (advanced propylitic) alteration at depth.

References

Gammons, C.H., and Williams-Jones, A.E., 1995, The solubility of Au-Ag alloy + AgCl in HCl/NaCl solutions at 300°C: new data on the stability of Au (1) chloride complexes in hydrothermal fluids. Geochimica et Cosmochimica Acta, v. 59, p. 3453-3468.

Gartman, A., Hannington, M., Jamieson, J.W., Peterkin, B., Garbe-Schönberg, D., Findlay, A.J., and Kwasnitschka, T., 2018, Boiling induced formation of colloidal gold in black smoker hydrothermal fluids: Geology, v. 46, p. 39-42.

Hannington, M., Hardardóttir, V., Garbe-Schonberg, D., and Brown, K., 2016, Gold enrichment in active geothermal systems by accumulating colloidal suspensions. Nature Geoscience, v. 9, p. 299-302.

Hannington, M., and Garbe-Schönberg, D., 2019, Detection of gold nanoparticles in hydrothermal fluids. Economic Geology, v. 114, p. 397-400.

Heinrich, C.A., Driesner, T., Stefánsson, A. and Seward, T.M., 2004.,Magmatic vapor contraction and the transport of gold from the porphyry environment to epithermal ore deposits. Geology, v. 32, p. 761-764.

Helgeson, H.C., and Garrels, R.M., 1968, Hydrothermal transport and deposition of gold. Economic Geology, v. 63, p. 622-635.

Hurtig, N.C., and Williams-Jones, A.E., 2014, An experimental study of the transport of gold through hydration of AuCl in aqueous vapour and vapour-like fluids. Geochimica et Cosmochimica Acta, v. 127, p. 305-325.

Krupp, R.E., and Seward, T.M., 1987, The Rotokawa geothermal system, New Zealand; an active epithermal gold-depositing environment. Economic Geology, v. 82, p. 1109-1129.

Peterson, E.C., and Mavrogenes, J.A., 2014, Linking high-grade gold mineralization to earthquake-induced fault-valve processes in the Porgera gold deposit, Papua New Guinea. Geology, 42(5), p. 383-386.

Petrella, L., Thébaud, N., Fougerouse, D., Evans, K., Quadir, Z., and Laflamme, C., 2020, Colloidal gold transport, a key to high-grade gold mineralization? Mineralium Deposita, v. 55, p. 1247-1254.

Stefánsson, A., and Seward, T.M., 2004, Gold (I) complexing in aqueous sulphide solutions to 500 C at 500 bar. Geochimica et Cosmochimica Acta, v. 68, p. 4121-4143.

Seward, T.M., 1973, Thio complexes of gold and the transport of gold in hydrothermal ore solutions. Geochimica et Cosmochimica Acta, v. 37, p. 379-399.

Sillitoe, R.H., and Hedenquist, J. W., 2003, Linkages between volcanotectonic settings, ore-Fluid compositions, and epithermal precious metal deposits, in Volcanic, Geothermal, and Ore-Forming Fluids: Rulers and Witnesses of Processes within the Earth. Society of Economic Geologists Special Publication 23, p. 315-345.

Simmons, S.F., Tutolo, B.M., Barker, S.L.L., Goldfarb, R.J., and Robert, F., 2020, Hydrothermal gold deposition in epithermal, Carlin, and orogenic deposits: Society of Economic Geologists Special Publication 23, p. 823-845.

Zhu, Y., An, F., and Tan, J., 2011, Geochemistry of hydrothermal gold deposits: a review. Geoscience Frontiers, v. 2, p. 367-374.

Zezin, D.Y., Migdisov, A.A., and Williams-Jones, A.E., 2011, The solubility of gold in H2O–H2S vapour at elevated temperature and pressure. Geochimica et Cosmochimica Acta, v. 75, p. 5140-5153.

CHAPTER 6

Conclusions

The overarching conclusions of this study are:

(1) Spherical nanoparticles of gold (electrum) and their flocculated aggregates occur in the bonanza-stage ore veins in the Brucejack deposit. Their presence indicates that colloidal suspensions, likely produced by boiling, circulated throughout the Brucejack hydrothermal system during formation of the deposit, thereby greatly increasing the capacity of the ore-forming fluid to carry gold by enabling its physical transport.

(2) Strong negative followed by positive shifts in $\delta^{34}S$ values from in situ secondary ion mass spectrometry (SIMS) analysis of hydrothermal pyrite from the Valley of the Kings zone of the deposit suggest that episodic and possibly long-lived boiling occurred in the Brucejack epithermal system before seawater mixed with hydrothermal fluids, which caused massive flocculation of colloidal gold suspensions during late-stage ore formation.

(3) Laser ablation-inductively coupled plasma-mass spectrometry (LA-ICP-MS) and electron microprobe analyser (EMPA) trace element and SIMS sulphur isotope data for hydrothermal pyrite demonstrate that the early mineralising fluids at Brucejack were of magmatic hydrothermal (porphyry) origin, and that these fluids evolved over time to become epithermal-type fluids during telescoping of the hydrothermal system.

(4) Detailed petrographic and paragenetic analyses show that epithermal quartz-carbonate veins commonly contain bonanza gold where these veins cross-cut earlier pyrite veins. This cross-cutting relationship, when considered together with LA-ICP-MS and EMPA trace element data for pyrite from the early pyrite veins, indicates that bonanza gold occurrences in the deposit formed through electrochemically-triggered flocculation of colloidal gold suspensions by semiconductive p-type arsenian pyrite.